

ELEC BME & TRON BME 5P06

Final Project Report

Magnetically Actuated Continuum Robot for ENT (Ear, Nose & Throat) Surgery

Stakeholders: Dr. Onaizah Onaizah

Co-supervisors: Dr. Alan Wassyng, Dr. Telex Ngatched

Instructors: Dr. Vincent Leung, Dr. Cheryl Quenneville, Dr. Ian Bruce

Team 5

Friday, April 11th, 2025

Jiaqi Du	duj35	400249700	Mechatronics + BME
Sharon Cai	cais12	400238851	Mechatronics + BME
Mackenzie Keeler	keelerm	400254177	Mechatronics + BME
Jack Flannery	flannerj	400244920	Electrical + BME
Saraf Raidah	raidahs	400266577	Electrical + BME

Summary

Ear, nose, and throat (ENT) surgeries often face significant challenges due to the intricate and narrow anatomy of the sinus pathways. Navigating these complex regions demands high precision and dexterity, which can be difficult to achieve using conventional rigid surgical instruments. These traditional tools frequently require invasive procedures, such as the removal of bone or surrounding tissue, to access targeted sites, resulting in prolonged recovery times, increased risks of complications, and higher healthcare costs. In response to these limitations, this project introduces a magnetically actuated soft-continuum robot designed to provide enhanced maneuverability and precision while minimizing invasiveness. This solution aims to improve surgical outcomes, reduce operative trauma, and optimize healthcare efficiency. The system as a whole integrates four key subsystems: a soft-continuum robot, a linear actuator, a magnetic actuation system, and a navigation interface.

The magnetic actuation system comprises three orthogonally arranged electromagnetic coils. By dynamically adjusting the currents supplied to each coil, controlled magnetic fields are generated to manipulate the robot's orientation within the surgical field. In parallel, the linear actuator, driven by a stepper motor, allows for precise extension and retraction of the robot along its axial direction, enabling targeted advancement through narrow pathways. The soft-continuum robot, made of silicone and a nitinol wire core, is designed to minimize trauma while inside anatomical pathways. Its magnetized tip interacts with magnetic fields to achieve precise directional control. To ensure intuitive and real-time control, a custom-built software interface has been developed. This graphical user interface (GUI) allows surgeons to control both the magnetic and linear actuation subsystems through an integrated platform. By visualizing the robot's position and direction, users can issue coordinated commands that are instantly translated into motion. Fail-safe mechanisms have also been incorporated to prevent unintended movements and enhance overall patient safety during operation.

The proposed robotic system is designed with the goal of seamless integration into existing clinical workflows. By offering a highly controllable, less invasive alternative to traditional rigid tools, it holds the potential to significantly improve operative efficiency, reduce procedure times, and enhance patient recovery. These clinical improvements also extend to broader economic and societal benefits, including reduced hospital stays, more sustainable use of medical resources, and advancement in personalized, patient-centered treatment approaches.

In summary, this magnetically actuated soft-continuum robot represents a novel and promising tool for ENT surgery. By combining mechanical adaptability, magnetic precision, and real-time software control, it sets a new benchmark for minimally invasive surgical technology. With the potential to reshape how complex anatomical regions are accessed and treated, this system may help redefine the standards of care in ENT procedures and beyond.

Brief Project Description

A magnetically actuated continuum soft robot designed for ENT surgeries. The design integrates electromagnetic coils as a magnetic actuation system for directional control, a linear actuation system for extension and retraction, and a soft continuum robot with a magnetized tip, which are all controlled using a user interface, enabling intuitive, precise, and dexterous surgical control.

Need Statement

Design a magnetically actuated continuum robot for use in ENT surgery, enhancing dexterity in navigating complex and confined anatomical spaces while remaining less invasive than current tools.

Declaration of Academic Achievement and Consent

As a future member of the engineering profession, the student is responsible for honestly performing the required work without plagiarism and cheating. Submitting this work with my name and student number is a statement of understanding that this work is my own and adheres to the Academic Integrity Policy of McMaster University and the Code of Conduct of the Professional Engineers of Ontario.

Submitted by [Jiaqi Du, duj35, 400249700]

As a future member of the engineering profession, the student is responsible for honestly performing the required work without plagiarism and cheating. Submitting this work with my name and student number is a statement of understanding that this work is my own and adheres to the Academic Integrity Policy of McMaster University and the Code of Conduct of the Professional Engineers of Ontario.

Submitted by [Sharon Cai, cais12, 400238851]

As a future member of the engineering profession, the student is responsible for honestly performing the required work without plagiarism and cheating. Submitting this work with my name and student number is a statement of understanding that this work is my own and adheres to the Academic Integrity Policy of McMaster University and the Code of Conduct of the Professional Engineers of Ontario.

Submitted by [Mackenzie Keeler, keelerm, 400254177]

As a future member of the engineering profession, the student is responsible for honestly performing the required work without plagiarism and cheating. Submitting this work with my name and student number is a statement of understanding that this work is my own and adheres to the Academic Integrity Policy of McMaster University and the Code of Conduct of the Professional Engineers of Ontario.

Submitted by [Jack Flannery, flannerj, 400244920]

As a future member of the engineering profession, the student is responsible for honestly performing the required work without plagiarism and cheating. Submitting this work with my name and student number is a statement of understanding that this work is my own and adheres to the Academic Integrity Policy of McMaster University and the Code of Conduct of the Professional Engineers of Ontario.

Submitted by [Saraf Raidah, raidahs, 400266577]

Table of Contents

Summary	2
Brief Project Description	2
Need Statement	3
Declaration of Academic Achievement and Consent	4
Table of Contents.....	5
List of Abbreviations and Symbols.....	10
List of Figures	11
List of Tables	17
Chapter 1	18
1.1 User Needs	18
1.1.1 Background	18
1.1.2 Impact	19
1.2 Design Inputs	20
1.2.1 Project Objective.....	20
1.2.2 Design Inputs	20
1.3 Design Process	25
1.3.1 Electromagnetic Fields.....	25
1.3.2 Magnetic Field Generation	26
1.3.3 Magnetic Forces.....	27
1.3.4 Mechanical Structure	29
1.3.5 Simulation and Mathematical Modeling.....	30
1.4 Preliminary Risk and Assessment.....	32
1.4.1 Health and Safety and Associated Risks.....	32
1.4.2 Relevant Standards.....	32
Chapter 1 References	34
Chapter 2	37
Summary	37
Brief Project Description	38
Need Statement	38
2.1 Design Outputs.....	38
2.1.1 Prototype Design Outputs	38
2.2 Final Decision: Concept.....	46
2.2.1 Soft Continuum Robot and Linear Actuation System	46

2.2.2 Magnetic Actuation System.....	48
2.3 Final Decision: Risk and Compliance Management.....	50
2.3.1 Health and Safety	50
2.3.2 Ethical Concerns	54
2.3.3 Standards and Codes	54
2.4 Final Decision: Proof-of-Concept and Verification.....	56
2.4.1 Soft Continuum Robot and Linear Actuation System	56
2.4.1.1 Set-up	56
2.4.1.2 Components	58
2.4.1.3 Design Calculations	58
2.4.1.4 Design Verification.....	58
2.4.2 Magnetic Actuation System.....	60
2.4.2.1 Set-up	60
2.4.2.2 Components	62
2.4.2.3 Design Calculations	62
2.4.2.4 Circuit Logic	63
2.4.2.5 Secondary Components	63
2.4.2.6 Design Verification.....	64
Chapter 2 References	66
Chapter 3	69
Summary	69
Brief Project Description	69
Need Statement	69
3.1 Design Prototype Plan.....	70
3.1.1 Magnetic Actuation System.....	70
3.1.1.1 Implementation	70
3.1.1.2 Coil Design: Initial Prototype	70
3.1.1.3 Coil Design: Next Prototype Iteration	71
3.1.1.4 Circuit Design for the Coils	75
3.1.1.5 Microcontroller for the Coils	77
3.1.1.6 Coil Simulation Software.....	77
3.1.1.7 Magnetic Actuation System Design Takeaways for Final Prototype	82
3.1.2 Soft Continuum Robot	82
3.1.2.1 Implementation	82

3.1.2.2 Robot Tip and Body: Multistep Prototyping	82
3.1.3 Linear Actuation System.....	85
3.1.3.1 Implementation	85
3.1.3.2 Microcontroller for the Motor.....	86
3.1.4 Robot Navigation Interface.....	87
3.1.4.1 Implementation	87
3.1.4.2 Framework	87
3.1.4.3 Software Architecture Feature	88
3.1.5 Implementation of Risk Mitigation and Compliance Strategies.....	88
3.2 Design Verification Plans	90
3.2.1 Verification of Prototype Design Outputs	90
Chapter 3 References	112
Chapter 4	114
4.1 Implementation	114
4.1.1 Magnetized Continuum Robot.....	114
4.1.1.1 Iterative Process	114
4.1.1.2 Final Prototype.....	116
4.1.1.3 Final Prototype Validation.....	117
4.1.2 Magnetic Actuation System.....	118
4.1.2.1 Iterative Process	118
4.1.2.2 Final Prototype.....	121
4.1.2.3 Coils	124
4.1.2.4 Motor Drivers.....	124
4.1.2.5 Final Prototype Validation.....	125
4.1.2.6 Magnetic Actuation System Risk Management.....	127
4.1.3 Linear Actuation System.....	127
4.1.3.1 Iterative Process	127
4.1.3.2 Final Prototype.....	129
4.1.3.3 Testing Methods.....	130
4.1.4 Robot Navigation Interface and Simulations.....	131
4.1.4.1 Framework	132
4.1.4.2 Software Architecture	133
4.1.4.3 Hardware Integration	135
4.1.4.4 Building, Testing, Verifying	135

4.2 Results and Discussions.....	140
4.2.1 Soft Continuum Robot	140
4.2.1.1 Verification Results	140
4.2.1.2 Modelling and Analysis Results	145
4.2.1.3 Technical, Non-Technical, Risk, and Compliance Strategies.....	147
4.2.1.4 Assumptions, Limitations, and Constraints	148
4.2.2 Magnetic Actuation System.....	149
4.2.2.1 Verification Results	149
4.2.2.2 Modelling and Analysis Results	154
4.2.2.3 Technical, Non-Technical, Risk, and Compliance Strategies.....	155
4.2.2.4 Assumptions, Limitations, and Constraints	156
4.2.3 Linear Actuation System.....	157
4.2.3.1 Verification Results	157
4.2.3.2 Modelling and Analysis Results	159
4.2.3.3 Technical, Non-Technical, Risk and Compliance Strategies.....	161
4.2.3.4 Assumptions, Limitations and Constraints	162
4.2.4 Robot Navigation Interface and Simulations.....	162
4.2.4.1 Verification Results	163
4.2.4.2 Modelling and Analysis Results	170
4.2.4.3 Technical, Non-Technical, Risk, and Compliance Strategies.....	175
4.2.4.4 Assumptions, Limitations, and Constraints	177
4.3 Future Work	179
4.3.1 Soft Continuum Robot	179
4.3.2 Magnetic Actuation System.....	180
4.3.3 Linear Actuation System.....	180
4.3.4 Robot Navigation Interface and Simulations.....	181
4.4 Reflections and Recommendations.....	182
4.4.1 Successes, Failures, and Setbacks.....	182
4.4.2 Advice to the Future Cohort	183
Chapter 4 References	184
Chapter 5	187
Summary	187
Implementation, Analysis and Results.....	187
Proposed Future Work	188

Appendix A: Design Output Calculations	189
Calculation 1: Coil Temperature.....	189
Calculation 2: Linear Actuation Resolution and Velocity.....	189
Appendix B: Software.....	191
Code 1: Coil Control.....	191
Code 2: Linear Actuation Control.....	192
Code 3: Python Simulation	195
Code 4: Python Interface	198
Code 5: Arduino Integration	209
Appendix C: Hazards and Risk Analysis.....	214

List of Abbreviations and Symbols

Table 1. List of abbreviations used in this report

Abbreviation	Definition
ENT	Ear, nose, throat
GUI	Graphical user interface
PWM	Pulse width modulation
EMI	Electromagnetic interference
DHF	Design history file
OR	Operating room
EMF	Electromagnetic Field

Table 2. List of symbols used for given equations

Symbol	Descriptor	Unit
F	Force	Newtons (N)
Q and q	Charge	Coulombs (C)
R and r	Distance	Meters (m)
ϵ_0	Permittivity of Free Space	$C^2/N * m^2$
E	Electric Field	Meters (m)
B	Magnetic Field	Tesla (T)
H	Magnetic Field Strength	Amperes per Meter (A/m)
μ	Magnetic Permeability	Newtons per Ampere Squared (N/A^2)
I	Current	Amperes (A)
m	Magnetic Moment	Amperes per Meter Squared (A/m^2)
θ	Angle Theta	Radians (rad)
Φ_B	Magnetic Flux	Webers (Wb)
T	Torque	Newton Meters (Nm)
l	Length	Meters (m)

\mathcal{C}	Configuration	N/A
$g(X)$	Position ($P(x)$) + Orientation ($R(x)$)	N/A
SE	Special Euclidean Group	(x, y, z)
$\Phi(X)$	Deformation Equation	N/A
ξ	Strain	N/A
q	Position or Orientation	Radians or Meters (m)
$M(q)$	Mass index/Inertia	Kilograms Meters Squared ($kg \cdot m^2$)
$q^.$	Velocity	Meters per Second (m/s)
$q^{..}$	Acceleration	Meters per Second Squared (m/s^2)
τ_R	Combined Input Forces	Newton's (N)
$G(q)$	Gravity Vector	Newton's (N)
$C(q, q^.)$	Coriolis and Centrifugal Effects	Force or Torque (N or Nm)

List of Figures

- Figure 1. Diagram showing two point charges, Q1 and Q2, experiencing vector force F, from the origin point [18]..... 25
 Figure 2. The magnetic field at a point P due to a current loop [18] 27
 Figure 3. A bar magnet in an external magnetic field with the applied force F shown [18]. 28
 Figure 4. Flowchart of magnetic field interactions for magnetization simulation..... 29
 Figure 5. Top-view and side view of dimensioned CAD drawing of the right half of the tip mould showing a tip diameter of 4 mm and length of 20 mm 43
 Figure 6. Results from the CMOS-Magview, measuring the magnetic field strength of the robotic tip, producing an optical and graphical representation of the field generated at its north pole. The

image on the top left shows the CMOS-Magview in use, the magnetized tip of the robot is placed such that the strength of the north pole can be read by the Magview sensor. The images on the top right and bottom are produced by the Magview system, the red indicates the north pole magnetic field, and the blue indicates the south pole magnetic field. Multiple measurements were taken for the north and south poles of the robot tip and the average of all the measurements was considered in the outputs.	43
Figure 7. The mass of the robotic tip is measured to be 0.86g on a CGoldenwall high precision lab scale.....	44
Figure 8. Nitinol wire with attached magnetized tip, showcasing 360 degrees flexibility of wire.	44
Figure 9. The image on the left shows the TLV493D-A1B6 magnetic sensor measuring generated magnetic field of coil from 10cm away. The graph in the top right presents the sensor reading in the Y plane on Infineon Magnetic Sensor app. The bottom right shows the navigation interface that actuates the coil activaton.	45
Figure 10. Top-view dimensioned CAD drawing of extruder gear showing an outer gear diameter of 9 mm.....	45
Figure 11. Integration of soft continuum robot, linear actuation system, and magnetic actuation system with user interface of proposed solution.....	46
Figure 12. The cantilever bending lever relative to point load P with resulting deflection δ_{max} , the angle of rotation θ , and the beam length l	47
Figure 13. Fault Tree Analysis (FTA) of proposed solution	51
Figure 14. Wiring connections between the power supply, Arduino microcontroller, L298 driver and stepper motor.....	56
Figure 15. Physical setup of linear actuator with all components	57
Figure 16. Physical component and labelled diagram of the extruder design of the linear actuator [29]	57
Figure 17. The period for each OUT pin was found to be 24.00ms, measured using the scope function from a Hantek 2D42 Oscilloscope.....	59
Figure 18. The before and after position of the wire after spinning the motor for one second with 2.4cm of insertion into pathway model.....	60
Figure 19. Labelled LTSpice simulation of the coil circuitry used in the proof-of-concept demo (Left), shown beside the actual circuit created and used in the demo (Right). Colour highlights are included to show how the LTSpice corresponds to the real circuit use	61
Figure 20.Photo of coil circuitry showing the LEDs and buttons associated with the two coils for proof-of-concept prototype.	61
Figure 21. A proof-of-concept mock-up (not to scale) showcasing the magnetic actuation system. There are three coils (middle three components) connected to a breadboard with surface mount components (top right), which are driven by a microcontroller (top left).	70
Figure 22. The Engineering Drawing for the base of one coil made in Autodesk Inventor 2024. The dimensioned drawing, with units in mm, above acts as the instructions to the laser printer on how to properly cut out the design: red lines are engraved superficially into the wood, blue lines are internal cuts that should be made first, and then green lines indicate external lines that should be cut at the end. The MDF wood piece cut into was 304.800 mm by 484.00 mm, and the blank piece with the sketches drawn on it reflects those exact dimensions.	73
Figure 23. The fully assembled solenoid coil base, constructed from laser-printed MDF wood. The structure consists of two end plates secured to the base and frame using 7/16" x 1-1/2" bolts,	

7/16" nuts, and washers. Three parallel slots provide designated spaces for wire winding, though no wires have been wrapped around it yet.....	74
Figure 24. The fully assembled solenoid coil base is constructed from laser-printed MDF wood, with 105 turns of 14-Gauge copper wire ($N_{turns} = 105$), showcasing a partially completed coil prototype.	75
Figure 25. Labelled LTSpice XVII simulation of the coil circuitry used in the prototype, where three coils are supplied with voltage from a power supply, and a microcontroller controls their ON and OFF states through MOSFET circuit logic.	76
Figure 26. Screen capture of Python visualization using MagPy and PyVista library. Two coils with same parameters pointed towards magnetic field sensor depicted by yellow sphere on the z-plane.....	79
Figure 27. Flowchart of executable steps in verification plan for software simulation.....	80
Figure 28. Infographic depicting the primary fabrication process for the soft continuum robot. This multi-step process covers the production and assembly of the robot's magnetized tip and body with uniform helical protrusions.....	83
Figure 29. 3D model and sketch of secondary mould with helical protrusions to form the robot's silicone body, made in Autodesk Inventor 2024.	84
Figure 30. Forward Actuation System design for linear movement of the soft-continuum robot. The stepper motor (top left), controlled by an Arduino microcontroller and related circuitry (bottom right), has a screw mechanism which holds the external portion of the robot's wire core (top right) steady during actuation.....	85
Figure 31. The circuit connecting the stepper motor to the ESP32 microcontroller using a TMC 2209 motor driver. The driver separates the 12V current from the input current from the microcontroller.....	86
Figure 32. Workflow between the robot navigation interface and the physical hardware with subsequent components outlined.	88
Figure 33. Schematic of the general set-up used for verification plan 4. A digital caliper will be utilized to gain accurate dimensional measurements. Above, the magnetized tip of the soft-continuum robot is measured to ensure consistency and adherence to design requirements.	91
Figure 34. Schematic of the general set-up used for verification plan 8. A tared scale will be used to measure the mass of the magnetized tip.	93
Figure 35. Schematic of the general set-up used for verification plan 9. The soft-continuum robot's flexibility and ability to bend in a 360° fashion can be demonstrated with a simplified version of bending analysis.....	94
Figure 36. Schematic of the general set-up used for verification plan 10. The soft-continuum robot is acted upon by a permanent magnet and the angle of deflection of measured.	94
Figure 37. Schematic of the general set-up used for verification plan 12, using a photo taken from the manual of the Extech EX470A [20]. The Extech EX470A temperature probe is connected to the multimeter and in direct contact with the coil, allowing for a temperature measurement of the coil to be taken.	96
Figure 38. 3D visualization of the coil's generated magnetic field using Python. The blue lines represent the electromagnetic coil with the magnetic sensor shown as a yellow sphere placed 16 cm away.	97
Figure 39. Photo of the general setup used for verification plan 13. The Infineon TLx493D-A1B6 3D Magnetic Sensor is placed near the coil, detecting the magnetic field being produced.	97

Figure 40. Schematic of the general set-up used for verification plan 15, using a photo taken from the manual of the Extech EX470A [23]. The Extech EX470A probes are connected to ground and the coil, allowing for a voltage measurement to be taken.....	98
Figure 41. Schematic of the general set-up used for verification plan 16, using a photo taken from the manual of the Hantek website [26]. The Hantek 2D42 oscilloscope probes are connected to ground and the coil, allowing PWM measurements to be taken.	99
Figure 42. Schematic of the general set-up used for verification plan 19. The position of the soft continuum robot before and after each movement will be recorded. The displacement measured will allow for comparison with theoretical values.....	100
Figure 43. Robot B, 4mm diameter and 0.5mm wire core, post-fabrication process detailed in section 3.1.2 of this report. The features of the magnetized tip and the body with helical protrusions are clearly visible. This iteration was essential in validating the fabrication process.	114
Figure 44. Resulting from its thinner nitinol core of 0.2mm, Robot C was very soft and flexible, providing it with the ability to interact with the generated magnetic fields to a greater degree than robots with the thicker nitinol wire core. Despite the advantages of flexibility and dexterity, the thinner wire resulted in failed linear translation.	115
Figure 45. Robot D, 2mm diameter and 0.2mm wire core, the magnetized tip has a very small surface area for interaction and the body of the robot has many flaws due to the difficult demoulding process for such small robots. This iteration was essential in highlighting the limitations of the fabrication process.	115
Figure 46. Robot A, 4mm diameter and a 0.5mm nitinol wire core. The thicker 1.2mm actuator wire can also be seen at the tail end of the robot. This robot was developed using the insights gained by previous iterations and meets all design requirements outlined in section 1 of the report.	116
Figure 47. Robot A, the final iteration, passing through the nasal opening into the sinus area within a large-sized anatomical phantom model. The magnetized tip and helical protrusions are clearly visible on Robot A.	116
Figure 48. Robot A, the final iteration, traverses through a clear modeled phantom pathway. .	117
Figure 49. Hand-Wound Coil (Iteration #1) – A custom built, hand-wound solenoid coil with a radius of 2.5 cm, length of 25 cm, and 145 turns of AWG 14 enameled copper wire.	119
Figure 50. The power supply unit features reverse polarity protection, a built-in breaker switch and is rated for up to 60V and 30A.....	119
Figure 51. Hand-Wound Coil (Iteration #2) – A custom built, hand-wound solenoid coil with a radius of 10 cm, length of 10 cm, and 87 turns of AWG 14 enameled copper wire.	120
Figure 52. An ESP32 on a breadboard with 2 MOSFET switch circuits; when the left button is pressed, the GPIO output will provide a PWM (Pulse Width Modulation) signal to the left MOSFET, which will connect the 9V power source to the coil, providing it with current. The same happens with the right button and right MOSFET. The MOSFET is rated up to 9V to protect the 9V battery from interacting with the ESP.....	121
Figure 53. Three custom built, hand-wound solenoid coils configured to be along the X, Y and Z planes, each with the same 5 cm radius, 5 cm length, and 450 turns using 14 AWG enameled copper wire. The coils generate a maximum field strength of 120mT at the center when powered by 30V/20A.....	122
Figure 54. Final design motor driver boards (x3) inside a box to conceal the wiring. The boards stored in the top left and bottom left are both AMC AB50A200I Motor Drivers. The bottom right	

stores a Cytron MDS40B Motor Driver, and the top right stores the ESP32 board with the amplification circuit.....	123
Figure 55. A photo of the custom-designed level-shifting circuit converting the ESP32's 3.3V PWM/direction signals to 5V logic required by motor drivers. The breadboard on top contains the MOSFET amplification circuit, and the breadboard below contains the ESP32, and the motor driver connected to the linear actuator. Note that the linear actuation system is unrelated to the magnetic actuation system and will be elaborated in subsequent sections.....	123
Figure 56. A PWM wave measured on a Hantek oscilloscope probed from the ESP32 output pin, before the amplification circuit. The oscilloscope is showing a PWM wave going from 0V to 3.3V with a Duty cycle at around 5%.....	126
Figure 57. A separate PWM wave measured on a Hantek oscilloscope, this time probed from after the amplification circuit. The oscilloscope is showing a PWM wave going from 0V to 4.72V, with a Duty cycle at around 95%. This showcases that the amplification circuit can get a 3.3V signal into a 5V signal.....	127
Figure 58. First iteration of the linear actuator and L298 motor driver.....	128
Figure 59. Second iteration of the linear actuator. Parts were printed from grey resin and red PLA.....	128
Figure 60. New TMC 2209 motor driver.....	129
Figure 61. Side view of the final prototype	130
Figure 62. The circuit of the TMC 2209 motor driver connected to an ESP32 microcontroller. The final integration combined the TMC2209 into the circuit of the magnetic actuation system.....	130
Figure 63. A tape was attached to a wire and placed at the 10mm mark of a ruler. The stepper motor is then instructed to rotate 360o, and the difference in initial and final position is measured.....	131
Figure 64. 3D visualization of robot navigation interface presenting control panels for the magnetic actuation system and linear actuation system as well as fail-safe mechanisms.....	132
Figure 65. Workflow between the robot navigation interface and the physical hardware with subsequent components outlined.....	133
Figure 66. Left image shows preliminary build of interface showcasing basic functionality of the magnetic actuation system in 2D space. Middle image presents the enhancement of the interface from the previous iteration with integration of linear actuation system in 2D space. Right image presents the final iteration of the interface presenting the magnetic actuation system, linear actuation system, and the safety mechanisms implemented in 3D space.....	136
Figure 67. Breadboard circuit applied in early testing phase to observe the Arduino logic housed by the ESP32 microcontroller that was initiated by the interface with visual indicators of the magnetic and linear actuation systems usage.....	137
Figure 68. Left image presents the robot behaviour to the activation of the X plane coil causing an attraction force of the robot to the coil. Right image presents the interface interaction that caused the X plane coil activation (in green), resulting in the robot position seen on the left... ..	138
Figure 69. Top image shows the integrated system at use inside phantom model with upwards orientation via attraction force from the magnetic actuation system on the robot using the interface. Bottom image shows the integrated system at use inside phantom model with downwards orientation via repulsion force from the magnetic actuation system on the robot using the interface.....	139
Figure 70. Experimental set up for Plan 4. Digital caliper can be seen with robots A to D.....	140

Figure 71. Test setup for Plan 6 with the CMOS-Magview sensor.....	141
Figure 72. Comparing the results from verification plans 6 and 10, demonstrating the relationship between robot nitinol wire core diameter, deflection angle, and magnetic field strength.....	146
Figure 73. Experimental set-up for 13. From left to right, the images show TLV493D-A1B6 Magnetic Sensor being used to measure a field at 10cm of the coil edges of iterations 1 and 2, then the final prototype.....	150
Figure 74. A screenshot of the resulting magnetic field measurements acquired using the TLV493D-A1B6 Magnetic Sensor. In these verification test cases, the X-axis (red) represented the field of interest.....	150
Figure 75. Experimental setup for 15. Sample Hantek1 2D42 oscilloscope outputs showing the PWM duty cycle set to 95% (left) and 0% (right). These photos were taken when testing the final prototype.....	151
Figure 76. Experimental set up for 16. Sample Hantek 2D42 oscilloscope outputs showing the direction pin voltage set to high (left) and low (right). These photos were taken when testing the final prototype.....	151
Figure 77. Plot of measured magnetic field vs. distance from the edge of the coil, for one of the final coils when various currents are applied to the coil.....	154
Figure 78. Plot of the measured magnetic field vs distance from the edge of the coil, for all three coils used in the final prototype. 15A were applied to all three coils. The plot shows agreement between the magnetic fields produced by all three coils.	155
Figure 79 (Left) and Figure 80 (Right). The initial and final positions of the wire under a load.	158
Figure 81 (Left) and Figure 82 (Right). Initial and final positions of the wire after ten oscillating extension and retraction motion.....	158
Figure 83. The repeatability test results of Plan ID 20.	159
Figure 84. Accuracy under load test results of Plan ID 21	160
Figure 85. Results of oscillation test of Plan ID 22.	160
Figure 86. The results of the wire compatibility tests of Plan ID 23.	161
Figure 87. Simulated results of magnetic field generated over varying distances with a constant current of 15A applied.	170
Figure 88.Simulated results of magnetic field generated over varying distances with a constant current of -15A applied.	171
Figure 89 Simulated and experimental magnetic field strength from positive current variations	172
Figure 90 Simulated and experimental magnetic field strength from negative current variations	172
Figure 91 Magnetic field superposition principle with positive current input of 15A	173
Figure 92Magnetic field superposition principle with negative current input of -15A	174
Figure 93. Table C.1 – Examples of hazards from ISO 14971:2019.....	214

List of Tables

Table 1. List of abbreviations used in this report.....	10
Table 2. List of symbols used for given equations	10
Table 3. Cost break-down of components for the final iteration.....	42
Table 4. Inventory list of all components used for the actuator for proof-of-concept prototype .	58
Table 5. Inventory list of all components used in the coil proof-of-concept demo.....	62
Table 6. Summary of all verification plans and associated tests.	105
Table 7. Verification results for Robot B.....	142
Table 8. Verification results for Robot C.....	143
Table 9. Verification results for Robot D	143
Table 10. Verification results for Robot A, the final iteration.....	144
Table 11. Verification results for magnetic actuation system iteration 1.....	152
Table 12. Verification results for magnetic actuation system iteration 2.	152
Table 13. Verification results for the final design of the magnetic actuation system.....	153

Chapter 1

1.1 User Needs

1.1.1 Background

The use of minimally invasive surgical procedures, particularly in ear, nose, and throat (ENT) surgery, is crucial due to the complexity of human anatomy and the limitations of traditional surgical instruments. ENT surgeries often involve navigating intricate and confined anatomical structures, such as the sinuses, which pose significant challenges for surgeons. Variations in sinus structure between patients, as well as differences between an individual's right and left sides, add to the complexity of these procedures [1].

As such, traditional surgical instruments, being rigid, limit a surgeon's ability to access these difficult areas without risking damage to surrounding tissues [2]. The limited flexibility and dexterity of these tools require surgeons to frequently switch between instruments, increasing operative time and the risk of complications [1][3]. In discussions with Dr. Sarah Khalife, an ENT surgeon who subspecialized in sinus surgery, it was noted that in certain procedures, such as sinus polyp removals, the large diameters and rigidity of the current tools often require expanding narrow passageways by surgically removing bone. This increases trauma and prolongs recovery, thus highlighting the need for more flexible, minimally invasive methods.

Magnetically actuated continuum robots (MCRs) present a promising solution by offering the flexibility and smooth movement necessary to navigate narrow, tortuous pathways, such as sinus cavities [4][2]. The use of external magnetic fields to control these robots allows for precise, remote manipulation, enhancing dexterity and minimizing trauma to the surrounding tissues. Magnetic actuation also eliminates the need for bulky onboard components, allowing for miniaturization while improving maneuverability in confined surgical spaces [4].

For sinus surgeries, where visibility and accessibility of the surgical area are key, the combination of magnetic actuation with continuum robot flexibility directly addresses major limitations of traditional tools.

Design a magnetically actuated continuum robot for use in ENT surgery, enhancing dexterity in navigating complex and confined anatomical spaces, while remaining less invasive than current tools.

1.1.2 Impact

The development of magnetically actuated continuum robots for ENT surgeries has the potential to significantly impact both healthcare providers and patient outcomes. From the perspective of surgeons, such a system would reduce operating time by minimizing the need for frequent tool exchanges and enabling more precise control in confined anatomical spaces [1]. Reducing operation time can result in significant cost savings for healthcare providers given that the mean cost of operation room time can be around \$36/minute [5].

Additionally, more precise robotic control can lead to fewer complications, reducing the need for follow-up surgeries or extended hospital stays [3]. Studies on similar minimally invasive techniques suggest that patients may experience shorter recovery times and less postoperative discomfort due to the minimally invasive nature of the procedures [6]. This would allow patients to have a shorter hospital stay and return to daily activities more quickly, alleviating both physical and financial burdens.

As mentioned previously, the use of magnetically actuated continuum robots could lead to substantial cost savings for healthcare systems. With the potential economic benefit resulting from reduced surgical times and better patient outcomes, healthcare providers can increase the number of surgeries performed, further boosting efficiency and revenue.

Socially and culturally, the shift toward advanced surgical technologies aligns with the growing demand for personalized healthcare. As surgical tools become more refined and capable of addressing individual anatomical variations, patient trust and satisfaction are expected to increase. By offering less invasive solutions, patients experience less postoperative pain, fewer complications, and faster recoveries, enhancing their overall quality of life. Additionally, as ENT surgeries become less invasive, they may become more widely accessible to patients who might otherwise have been hesitant due to the potential risks and complications associated with traditional surgical methods. This technology also supports the broader societal trend toward more personalized and less disruptive healthcare [1][5].

In conclusion, magnetically actuated continuum robots represent a promising advancement in surgical technology. By addressing the critical needs of surgeons and offering improved patient outcomes, this technology has the potential to reshape ENT surgeries, bringing economic, societal, and environmental benefits.

1.2 Design Inputs

1.2.1 Project Objective

The purpose of this project will be to design and create a magnetically actuated continuum robot for sinus surgeries. The robot will assist surgeons when performing procedures within the narrow, nonlinear, and anatomically unique sinus cavities. The first objective will be to create a functional prototype of a continuum robot that can be magnetically actuated. A time-dependent second objective would be to add a specialized application to the robot. Potential applications to aid in the surgical intervention include graspers to take biopsies, lasers for polyp removal, a balloon for sinus dilation, a camera for improved visualization, and medication injection. Expected outcomes of the project include a reduction in the level of invasion for the procedures and seamless integration with the technologies and workflows in the OR.

1.2.2 Design Inputs

Below are limits and constraints that apply to the final prototype's design, as well as some evaluation criteria for these design concepts.

1. High-level system requirements

1.1. Ergonomic Usability and Ease of Control: Compliance to ISO 62366-1.

Justification: Usability and ISO guidelines are necessary for approval of device in the market. ISO 62366-1 outlines requirements for the application of usability engineering to medical devices, aiming to reduce use errors and improve overall user performance and safety.

1.2. Electrical Safety and Thermal Limits: Compliance to IEC 60601-1.

Justification: Electrical safety and thermal limits apply especially to the magnetic actuation system of the system. IEC 60601-1 defines general requirements for the basic safety and essential performance of medical electrical equipment. Electrical safety ensures that the device does not pose a risk of electric shock to the patient or operator, while thermal safety ensures that heat generated by motors, magnetic coils, or power circuits does not lead to tissue damage or device malfunction. Therefore, compliance with this standard is important to meet regulatory requirements, minimize hazards, and ensure the safe integration of the system into surgical environments.

1.3. Biocompatibility of Materials: Compliance to ISO 10993-1.

Justification: Test for the biocompatibility of the nitinol wire and robotic tip materials to ensure safety within the patient without adverse effects. ISO 10993-1 provides a framework for evaluating the biocompatibility of medical device materials that come into direct or indirect contact with the human body. Testing according to ISO 10993-1 ensures that all materials used are safe for the intended duration and type of contact.

2. Soft-continuum robot requirements

- 2.1. Magnetization of robotic tip: the tip must be sufficiently magnetized to produce a magnetic field of at least 20mT in magnitude.

Justification: A magnetic field of at least 20mT is necessary to ensure effective actuation by the external coil system. This threshold is based on previous research and experimental findings on soft magnetic robots. A magneto-optical sensor, the CMOS-Magview, will be used to measure the field strength of the tip.

- 2.2. Magnetization of wire: the wire should not be magnetized.

Justification: Magnetic interference from the wire could lead to uncontrolled or unpredictable actuation of the robotic tip. Ensuring the wire remains non-magnetic preserves the precision of the actuation system. This will be verified using a magneto-optical sensor, the CMOS-Magview, to check for unintended magnetization.

- 2.3. Materials of robotic tip: the materials of the robotic tip must be biocompatible, and thus safe for use within a nasal cavity.

Justification: An important consideration is that uncoated, NdFeB magnets are cytotoxic [9]. Therefore, it is crucial that the magnets are not left bare and are embedded within biocompatible materials [17].

- 2.4. Materials of wire: the materials of the wire must be biocompatible, and safe for use within a nasal cavity.

Justification: Given that this device is designed to go inside the human body, all materials must be biocompatible.

- 2.5. Weight: the weight of the tip must not exceed 1 g.

Justification: A lightweight tip ensures minimal strain on the actuation system and reduces the risk of excessive force on the nasal structures. Weight measurements using a precision scale will verify compliance.

- 2.6. Flexibility: the robot should be able to bend to a 120° angle.

Justification: A high degree of flexibility is necessary for effective navigation through curved anatomical structures.

- 2.7. Robot magnetic deflection: the robot should be responsive to the magnetic fields generated by the actuation system and have a minimum deflection angle of 15°.

Justification: A significant degree of deflection will allow the magnetic actuation system to have adequate control of the robot direction.

- 2.8.** Helical protrusion uniformity: the body of the robot should have uniform helical protrusions.

Justification: The helical protrusions promote rotation and aim to reduce excessive force being exerted by the robot as it travels through passageways. The helical protrusions should be uniform in order to achieve this goal.

3. Magnetic actuation system requirements

- 3.1.** Temperature: the temperature of the coils should not exceed 100° Celsius.

Justification: This ensures the longevity and reliability of the system. Higher temperatures can degrade the insulation, increase electrical resistance, and compromise the stability of the magnetic field, which is especially critical for precise actuation. Keeping the temperature below this threshold also reduces the risk of damage to nearby components or materials.

- 3.2.** Magnetic Field Strength: a field must be produced with a strength of 5mT within 10cm from the source of the field, and 2mT within 20cm from the source of the field.

Justification: Based on measurements taken in the HeART lab with pre-existing coils, it will take approximately 5 mT of magnetic field to actuate silicone with magnetic particles embedded in. The coils should sit somewhere around 10 cm away from the patient during the procedure, to avoid getting in the surgeons' workspace. The field can be measured using a gaussmeter at the specified distance.

- 3.3.** Voltage needs: the coils should not require more than 60 V to produce their required magnetic field.

Justification: A voltage limit ensures compatibility with common power supplies and prevents overheating or excessive power consumption.

- 3.4.** Directionality: the magnetic field generated by the coils should be able to exert an attraction and repulsion force, respectively.

Justification: The directionality of the coil current is enabled with a controllable directionality pin on the driver. The ability to apply either an attraction or repulsion force when required is executed intuitively in the interface dependant on the robot tip positioning intended.

- 3.5.** Indication: there should be a physical indication showing the status of each coil.

Justification: Providing clear feedback on coil status ensures that the operator can quickly verify functionality. This can be evaluated by incorporating LED indicators or a user interface.

4. Linear actuation system requirements

- 4.1.** Resolution: the linear actuator should have a minimum resolution of 1600 steps/revolution.

Justification: A higher step resolution allows for precise control over the movement of the robotic tip, ensuring smooth and accurate positioning.

- 4.2.** Load: the linear actuator should be able to retract or extend a load of 150g.
Justification: The robot needs to overcome frictional forces when retracting and extending.
- 4.3.** Directionality: the linear actuator should be able to move the tip for extension and retraction.
Justification: Bidirectional movement is necessary for precise control and repositioning of the robotic tip during procedures. This can be verified by performing controlled actuation tests in both directions.
- 4.4.** Size compatibility: the linear actuator can extend and extrude with wires between 1-4mm in diameter.
Justification: The design of the actuator should not need to be redesigned if the robot size changes in the future iterations.

5. Navigation interface and simulation requirements

- 5.1.** Simulated field strength: the simulation must demonstrate that the magnetic actuation system can generate a magnetic field between 0 and 10 mT in consistency with the physical setup.
Justification: This range is sufficient to actuate the magnetized tip with safety considerations for nearby tissues. The simulation results should align with the experimental results measured using an electromagnetic sensor.
- 5.2.** Magnetic field direction: the interface must align with the directionality of the expected generated magnetic field in all three axes (X,Y,Z) based on activated solenoids.
Justification: the robot tip must move in 3D space with accuracy of which solenoids must be activated for the intended movement of the tip
- 5.3.** Magnetic field superposition: the simulation must verify that the generated magnetic field of activated solenoids follows the superposition principle and the resultant field magnitude and direction are accurately represented.
Justification: the superimposed magnetic field from multiple solenoids leads the directional control of the robot's navigation. This validates the feasibility of using electromagnetic coils opposed to permanent magnets for real time motion control of the robot tip.
- 5.4.** Linear actuation mechanism: the interface must actuate the linear actuation to extend or retract the robot.
Justification: the extension/retraction mechanism on the interface leads to the extension/retraction of the robot in the physical setup. This validates the feasibility of using interactive buttons on the interface for real time linear actuation of the robot.

- 5.5.** Linear and magnetic actuation mechanism in conjunction: the interface must actuate the linear actuation to extend or retract the robot while simultaneously controlling the magnetic actuation system.

Justification: the extension/retraction mechanism on the interface leads to the extension/retraction of the robot in the physical setup. As well, the magnetic actuation on the interface leads to positional changes of the robot in the physical setup. This validates the feasibility of using both mechanisms simultaneously on the interface for real time linear and magnetic actuation of the robot.

- 5.6.** Safety mechanisms: the interface can execute the Complete Turn and Emergency STOP mechanisms that are meant to halt operations between or both linear and magnetic actuation systems.

Justification: the fail-safe mechanisms on the interface leads to the deactivation of the robot in the physical setup to the linear and/or magnetic actuation systems. This validates the feasibility of using interactive buttons on the interface for real time fail-safe operations of the robot.

1.3 Design Process

Using a solution-neutral lens and remaining at a high level, the use of magnetic actuation as a control method for a continuum robot requires an understanding of electromagnetism concepts that should be applied in the context of this project.

1.3.1 Electromagnetic Fields

Firstly, electric fields form around point charges or charged stationary objects to create an electric field. Stationary charges interact with each other to generate forces such that two point charges Q_1 and Q_2 which are a distance R_{12} apart (see Figure 1), would experience a force of:

$$F_{12} = \frac{Q_1 Q_2}{4\pi\epsilon_0 R^3} R_{12} \quad (1)$$

This force is relevant since this interaction results in an electric field, where the electric field intensity (or electric field strength) E is the force that a unit of positive charge experiences when placed in an electric field. The force can be measured as:

$$F = qE \quad (2)$$

where this force is along the electric field vector and starts and ends at the charges. Introducing more than just two-point charges can cause the force to vary. Using the principle of superposition, as N charges are added, the resultant force F , experienced by the point charge is [18]:

$$E = \frac{1}{4\pi\epsilon_0} \sum_{k=1}^N \frac{Q_k(r-r_k)}{|r-r_k|^3} \quad (3)$$

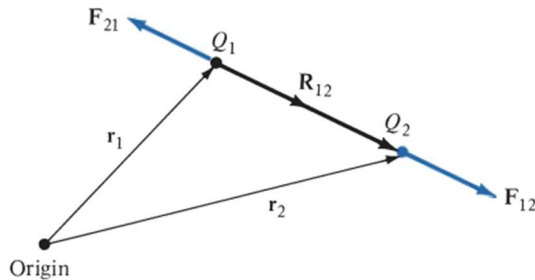


Figure 1. Diagram showing two point charges, Q_1 and Q_2 , experiencing vector force F , from the origin point [18].

Now, a magnetic field characterized by either B or H is a region around a moving charge or a magnetic material containing a dipole, where any other moving charges or magnets experience a force within the field. The magnetic field B forms closed loops around current-carrying wires, and it exerts a force on moving charges, like current. The strength of the magnetic field due to a current-carrying wire is:

$$B = \frac{\mu_0 I}{4\pi} \quad (4)$$

where μ_0 is the permeability of free space, I is the current in the wire, and r is the distance from the wire generating the field. Measured in units of Tesla, these fields are controlled by changing the I and are inversely proportional to the distance r . H is proportional to B through the permeability of free space (μ_0) and the magnetic properties of the material (r) [18]:

$$B = \mu_r \mu_0 H \quad (5)$$

Various magnetic fields interact with one another, similar to the point charge interactions, through the superposition principle. If there are magnetic fields $B_1, B_2 \dots B_n$ from different sources at a point, the total magnetic field B , B_{total} , can be calculated as:

$$B_{total} = \sum_{i=1}^n B_i \quad (6)$$

Given that these fields are vectors in a three-dimensional space, directionality and magnitude must be considered in their summation. Therefore, as an example, if two magnetic fields B_1 and B_2 are acting at a point of interest, apply the superposition principle to conclude the following:

$$B_{total} = (B_{1x} + B_{2x}) \cdot \hat{i} + (B_{1y} + B_{2y}) \cdot \hat{j} + (B_{1z} + B_{2z}) \cdot \hat{k} \quad (7)$$

Where \hat{i} , \hat{j} , and \hat{k} , are the unit vectors in the x , y , and z directions, respectively, and each B is broken into its directional magnitude components.

These fields are of interest since the intensity and directionality of these fields can be manipulated through constructive or destructive interference, wherein the fields sum or subtract. This has the potential to be a driving principle behind the execution of the robot's magnetic actuation. Optimizing these interactions to result in specific fields at specific points along the continuum robot's path is a method of specific and measurable control on the robot that can be leveraged to assist the surgeons using this robot.

1.3.2 Magnetic Field Generation

A magnetic field can be generated with a polarized dipole magnet or a wire with a running current. The magnetic field B at an observation point $P(r, \theta, \varphi)$ due to a magnetic dipole (which could be a bar magnet, or circular loop carrying current I), the setup of which is represented in Figure 2. It can be shown that an external field of distance r and angle from the center of the magnetic dipole, (wherein $r \gg$ center point) the point P will experience field [18]:

$$B = \frac{\mu_0 m}{4\pi r^3} (2\cos\theta a_r + \sin\theta a_\theta) \quad (8)$$

Where m is the magnetic moment of the loop.

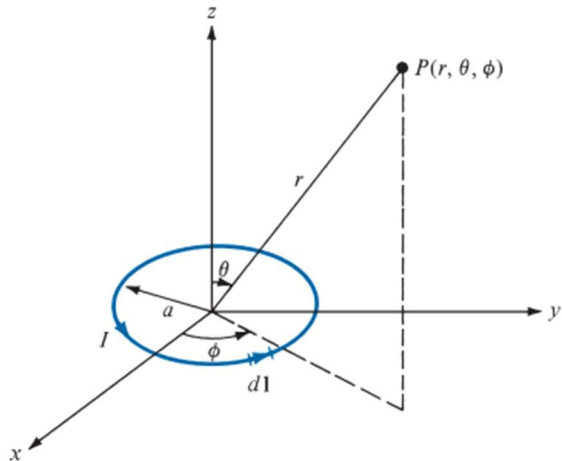


Figure 2. The magnetic field at a point P due to a current loop [18].

While these dipole moments of bar magnets, or current-carrying wires successfully generate fields, another method could be through wire coils, such as a solenoid or inductor. When calculating the generated field from these different sources, the equation changes. As the number of coils changes and/or the axial distance of the coil changes, the field also varies. This has implications on the magnetic flux Φ_B which represents the total amount of magnetic field passing through a point or surface. The advantage of this variability in the magnetic field generated by a coil, as opposed to a magnet, is the precision of the field created. If a magnet is placed near a point of interest, the strength of the field is proportional only to the distance of the magnet. If a user were to bring the magnet closer, the flux on the point of interest would increase, and as it is taken away, it would weaken. However, these changes in field strength vary with distance and can be prone to human error. Meanwhile, a coil can vary its field with respect to the amount of current passed through it, which has a more controlled change to the magnetic field, allowing the component to stay stationary.

However, these coils create a strong field internal to the coil loops, so to create a meaningful field outside of the coil, the coils would need to be quite large; Helmholtz coils are examples of coils that create a larger uniform magnetic field [19].

1.3.3 Magnetic Forces

Like electric fields, magnetic fields can result in a force. More specifically, torque force T results from the magnetic field interacting with the magnetic dipole experiencing the force. When m is the magnetic moment vector of the magnet (its direction and magnitude), the cross product of B is taken with m , thus generating torque:

$$T = m \times B \quad (9)$$

Assuming that the point of interest interacting with the field is a magnet containing a dipole moment, Q_m is the isolated magnetic charge (pole strength) and l is the length of the bar. The bar has a dipole moment $Q_m l$. Therefore,

$$T = m \times B = Q_m l \times B \quad (10)$$

And \mathbf{l} points south to north (with respect to the magnetic dipole) and as such, the torque tends to align the bar with the external magnetic field, as seen in Figure 3. The force acting on the magnetic charge is given by:

$$\mathbf{F} = Q_m \times \mathbf{B} \quad (11)$$

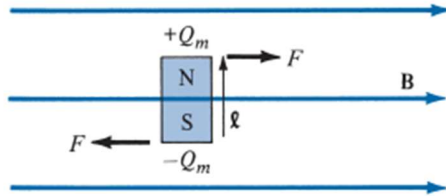


Figure 3. A bar magnet in an external magnetic field with the applied force F shown [18].

Given the review of concepts related to magnetism and electromagnetic waves written above, the design process can take place given this context. Without compromising the solution-neutral nature of this stage of the design process, the current priority is to narrow down and specify magnetic field interactions to optimize different fields on a moving point in a 3-dimensional space. By mapping out how different magnetic fields originating from different sources interact at a given point of interest, the torque on that point of interest can then be measured and manipulated. Knowing these torque interactions would help define the parameters for which the form of magnetic actuation should be reached. Thus, a design can be developed based around these parameters, using a combination of coil topology, bar magnets, a combination of both, or a variety of other methods. With the goal of creating a simulation-based user interface to be able to map these interactions, a flowchart seen in Figure 4, will guide the process. After this, potential circuit topology could be considered and prototyping (with respect to the method of magnetic actuation) can begin.

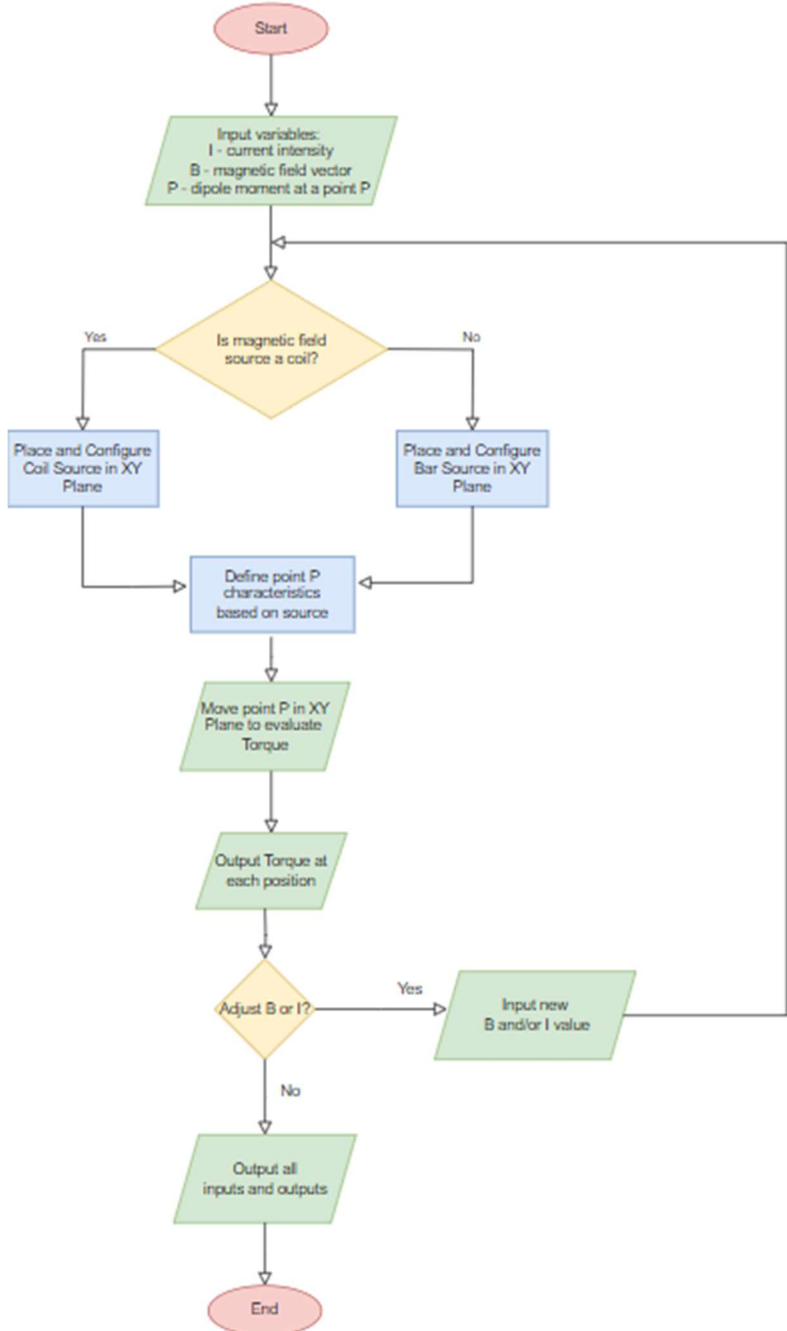


Figure 4. Flowchart of magnetic field interactions for magnetization simulation.

1.3.4 Mechanical Structure

For the general mechanical structure of the continuum robot, there are a few existing baseline designs to take inspiration from. Continuum robots are characterized by a compliant backbone capable of continuous bending [2]. They can be tethered, meaning there is a tip which is actuated and a wire-like continuum structure that is partially inside the body and partially outside. They can also be untethered, meaning the robot is wireless and is fully immersed in the body [4]. In terms of locomotion, extrinsic actuation involves generating motion from the base of the backbone and transmitting that motion along the mechanical elements. This is particularly

useful for miniaturized robots and can be accomplished in a few different ways. The first method is tendon-driven, where a set of tendons along the backbone are actuated. Another option is motion via concentric tubes, where pre-curved tubes are nested inside of each other. Additionally, there are rod-driven robots where parallel backbone rods are pushed and pulled to move the robot [2]. Intrinsic actuation involves direct local control over the shape of the backbone through methods like pressurized working fluid, shape-memory alloys (SMA) and dielectric actuators. Other existing advance units employ friction-roller-drive mechanisms which can accommodate different diameters and pitch angles with unlimited driving length [3]. Having motorization stem from external components that can be protected using autoclavable and sterile barriers is an additional consideration for robots used in operating rooms.

Commonly, continuum robotic systems have a soft tip to avoid fracturing during operation and causing damage to any tissues. While elastomers like Polydimethylsiloxane (PDMS) are commonly used in biomedical applications for its mechanical and biocompatible properties, it is likely too rigid for a soft continuum robot [20]. Silicone is a versatile synthetic polymer that is suitable for biomedical use with an inert nature, hydrophobic surface, and wide range of flexibility. This material is also easy to manufacture and maintains its mechanical properties between temperatures of -40°C to $+185^{\circ}\text{C}$ [21].

For the magnetic component of the continuum robot, neodymium magnet (NdFeB), an alloy of neodymium, iron and boron, is widely used in biomedical applications for its strong magnetization and easy fabrication [4]. Research has been conducted showing that parylene C (Par) coatings significantly improve the biocompatibility of NdFeB magnets [23].

After the structure, locomotion, and actuation of the robot has been finalized, the robot can then be modeled and then simulated. Depending on the complexity of the simulations, there are a few simulation options to choose from, notably: MagPy library with PyVista library, which are Python based libraries used to perform electromagnetic field interactions and visualizations. There are multiple avenues that can be taken to model the robotic system, but the Python-based libraries will be most likely applied as the model.

1.3.5 Simulation and Mathematical Modeling

Before prototyping, the robot can be modeled with calculations. Although the designs have not been finalized, there is a general approach to modeling the robot. The idea is to start with a basic kinematic model, which would most likely dissect the continuum robot into a finite equation [24]. Then, integrate the dynamics of the extension and retraction actuation, and directional movement from the magnetic fields and magnetic actuation. Finally, implement a control interface, which intuitively handles the electromagnetic field interactions to execute specific robot positionings which will update and control the robot in real time accordingly.

When modelling the continuum robot itself, there are a few approaches: Cosserat rod theory, piecewise constant curvature models (PCC), arc segment models, and others [25] [26]. These models are similar in that they aim to describe the position and orientation of the continuum robot, and can be summarized by this equation:

$$\mathcal{C} = \{g: X \in [0,1] \rightarrow g(X) \in \text{SE}(3)\} \quad (12)$$

Within the scope of this project, it will be more realistic to model the robot as a finite equation, as in equation 12. $SE(3)$ is the Special Euclidean Group in three dimensions, which combines the translations and rotations of the robot. Therefore, it encompasses both position $p(X,t)$ and orientation $R(X,t)$ [24]. This is a rigid body transformation, except that it is applied continuously along a flexible structure. Note that this is only a general model, and a precise model will depend on the structure of the design, such as its segments, curvature, and tendons.

Alternatively, it can also be ideal to use continuous equations for a continuum robot. Firstly, the strain, ξ , can be linked with coordinates q , where $\Phi(X)$ is a function to map the deformation of the robot under strain to the coordinates. So, this general equation represents the format of the model used to represent the robot's state [25]:

$$q = \Phi(X)\xi \quad (13)$$

Finally, either Euler-Lagrange or Hamiltonian dynamics can be applied to represent the dynamic behavior of the robot, using the q value from equation 13 [27]:

$$\mathbf{M}(q)\ddot{\mathbf{q}} + \mathbf{C}(\mathbf{q}, \dot{\mathbf{q}})\dot{\mathbf{q}} + \mathbf{G}(\mathbf{q}) = \boldsymbol{\tau}\mathbf{R} \quad (14)$$

Where $\mathbf{M}(q)$ is the mass matrix describing the inertia of the robot, $\mathbf{C}(\mathbf{q}, \dot{\mathbf{q}})\dot{\mathbf{q}}$ is the Coriolis term, which is the variable that is changed based on the configuration/structure of the robot and represent the effect of previous segments on the robot, $\mathbf{G}(\mathbf{q})$ is gravity, and $\boldsymbol{\tau}\mathbf{R}$ is the input torque from the magnetic actuation.

1.4 Preliminary Risk and Assessment

1.4.1 Health and Safety and Associated Risks

The guidance given in the ISO 14971:2019 document is followed to conduct a proper risk assessment [28]. The document highlights steps to systematically identify, evaluate and mitigate risks found in a project. For the preliminary risk assessment, the “risk analysis” section was followed, which instructs the identification of the device’s intended use and reasonably foreseeable misuse, characteristics related to safety and hazards/hazardous situations.

The robot’s intended use is for minimally invasive surgeries in the ENT region. Improper navigation could lead to misuse of the device, where the robot is guided into the tissue walls, which may damage the surgical area, from excessive extension/retraction or rotation force. These are related to mechanical hazards. The durability of the robot is also important, as the inside nitinol wire would be dangerous if exposed, as it can act as a needle inside the body cavity.

Improper sterilization would also be considered reasonable misuse, which would be considered a biological hazard. Sterilization procedures are outlined in ISO 17664, which give guidelines on sterilizing medical devices [29].

There are also multiple risks associated with the software component of the device. Real-time communication can suffer from latency or continuous signals, leading to improper navigation, which was mentioned above. Software issues could be caused by system errors, or outside interferences, such as a power outage.

Finally, electrical hazards pose the biggest risk, since the coil is powered by a significant current and voltage. Failure of any electronic component caused by a short can be a fire hazard, or cause tissue burns. Additionally, the coils emit electromagnetic fields, therefore it will be important to reference IEC 60601-1-2 throughout the design, prototyping and manufacturing process, as it outlines EMI safety in medical devices [30]. For example, pacemakers or imaging systems may malfunction in the presence of strong magnetic fields [31]. The standard dictates device testing under various electromagnetic conditions, to identify risks such as the example mentioned above.

1.4.2 Relevant Standards

The standards mentioned above are all relevant and should be referenced throughout the device’s design process. First, ISO 14971:2019 *Application of Risk Management to Medical Devices*. This standard addresses the general approach in both evaluating the risk, as well as mitigating it [28]. It highlights the creation and maintenance of risk management file, which is updated throughout the entire device’s progress.

IEC 60601-1-2 outlines the general requirements for basic safety and essential performance when working with electrical fields [30]. Specifically, it focuses on the electromagnetic compatibility of the device and sets standards so that devices do not interfere with other electronic systems. As mentioned, should there be any medical devices such as pacemakers, the

electromagnetic fields should not be able to interfere with that device. The guide dictates that testing is necessary to determine whether these fields will be unsafe at any condition in a clinical setting.

ISO 17664 *Processing of Health Care Products – Information to be Provided for the Processing of Medical Devices* discusses sterilization, such as the use of sterile barriers [29]. This is relevant since many of the robot's actuation system components are not single-use, therefore sterilization is necessary. The guideline also mandates what information a manufacturer must provide for the processing of re-sterilizable medical devices. For tools that can be integrated with the continuum robot, the parts must be designed to be cleaned, disassembled and sterilized using standardized methods.

Finally, ISO 63266-1 *Application of Usability Engineering to Medical Devices*, talks about intuitive design. It outlines that devices should minimize the risk of user error that could cause harm, by ensuring an interface that prevents the user from entering an improper input [32]. It also details clear instructions on successful interfaces, and necessary warnings before important tasks. For example, the user interface should provide intuitive guidance during navigation.

There are currently not many significant ethical concerns regarding this robot. One concern is the consequential need for less staff when using the continuum robot in the operating room. For example, during a procedure involving an endoscope, a secondary hand is needed to secure the endoscope, etc. With the actuation being handled by the magnetic fields, only one surgeon may be necessary. This raises the ethical concerns related to robots replacing a field job, regardless of the operating time that could be saved. Finally, the last ethical concern is liability. There are many components and moving parts to this device, and there are no set standards for liability if anything malfunctions and harms the patient. It is difficult to unpack who is ultimately liable and responsible for the harm done to the patient.

Chapter 1 References

- [1] M. A. Tsitsika et al., “A Systematic Review of Current Practices, Challenges, and Future Directions for the Use of Robotic Surgery in Otolaryngology in Greece,” *Cureus*, vol. 16, no. 11, p. e74458, 2024, doi: <https://doi.org/10.7759/cureus.74458v>
- [2] M. Russo et al., “Continuum Robots: An Overview,” *Advanced intelligent systems*, vol. 5, no. 5, pp. 2200367–2200367, Mar. 2023, <https://doi.org/10.1002/aisy.202200367>.
- [3] R. Dreyfus et al., “Dexterous Helical Magnetic Robot for Improved Endovascular Access.” *Science Robotics*, vol. 9, no. 87, 14 Feb. 2024, <https://doi.org/10.1126/scirobotics.adh0298>.
- [4] Z. Yang, H. Yang, Y. Cao, Y. Cui, and L. Zhang, “Magnetically actuated Continuum Medical Robots: A Review,” *Advanced Intelligent Systems*, vol. 5, no. 6, Mar. 2023. doi:10.1002/aisy.202200416.
- [5] C. P. Childers and M. Maggard-Gibbons. “Understanding Costs of Care in the Operating Room.” *JAMA Surgery*, vol. 153, no. 4, 18 Apr. 2018, p. e176233, <https://doi.org/10.1001/jamasurg.2017.6233>.
- [6] K. Mohiuddin and S. J. Swanson, “Maximizing the benefit of Minimally Invasive Surgery,” *Journal of Surgical Oncology*, vol. 108, no. 5, pp. 315–319, Aug. 2013. doi:10.1002/jso.23398
- [7] Z. Koszowska, et al. “Independently Actuated Soft Magnetic Manipulators for Bimanual Operations in Confined Anatomical Cavities.” *Advanced Intelligent Systems*, vol. 6, no. 2, 27 July 2023, <https://doi.org/10.1002/aisy.202300062>.
- [8] Medtronic, “Surgical Navigation Systems - stealthstation,” *Medtronic*, <https://www.medtronic.com/ca-en/healthcare-professionals/products/neurological/surgical-navigation-systems/stealthstation.html> (accessed Oct. 22, 2024).
- [9] V. E. Donohue, F. McDonald, and R. Evans, “in vitro cytotoxicity testing of neodymium-iron-boron magnets,” *Journal of Applied Biomaterials*, vol. 6, no. 1, pp. 69–74, Mar. 1995. doi:10.1002/jab.770060110
- [10] “Nasal cavity phantoms,” *CFD Research*, <https://www.cfd-research.com/products/nasal-cavity-phantoms/> (accessed Oct. 22, 2024).
- [11] Z. Lai et al., “The effect of coil polarity on electromagnetic forming using a multi-coil system,” *The International Journal of Advanced Manufacturing Technology*, vol. 103, no. 1–4, pp. 1555–1566, Apr. 2019. doi:10.1007/s00170-019-03656-8
- [12] J. Murphy, “Gaussmeter applications,” *Proceedings: Electrical Insulation Conference and Electrical Manufacturing and Coil Winding Conference (Cat. No.99CH37035)*, pp. 573–576, Apr. 2002. doi:10.1109/eeic.1999.826272
- [13] J. R. Lewis, “The system usability scale: Past, present, and future,” *International Journal of Human–Computer Interaction*, vol. 34, no. 7, pp. 577–590, Mar. 2018. doi:10.1080/10447318.2018.1455307
- [14] F. D. Davis and A. Granić, “The Technology Acceptance Model,” *Human–Computer Interaction Series*, 2024. doi:10.1007/978-3-030-45274-2
- [15] J. Drèze and N. Stern, “Chapter 14 the theory of cost-benefit analysis,” *Handbook of Public Economics*, pp. 909–989, 1987. doi:10.1016/s1573-4420(87)80009-5
- [16] R. Robinson, “Cost-effectiveness analysis.,” *British Medical Journal*, vol. 307, no. 6907, pp. 793–795, Sep. 1993. doi:10.1136/bmj.307.6907.793

- [17] “Polydimethylsiloxane films doped with NdFeB powder: magnetic characterization and potential applications in biomedical engineering and microrobotics | Biomedical Microdevices.” Accessed: Dec. 05, 2024. [Online]. Available: <https://link.springer.com/>
- [18] M. N. O. Sadiku and S. Nelatury, *Elements of Electromagnetics*, 7th ed. New York: Oxford University Press, pp.187-204. 2021.
- [19] R. Beiranvand, "Effects of the Winding Cross-Section Shape on the Magnetic Field Uniformity of the High Field Circular Helmholtz Coil Systems," in *IEEE Transactions on Industrial Electronics*, vol. 64, no. 9, pp. 7120-7131, Sept. 2017, doi: 10.1109/TIE.2017.2686302
- [20] I. Miranda et al., “Properties and applications of PDMS for Biomedical Engineering: A Review,” *Journal of Functional Biomaterials*, vol. 13, no. 1, p. 2, Dec. 2021. doi:10.3390/jfb13010002
- [21] M. Zare, E. R. Ghomi, P. D. Venkatraman, and S. Ramakrishna, “Silicone-based biomaterials for biomedical applications: Antimicrobial strategies and 3D Printing Technologies,” *Journal of Applied Polymer Science*, vol. 138, no. 38, May 2021. doi:10.1002/app.50969
- [22] E. Hempel et al., “An MRI-compatible surgical robot for precise radiological interventions,” *Computer Aided Surgery*, vol. 8, no. 4, pp. 180–191, Jan. 2003. doi:10.3109/10929080309146052
- [23] V. Iacovacci et al., “Stability and in vivo safety of gold, titanium nitride and parylene C coatings on NdFeB magnets implanted in muscles towards a new generation of myokinetic prosthetic limbs,” *RSC Advances*, vol. 11, no. 12, pp. 6766–6775, Feb. 2021. doi:10.1039/d0ra07989h
- [24] H. Wang, Y. Mao, and J. Du, “Continuum Robots and magnetic soft robots: From models to interdisciplinary challenges for medical applications,” *Micromachines*, vol. 15, no. 3, p. 313, Feb. 2024. doi:10.3390/mi15030313
- [25] F. Renda, F. Boyer, J. Dias, and L. Seneviratne, “Discrete cosserat approach for multisection soft manipulator dynamics,” *IEEE Transactions on Robotics*, vol. 34, no. 6, pp. 1518–1533, Dec. 2018. doi:10.1109/tro.2018.2868815
- [26] S. Hasanzadeh and F. Janabi-Sharifi, “An efficient static analysis of Continuum Robots,” *Journal of Mechanisms and Robotics*, vol. 6, no. 3, Apr. 2014. doi:10.1115/1.4027305
- [27] H. Poincaré, “Sur une forme nouvelle des équations du problème des Trois Corps,” *Bulletin astronomique*, vol. 14, no. 1, pp. 53–67, 1897. doi:10.3406/bastr.1897.11200
- [28] “Medical devices—guidance on the application of ISO 14971,” AAMI/ISO TIR24971: 2020; *Medical devices—Guidance on the application of ISO 14971*, Dec. 2019. doi:10.2345/9781570207372.ch1
- [29] ISO, “ISO 17664-1 Processing of health care products — Information to be provided by the medical device manufacturer for the processing of medical devices,” *International Organization for Standardization*, 2021.
- [30] “Basic introduction to the IEC 60601 series,” AAMI CR500:2019; *Basic Introduction to the IEC 60601 Series*, Dec. 2019. doi:10.2345/9781570207334.ch1
- [31] A. Napp et al., “Are patients with cardiac implants protected against electromagnetic interference in daily life and occupational environment?,” *European Heart Journal*, vol. 36, no. 28, pp. 1798–1804, Apr. 2015. doi:10.1093/eurheartj/ehv135

[32] ISO, "ISO 62366:2019 - Medical devices - Application of usability engineering to medical devices,"

Chapter 2

Summary

Ear, nose, and throat (ENT) surgeries are frequently performed to manage chronic sinus conditions but are often constrained by the limitations of traditional surgical instruments. There are significant challenges due to the intricacies of the sinus pathways and variations in patient anatomy. Current tools often necessitate invasive procedures, such as bone removal, to navigate through narrow passages which leads to prolonged recovery times, increased risks, and higher healthcare costs.

To address these limitations, this project aims to design a magnetically actuated continuum soft robot for ENT surgeries. This robot will navigate through the complex pathways of the nasal cavity under a surgeon's control, utilizing the following key components: a soft continuum robot, a linear actuation system, and a directional magnetic actuation control system. The magnetic actuation system consists of three electromagnetic coils that will generate an accumulated magnetic field to precisely adjust the robot's orientation in real time. This method for directional control provides a fail-safe mechanism where immediate deactivation of the coils can prevent unintended interactions during surgery. For the linear actuation system, the stepper motor enables the robot to advance with a smooth extension/retraction movement through nasal pathways. The tip-magnetized continuum robot has a soft silicone body that is biologically inert and reinforced with a thin nitinol wire core. This design is intended to minimize trauma and enhance adaptability to anatomical variations. The magnetized tip, embedded with Neodymium (NdFeB) particles, interacts with the magnetic field generated by the control system, enabling seamless navigation. Using a "Follow the Leader" (FTL) mechanism, the tip advances while the rest of the body follows its movements. The complete robot will enter through the nose, with its actuation guided by the surgeon and controlled by the linear and magnetic actuation systems. To validate its performance, the robot will be tested in a phantom model that simulates the sinus environment, evaluating its precision, accuracy, and maneuverability. The proposed solution can be seamlessly integrated into current surgical workflows and is compatible with existing surgical technologies.

The expected impact from the solution is substantial. For surgeons, the robot offers enhanced control, improved visibility and access, as well as reduced operative times, resulting in better resource utilization. Patients benefit from reduced recovery time, fewer complications, and improved post-operative outcomes due to the robot's minimally invasive approach. Furthermore, the technology can make complex and advanced ENT surgeries safer and more accessible, addressing procedures previously deemed too risky. Beyond clinical advantages, the broader economical and societal benefits are significant and include increased healthcare efficiency, sustainable resource use, and improved personalized patient-centered surgical methodologies. Ultimately, by addressing the critical challenges of current ENT surgical practices, the solution has the potential to revolutionize the field and establish new standards for exceptional patient care.

Brief Project Description

A magnetically actuated continuum soft robot designed for ENT surgeries. The design integrates electromagnetic coils as a magnetic actuation system for directional control, a linear actuation system for extension and retraction, and a soft continuum robot with a magnetized tip, which are all controlled using a user interface, enabling intuitive, precise, and dexterous surgical control.

Need Statement

Design a magnetically actuated continuum robot for use in ENT surgery, enhancing dexterity in navigating complex and confined anatomical spaces, while remaining less invasive than current tools.

2.1 Design Outputs

Design outputs are to be linked to design inputs. To keep the outputs as clean and simple as possible, all Figures and Tables can be found below the complete list of design outputs. All relevant calculations for just the design outputs can be found in Appendix A: Design Output Calculations. The design outputs have been formatted like the design inputs and were divided into four categories: high level system outputs, robotic subsystem outputs, electrical subsystem outputs, and linear actuator subsystem outputs. These design outputs pertain to the final iteration of the design, utilizing many of the same methods for verification and measurement applied to the proof-of-concept.

2.1.1 Prototype Design Outputs

1. High level system outputs

1.1.Ergonomic Usability and Ease of Control: Compliance to ISO 62366-1. This conforms with design input 1.1.

Justification: Usability and ISO guidelines are necessary for approval of device in the market. ISO 62366-1 outlines requirements for the application of usability engineering to medical devices, aiming to reduce use errors and improve overall user performance and safety.

1.2.Electrical Safety and Thermal Limits: Compliance to IEC 60601-1.

Justification: Electrical safety and thermal limits apply especially to the magnetic actuation system of the system. IEC 60601-1 defines general requirements for the basic safety and essential performance of medical electrical equipment. Electrical safety ensures that the device does not pose a risk of electric shock to the patient or operator, while thermal safety ensures that heat generated by motors, magnetic coils, or power circuits does not lead to tissue damage or device malfunction. Therefore, compliance with this standard is important to meet regulatory

requirements, minimize hazards, and ensure the safe integration of the system into surgical environments.

1.3.Biocompatibility of Materials: Compliance to ISO 10993-1.

Justification: Test for the biocompatibility of the nitinol wire and robotic tip materials to ensure safety within the patient without adverse effects. ISO 10993-1 provides a framework for evaluating the biocompatibility of medical device materials that come into direct or indirect contact with the human body. Testing according to ISO 10993-1 ensures that all materials used are safe for the intended duration and type of contact.

2. Soft continuum robot system outputs

2.1.Size of the robotic tip: the diameter and length of the tip are 4 mm and 20 mm respectively. This conforms with design input 2.1.

*Justification: the tip was made using a 3D printed mould. The dimensioned CAD drawing for the mould can be seen in **Error! Reference source not found.***

2.2.Size of the wire: the gauge and length of the wire are 0.5mm and 245mm respectively. The gauge and length conform with design input 2.2

Justification: The gauge and length of the wire were measured using a digital caliper.

2.3.Magnetization of robotic tip: in its final iteration, the tip of the robot is sufficiently magnetized to produce a magnetic field of strength averaging 32.3mT in magnitude at its north pole and 25.93mT at its south pole. This conforms with design input 2.3.

Justification: the magnetic field produced by the tip was measured with a magneto-optical sensor, the CMOS-Magview. An image of the sensor's output can be seen in Figure 6.

2.4.Wire is magnetically inert: the wire is non-magnetized. This conforms with design input 2.4.

Justification: the wire is made of nitinol, which is a non-ferromagnetic material, meaning it is not magnetic [1].

2.5.Materials of robotic tip and body: the materials of the robot are biocompatible and thus safe for use within a nasal cavity. This conforms with design input 2.5.

Justification: the tip was made of NdFeB powder mixed with a silicone resin called EcoFlex 00-30. When embedded in a biocompatible polymeric matrix, NdFeB powders are also biocompatible [2]. When properly cleaned and fully cured, prints made of EcoFlex 00-30 pass the ISO 10993-5 cytotoxicity biocompatibility test [3].

2.6.Materials of wire: the materials of the wire are biocompatible, and thus safe for use within a nasal cavity. This conforms with design input 2.6.

Justification: the wire is made of nitinol, which is commonly used for biomedical applications due to its corrosion resistance and biologically inert nature, thus leading to its common use in biomedical applications [4],[5].

2.7.Mass: the mass of the tip is 0.86g. This conforms with design input 2.7.

Justification: the tip was weighed on a scale, which is shown in Figure 7.

2.8.Flexibility: the robot can bend to a 360° angle. This conforms with design input 2.8.

Justification: the nitinol wire used for the robot's core backbone can easily bend 360°, which is shown in Figure 8.

2.9.Robot magnetic deflection: the robot is responsive to the magnetic fields generated by the actuation system and has a deflection angle of 26°. This conforms with design input 2.9

Justification: The degree of deflection was measured using a Mastercraft Digital Angle Finder Ruler.

2.10.Helical protrusion uniformity: the body of the robot has uniform helicalprotrusions with a pitch of 10mm. This conforms with design input 2.10.

Justification: The helical pitch of the robot was measured using a digital caliper.

3. Magnetic actuation system outputs

3.1.Temperature: the temperature of the coils does not exceed 100°C. This conforms with design input 3.1.

Justification: Appendix A: Design Output Calculations, subsection Calculation [6], shows that the coil should not surpass 27.195°C while being powered.

3.2.Magnetic Field Strength: the coils produce a magnetic field strength of 5mT. This conforms with design input 3.2.

Justification: The magnetic field was measured using a TLV493D-A1B6 magnetic sensor; the coils measured an emitted field of approximately 5mT, which can be seen in Figure 9.

3.3.Voltage needs: the coils require 30 V to produce their magnetic field. This conforms with design input 3.3.

Justification: a power supply unit up to 60V was used to power the coil circuitry. Each coil is allotted 30V of power which is sufficient to generate the expected range of magnetic field.

3.4.Directionality: the magnetic field generated by the coils should be able to exert an attraction and repulsion force, respectively. This conforms with design input 3.4.

Justification: The directionality of the coil current is enabled with a controllable directionality pin on the driver. The ability to apply either an attraction or repulsion force when required is executed intuitively in the interface dependant on the robot tip positioning intended.

3.5.Indication: there is a physical indication showing when each coil is on or off. This conforms with design input 3.5.

Justification: In the proof-of-concept, the breadboard of the prototype has two LEDs that correspond to the status of either coil. In the final iteration, the navigation interface has interactive visual buttons that control the coil activation and deactivation with visual indicators.

4. Linear actuation system outputs

4.1. Resolution and repeatability: the linear actuator has a resolution of 200 steps/revolution. This conforms with design input 4.1.

Justification: based on the step angle provided in the datasheet [7], the resolution can be calculated. This calculation is shown in Appendix A: Design Output Calculations, subsection Calculation 2

4.2. Load: the linear actuator can handle a load of up to 150g. This conforms with design input 4.2.

Justification: The robot is able to overcome friction forces when retracting the robot from its original position.

4.3. Directionality: the linear actuator can move the robot in extension and retraction. This conforms with design input 4.3.

Justification: shown in Appendix B: Software Implementation, subsection Code 2, the stepper motor is programmed to create extension/retraction of the robot.

4.4. Size Compatibility: the linear actuator can satisfy design input 4.1 with wire gauges between 1-4mm. This satisfies design input 4.4.

Justification: Various robot iterations were used with the actuator, varying in size.

5. Navigation Interface and simulation outputs

5.1. Simulated field strength: the simulation can generate a magnetic field between 0 and 10 mT, which is consistent with the field of the physical setup of 5mT about 10cm equidistant from each coil.

Justification: This range is sufficient to actuate the magnetized tip with safety considerations for nearby tissues. The simulation results align with the experimental results measured using an electromagnetic sensor.

5.2. Magnetic field direction: the interface aligns with the directionality of the expected generated magnetic field in all three axes (X,Y,Z) based on activated solenoids.

Justification: the robot tip moves in 3D space with accuracy of which solenoids are activated for the intended movement of the tip

5.3. Magnetic field superposition: the simulation verifies that the generated magnetic field of activated solenoids follows the superposition principle, and the resultant field magnitude and direction are accurately represented in the physical setup.

Justification: the superimposed magnetic field from multiple solenoids results in the directional control of the robot's navigation seen in simulation and experimental.

5.4. Linear actuation mechanism: the interface can perform linear extension/retraction of the robot on command using the linear actuation system, resulting in the corresponding physical movement.

Justification: this confirms that interactive controls on the system's variability

5.5. The interface can perform linear actuation and magnetic actuation simultaneously, resulting in combined movement of the robot in the physical setup.

Justification: the ability to coordinate both the magnetic and linear actuation systems in real life confirms the system's ability to execute complex maneuvers which aligns the interface outputs with the observed physical responses.

5.6. Safety mechanisms output: the interface successfully halts linear and/or magnetic actuation upon activation of the “Complete turn” or “Emergency STOP” mechanisms,

Justification: real-time deactivation of the magnetic and linear actuation systems ensures safety and responsiveness of the robot during operations, such that the interface fail-safes directly translate to the physical system's shutdown.

Table 3. Cost break-down of components for the final iteration.

Component	Cost
NdFeB Magnetic Particles	\$1.80
EcoFlex 00-30 Silicone Resin	\$1.44
Nitinol Wire Core	\$16.58
Actuation Wire	\$26.36
Stepper Motor	\$20.33
Motor Driver LCM2209	\$38.41
Logic Level MOSFET	\$11.29
Screws, nuts, bolts	\$64.82
Bread boards	\$14.68
ESP32-PICO-KIT V4	\$14.50
Motor driver boards (x3)	\$155.91
14-gauge copper wire	\$433.80
MDF Board for Coils	\$33.89
Crimp Connectors	\$14.68
Terminal Blocks	\$39.30
Housing boxes	\$33.88
Resistors and additional wires	\$5.67
Total	\$927.34

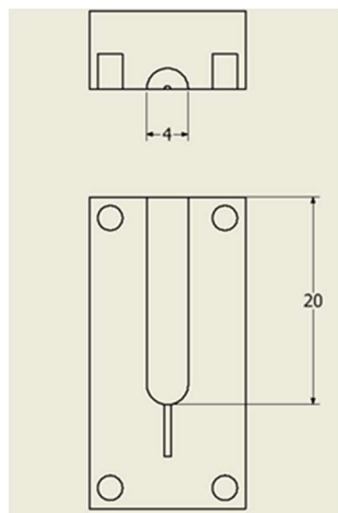


Figure 5. Top-view and side view of dimensioned CAD drawing of the right half of the tip mould showing a tip diameter of 4 mm and length of 20 mm

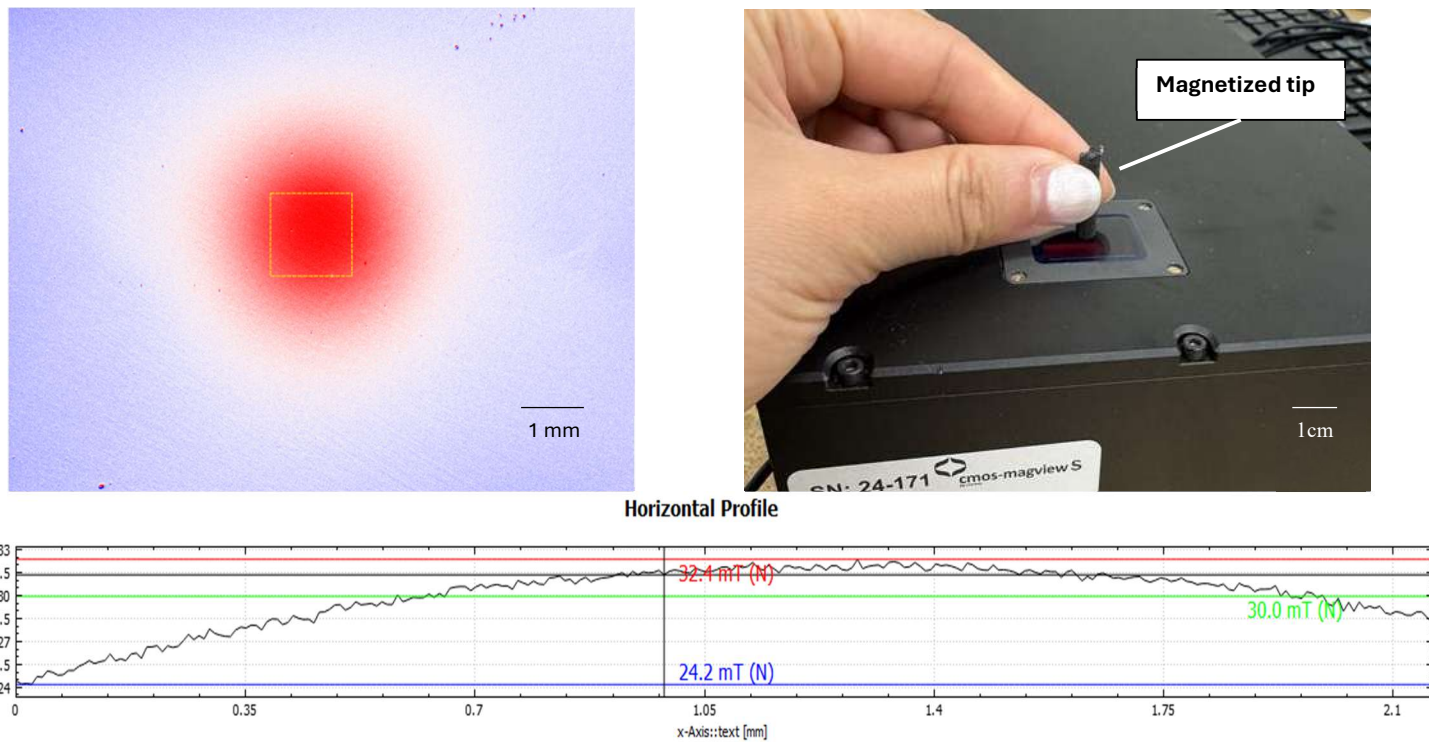


Figure 6. Results from the CMOS-Magview, measuring the magnetic field strength of the robotic tip, producing an optical and graphical representation of the field generated at its north pole. The image on the top left shows the CMOS-Magview in use, the magnetized tip of the robot is placed such that the strength of the north pole can be read by the Magview sensor. The images on the top right and bottom are produced by the Magview system, the red indicates the north pole magnetic field, and the blue indicates the south pole magnetic field. Multiple measurements were taken for the north and south poles of the robot tip and the average of all the measurements was considered in the outputs.

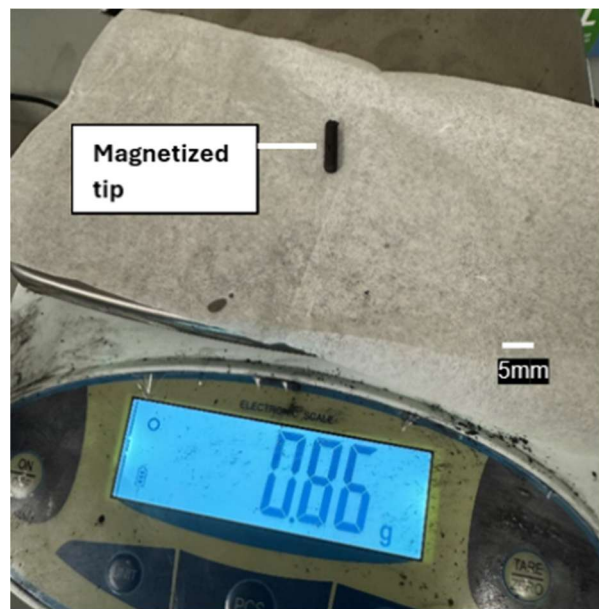


Figure 7. The mass of the robotic tip is measured to be 0.86g on a CGoldenwall high precision lab scale.

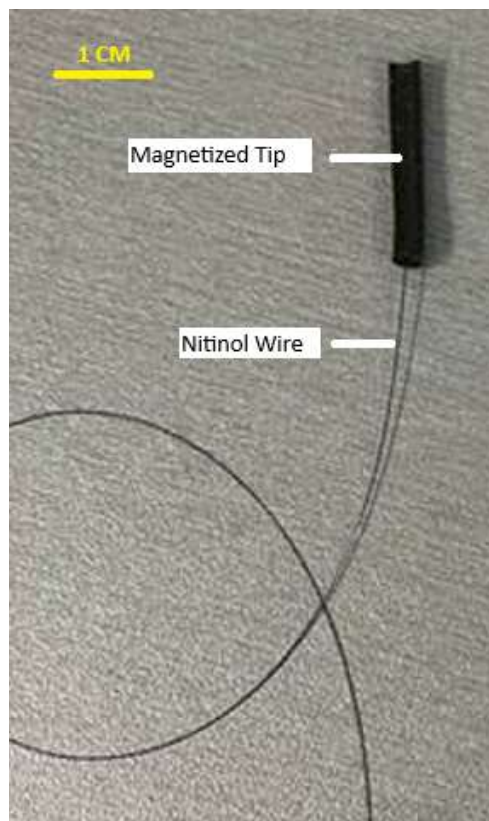


Figure 8. Nitinol wire with attached magnetized tip, showcasing 360 degrees flexibility of wire.

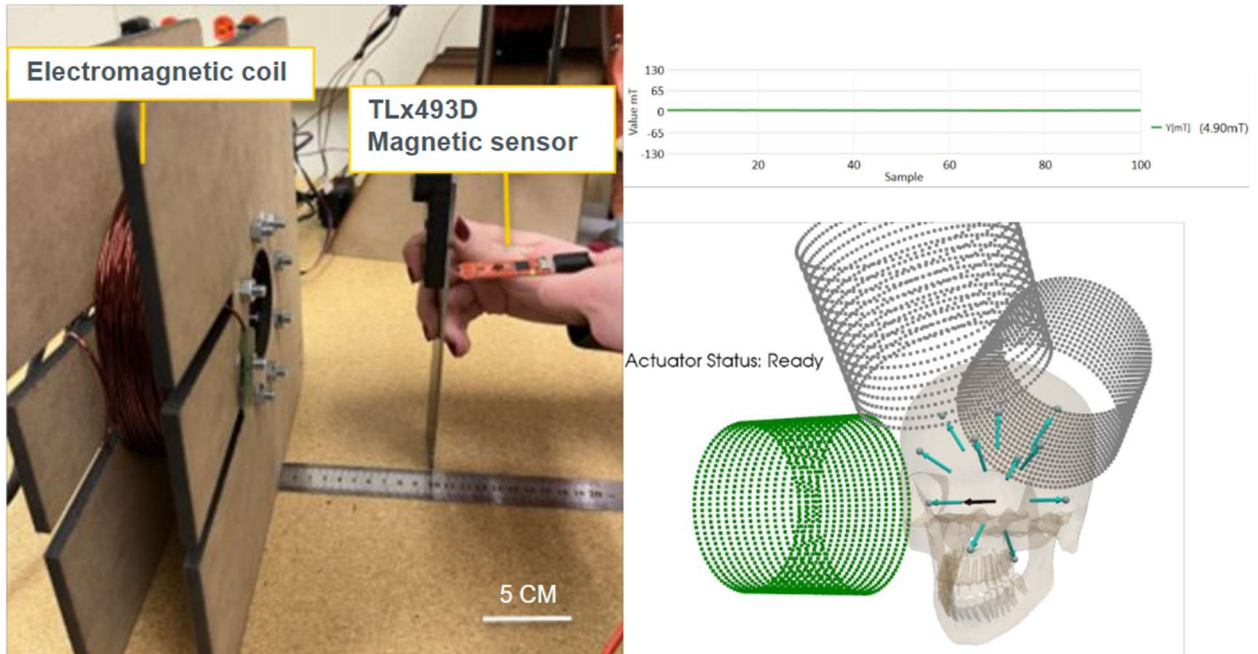


Figure 9. The image on the left shows the TLV493D-A1B6 magnetic sensor measuring generated magnetic field of coil from 10cm away. The graph in the top right presents the sensor reading in the Y plane on Infineon Magnetic Sensor app. The bottom right shows the navigation interface that actuates the coil activation.

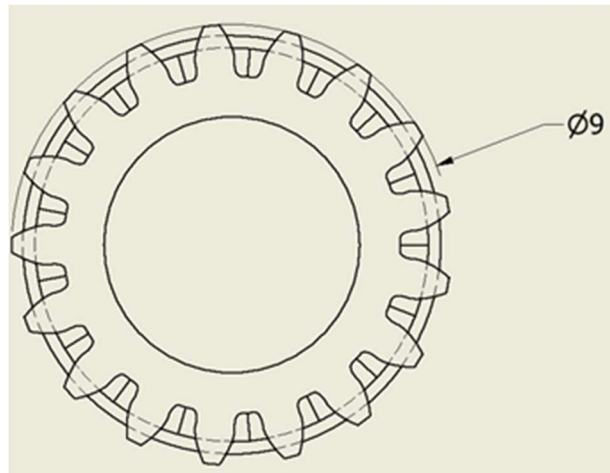


Figure 10. Top-view dimensioned CAD drawing of extruder gear showing an outer gear diameter of 9 mm.

2.2 Final Decision: Concept

The final design will be a combination of the key components (the soft continuum robot, the linear actuation system, and the magnetic actuation system) integrated into one system controlled by a user interface as seen in Figure 11.

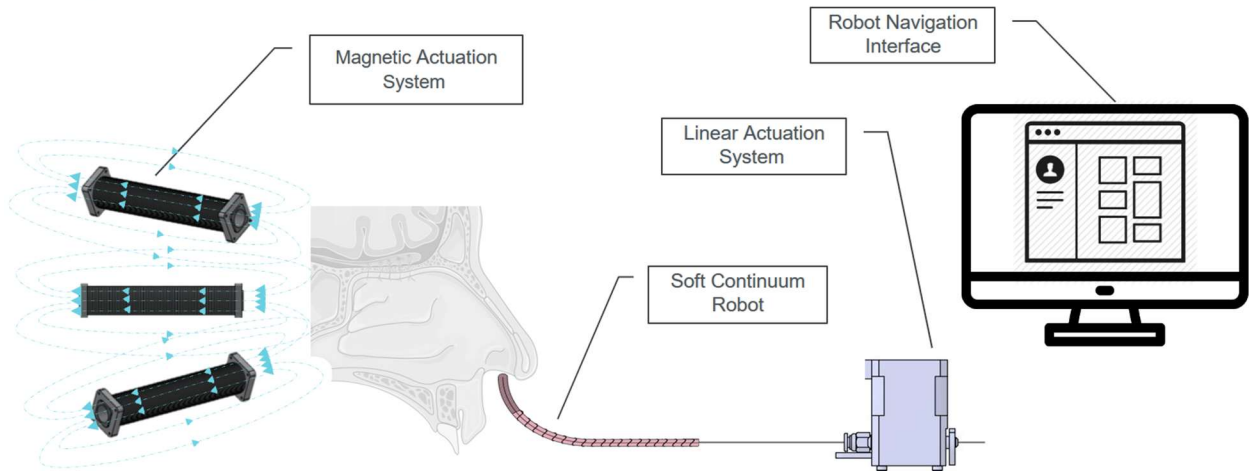


Figure 11. Integration of soft continuum robot, linear actuation system, and magnetic actuation system with user interface of proposed solution

2.2.1 Soft Continuum Robot and Linear Actuation System

The continuum robot itself will be specifically designed to interact with the two actuation systems when initiated by the navigational interface. The tip of the robot will be magnetized for directional control initiated by the magnetic actuation system, and the body of the robot will be moulded to have a raised helical structure, allowing for both bidirectional linear motion. This combination will allow for smooth navigation and full range of movement across the pathways in the ENT.

The decision to magnetize only the tip of the robot was based on simplifying the directional aspect of control. Since linear movement is being controlled by a separate system, it was determined that the tip of the robot would only be magnetized in one. Isolating a singular magnetization direction and magnetic location allows for predictable and simple movement of the robot, which further enables dexterous yet precise navigation. This design decision also simplifies the control algorithms required to guide the robot's directional movement, reducing computational complexity to meet the scope of this project. Only magnetizing the tip minimizes interference from surrounding magnetic forces that could have affected the body of the robot. One aspect of the calculations for this system includes determining the bending amount of the robot body based on the force applied to its tip by the external coils. Using the beam deflection formula for a cantilever beam, the deflection (δ) of the wire can be calculated as:

$$\delta_{wire} = \frac{FL^3}{48EI} \quad (15)$$

Where F is the force applied to the tip in Newtons, L is the length of the wire in meters, E is Young's modulus of the robot in Pascals, and I is the moment of inertia of the wire's cross section in $kg \cdot m^2$, as shown in Figure 12 [8]. Using a silicone body of 4mm in diameter, encasing a

0.5mm diameter nitinol wire, the moment of inertia can be simplified to the following equation [8]:

$$I = \frac{\pi(d_{outer}^4 - d_{inner}^4)}{64} = 1.256 \times 10^{-11} \text{ kg} \cdot \text{m}^2 \quad (16)$$

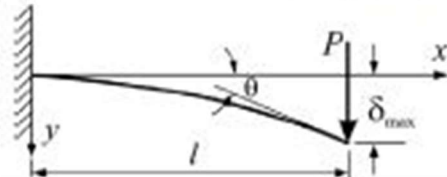


Figure 12. The cantilever bending lever relative to point load P with resulting deflection δ_{max} , the angle of rotation θ , and the beam length l .

A nitinol wire of 0.5 mm ensures the requirement of 120° bending movement, input 2.8, is met and surpassed. Bending thicker wire requires a force that is likely unattainable by the coils and magnetized tip.

Although this formula greatly simplifies the system allowing for advantageous quantification of parameters, there are a few limitations. First, the wire's length and force cannot be accurately calculated, as the pathways of the body will bend the wire at will, and there is no way to anchor the base of the wire to fit the ideal scenario of this formula. Also, the calculations simplify the distributed gradient force across the entire magnetized tip into a single point force on the end of the robot. Additionally, the applied force on the tip by the coils will be substantially damped by the human body, so it is difficult to calculate the force applied by the magnetic field of the coil, without using complex calculations that are outside the scope of the resource of this project. It should be noted that the Python library called MagPy can be used to execute these calculations for precise modelling of magnetic field distributions in real-time along with NumPy [9]. With the implementation of simulations and a user interface using the MagPy and PyVista library, the team can analyze field interactions that were generated by electromagnetic coils to estimate the resultant force experienced by the magnetic tip for intuitive control of the robot. This is further explored in later chapters.

The helical protrusions on the silicone body of the robot are designed to promote rotation when force along the robot body is encountered to reduce any potential trauma as the robot is extended or retracted.

Additionally, the overall design will limit the robot's area of contact inside the body, further decreasing the friction and strain on the body through the movement force [10]. Limiting the unidirectional force applied to the tissues in the form of friction and instead turning it into desired rotation improves the reliability of the solution and ensures consistent performance throughout.

The nitinol wire core was chosen compared to a pure silicone system for its mechanical stability, sustaining the linear actuation force throughout the robot body, while maintaining its flexibility and ability to turn in 360 degrees [11]. The outer silicone layer, in addition to providing the helical outer structure, will provide cushioning and protection to the inner core, as well as better control by increasing the circumferential size of the robot. Furthermore, silicone will decrease the deployment force on internal body surfaces, due to its smoother surface, as well as improve biocompatibility [12]. This design is meant to optimize the ratio between weight, control, structural integrity and biocompatibility of the robot.

The design of the linear actuator will take inspiration from extruders, such as those used in 3D printers. A stepper motor will drive the gears, which turn in a counter motion to move the robot

for extension or retraction. The gears will interact with an external portion of the wire core that is continuous throughout the robot. This will allow the actuator to interact with the robot, applying translational forces without otherwise affecting the silicone body of the robot that will enter the body. This design ensures that the linear motion is guided directly by the actuator without compromising the structural integrity of the robot.

2.2.2 Magnetic Actuation System

The final portion of the design is the magnetic actuation system, intended to directionally control the continuum robot while inside the patient using an intuitive navigation interface. This system will work in tandem with the linear actuation system to allow for specific and intentional control of the robot as it navigates narrow and winding sinus pathways.

There are similar solutions currently available for medical applications, but they do not address the unique requirements of ENT surgeries specifically [13], [14]. A significant limitation of these designs currently being tested for the market would be their use of permanent magnets [13]. Using a permanent magnet to magnetically actuate a surgical robot limits the precision of control; If a permanent magnet is placed near a point of interest, such as the magnetic robot, the strength of the field applied to that point is proportional to the magnet's distance. As the magnet is brought closer to the robot tip, the force on the robot increases; as it moves away, the force weakens [15][16]. However, these changes in field strength are imprecise and prone to human error due to their reliance on distance [13]. A key objective set for this design is to eliminate the need for manual adjustment of the magnet's positions as the sole method of controlling field strength. Furthermore, a permanent magnet continuously emits a magnetic field with no mechanism to stop the generation, which can pose safety risks and concerns. Therefore, an essential design constraint is the inclusion of an immediate shutdown mechanism that disables the device should unsafe conditions or a critical failure occur. This would ensure patient safety in case the magnetic field causes any adverse reaction. As a result, the final concept for magnetically actuating the robot will utilize custom electromagnetic coils as they can provide precise control, can be deactivated instantly for safety, and eliminate limitations posed by permanent magnets.

Designing the actuation system's magnetic field to be output from solenoid coils enables dynamic and precise magnetic field control. The resulting magnetic fields are proportional to the current being passed into the coil [15][16], and increasing the current will increase the magnetic field output. The relationship between the applied current and resulting magnetic field is quantitatively defined by the formula for the magnetic field of a solenoid coil:

$$B = I \frac{\mu_0 N}{l} \quad (17)$$

where B (magnetic field in T) is directionally proportional to I (applied current in A). This equation highlights the dependence of the magnetic field on key parameters such as number of turns N and coil length l . Furthermore, reversing the current direction will also reverse the field direction, causing either an attraction or repulsion force by the coil (design input 3.4). Therefore, the direction and strength of the field generated by the solenoid do not rely on manual adjusting the distance of the actuation system to the point of interest. Instead, the microcontroller can electronically vary the magnetic field using the interface; this showcases how coils meet the objective set above, previously impossible with the use of permanent magnets. The coils enable the magnetic field exerted to have a specific upper bound (design input 3.2) which can be calculated and integrated into the design. Furthermore, given the current's proportionality to the field exerted from the coil, when no current is passed ($I = 0A$), the field will stop generating ($B = 0T$). This introduces a

failsafe mechanism to stop supplying the magnetic field onto the robot immediately (design input 5.6). As the magnetic field is directly responsible for the robot's motion, cutting the field effectively results in immediate loss of motion such that the system can safely halt. Thus, the choice of coils meets the safety constraint set out for this design by adding an immediate fail-safe into the interface with regards to magnetic field generation.

The next design objective of the magnetic actuation system is to enable the robot to achieve three degrees of freedom, allowing for precise control of its motion in the coronal, sagittal, and transverse planes. This will facilitate movement along the anterior-posterior, lateral-medial, and vertical axes, ensuring the robot can be accurately positioned and oriented in three-dimensional space. Various magnetic fields predictably interact with one another through the superposition principle. With multiple magnetic fields $B_1, B_2 \dots B_n$, generated from different coil sources, the total magnetic field can be calculated as:

$$B_{total} = \sum_{i=1}^n B_i \quad (18)$$

Given that these fields are vectors in a three-dimensional space, directionality and magnitude must be considered in their summation. Therefore, as an example, if two magnetic fields B_1 and B_2 are acting at a point of interest, the superposition principle can be applied to conclude the following:

$$B_{total} = (B_{1x} + B_{2x}) * \hat{i} + (B_{1y} + B_{2y}) * \hat{j} + (B_{1z} + B_{2z}) * \hat{k} \quad (19)$$

Where \hat{i} , \hat{j} , and \hat{k} , are the unit vectors in the x , y , and z directions, respectively, and each B is separated into its directional magnitude components. In this application, biomedical planes (sagittal, coronal, transverse) align with the x , y , and z axes in engineering for consistent analysis of magnetic field components.

These field components are of interest as the intensity and directionality of the generated fields can be manipulated through constructive or destructive interference, wherein the fields sum or subtract through interactions. This is the driving principle behind the execution of the robot's magnetic actuation. Since the objective set out is to control the robot with three degrees of freedom, that means three coils is sufficient to control the robot.

Each of the three coils will need to be independently controlled by a microcontroller using the interface such that combinations of on/off states and binary directionalities can be manipulated to generate desired fields. The implementation of three coils correspond to the three principal planes in which the magnetic field must be controlled. By aligning each coil along one of the three orthogonal axes, the system can be manipulated the magnetic field in a three-dimensional space. As a result, the circuit uses logic-level MOSFETs connected to a microcontroller to drive the logic independently, which is prompted by the Python software interface to turn the coils on/off with directionality changes to produce different fields. A navigation interface will be used by surgeons and operators of this system to easily understand how the system functions without requiring users to have a comprehensive understanding of electromagnetic fields. More clearly, the field interactions will be calculated and implemented on the back end, and the user will easily be able to control the robot. There is also visual feedback on the interface to indicate which exact coil is active for further monitoring. By controlling the three coils, the system will generate a magnetic field strength of at least 2mT (design input 3.2 and 5.1). Since the coils will be turned on and off to provide directional control, the limited amount of time that any given coil is activated will mitigate the heat generated such that it does not surpass 100° Celsius and impose risk (design input 3.1).

2.3 Final Decision: Risk and Compliance Management

2.3.1 Health and Safety

For this project, a Fault Tree Analysis (FTA) was conducted instead of a Failure Modes and Effects Analysis (FMEA) to identify health and safety risks associated with the implementation, prototyping, validation, manufacturing, and deployment of the magnetically actuated continuum robot. This decision was made with the primary goal of identifying and mitigating critical hazards directly linked to the system, which aligns with the top-down approach of FTA. An FMEA requires detailed component-level analysis and exhaustive consideration of all possible failure modes, which is very complex given the current prototyping stage and the overall project timeline. Dr. Alan Wassyng, an expert in safety and risk analysis, also recommended FTA as a suitable alternative to address the project's needs effectively. By focusing on high-level hazards and tracing them to root causes, an FTA allows for the development of safety requirements early in the design and prototyping phases.

In this health and safety risk analysis, the guidance provided by ISO 14971:2019 is followed to systematically identify, evaluate, and mitigate risks associated with the project [17]. The risk management process outlined in this standard begins with defining the device's intended use and reasonably foreseeable misuse [17]. For example, as defined previously, the intended use of the robot is for minimally invasive ENT surgeries, where it will navigate complex pathways to reduce tissue trauma. Foreseeable misuse, however, could include scenarios such as improper calibration leading to excessive force applied by the robot. This scenario highlights a potential hazard that must be addressed during design and testing. Additionally, major safety-related components have been identified, including the robot's magnetized tip as well as its actuation and directional systems, where their failure could compromise patient safety.

The FTA is constructed by systematically tracing a primary hazardous situation—patient harm—to specific hazards and their root causes. This structured approach targets and mitigates these root causes and hazards effectively, ensuring that the health and safety risks associated with the project are addressed comprehensively. Table C.1 in ISO 14971, as seen in Appendix C: Hazards and Risk Analysis, categorizes hazards into energy hazards, biological and chemical hazards, and performance-related hazards, which help serve as a framework for this analysis [17]. For this magnetically actuated soft continuum robot, hazards that would result in the patient being harmed would include electrical energy, mechanical energy, potential energy, thermal energy, biological agents, chemical agents, and loss of functionality. These hazards will be discussed in detail with their root causes, consequences, and mitigation strategies.

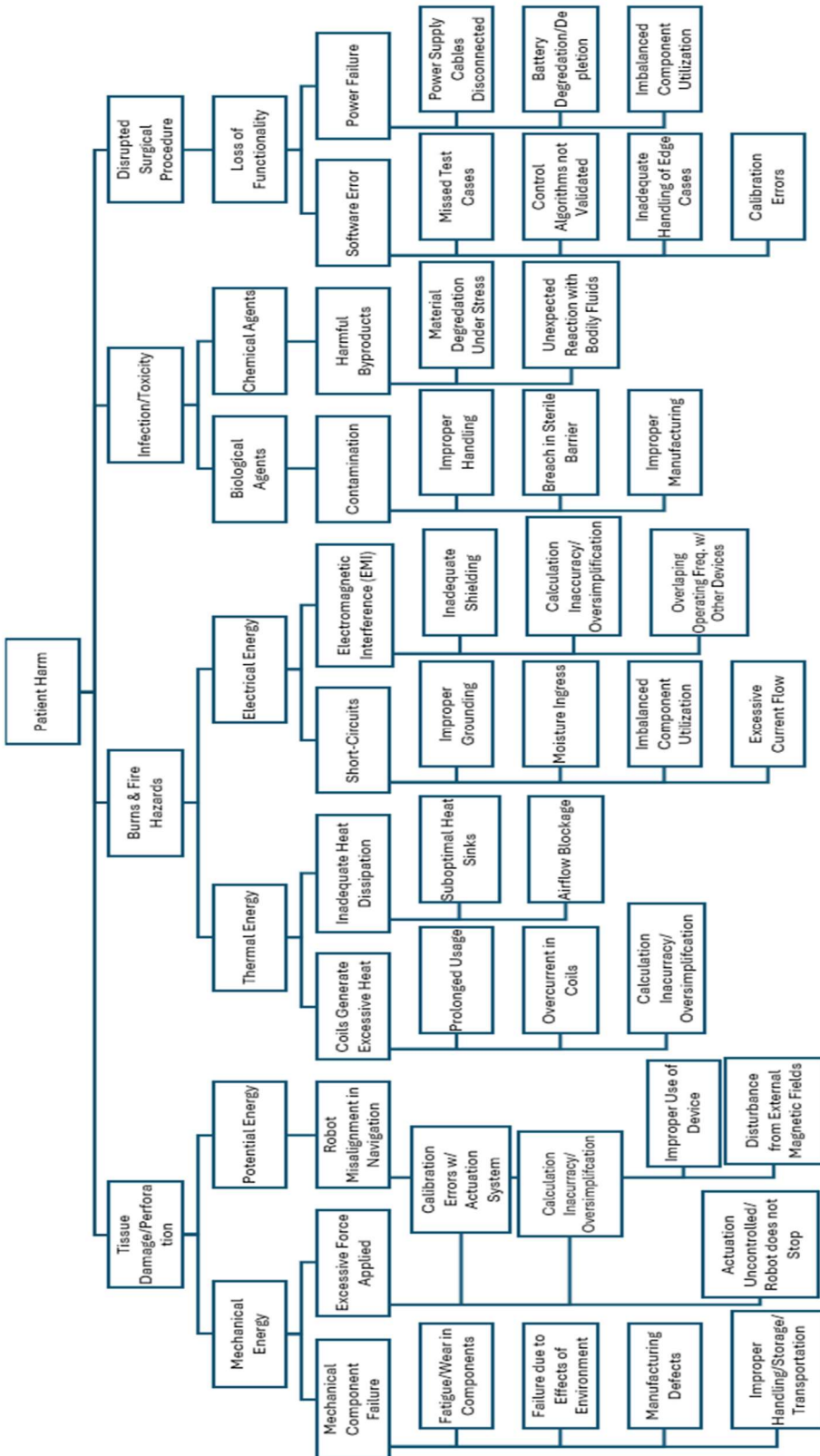


Figure 13. Fault Tree Analysis (FTA) of proposed solution

Electrical energy poses significant risks during the operation of the robot, primarily in the event of electrical short circuits in the coils, electronics component failure or electromagnetic interference (EMI) with nearby surgical equipment. Such failures can result in fire hazards, tissue burns due to excessive current exposure, or disruptions in the functionality of other devices in the operating room. Both voltage and current hazards must be independently considered. Voltage hazards will increase the risk of insulation breakdown and failure which could result in component damage or excessive heating. Current hazards can cause overheating, fire, or direct tissue burn from prolonged exposure. To mitigate these risks, safety measures will include selecting components with parameters well above the expected operating conditions, ensuring they can handle far more than the system's typical values. For example, surface-mount logic-level MOSFETs are used to separate the logic control of the coils from the power supply, ensuring that the Arduino is protected from potential damage caused by the high current and voltage supplied to the coils. Additionally, robust protective shielding will be implemented to prevent short circuits and contain electromagnetic fields. The design will undergo stringent EMI testing to ensure the device operates harmoniously within a surgical environment. Additionally, backup systems such as surge protection and automated error-detection protocols testing for abnormal voltage spikes and excessive current will be integrated to correct anomalies in real time, minimizing the risk of harm to both the patient and other equipment. These decisions align with best practices outlined in IEC 60601-1-2, which governs EMI safety in medical devices [18]. This standard and all others will be elaborated on in section 2.3.3.

Mechanical energy hazards arise primarily from excessive force applied by the robot to anatomical structures in the body and mechanical component failures, such as breakage of the nitinol wire. These issues could result in tissue damage, perforation, or loss of robot control during surgery which could lead to unintended movement or surgery incompleteness. Preventive measures include the integration of real-time force sensors to monitor applied forces and maintain them within safe thresholds. Mechanical components, such as the nitinol wires, will undergo fatigue testing to validate durability under expected operational stresses and as part of the standard calibration process. Additionally, training protocols for medical personnel will emphasize the importance of proper device handling and operation to prevent excessive mechanical stress on nitinol wire, specifically during procedures where the bending radius of the robot capabilities were exceeded. A maximum bending strain threshold based on the material's fatigue data will be established to prevent premature wire failure. These mechanical design choices are supported by ASTM F2063, the standard specification for nitinol medical devices [19].

The sudden release of stored potential energy, often due to loss of control or misalignment of the robot's navigation system poses a critical risk. Such scenarios can lead to accidental damage to sensitive tissues or failure to complete surgical objectives. To address this, robust failsafe mechanisms will be implemented to halt robot motion during emergencies. Calibration checks will be conducted before every procedure to ensure that all navigation systems are properly aligned and functional. Furthermore, regular maintenance schedules will be established to inspect and repair any wear or degradation in actuation mechanisms. As well, similar fail-safes have been integrated into other robotic-assisted surgical devices such as the Da Vinci system to prevent unintended motion [20].

Thermal energy hazards can stem from prolonged operation of the electromagnetic coils and inadequate heat dissipation. Excessive heat can cause damage to surrounding areas and degrade biocompatible materials. Mitigation involves the aforementioned regular shutoff mechanisms – ensuring the coils are only on momentarily – and the use of heat-resistant materials

to regulate temperature and improve heat dissipation. Regular thermal stress testing under simulated surgical conditions will ensure the device maintains safe operational temperatures.

Biological hazards include contamination of the device due to improper handling or breaches in sterile barriers during surgery. These situations can result in post-operative infections, significantly prolonging the patient's recovery time. To mitigate these risks, strict sterilization protocols will be established, ensuring all reusable components are properly sanitized. The sterilization process will be tailored towards the material properties of each component. The metallic components, which include the structural elements of the linear actuation system, will be designed to withstand autoclaving at high temperatures above 120°C. Select components will be tested for UV exposure tolerance for non-contact sterilization methods. Wherever feasible, disposable or sterile-packaged components will be used to reduce the risk of contamination. The solution is set to be reusable for the magnetic actuation system and linear actuator, however, the silicon, nitinol wire, and magnetized tip will be of one-time usage. Training programs will be provided to medical personnel to ensure proper handling and maintenance of the device in clinical environments. These procedures align with ISO 17664, which provides guidelines for sterilization of medical devices [21].

Chemical hazards arise from the degradation of materials, releasing harmful byproducts, or from reactions with bodily fluids. This can lead to toxic reactions in tissues or compromise the device's structural integrity. Mitigation strategies include the selection of biocompatible materials and integrated particles. The selection of biocompatible materials follows ISO 10993 which is the standard used for biocompatibility testing [22]. Long-term stability tests will confirm the material's safety and durability under clinical conditions.

Loss of functionality, caused by software errors or power failures during operation, poses a substantial risk to patient safety. Such failures can result in incomplete or unsafe procedures and prolong surgery, increasing the overall risk to the patient. To mitigate this, software fail safes will be integrated to detect and address errors in real time, ensuring continuous operation. Key conditions to be monitored will be system temperature, real-time communication between the robot and the control unit, as well as power stability to detect anomalies that can result in loss of functionality. Redundant communication pathways and backup power systems will provide additional reliability during use. Extensive preclinical validation, including software stress tests and failure mode simulations, will be performed to ensure robust performance in varying real-world scenarios. In specifics to clinical settings, conditions such as scheduled vs emergency use, prolonged operation usage, and varying patient-specific anatomical constraints will be performed to ensure compatible usage. Regular maintenance and firmware updates will also be implemented to address potential system vulnerabilities over time. To prevent disruptions during usage, firmware updates will not occur during real-time procedures but scheduled in accordance with hospital IT systems for appropriately timed maintenance updates. These updates can be deferred prior to usage for the system to remain functional. If required in an emergency setting, a special firmware mode can be implemented to suspend updates automatically.

In terms of power failure, regular verification of the components will be maintained to ensure sufficient usage. This includes ensuring the power supply is adequate and the components are well connected. Although most hospitals have backup power systems, in an event where there may be a delay between power source switching, the device will incorporate an internal power supply to maintain continuous operation such that no unintended interruptions would impact the operation. Once restored in power, the robot will resume in executing the previously calibrated

state with next procedural step in queue. If misalignment occurs, the robot can recalibrate its positioning to ensure precision in operation.

The identified hazards highlight the multifaceted risks associated with the magnetically actuated continuum robot. Through detailed analysis of root causes and consequences, targeted mitigation strategies have been developed to address these risks comprehensively.

2.3.2 Ethical Concerns

Developing a magnetically actuated continuum robot for ENT surgery presents several ethical risks that must be carefully managed to ensure responsible integration into clinical settings. These risks include potential impacts on healthcare staffing, liability issues, accessibility disparities, and challenges related to informed consent.

Concerns about the robot's potential impact on healthcare staffing must be addressed. While this technology may reduce the need for additional personnel in surgical settings, it should be positioned as an enhancement to human expertise rather than a replacement. Providing training programs that equip healthcare staff to work effectively with robotic systems can foster a balanced integration into surgical environments.

Liability and accountability are also critical ethical considerations, and as outlined by Razek, concerns related to potential harm caused by the robot raise complex questions around legal and ethical responsibility [23]. Defining clear roles and responsibilities through well-documented protocols and contracts ensures accountability among manufacturers, operators, and healthcare providers, minimizing this risk. Transparent reporting of any adverse events and establishing mechanisms to investigate and address them promptly is very important as well. Ensuring informed consent involves providing patients with comprehensive, understandable information about robot-assisted procedures, including potential risks and benefits, to support the autonomous decision-making of the patient.

Additionally, ensuring equitable access to this technology is important to prevent disparities in patient care. Designing the robot for cost-effective manufacturing and seamless integration with existing surgical equipment can make it more accessible to a broader range of healthcare providers, including those in resource-constrained settings.

By recognizing and employing various strategies to reduce the ethical risks, the development and implementation of the magnetically actuated continuum robot can uphold patient welfare, ensure equitable access, and foster trust among users and stakeholders. This approach aligns with ethical considerations in emerging technologies, as discussed in the literature.

2.3.3 Standards and Codes

To ensure the safety, effectiveness, and regulatory compliance of the magnetically actuated continuum robot, relevant standards, codes, and legal factors applicable to its design, manufacturing, and use in surgeries have been identified and addressed.

Adhering to ISO 14971:2019 *Application of Risk Management to Medical Devices*, the project design implemented a structured approach to identifying, evaluating, and mitigating risks associated with the robot. This standard emphasizes proactive hazard identification and systematic risk evaluation throughout the lifecycle of a medical device, ensuring patient safety remains the central focus [17]. To align with this standard, a Fault Tree Analysis (FTA) was conducted to systematically identify potential hazards, root causes, and their impact on patient safety. This

approach ensures that key risks, such as tissue damage, electromagnetic interference, and infection, are addressed through the mitigation strategies detailed earlier. ISO 14971 also notes the importance of maintaining a risk management file, which will be actively updated throughout the design, prototyping, and validation phases. This iterative process ensures new risks are promptly addressed, and risk controls are verified and validated for proper effectiveness. Additionally, the standard emphasizes the necessity of residual risk evaluation, ensuring that the risks remaining after mitigation are acceptable when weighed against the robot's clinical benefits.

In addition to risk management, the robot will be designed to meet critical standards for medical devices. IEC 60601-1-2 *Electromagnetic Compatibility (EMC) for Medical Devices*, is a standard that ensures the robot does not emit harmful electromagnetic interference (EMI) and is not adversely affected by surrounding electromagnetic fields [18]. Shielding materials will be incorporated around the coils to ensure compliance with CISPR 11 for radiated emissions, as defined in IEC 60601-1-2 [24]. Also, electromagnetic emissions testing will be done to ensure magnetic fields generated by the coils remain well below 40mT at the patient's tissues and especially near sensitive areas like the brain. Immunity Testing will ensure the robot can resist interference from external devices operating at up to 10 V/m in the frequency range of 80 MHz–2.7 GHz, typical in surgical environments [18]. ISO 10993-1 *Biological Evaluation of Medical Devices* covers the biocompatibility of materials used in medical devices, particularly those in prolonged contact with human tissue [22]. In compliance with this standard, the robot's soft body and magnetized tip will be fabricated using biocompatible materials, including medical-grade silicone and nitinol wire. Rigorous biocompatibility testing, including cytotoxicity, sensitization, and irritation tests, will validate material safety [22]. ISO 17664 *Processing of Health Care Products – Information to be Provided for the Processing of Medical Devices*, provides information on sterilization which is pertinent for the actuation components that are not single use like the robot itself. The use of sterile barriers to protect these units during procedures will ensure compliance with hygiene requirements and mitigate the risk of contamination and maintaining the functionality of the reusable components, thus aligning with this standard's requirements [21]. To minimize the risk of user error and enhance operational safety, the robot's interface will comply with ISO 62366-1 *Application of Usability Engineering to Medical Devices*. This standard requires the integration of intuitive controls and feedback mechanisms, designed to reduce the cognitive load on the user during surgery [25]. Usability evaluations with surgeons would assess how well the robot integrates into current surgical workflows, and training materials, including simulations, would be developed to ensure medical personnel can operate the device safely and effectively.

Furthermore, adherence to regulatory frameworks, such as Canadian Medical Device Licensing (MDL) and the FDA Class II Device Requirements ensures the robot meets the stringent legal and safety requirements for clinical usage. In Canada, obtaining a Medical Device License (MDL) under Health Canada's regulatory framework necessitates meeting stringent requirements for safety and efficacy, with particular emphasis on devices used in minimally invasive surgeries [26]. Adhering to these regulatory steps ensures that the robot can be introduced into surgical workflows with the assurance of meeting high safety standards for the Canadian market.

In the USA, the robot would fall under FDA Class II Device Requirements, since it poses moderate risk to patients if malfunction or misuse occurs but is not Class III as it does not support or sustain life, is not implanted, and does not replace critical bodily functions. Compliance in the American market requires the submission of a premarket notification – a 510(k) – to demonstrate substantial equivalence to an existing legally marketed device. This process includes providing comprehensive validation data to confirm the robot's safety, effectiveness, and biocompatibility,

ensuring it meets regulatory expectations for minimally invasive surgical tools [27]. Like many other Class II devices, there are existing surgical robots and magnetically actuated instruments that act as precedents in terms of being cleared for safety and function approval. Referencing these devices, like the Sensei Robotic Catheter System (510(k) number: K141822) from Hansen Medical, which navigates complex anatomical pathways with precision, provides a pathway for demonstrating substantial equivalence and compliance with the FDA 510(k) process [28].

By mitigating health and safety risks, addressing ethical concerns, and ensuring compliance with key standards, this magnetically actuated robot for ENT surgery can be considered both safe and effective.

2.4 Final Decision: Proof-of-Concept and Verification

The major focus of the proof-of-concept is the ability to successfully move the end effector of the robot in a reachable 2D workspace. The objective of the prototype is to successfully manipulate the robot's horizontal direction using coils and vertical linear direction using the actuator. The final iteration of this magnetically actuated soft continuum robot will incorporate a fully formed soft robot that will be capable of multidirectional motion in a 3D workspace as it is acted on by the magnetic and linear actuation systems with overall control from the navigation interface. This final iteration and its verification will be covered in depth in later chapters.

2.4.1 Soft Continuum Robot and Linear Actuation System

2.4.1.1 Set-up

For the proof of concept, a frictional extruder design was used to demonstrate proper motor control and bidirectional movement of the robot. The stepper motor was driven using an L298 driver, powered by a 9 V power supply and controlled by an ESP32 microcontroller. The setup is shown in Figure 14 below:

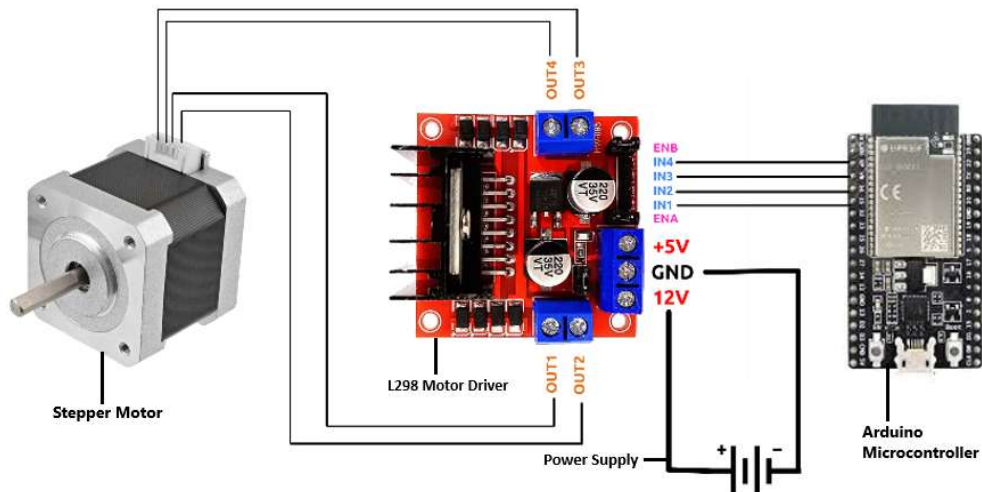


Figure 14. Wiring connections between the power supply, Arduino microcontroller, L298 driver and stepper motor.

To control the motor to spin in both directions, two buttons were wired to the microcontroller, spinning the motor in either direction when pressed. The setup is shown in Figure 15. Notably, instead of physical buttons, the linear actuator is controlled using a navigational interface for ease of application in the final iteration.

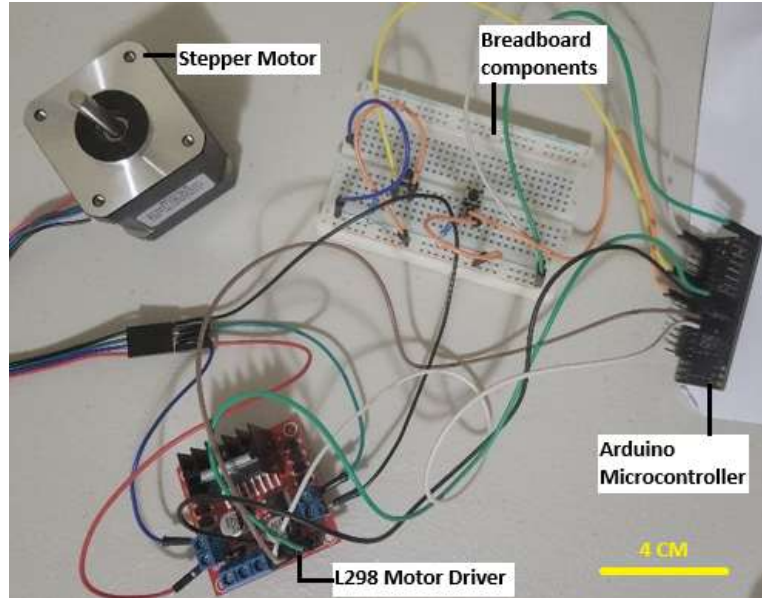


Figure 15. Physical setup of linear actuator with all components

To move the wire for extension and retraction, the design uses two gears held in place by a spring to push the gears together and maintain friction on the wire. As the stepper motor turns, it drives both the idler roller and toothed wheel to rotate inwards, causing the robot to extend forward (extension). If it turns in the other direction, the idler roller and toothed wheel to rotate outward causing the wire to retract backwards (retraction). This allows the actuator to achieve the desired bidirectional linear movement. Figure 11 demonstrates visually the concept and application of this design.

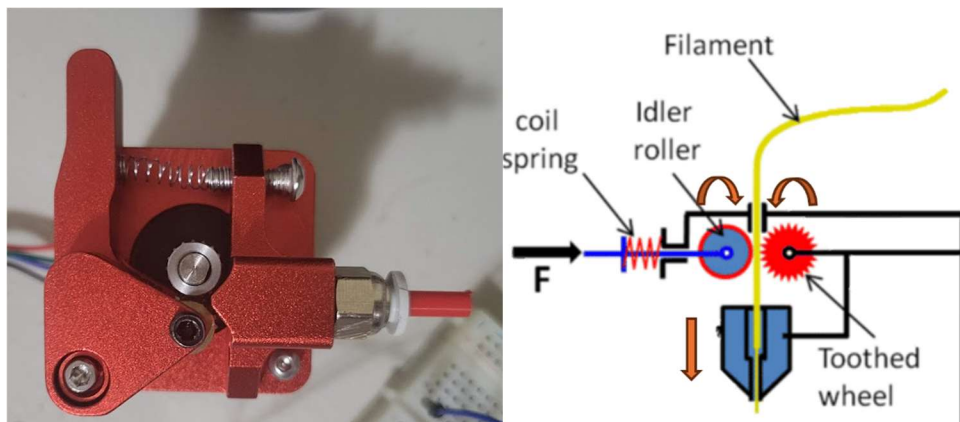


Figure 16. Physical component and labelled diagram of the extruder design of the linear actuator [29]

2.4.1.2 Components

Table 4. Inventory list of all components used for the actuator for proof-of-concept prototype

Component	Quantity	Descriptor
Microcontroller (ESP32 Pico)	1	Control the logic of the circuit
12V Soulbay Power Supply	1	Supplies voltage to stepper motor
L298 Driver	1	Intermediary between low-power control signals of the microcontroller and the 12V power supply
Extruder	1	Push the gear for extension and retraction
Buttons	2	Wired with the microcontroller to turn the stepper motor in both direction

2.4.1.3 Design Calculations

The formula for the linear speed of the motor, along with the appropriate calculations, can be found in Appendix A: Design Output Calculation, subsection Calculation 2.

Given a step interval of 6 ms, the code checks every millisecond if 6 ms has elapsed and if it has, increases the step of the motor by one. Note that the stepper motor has a step angle of 1.8° , so a one step increase will turn the motor by 1.8° , requiring 200 steps for a full 360° revolution. However, due to computational delays, it is not guaranteed for the code to check at exactly 1 ms intervals. Therefore, the RPM is most likely slower than the calculated time. Design verification will determine if there is a delay in the system.

2.4.1.4 Design Verification

To check the rotational speed of the motor, a Hantek 2D42 oscilloscope was connected to the input of the driver, which outputs a voltage every step. By calculating the frequency, the RPM can be calculated using:

$$RPM = f \times \frac{60}{200} \quad (22)$$

Where 200 is the number of steps required to make a full revolution.

The oscilloscope was connected to measure one of the four OUT signals output by the driver to the stepper motor. The oscilloscope shows a period of exactly 24.00 ms, as seen in Figure 17. This period was found to be consistently 24.00 ms throughout multiple measurements.



Figure 17. The period for each OUT pin was found to be 24.00ms, measured using the scope function from a Hantek 2D42 Oscilloscope.

This is completely accurate to the set step interval of 6 ms, since for every 6 ms, the driver sends a signal to the next OUT pin, looping back after the fourth pin. Therefore, it takes 24 ms before a high signal is sent to the same pin. Therefore, the frequency of each step can be calculated as:

$$f = \frac{4}{P} = 166.67\text{Hz} \quad (23)$$

$$RPM = 50$$

Where P is the period = 24 ms. The frequency obtained is completely accurate to the design calculations above, so it can be assumed that there are no delays in the RPM of the motor.

Now that the motor is calculated to be exactly 50 RPM, it is important to verify the linear speed, which can decrease due to lack of friction. To verify linear velocity loss due to slippage of the gear on the robot, code the controller to move the stepper motor at 50 RPM for exactly one second, and measure the initial and final position of the wire. Since the code was already shown to be accurate, this will be a reliable test. The process is repeated multiple times in both directions to check repeatability and accuracy of the actuator. This is shown in **Error! Reference source not found.**, and after five tests, the wire consistently lands between 23 and 24 mm on the ruler. This verification introduces human error, since the measurement of a ruler when using the human eye cannot be completely accurate. However, the consistency of a measurement between 23 and 24 mm indicates that the wire can be within ± 1 mm/s.

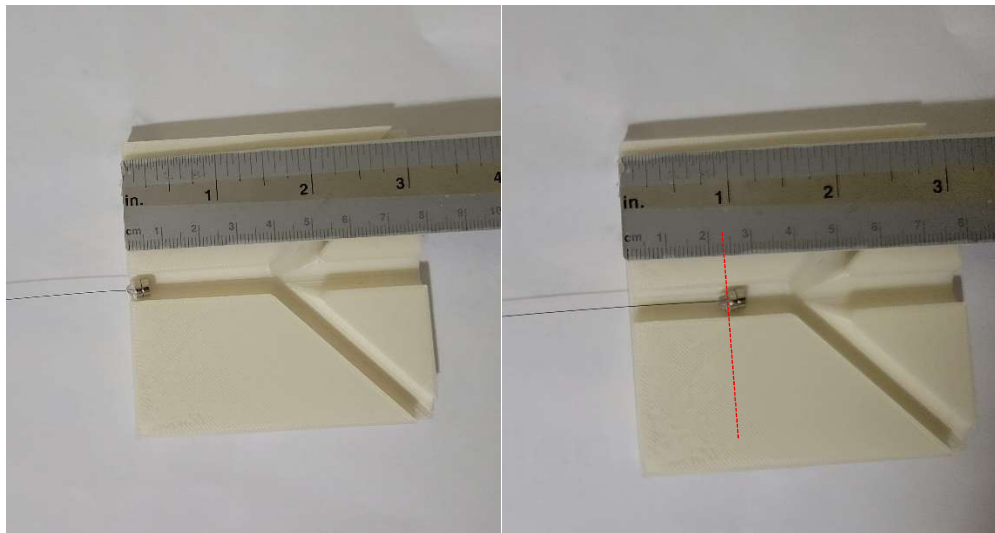


Figure 18. The before and after position of the wire after spinning the motor for one second with 2.4cm of insertion into pathway model

Another limitation to this test is that there is no measurement of static friction from the robot's interactions with the human body. There is currently no resource available to test the amount of force needed to cause slippage in this device, as part of justification behind the helical design was to prevent errors due to static friction buildup. Overall, the proof-of-concept demonstrates the precision of the microcontroller and stepper motor to accurately drive the robot linearly.

2.4.2 Magnetic Actuation System

2.4.2.1 Set-up

To demonstrate the feasibility of the magnetic coil actuation system, a smaller scale circuit was created with the goal of independently controlling two coils for proof of concept. The circuit, simulated through LTSpice in Figure 19, utilizes a power supply connected to the coils through independent logic-level MOSFETs, with connections to the drain and supply terminals. The gate terminal of the MOSFET is controlled by a microcontroller, which applies either a positive voltage or no voltage to the gate. When voltage is applied, it causes the MOSFET to saturate, allowing current to flow from the power supply, through the coil, and to ground. When the microcontroller stops applying voltage, the power supply and coil become an open circuit thus stopping the coil from producing a magnetic field. This circuitry is made such that the coils can be controlled independently through the push of a button with associated LEDs as a visual indication for proof of concept. The entire proof of concept system can be seen in Figure 20. However, in the final iteration, a navigational interface is applied to intuitively control the directionality of the robotic tip with status indicators discussed in later chapters.

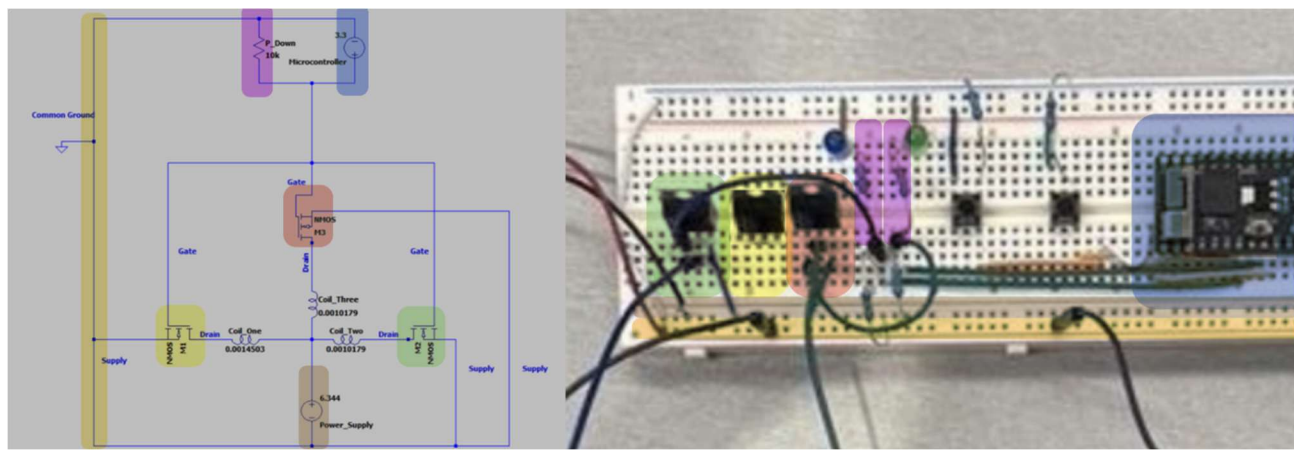


Figure 19. Labelled LTSpice simulation of the coil circuitry used in the proof-of-concept demo (Left), shown beside the actual circuit created and used in the demo (Right). Colour highlights are included to show how the LTSpice corresponds to the real circuit use

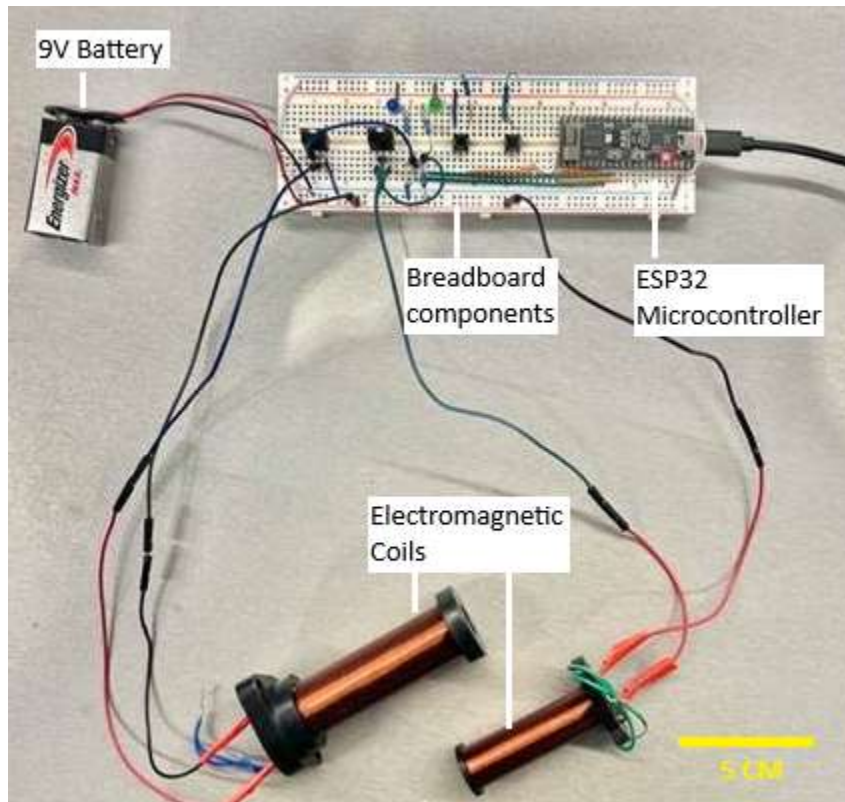


Figure 20. Photo of coil circuitry showing the LEDs and buttons associated with the two coils for proof-of-concept prototype.

2.4.2.2 Components

Table 5. Inventory list of all components used in the coil proof-of-concept demo.

Component	Quantity	Descriptor
Microcontroller (ESP32 Pico)	1	Control the logic of the circuit
9 V Battery (Energizer)	1	Supplies voltage to the coils
Logic Level MOSFETs (RFP30N06LE)	2	Individually connects each coil to the power supply and is connected to the microcontroller to control the ON and OFF states of the coil.
Coil (49mm diameter)	1	Wide diameter coil used to generate magnetic field
Coil (24mm diameter)	1	Narrow diameter coil used to generate magnetic field
LEDs	2	Used to visually indicate when a coil is on or off.
Resistors	6	Used to manage button logic, LEDs and pull-down resistor for the microcontroller's varying output.
Buttons	2	Wired with the microcontroller to turn on and off the coils when pressed.

2.4.2.3 Design Calculations

The motivation behind this design is the creation of magnetic fields, thus the most important step was figuring out how to generate a field using a coil system. Given that the goal, as outlined in design input 3.1, was to generate a magnetic field of around 2 mT within 20cm of the source, the first step was calculating how that would be achievable with the coils purchased. Two different-sized coils were purchased for the sake of prototype testing variation. This allowed for testing and optimizing different coil parameters and seeing how they can generate various magnetic fields. The equation below can be used to isolate the current required based on the coils.

$$B_{solenoid} = \frac{\mu_0 \cdot I_{solenoid} \cdot N_{turns}}{l_{solenoid}} \quad (24)$$

Where $B_{solenoid}$ is the field generated by the coil, μ_0 is the permeability constant (always equal to $4\pi \cdot 10^{-7} \text{H/m}$), I is the current in Amps, N is the number of turns on the coil, and l is the length of the coil in meters [15][16]. Thus, given the predefined parameters of the coils being set such that $N = 200$ turns and $l = 0.0527$ m, and the goal of 2 mT within 20cm being set, the required current can be calculated.

$$0.002 \text{ T} = \frac{4\pi \cdot 10^{-7} \cdot I \cdot 200}{0.0527}$$

$$I = 0.419 \text{ Amps}$$

Note: the radius of the coils does not impact the calculation of the internal field generated. It will impact the outward field calculations and as a larger radius can result in a more spread-out field at the ends of the solenoid, making the field weaker externally. Within the scope of this proof-of-concept, the coils were kept nearby, thus the way the radius changing would impact the field at distances far away from the coil was not accounted for. With respect to this proof-of-concept, the radius calculations are not relevant. Thus, for this case, these two coils of varying radius can be treated the same, since they are the same length, and therefore both need 0.419 A of current supplied to generate 2 mT. The final iteration is much larger and has more turns to generate

sufficient magnetic fields up to a certain distance away from the source. However, increasing coil size will influence heat dissipation as the greater surface area will effectively dissipate the heat effectively and reduce risk of thermal buildup. This consideration is crucial for ensuring compliance with design input 3.1, limiting the coil temperature to 100°C.

To decide on how much voltage needs to be supplied to the current, Ohm's Law is used [15][16]. But first, the resistance of the coils was measured using an Extech EX470A multimeter, since the data sheet did not indicate the resistance of the coils. Both coils have the same resistance measured about 20 Ω. Therefore:

$$\begin{aligned} V &= I \cdot R \quad (25) \\ V &= 0.419 \cdot 20 \\ V &= 8.38 \end{aligned}$$

Given that the calculated voltage is 8.38 V, a 9 V power source can be used.

2.4.2.4 Circuit Logic

A circuit was designed to meet the requirements for voltage and current, with the PICO ESP32 microcontroller controlling the logic of the circuit—specifically, turning the coils on and off independently. As mentioned, in the final iteration, this logic is driven by a navigational interface. Before constructing the physical circuit, it was simulated in LTSpice to validate its functionality. This simulation revealed the first major roadblock: while the microcontroller can output control signals, it cannot generate more than 5V, and its GPIO pins are limited to 3.3V. Therefore, to handle the higher voltage and current requirements of the coils, calculated above, an external power supply was needed. By introducing an external power supply for the coils, MOSFETs were then also chosen as the switching components to independently control the coils.

However, the choice of MOSFET introduced a challenge as standard MOSFETs with high gate threshold voltages $V_{GS}(Threshold)$ require a larger drive voltage than the microcontroller can provide. Specifically, the gate voltage (V_G) of the proof-of-concept would need to be at least 10 V or higher to ensure the MOSFET is fully turned on and can conduct the 9 V supply to the drain. Therefore, given the 3.3V GPIO pin voltage output from the controller, using these MOSFETs as a switch would not be possible due to insufficient gate drive. Furthermore, trying to increase the voltage could cause damage to the microcontroller due to excessive current draw.

Given this, the solution was to use logic-level MOSFETs, which are specifically designed to achieve full saturation with gate voltages as low as 3.3V or 5V—well within the output capability of the microcontroller's GPIO pins. The specific component that was sourced has a $V_{GS}(Threshold)$ of 1 V minimum, therefore the 3.3 V GPIO pin output from the microcontroller is more than sufficient for this application. This allowed efficient switching of the high voltage and current needed by the coils while ensuring the microcontroller operated safely, with consideration of navigation interface integration.

2.4.2.5 Secondary Components

After computing magnetic field calculations, the final component was to design a circuit that can be used in tandem with the PICO ESP microcontroller. The microcontroller has an Arduino code to drive the logic of button presses, queuing the microcontroller to output voltage

that will saturating the MOSFET, and thus provide the coils with 9 V and 0.45 A to drive the coil's magnetic field output. Notably, it was acknowledged that the battery could exceed 9V which had raised concerns regarding standard variance. As a result, multiple batteries from the same package were tested using an Extech EX470A multimeter to confirm it could perform within an acceptable range. The code isolates the buttons so that they can be turned on and off independently and still function regardless of the combination of on/off between the two buttons. An additional pin was initialized to provide power to an LED light, so that it turns on when its respective coil is being powered. This allowed for the circuit logic to be governed by the microcontroller, such that when the button is pushed, the light turns on, and the coil generates field. This was executed with future integration of the coils with a navigation interface for ease of application. This code can be seen in Appendix B: Software Implementation, subsection Code 1: Coil Control.

2.4.2.6 Design Verification

Given the set up, it was important that the functionality of the device was verified, but also take it one step further, and check the precision of the outputs. Given the LTSpice simulation verified the circuit calculations done by hand, the team progressed onto seeing if the buttons and LEDs functioned in tandem correctly. All four combination of coil states (OFF, OFF), (ON, OFF), (OFF, ON) and (ON, ON) were checked. The buttons, LEDs and coils all worked and were able to move the magnetic robot around. Furthermore, test points were added into the circuit to measure voltage at specific points. Specifically, the MOSFET's drain, gate and supply channels accurately measured ~ 9.37 V, ~ 3 V and 0 Vs respectively. The only thing to note is that the battery was producing more than 9 V, which while not a problem, is important to consider for future calculations. Therefore, this process of confirmation testing the button and LED logic paired with using an Extech EX470A multimeter and test points to verify coil logic can appropriately verify the design is functioning correctly.

In verifying the precision of the design, a magnetic sensor was applied. This sensor is a device that measures the strength and direction of a magnetic field. It can measure both static (DC) and dynamic (AC) magnetic fields. Specifically, the magnet sensor TLV493D-A1B6, made by Infineon, is a 3D magnetic sensor that uses three-axis magnetic sensor technology to measure the magnetic field strength along the X, Y, and Z axes [30]. For the sake of verification testing, the goal was to ensure the predicted field output matches the actual measured field and thus, fits out design output criteria. By using the Infineon Magnetic Sensor App, the sensor can be used to measure the field strength generated by the coil to see if the design outputs accurate field strength.

The calculations for the circuit given the 9.37 V measured from the battery, the current expected to be passing through the coil would be:

$$I_{solenoid} = \frac{V_{battery}}{R_{solenoid}} = \frac{9.37V}{20\Omega} = 0.4685 A \quad (26)$$

Therefore, given the current going into the circuit coil, the predicted field emitted from the coil can be calculated as:

$$B_{solenoid} = \frac{\mu_0 \cdot I_{solenoid} \cdot N_{turns}}{l_{solenoid}} \quad (24)$$

$$B_{solenoid} = \frac{4\pi \cdot 10^{-7} \cdot 0.4685 \cdot 200}{0.0527}$$

$$B_{solenoid} = 2.23mT$$

Given that the expected magnetic field strength was calculated to be 2.23mT, sensors can be used to measure the actual value. The specific set up for verification can be seen in Figure 9, where the magnetic sensor is connected to a laptop with the Infineon sensor software open. The coil is activated, indicated by the blue light, and the sensor is positioned inside the coil, oriented such that the magnetic field passes through the x-axis accurate measurement. Figure 5 shows the measured field as 2.45mT which is greater than the anticipated field. This is an unexpected phenomenon at first, however, it is important to note that upon research, the coils purchased were lower cost models which had limited documentation on the quality process control and impacted the unknown exact number of turns of the coils. In deriving this parameter, it is also difficult due to variations in winding or potential manufacturing inconsistencies making it hard to solve with high accuracy. All other values impacting the field were cross verified. The resistance, and length, were values that were analytically confirmed through using an Extech EX470A multimeter and calipers respectively. However, the coil's turn count remains uncertain. Therefore, the discrepancy between the expected and measured field strength can be attributed to the inability to confirm the precise number of turns in the coil. Despite this discrepancy, the magnetic field emitted is still within the design output specification defined earlier (design output 3.2).

Chapter 2 References

1. T. Duerig, A. Pelton, and D. Stöckel, “An overview of nitinol medical applications,” *Mater. Sci. Eng. A*, vol. 273–275, pp. 149–160, Dec. 1999, doi: 10.1016/S0921-5093(99)00294-4.
2. “Polydimethylsiloxane films doped with NdFeB powder: magnetic characterization and potential applications in biomedical engineering and microrobotics | Biomedical Microdevices.” Accessed: Dec. 05, 2024. [Online]. Available: <https://link.springer.com/>
3. “SuperElastic 3D Printer Resin, Softness 60A Simulating Soft Silicone, Made in Korea by 3DMaterials (500g, Clear) : Amazon.ca: Industrial & Scientific.” Accessed: Dec. 05, 2024. [Online]. Available: <https://www.amazon.ca/SuperElastic-Resilience-Simul>
4. A. R. Pelton, D. Stöckel, and T. W. Duerig, “Medical Uses of Nitinol,” *Mater. Sci. Forum*, vol. 327–328, pp. 63–70, Jan. 2000, doi: 10.4028/www.scientific.net/MSF.327-328.63.
5. I. Gotman, “Characteristics of Metals Used in Implants,” *J. Endourol.*, vol. 11, no. 6, pp. 383–389, Dec. 1997, doi: 10.1089/end.1997.11.383.
6. J. H. Dellinger, The Temperature Coefficient of Resistance of Copper. U.S. Department of Commerce and Labor, Bureau of Standards, 1911.
7. “17HS4401 pdf, 17HS4401 Download, 17HS4401 Description, 17HS4401 Datasheet, 17HS4401 view :: ALLDATASHEET ::” Accessed: Dec. 05, 2024. [Online]. Available: <https://www.alldatasheet.com/datasheet-pdf/download/1245671/NINGBO/17HS4401.html>
8. D. Baker and W. Haynes, “Moments of Inertia,” in *Engineering Statics: Open and Interactive*, Tacoma, WA: PreTeXt, 2020, pp. 344–350. Accessed: Dec. 05, 2024. [Online]. Available: [https://eng.libretexts.org/Bookshelves/Mechanical_Engineering/Engineering_Statics%3A_Open_and_Interactive_\(Baker_and_Haynes\)/10%3A_Moments_of_Inertia/10.04%3A_Moment_of_Inertia_of_Composite_Shapes](https://eng.libretexts.org/Bookshelves/Mechanical_Engineering/Engineering_Statics%3A_Open_and_Interactive_(Baker_and_Haynes)/10%3A_Moments_of_Inertia/10.04%3A_Moment_of_Inertia_of_Composite_Shapes)
9. M. Ortner and L. G. Coliado Bandeira, “Magpylib: A free python package for Magnetic Field Computation,” ScienceDirect, <https://www.sciencedirect.com/science/article/pii/S2352711020300170> (accessed Feb. 6, 2025).
10. R. Dreyfus *et al.*, “Dexterous helical magnetic robot for improved endovascular access,” *Science robotics*, vol. 9, no. 87, Feb. 2024, doi: <https://doi.org/10.1126/scirobotics.adh0298>.
11. P. Ducheyne, *Comprehensive biomaterials / 6, Biomaterials and clinical use*. Amsterdam: Elsevier, 2011.
12. C.-H. Park, L. D. Tijing, H. K. Shon, and C. S. Kim, “SILICONE-COATING OF NITINOL STENT WIRES BY ELECTROSPINNING: CATHETER DEPLOYMENT TEST,” Jan. 2014.
13. Zaneta Koszowska *et al.*, “Independently Actuated Soft Magnetic Manipulators for Bimanual Operations in Confined Anatomical Cavities,” *Advanced Intelligent Systems*, vol. 6, no. 2, Feb. 2024, doi: <https://doi.org/10.1002/aisy.202470009>.
14. Z. Yang, H. Yang, Y. Cao, Y. Cui, and Z. Zhang, “Magnetically Actuated Continuum Medical Robots: A Review,” *Advanced intelligent systems*, vol. 5, no. 6, Mar. 2023, doi: <https://doi.org/10.1002/aisy.202200416>.
15. M. N. O. Sadiku, *Elements of electromagnetics*, 7th ed. New York: Oxford University Press, 2018.

16. David Jeffrey Griffiths and Cambridge University Press, *Introduction to Electrodynamics*, 4th ed. Cambridge I Pozostałe: Cambridge University Press, 2018.
17. ISO, "ISO 14971:2019 - Medical Devices – Application of Risk Management to Medical Devices," International Organization for Standardization, Geneva, Switzerland, 2019.
18. IEC, "IEC 60601-1-2:2014 - Medical Electrical Equipment – Part 1-2: General Requirements for Basic Safety and Essential Performance – Collateral Standard: Electromagnetic Compatibility," International Electrotechnical Commission, Geneva, Switzerland, 2014.
19. ASTM F2063 – 12. Standard Specification for Nickel-Titanium Shape Memory Alloy for Medical Devices and Surgical Implants. ASTM International, West Conshohocken, PA, 2012. <https://doi.org/10.1520/F2063-12>
20. "Da Vinci Safety," Yakima Urology Associates PLLC, <https://www.yua.com/da-vinci-safety/#:~:text=Finally%20during%20the%20course%20of%20an%20operation%2C,to%20remain%20in%20control%20of%20the%20procedure> (accessed Apr. 1, 2025).
21. ISO, "ISO 17664:2017 - Processing of Health Care Products – Information to Be Provided for the Processing of Medical Devices," International Organization for Standardization, Geneva, Switzerland, 2017.
22. ISO, "ISO 10993-1:2018 - Biological Evaluation of Medical Devices – Part 1: Evaluation and Testing Within a Risk Management Process," International Organization for Standardization, Geneva, Switzerland, 2018.
23. R. M. A. M. A. Razek, "Criminal Responsibility for Errors Committed by Medical Robots: Legal and Ethical Challenges," *Journal of Law and Sustainable Development*, vol. 12, no. 1, pp. e2443–e2443, Jan. 2024, doi: <https://doi.org/10.55908/sdgs.v12i1.2443>.
24. IEC, "CISPR 11:2015 - Industrial, Scientific and Medical Equipment - Radio-Frequency Disturbance Characteristics - Limits and Methods of Measurement," International Electrotechnical Commission, Geneva, Switzerland, 2015.
25. ISO, "ISO 62366-1:2015 - Medical Devices – Part 1: Application of Usability Engineering to Medical Devices," International Organization for Standardization, Geneva, Switzerland, 2015.
26. Health Canada, "Medical Device Licensing and Requirements in Canada," Health Canada, Ottawa, Canada, 2023.
27. U.S. Food and Drug Administration, "FDA Notification 510(k) Requirements," *FDA*, <https://www.fda.gov/medical-devices/premarket-submissions/510k-clearances>.
28. U.S. Food and Drug Administration, "510(k) Clearance for Sensei X Robotic Catheter System (K141822)," *FDA*, Aug. 5, 2014. <https://www.accessdata.fda.gov/scripts/cdrh/cfdocs/cfPMN/pmn.cfm?ID=K141822>.
29. ALICE, "Everything You Need to Know About 3D Printer Extruder Types," *Goldsupplier*, Sep. 24, 2024. <https://blog.goldsupplier.com/3d-printer-extruder-types/> (accessed Dec. 05, 2024).
30. TLV493D-A1B6 3D Magnetic Sensor pdf, TLV493D-A1B6 3D Magnetic Sensor Download, TLV493D-A1B6 3D Magnetic Sensor Description, TLV493D-A1B6 3D Magnetic Sensor Datasheet, TLV493D-A1B6 3D Magnetic Sensorview :: Digikey::" Accessed: Dec. 01, 2024. [Online]. Available:

https://mm.digikey.com/Volume0/opasdata/d220001/medias/docus/956/TLV493D-A1B6_Rev1.1_4-9-19.pdf

Chapter 3

Summary

Ear, nose, and throat (ENT) surgeries often face significant challenges because of the intricate and tight sinus pathways being navigated. Conventional surgical instruments often require invasive procedures, such as bone removal, which can lead to prolonged recovery, higher risks, and increased costs. To address these limitations, this project proposes a magnetically actuated soft-continuum robot designed to improve upon traditional tools.

The robot integrates four key subsystems: a directional magnetic actuation system, a gear-driven linear actuator, and a soft-continuum robot with a magnetized tip which are all controlled using a robot navigation interface. The magnetic actuation system uses three electromagnetic coils to generate a desired magnetic field, enabling real-time orientation adjustments. The linear actuator uses a stepper motor to allow the robot to advance and retract. The soft-continuum robot, made of a flexible silicone body with a nitinol wire core, is designed to minimize trauma while adapting to narrow anatomical pathways. Its magnetized tip, embedded with Neodymium (NdFeB) particles, interacts with the magnetic field to achieve precise navigation using a "Follow the Leader" mechanism. Lastly, the final component is the robot navigation interface, which allows the user to control key system elements—such as the linear actuator and electromagnetic coils—for precise positioning of the magnetized tip. Additionally, fail-safe mechanisms are integrated to enhance patient safety and prevent unintentional actions.

To verify its design requirements and functionality, the robot will undergo various tests to evaluate technical and nontechnical requirements. The proposed system is designed to seamlessly integrate into existing surgical workflows, offering enhanced control, reduced operative times, and improved patient outcomes. These clinical advantages translate into broader economic and societal benefits, such as increased healthcare efficiency, more sustainable resource use, and advancements in personalized, patient-centered surgical methodologies. By optimizing both surgical performance and systemic healthcare outcomes, this solution has the potential to revolutionize ENT surgery, setting new standards for patient care.

Brief Project Description

A magnetically actuated continuum soft robot designed for ENT surgeries. The design integrates electromagnetic coils for directional control, a linear actuation system for extension and retraction, and a soft continuum robot with a magnetized tip, which are all controlled using a user interface, enabling intuitive, precise, and dexterous surgical control.

Need Statement

Design a magnetically actuated continuum robot for use in ENT surgery, enhancing dexterity in navigating complex and confined anatomical spaces while remaining minimally invasive, aiming to reduce operation time and minimize surgical complications.

3.1 Design Prototype Plan

The design prototype plan outlines the implementation and construction of the magnetically actuated continuum soft robot, expanding on the proof-of-concept from Chapter 2. It details how key subsystems, including the coil-based magnetic actuation system, soft-continuum robot, and linear actuation system, will be developed and integrated with an intuitive user interface for robot navigation. Risk mitigation strategies identified in Chapter 2 have been embedded into the design inputs to address potential hazards and ensure compliance with relevant standards. Assumptions, limitations, and constraints influencing the final prototype are also discussed to guide future design optimizations and performance verification.

3.1.1 Magnetic Actuation System

3.1.1.1 Implementation

The magnetic actuation system will be implemented through the use of three magnetic coils connected to an Arduino microcontroller, which will independently apply voltage as needed. Surface mount logic-level MOSFETs are used to isolate each coil from the power supply until the microcontroller signal is sent to drive the power into the coil; this also allows for each coil to have independent and variable current (i.e. turning one coil on does not turn on all three). This further isolates the channel that controls the logic of the coils from the power supply to the coils, protecting the Arduino from potentially being damaged by the high levels of current and voltage provided by the power supply. The implementation of the magnetic actuation system is divided into three distinct components: the coil design, the circuit design, and the microcontroller design, as illustrated in the high-level system overview in Figure 21.

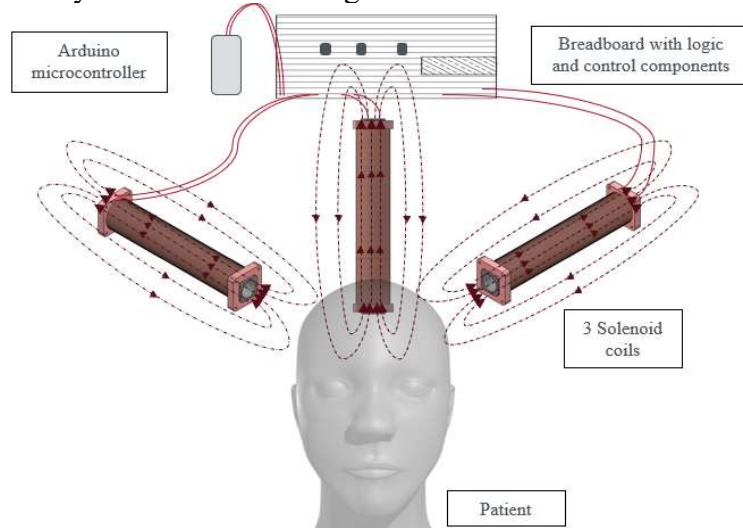


Figure 21. A proof-of-concept mock-up (not to scale) showcasing the magnetic actuation system. There are three coils (middle three components) connected to a breadboard with surface mount components (top right), which are driven by a microcontroller (top left).

3.1.1.2 Coil Design: Initial Prototype

As documented in previous chapter reports, the earlier stages of the design used only two coils to test the overall design feasibility. These two coils were purchased pre-assembled from a third-party seller, with predetermined specifications that were within an initial range of interest.

Specifically, initial continuum robot prototyping showed responsiveness to 2mT of magnetic field. Thus, given a set specification of generating 2mT of magnetic field, it was possible to isolate the current needed by the coils.

$$B_{\text{solenoid}} = \frac{\mu_0 \cdot I_{\text{solenoid}} \cdot N_{\text{turns}}}{l_{\text{solenoid}}} \quad (24)$$

Where B_{solenoid} is the field generated by the coil in Tesla, μ_0 is the permeability constant (always equal to $4\pi \cdot 10^{-7}$ and is unitless), I is the current in Amps, N is the number of turns on the coil, and l is the length of the coil in meters [1, 2]. Thus, given the predefined parameter specifications of the coils being set such that $N = 200$ turns and $l = 0.0527$ m, and the goal of 2 mT being set, the required current can be calculated.

$$0.002 \text{ T} = \frac{4\pi \cdot 10^{-7} \cdot I \cdot 200}{0.0527}$$

$$I = 0.419 \text{ Amps}$$

To decide on how much voltage needs to be supplied to the current, Ohm's Law is used [1, 2]. First, the resistance of the coils was measured using an Extech EX470A multimeter, since the data sheet of the purchased coils did not note the resistance of the coils. Both coils had the same resistance measured at about 20Ω . Therefore:

$$V = I \cdot R \quad (25)$$

$$V = 0.419 \cdot 20$$

$$V = 8.38$$

Given that the calculated voltage is 8.38 V, a 9 V power source can be used.

However, upon implementing this proof-of-concept design, it was seen that the 2mT magnetic field generated from the coils was not enough to move the robot from a far enough distance away to practically aid in surgical procedures. Given that the coil will need to be able to move the robot from at least 16 cm away to be useful in a surgical setting [3], the generated field from the magnetic coil actuation system will need to drastically increase. For the next stage of prototyping, it was assumed 10mT will need to be generated in order to control the robot from a meaningful distance away. This assumption was decided upon via the Python simulations run, which are elaborated upon later in this report. The final limitation with the old prototype was the use of only two coils. For the magnetic actuation system to provide three degrees of freedom in movement to the robot, three coils will be needed. Given these limitations and errors in the initial prototype design, a new prototype was created to overcome these shortcomings.

3.1.1.3 Coil Design: Next Prototype Iteration

The next coil prototype is fabricated entirely from scratch to meet the specific requirements set out, while remaining in budget. The first step is calculating the parameters that will achieve a 10mT output. Given that the coil is being created from scratch, some parameters needed to be assumed in order to begin optimizing for 10mT. As such, the following assumptions were made: the length of the solenoid, $l_{\text{solenoid}} = 0.25$ m, the radius of the solenoid $r_{\text{solenoid}} = 0.05$ m, the number of turns $N_{\text{turns}} = 250$, and the current applied to the solenoid $I = 10$ A. The final assumption to note is that 14-Gauge copper wire will be used. These assumptions are based in part on successful solenoids previously fabricated in the HeART Lab, where similar standards have been effectively applied [4], serving as a foundation for optimizing the prototyping calculations.

Therefore, once again, the calculation for the field of a solenoid is:

$$B_{solenoid} = \frac{\mu_0 \cdot I_{solenoid} \cdot N_{turns}}{l_{solenoid}} \quad (24)$$

$$B_{solenoid} = \frac{4\pi \cdot 10^{-7} \cdot 10 \cdot 250}{0.25}$$

$$B_{solenoid} = 0.01257 T = 12.57 mT$$

Therefore, with the 10mT specification being successfully met, the rest of the design parameters required to build this coil can be calculated.

The length of copper wire, in meters, required for one solenoid is:

$$l_{wire} = 2 * \pi * r_{solenoid} * N_{turns} \quad (22)$$

$$l_{wire} = 2 * \pi * 0.05 * 250$$

$$l_{wire} = 78.5398 m$$

It is important to note that it is assumed that the radius of the coil stays the same throughout the entire coil since additional layers will introduce negligible differences; this calculation is only being used to gauge how much wire will need to be purchased and sourced to build it.

To calculate the required voltage to power each coil, the resistance of the wire is needed first. It is important to note that the cross-sectional area of a 14-Gauge copper wire $A_{wire} = 2.08 * 10^{-6} m^2$, and the resistivity of copper $\rho_{copper} = 1.68 * 10^{-8} \Omega$ [4, 5].

$$R_{wire} = \frac{\rho_{copper} * l_{wire}}{A_{wire}} \quad (23)$$

$$R_{wire} = \frac{1.68 * 10^{-8} * 78.5398}{2.08 * 10^{-6}}$$

$$R_{wire} = 0.6244 \Omega$$

Therefore, using Ohm's Law, the required voltage, in Volts, is calculated:

$$V = I * R_{wire} \quad (21)$$

$$V = 10 * 0.6244 = 6.344 V$$

Given the design parameters calculated above, the physical prototyping process started with designing a base for the coil. Using a laser cutter, a piece of medium-density fiberboard (MDF) wood was cut to create a holder that meets the exact specifications of the coil. A laser cutter requires instructions in the form of an Autodesk Inventor Engineering Drawing. Figure 22 shows the engineering drawing design that was made for the laser printer; once it was cut and assembled, Figure 23 shows the final base of the solenoid.

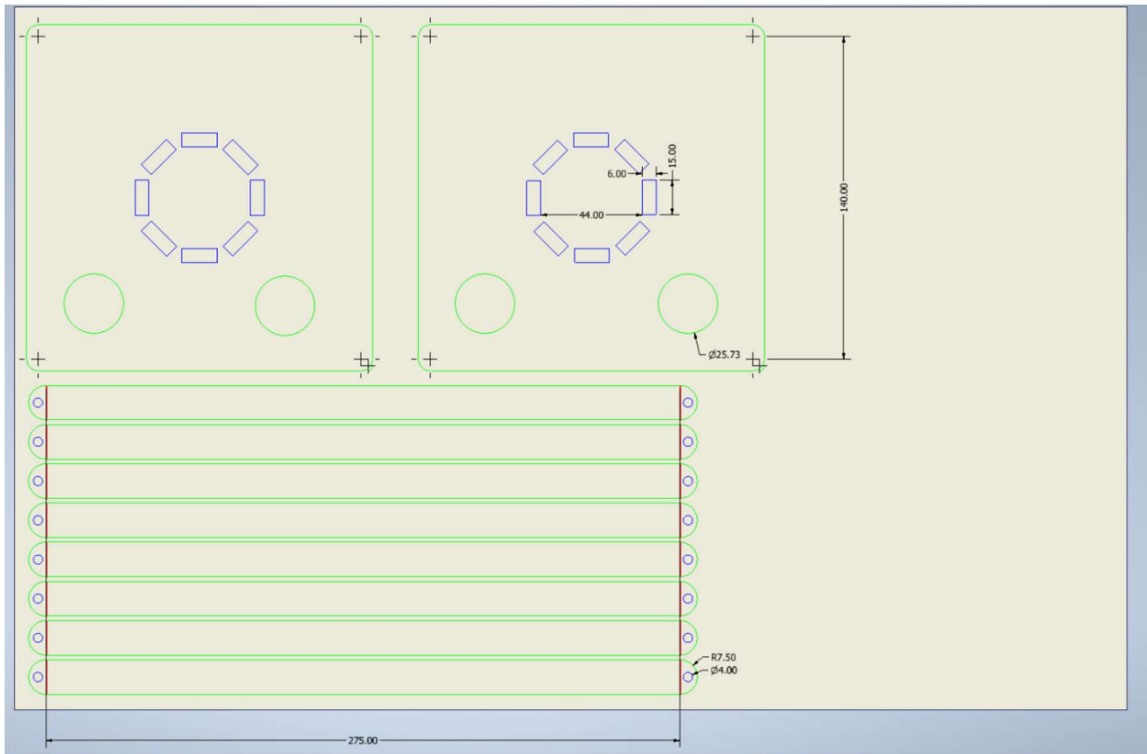


Figure 22. The Engineering Drawing for the base of one coil made in Autodesk Inventor 2024. The dimensioned drawing, with units in mm, above acts as the instructions to the laser printer on how to properly cut out the design: red lines are engraved superficially into the wood, blue lines are internal cuts that should be made first, and then green lines indicate external lines that should be cut at the end. The MDF wood piece cut into was 304.800 mm by 484.00 mm, and the blank piece with the sketches drawn on it reflects those exact dimensions.

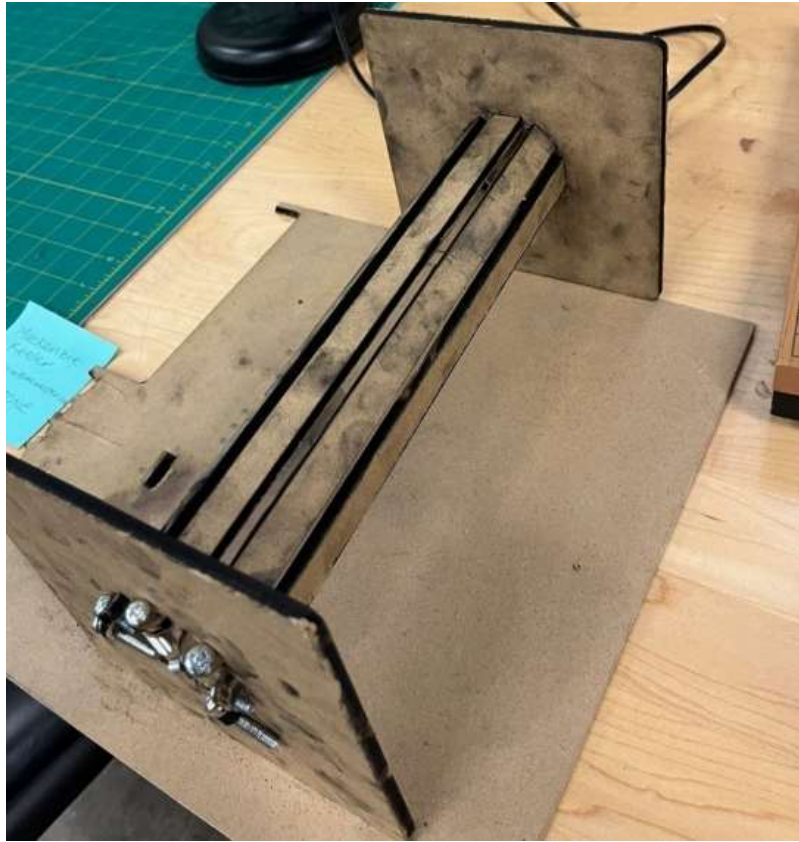


Figure 23. The fully assembled solenoid coil base, constructed from laser-printed MDF wood. The structure consists of two end plates secured to the base and frame using 7/16" x 1-1/2" bolts, 7/16" nuts, and washers. Three parallel slots provide designated spaces for wire winding, though no wires have been wrapped around it yet.

With the coil base built, the next stage of prototyping involves manually winding the wire around the base to create the coil calculated above. Figure 24 shows the initial stages of this process. A key limitation of fabricating custom coils manually is the introduction of human error, which can affect the coil's performance. Specifically, uneven winding, inconsistent tightness, and variability in wire tension can lead to differences in coil density, affecting the overall inductance and magnetic field strength. Additionally, misalignment of coil layers and variations in the spacing between turns can result in deviations from the intended coil geometry, potentially impacting whether the 10mT specification is met. While pre-manufactured coils would offer greater precision, the need for specific design parameters makes manual fabrication necessary. As a result, some trial and error will be required to verify that the calculated field strength is achieved despite these potential discrepancies.

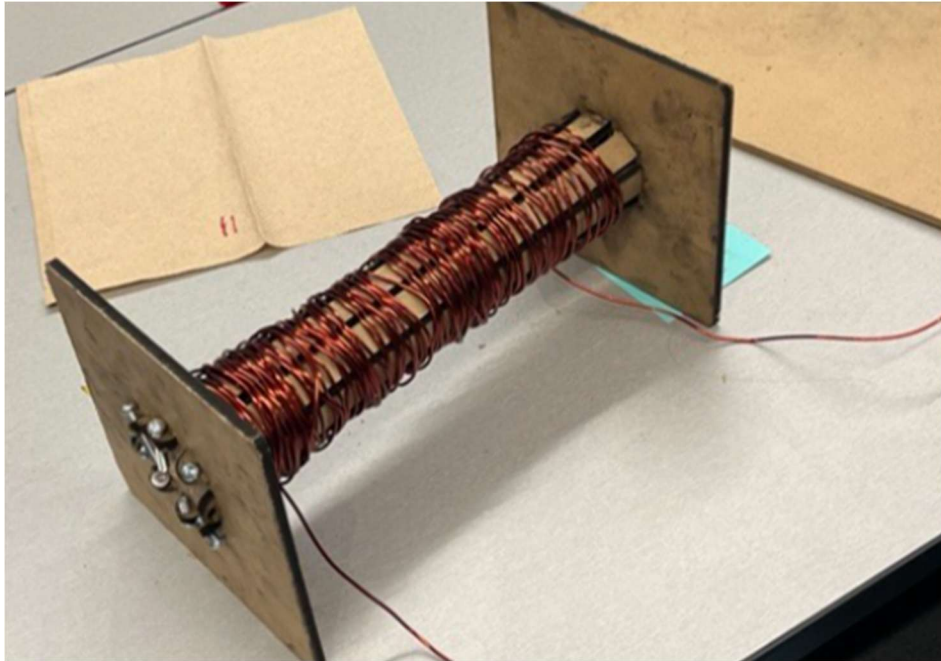


Figure 24. The fully assembled solenoid coil base is constructed from laser-printed MDF wood, with 105 turns of 14-Gauge copper wire ($N_{\text{turns}} = 105$), showcasing a partially completed coil prototype.

The biggest risk introduced by the coil portion of the magnetic actuation system is the excessive heat introduced by powering the coils. The risk of excessive thermal energy dissipating from the electromagnetic coils can potentially cause burns to surrounding tissues and degrade biocompatible materials; these parameters were calculated to not generate over 100°C, following the calculations done in Appendix A: Design Output Calculations, subsection Calculation 1. With respect to the prototyping process, the biggest mitigation technique implemented will be strict time limits when powering the device. There is no need for the coils to be on for more than seconds. By not powering it for prolonged periods, the risk of excessive heat is meaningfully mitigated during the prototyping process.

3.1.1.4 Circuit Design for the Coils

To drive the power supply into the coils, a circuit was created with the goal of independently controlling three coils. The circuit, simulated through LTSpice XVII as seen in Figure 25 utilizes a power supply connected to the coils through independent logic-level MOSFETs, with connections to the drain and supply terminals. The gate terminal of the MOSFET is controlled by a microcontroller, which applies either a positive voltage or no voltage to the gate. When voltage is applied, it causes the MOSFET to saturate, allowing current to flow from the power supply, through the coil, and to ground. When the microcontroller stops applying voltage, the power supply and coil become an open circuit thus stopping the coil from producing a magnetic field. The microcontroller is outputting the ON/OFF signal from different GPIO pins; thus, the circuitry is made such that the coils can be controlled independently. Specifically, the circuit has also been set up such that the coils can be turned on and off through the push of a button; this was a design decision introduced to simplify the testing process. An LED light has also been assigned to each coil to visually indicate when the coil is on or off.

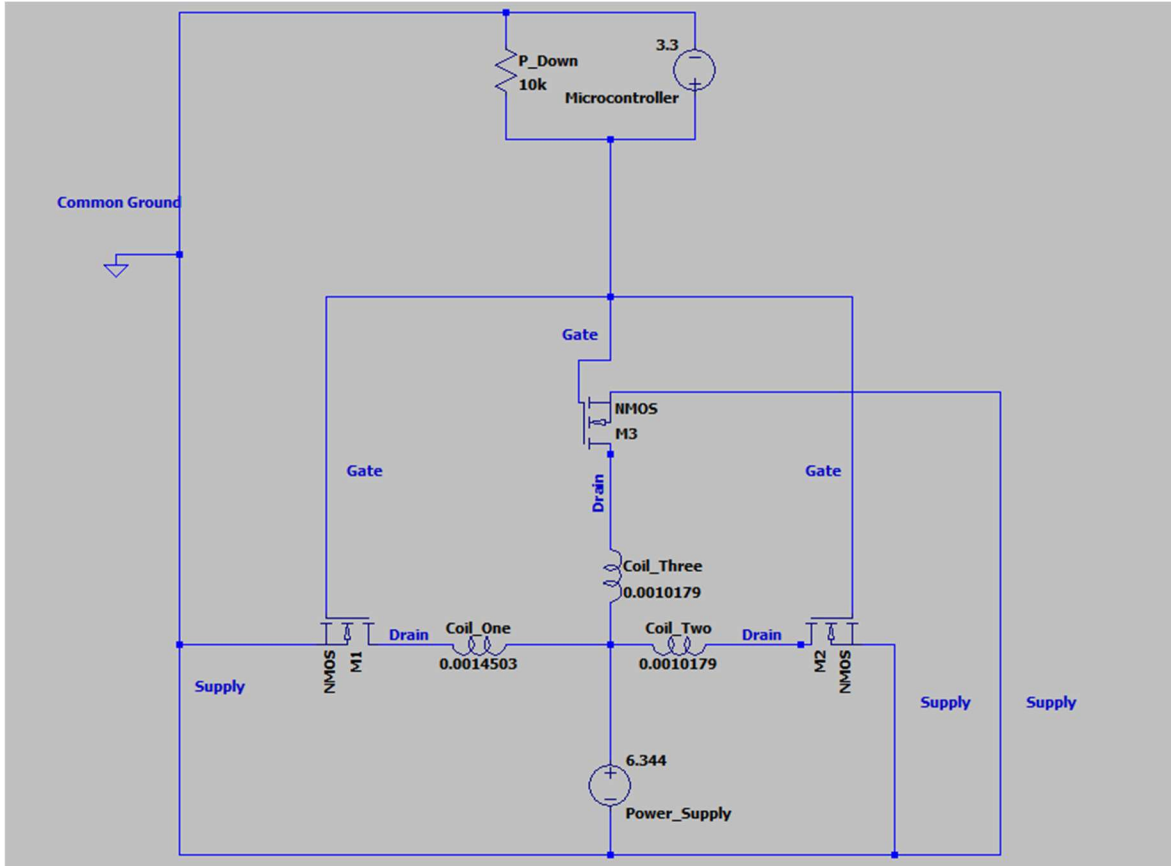


Figure 25. Labelled LTSpice XVII simulation of the coil circuitry used in the prototype, where three coils are supplied with voltage from a power supply, and a microcontroller controls their ON and OFF states through MOSFET circuit logic.

The use of surface mount components to drive the coils is not ideal as it introduces the potential for weak or easily disturbed connections. A custom-printed circuit board (PCB) would be more ideal; however, the focus of this project has been more on the fabrication and calculation of the magnetic fields and creation of the coils. As a result, time has been a limiting factor, constraining the creation of any PCBs. Given the success of the circuit board with surface mount components, there is no immediate need to iterate upon the circuit and create a PCB, however, with more time, in the future, this is an aspect that could be added. As of right now, the circuit is sufficient in meeting the specifications of the project. Given that the circuit functions as intended, moving forward, the circuit should not see any changes. Regardless of whether specific coil parameters change (e.g. increasing the voltage applied or number of loops in the coil) the circuit configuration will not change. In the most extreme case, should the voltage required to power the coil increase beyond the rated limit of voltage specified by the MOSFETs, the circuit will still stay the same, and higher rated voltage MOSFETs will replace the insufficient ones.

Since the Arduino microcontroller is not rated to handle more than 5V, the 6.344V required from the power supply exceeds its safe operating limit. To address this, the circuit design isolates the power supply from the microcontroller using MOSFET-based logic. This approach fully mitigates the risk by allowing the microcontroller to control the circuit without being directly exposed to high voltage. The MOSFETs, rated for up to 15V, provide a safe interface, enabling higher voltages to be applied to the coils without risk of damaging the microcontroller.

3.1.1.5 Microcontroller for the Coils

The coils are controlled through a PICO ESP microcontroller, previously detailed in earlier chapters, which runs Arduino code to manage button inputs. When a button is pressed, the microcontroller outputs a signal that saturates the corresponding MOSFET, allowing 6.344 V from the power supply to flow to the coil and generate a magnetic field. Each of the three buttons independently controls one coil, and the code is designed to allow any combination of button presses to function without interference. Additionally, an extra pin is programmed to power an LED indicator for each coil, turning on when its respective coil is active. This enables clear feedback and ensures the circuit logic remains fully governed by the microcontroller. The full code can be found in Appendix B: Software Implementation, subsection Code 1: Coil Control.

In the newest iteration of the Arduino code, a new feature has been introduced such that after five seconds of turning a coil on, the Arduino will automatically stop providing power to the coil, if not otherwise already specified by pushing the button. This was implemented to mitigate the risk of coil overheating, as prolonged activation can lead to excessive heat buildup that poses safety and performance concerns. Based on experimental observations and system requirements, five seconds is sufficient to generate the desired magnetic field strength for orientation or actuation tasks, without compromising the field's effectiveness. This timeout interval ensures that the magnetic field is applied long enough to be functionally useful while preventing unnecessary thermal strain. By automating this shutoff, the system reduces reliance on human oversight and proactively addresses overheating risks, as identified in the risk assessment.

3.1.1.6 Coil Simulation Software

An integral aspect of the design prototype plan focuses on simulating the core functionalities of the magnetic actuation system, specifically the coil subsystem. In Chapter 2, the focus was on using theoretical knowledge to develop a proof-of-concept and present the feasibility of manipulating magnetic fields to navigate the robot through ear, nose, and throat pathways. To further understand the expected behavior of the robot, the prototype plan for this phase included the usage of the MagPy (v5.0.1), NumPy (v1.26.4), and PyVista (v0.44.1) libraries in Python (v3.10.0) to provide detailed analyses of the magnetic field, with each tool serving complementary roles. All of the aforementioned libraries and software were last updated in November 2024.

In Chapter 2, through exploring the magnetic forces required to control the robot, some key parameters such as required field strength, alignment of the magnetic sources, as well as the potential challenges of operating in complex geometries were explored. The theoretical background analyzed previously will be applied in the software development presented in Chapter 3.

Python serves as an ideal platform to set up the initial models as well as explore various configurations of the magnetization sources with the MagPy library offering the required tools to model magnetic field interactions. The MagPy library is an open-source Python package used for efficient computation of static magnetic fields from various magnetic sources like bar magnets, coils, etc. [7]. The built-in vectorized analytical calculations allow for flexible parameter adjustments such as orientation, field strength, and geometry of the coils as well as high-quality visualizations of the proposed prototype model with the use of NumPy. Also, PyVista will be utilized for 3D visualization of the physical setup. Although Python and MagPy were not explicitly

mentioned in the previous chapter, the introduction of these tools in this chapter further builds on the project's need to apply an adaptive and efficient model to analyze the field interactions through various configurations.

The efficacy of the MagPy library to simulate magnetic fields has been demonstrated in studies where the results of the library were consistent with other tools such as MATLAB and COMSOL Multiphysics. For example, studies compared MagPy's simulation results with COMSOL element analyses and MATLAB's numerical output for field strength across complex environments. The studies demonstrated that the MagPy library can achieve comparable accuracy which validates the suitability of the chosen tools in evaluating magnetic field interactions [6,7].

The software used to analyze the electromagnetic field produced by the coils was developed using a combination of theoretical modeling and experimental validation. To run the simulation, firstly the coil parameters are defined such as length, current, radius, and number of turns. Using both the MagPy and NumPy library, the software builds the visualization of the coil using a collection of circular loops, where each carries the predefined current input arranged on different planes as seen Figure 26. To support the 3D visualization, a different Python library called PyVista is implemented to provide an interactive representation. When evaluating the coil's magnetic field, the code generates a 3D grid of points and computes the field vector at each location to obtain the resultant magnetic field at any given point. A critical component of the simulation is the magnetic field sensor available in the library, which when compared to the hand-done calculation for $B_{solenoid}$ above, can validate the correctness of the resulting specifications. The sensor is able to retrieve the corresponding magnetic field components along the X, Y, and Z directions which can be accumulated to present the total magnetic field. The resultant magnetic field from the X, Y, and Z plane at a specific point is computed using this following equation:

$$|B_{total}| = \sqrt{B_x^2 + B_y^2 + B_z^2} \quad (27)$$

Notably, the visualization included arrows to help represent the field vectors that display both the strength and direction of the magnetic field across the grid. Overall, the simulation presents an established electromagnetic coil analysis that can visualize the magnetic field interactions, validate theoretical predictions and provide feedback for further design refinement. It can be found in Appendix B: Software Implementation, subsection Code 3.

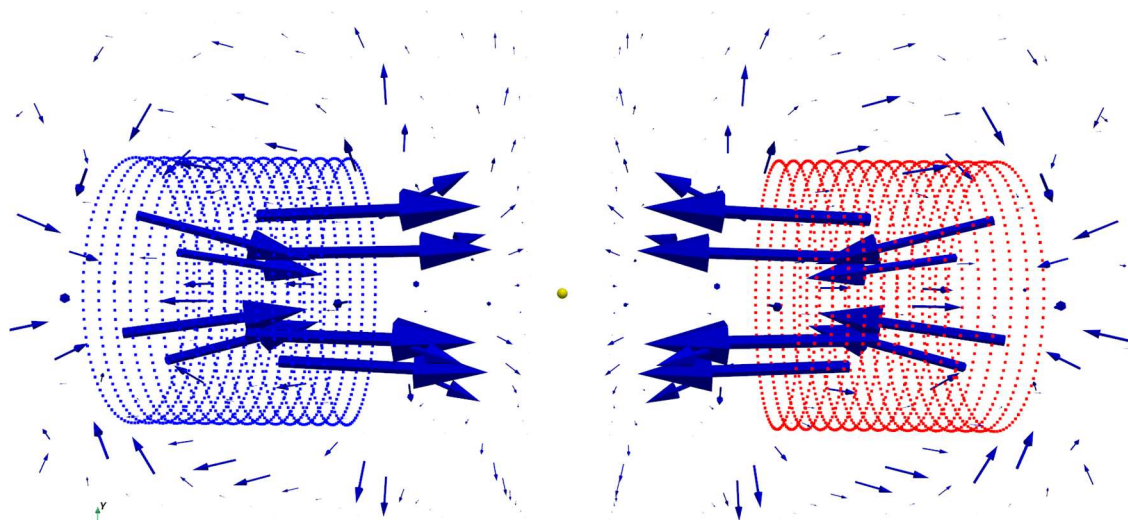


Figure 26. Screen capture of Python visualization using MagPy and PyVista library. Two coils with same parameters pointed towards magnetic field sensor depicted by yellow sphere on the z-plane.

The results obtained from the Python simulations can be compared against experimental outputs to ensure robust analysis of the magnetic field interactions for the precision requirements of the robot using the workflow presented in Figure 27. This ensures that the Python implementation aligns with the theoretical and physical expectations by addressing any discrepancies between the two for reliability in the results.

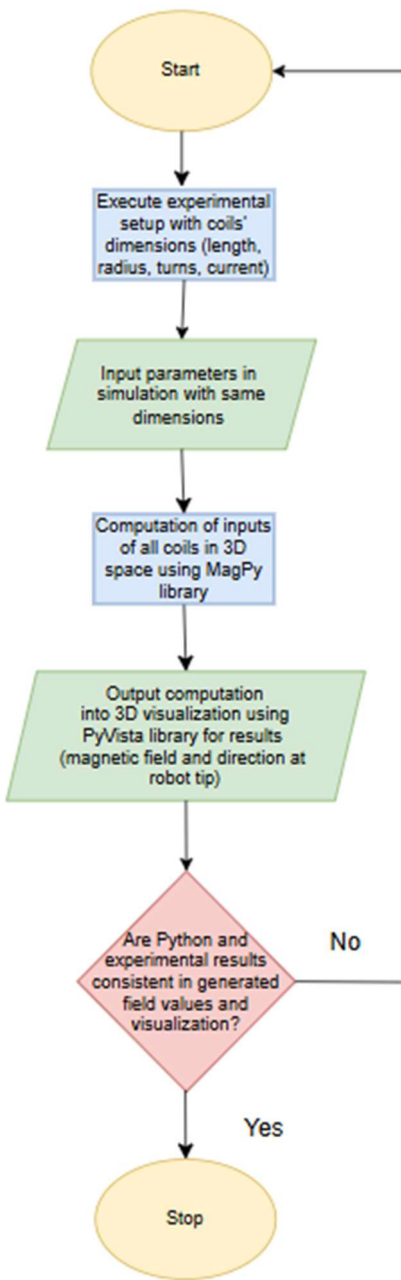


Figure 27. Flowchart of executable steps in verification plan for software simulation.

The final design is expected to execute different system configurations with varying input voltages to result in varying magnetic field outputs, therefore, it is critical to model and analyze the affected magnetic field interactions validate the Python model framework. By continuously refining the Python simulations and validating them with the experimental results of the physical prototype, it allows for consistent improvement of the model's accuracy and reliability.

A primary assumption of the simulation design is that the magnetic field models developed in Python accurately represent real-world interactions under ideal conditions, meaning the

idealized mathematics in the MagPy library aligns with the practical magnetic field behavior generated by the given sources. Additionally, it is presumed that external factors, such as material imperfections, have a negligible impact on simulation results.

Although the assumptions are a good starting point, the limitations of both tools must be acknowledged. A limitation to consider with the Python simulations is that it may not be possible to capture the full environment due to the simplified built-in analysis in the MagPy library. As previously stated, the library is designed to capture static magnetic field calculations, which potentially lack the complexity of the dynamic interactions of the generated magnetic field. For now, the project scope remains within the static field which is consistent with the requirements of the robot. For example, non-linear material behaviors may not be accurately captured, which restricts the scope of the Python simulation to simpler situations. Deviations from the real-world model can lead to major discrepancies with the simulation, resulting safety concerns of the prototype.

In terms of constraints, there are a few that impact the simulation process. One constraint is the availability of computation resources such as memory and power. Both of the MagPy and PyVista libraries in Python require significant computational capacities, especially when running both concurrently. Limited hardware can impact the simulation resolution, so it is important to consider what level of detail is expected from the simulation within a reasonable timeframe.

To address the identified limitations and robustness of the design, there are several risk mitigation strategies implemented into design requirements and considered additionally. For the Python simulation, the MagPy library's simplified analysis is minimized through the execution of parameter sweeps and sensitivity assessments to capture a broader range of situations. This assures that regardless of the static constraints of the magnetic field computations with the MagPy library, the framework is adaptable to various configurations. For instance, a parameter sweep in Python can be performed by varying the applied current from 0.1A to 1.0A to analyze the magnetic field distribution. This simulation can help with identifying optimal experimental model configurations while ensuring the framework is applicable under different operational conditions.

Computational efficiency is prioritized by optimizing the Python simulations with modular design along with applying stress tests to handle potential errors when using extreme parameter ranges. Furthermore, validation checkpoints are integrated into testing to compare the simulation results against theoretical calculations and experimental data to ensure that discrepancies are addressed early in the development process. Also, rigorous testing will be applied to ensure there are approximate results between the theoretical and experimental along with the simulation.

To ensure adherence to regulatory standards and guidelines, the project aligns with the outlined compliance strategies. The Python scripts adhere to IEEE 29119 software testing standards, which involve the implementation of unit tests to validate the modules against theoretical calculations. Additionally, by using GIT as the version control system, there is traceability in the development of the simulations. These validated results will guide upcoming project decisions such as coil designs and geometric configurations to optimize field strength and overall improve the system's performance. As all design iterations and results are documented in the Design History File, this complies with FDA guidelines for reproducibility. The accumulated

strategies enhance the accuracy and compliance of the prototype to mitigate potential risks to ensure the project meets the objectives.

3.1.1.7 Magnetic Actuation System Design Takeaways for Final Prototype

Although the earlier prototype designs were not directly used in the final iteration, they provided valuable insights into the prototyping process. For the coil component, the prototyping process confirmed that the laser cutter could produce a functional base, and the winding method was both validated and ultimately adopted in the final magnetic actuation system iteration. While the core calculations remained consistent throughout prototyping, the voltage was increased, and the verification specifications were refined to better align with user needs for the final iteration. The circuit design and microcontroller logic were also successfully validated, establishing a framework to support future power supply adjustments. Additionally, simulations and calculations from earlier stages directly informed the optimization of the final prototype. Extensive detail of this final implementation is presented in Chapter 4 of this report.

3.1.2 Soft Continuum Robot

3.1.2.1 Implementation

The final design aspect of the soft continuum robot body is intended to provide the flexibility and adaptability necessary for navigating the complex pathways of the nasal cavity during minimally invasive ENT surgeries. The robot's body integrates a nitinol wire core encased in a biocompatible silicone-based exterior, allowing it to achieve the desired flexibility while maintaining structural integrity. These material choices are in compliance with ISO 10993-1 standards for medical materials [8]. The outer surface of the robot features a helical protrusion, which promotes rotational motion when external force is met during the linear movement produced by the linear actuation system. This design balances mechanical flexibility, biocompatibility, and precise motion control, essential for minimizing trauma during surgical navigation.

3.1.2.2 Robot Tip and Body: Multistep Prototyping

The multi-step process illustrated in 28 below enables the development of a soft continuum robot that closely meets the desired design specifications and performance criteria. The fabrication process begins. The fabrication of the robot began with 3D printing a mould to form the magnetized tip. Once the tip was created and fully magnetized, it was reinserted into different mould to shape the rest of the body, including the helical structure needed for motion control. Demoulding after the body is formed leaves a soft continuous robot capable of linear and magnetic actuation.

Once step one – the mould for the robot tip – was complete, EcoFlex 00-30 Silicone Resin was mixed with rare earth magnetic particles in a 1:1.5 ratio of silicone to magnetic particles (NdFeB Powder). Once well-combined, this silicone and magnetic particle mixture was slowly poured into the mould, encasing the carefully aligned nitinol wire core that serves as the robot's backbone and central axis guide. This nitinol core was chosen for its superior elasticity and its ability to withstand the forces required for bending and navigating 360° without permanent deformation. Additionally, research studies have validated the mechanical stability of nitinol in similar robotic applications, confirming its durability under repeated bending and torsional forces

[9]. As seen in 28 step 4, after the silicone was fully set, the newly formed magnetic tip was demoulded.

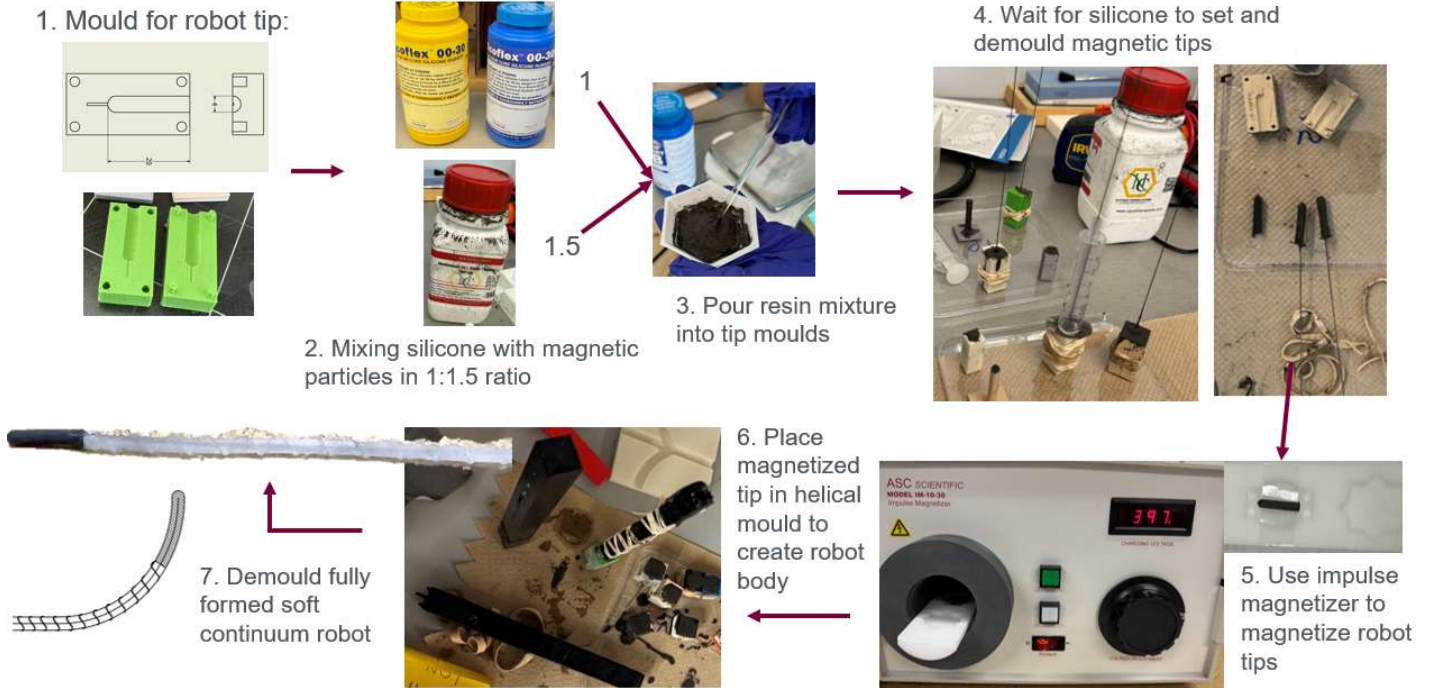


Figure 28. Infographic depicting the primary fabrication process for the soft continuum robot. This multi-step process covers the production and assembly of the robot's magnetized tip and body with uniform helical protrusions.

The magnetization of the robot tip is critical for its ability to interact with the coil-based magnetic actuation system and achieve precise directional control. The specific magnetization mechanism used in the fabrication process for the final iteration involves placing the robot tip in the magnetization chamber, i.e., the magnetizing coil, of an ASC Scientific Impulse Magnetizer Model IM-10-30. This device generates a brief but powerful magnetic pulse that aligns the magnetic domains within the embedded particles, permanently magnetizing the material [10]. The magnitude and direction of magnetization can be controlled by adjusting the pulse strength and orientation of the tip during the process. In earlier iterations, magnetization was achieved by placing the magnetic tip between two closely positioned 1-inch magnets with opposing poles. While this method produced a magnetized tip, it lacked precision and consistency in both field strength and orientation. In contrast, the impulse magnetizer offers a far more controlled and repeatable process, ensuring uniform magnetization aligned precisely with the design requirements—significantly improving the performance and reliability of the final prototype. This comparison is seen especially clearly in the data collected in Chapter 4 regarding the verification plans. Thus, using the impulse magnetizer allows the magnetized tip to interact most effectively with the electromagnetic field generated by the magnetic actuation system, with the fully saturated magnetic tip aiding to provide precise directional control.

After the robot tip has been magnetized, it is carefully placed back into a second mould to form the flexible silicone-based body with its outer helical protrusions. The mould, as shown in Figure 29, is designed with precise dimensions to securely hold the magnetized tip at one end while allowing for the proper alignment of the helical pattern along the body's length. Once the tip is positioned, a silicone mixture without any magnetic particles within it is poured into the mould.

This begins extending the robot beyond the magnetized tip, continuing to embed the nitinol wire core within. As detailed previously, the silicone mixture is selected for its flexibility, smooth surface, and ability to minimize tissue trauma during navigation. As the silicone sets, the helical protrusions are formed along the exterior, providing the ideal mechanical interface for the robot's body to rotate when in forceful contact with any surface. The pitch of the helical protrusions is 10mm, ideal for the rotational motion incorporated within the forward actuation system [11]. Once fully cured, the soft continuum robot is fully formed with a strong bond between the magnetized tip and the flexible body, optimizing both structural integrity and functionality.

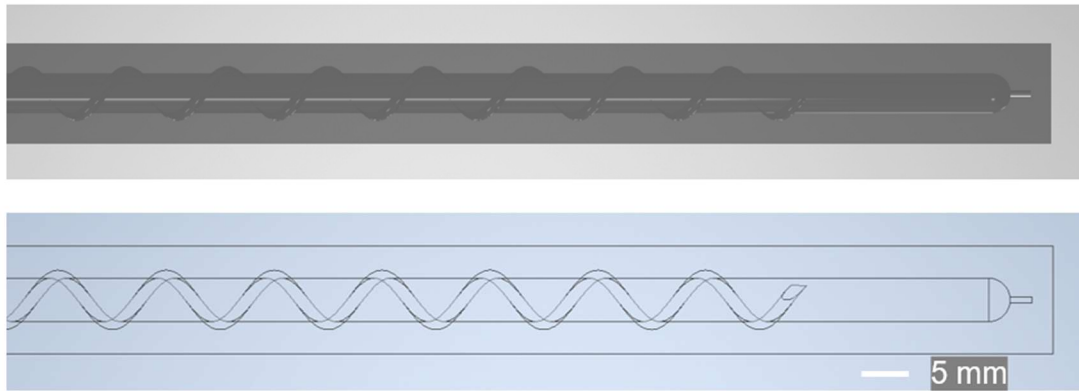


Figure 29. 3D model and sketch of secondary mould with helical protrusions to form the robot's silicone body, made in Autodesk Inventor 2024.

This fabrication process, including the selection of biocompatible materials, complies with ISO 10993-1 standards. Complying with this standard ensures that the robot is both safe for clinical use and mechanically robust, making it suitable for the challenges of ENT surgeries [8]. However, several constraints remain, with one of the most significant being the robot's size. The robot body has a diameter of 4 mm which is suitable for the scope of this project, but reducing the size further could improve navigation through confined anatomical pathways. Achieving this miniaturization depends on overcoming several key challenges and working within the constraints of available materials and fabrication facilities. First, access to stronger magnetic particles is necessary to ensure adequate actuation at smaller scales; however, such materials are currently unavailable in the lab. This constraint is also related to the composition of the silicone body, which cannot exceed a 1:1.5 ratio of silicone to magnetic particles, as higher concentrations would prevent proper curing. Second, the coils must generate a magnetic field strong enough to effectively actuate the robot, a requirement that has been confirmed through verification testing of different sizes of the robot, the results of which can be found in later chapters. Additionally, the design assumes that the helical protrusions and linear actuation system will provide sufficient rotational and translational movement, even as the robot size is reduced. Maintaining structural integrity and flexibility is also crucial, requiring optimization of the nitinol core and the silicone material to ensure the robot can bend effectively without mechanical failure and buckling as it scales down. Importantly, the design also assumes uniform magnetization of the robot tip—a simplification that would need to be reevaluated for more precise modeling and control. These factors collectively represent key considerations in the development of a smaller, more effective final design.

3.1.3 Linear Actuation System

The linear actuation system is essential for providing precise, bidirectional linear and rotational movement of the soft continuum robot, enabling navigation through complex sinus pathways. This system is driven by a stepper motor that engages with the nitinol wire core of the robot's body to achieve smooth and controlled forward movement. The design will incorporate a double fixed gear in counter rotational movement, this will “pinch” the wire to extend and retract the robot. This also allows for precise translation with minimal movement loss due to slippage, heightening the robot's ability to traverse curved and confined anatomical pathways.

3.1.3.1 Implementation

The motor employed in the forward actuation system is a modified stepper motor with high precision and thus the ability to provide discrete movements corresponding to the robot's navigational needs. This level of precision is critical to maintaining safe contact with tissue and reducing strain on the nitinol wire and silicone body. Figure 30 showcases the overall design of the prototype at a high level.

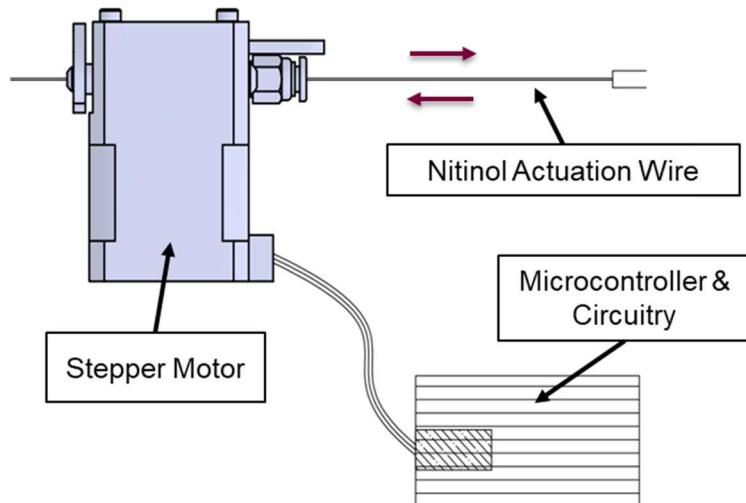


Figure 30. Forward Actuation System design for linear movement of the soft-continuum robot. The stepper motor (top left), controlled by an Arduino microcontroller and related circuitry (bottom right), has a screw mechanism which holds the external portion of the robot's wire core (top right) steady during actuation.

Studies have demonstrated the effectiveness of stepper motors in flexible robotics, highlighting their ability to balance torque and precision in surgical applications [12]. The mechanism of action for the prototype makes use of the friction of two gears to actuate the robot combined with a pitched frictional roller. Another key component of the system is the screw mechanism, which securely clamps and unclamps the robot wire core, ensuring stability during operation and preventing unwanted movement.

To minimize the risk of mechanical failure, the motor torque is optimized to provide sufficient force for actuation while preventing excessive wear on the nitinol wire core—responsible for transmitting force through the forward actuation system—and the silicone body, which interfaces with the patient. The torque levels are selected to remain within the tolerance limits for cyclic

stress and fatigue as detailed in manufacturer datasheets and supported by prior studies involving nitinol actuators in soft robotic applications [9]. Calibration protocols are incorporated to align the helical protrusions with the pitched gear, ensuring accurate engagement and consistent motion. The stepper motor's speed and torque are adjusted dynamically to achieve the desired balance between travel speed and control.

3.1.3.2 Microcontroller for the Motor

The forward actuation system is controlled using an Arduino microcontroller, which regulates the motor's speed, direction, and step intervals. Connected to the Arduino through Bluetooth, a wireless control setup provides flexibility and ease of operation for the surgeon and other operational staff. The system circuit has been designed using a TMC 2209 motor driver, which separates the higher and lower voltage currents, to prevent current surges and electrical failures, as shown in

Figure 31.

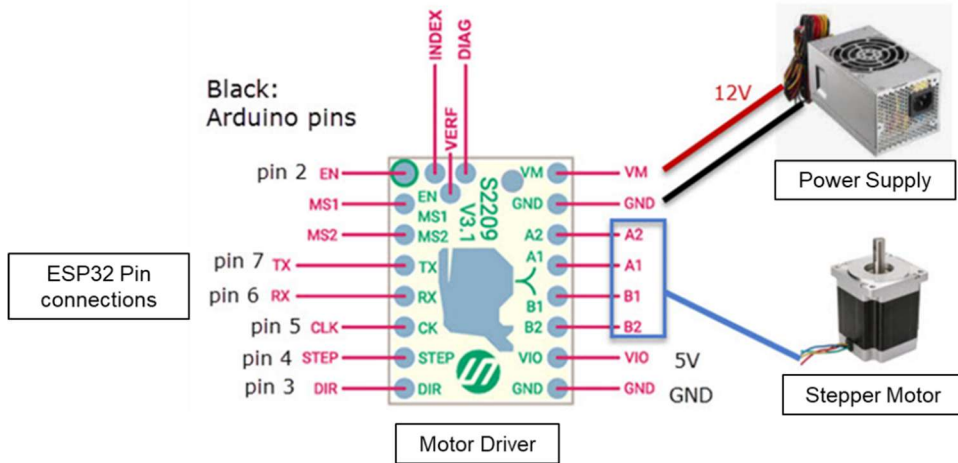


Figure 31. The circuit connecting the stepper motor to the ESP32 microcontroller using a TMC 2209 motor driver. The driver separates the 12V current from the input current from the microcontroller.

To further ensure safety and compliance, the motor's electronic control system follows guidelines set by IEC 60601-1, addressing electrical safety requirements in medical devices [13]. An additional part of the risk mitigation, especially during the prototyping stages, a manual override switch is necessary, allowing the system to be shut off immediately in case of unexpected behavior or emergencies. Additionally, concerns regarding mechanical wear and fatigue of the nitinol wire will be addressed through periodic testing and verification, ensuring that the system can withstand repetitive bending without structural failure.

One assumption made when utilizing the forward actuation system is that the helical protrusions on the robot's body are consistent and well-defined. One of the key constraints in the design is the mechanical performance of the pitched gear system. The gear mechanism must maintain sufficient friction and traction without excessive force that could lead to mechanical

damage or slippage. Further refinements in speed, gear engagement, and structural durability are ongoing to meet the specific requirements of minimally invasive ENT surgeries.

3.1.4 Robot Navigation Interface

3.1.4.1 Implementation

A graphical user interface (GUI) is to be designed to integrate and control the system's components: soft-continuum robot, magnetic actuation and linear actuation system. The interface uses spatial reference and visual feedback for ease of use.

The GUI establishes serial communication with the ESP32 microcontroller, where it will control both the magnetic and linear actuation systems. Python will be used to send commands to the ESP32 using Arduino IDE, using a serial library. The UI should be used for 3D visualization of the coil and actuation system, with options to extend and retract the robot in tandem with individual coil control.

The GUI will be based on the simulations used for coil verification. Various safety features will be implemented such as an emergency stop, and coil shut down after specific commands.

3.1.4.2 Framework

A flowchart was created to visualize the control implementation of the software, shown in Figure 32. The interface should include real-time control over two domains: the linear and magnetic actuation systems. The microcontroller serial communication should be automatically established upon loading of the GUI, and the user should be alerted upon the error. The framework should include clear indications of which systems are turned on, as well as intuitive coil placements to properly indicate coil visualization in a 3D space without confusion.

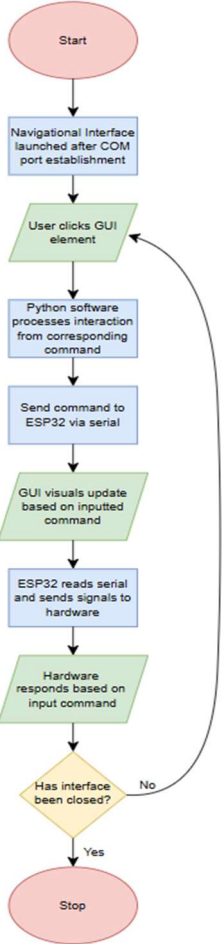


Figure 32. Workflow between the robot navigation interface and the physical hardware with subsequent components outlined.

3.1.4.3 Software Architecture Feature

An emergency stop button shall be implemented as the main safety feature, to prioritize patient safety. Upon opening or closing the interface, a serial command should be sent out to shut off all systems. Additionally, there should be a large button on the screen to immediately shut off all devices upon activation. The status of the linear actuator should also be clearly indicated, indicating whether it is shut off, extending or retracting in real-time.

3.1.5 Implementation of Risk Mitigation and Compliance Strategies

In designing the magnetically actuated soft continuum robot, specific risk mitigation strategies are incorporated into the prototype to address identified hazards related to the coil-based magnetic actuation system, the linear actuation system, and the soft continuum robot itself. The Fault Tree Analysis (FTA) conducted as per ISO 14971:2019 during the design configuration phase – as detailed in Chapter 2 – was extensive and identified numerous potential hazards associated with the magnetically actuated continuum robot [14]. However, due to time constraints and project scope limitations, only the most critical mitigation strategies were prioritized for implementation. The integration of compliance strategies also ensures the design adheres to

appropriate regulatory standards, such as ISO 10993-1 for biocompatibility, IEC 60601-1 for electrical safety, and IEC 60601-1-2 for electromagnetic compatibility, ensuring that the design is safe for clinical applications [8, 13].

While there were significant risk mitigation efforts made during the prototyping process, the key strategies have been systematically embedded into the design and safety requirements as part of the design inputs. This approach ensures that the safety constraints identified through the FTA guide the prototype's development at every stage. The design outputs directly reflect this integration, with safety measures and limits specified to minimize risks. For instance, in the coil-based magnetic actuation system, the design input includes a requirement that the coil temperature must not exceed 100°C to prevent overheating and potential damage to surrounding tissues. By building this requirement into the design and implementing the temperature calculations found in Appendix A: Design Output Calculations, subsection Calculation 1, the system can be implemented such that the coils are never on for longer than seconds at a time, reducing the risk of overheating. Furthermore, the magnetic field strength of the coils is capped at 40mT to ensure safe operation and avoid unintended interactions with surrounding surgical equipment or sensitive tissue.

Both actuation systems are designed with an on/off mechanism for safety. Activating the emergency stop sends a shut-off command to the Arduino, which is programmed to disable both the magnetic and linear actuation systems. This ensures that all actuation ceases immediately, preventing unintended forward or backward movement of the robot. Furthermore, for the linear actuation system, mechanical slippage and force imbalances are mitigated through proper calibration and the alignment of the helical protrusions with the actuation gear, which minimizes stress on the robot's body.

Mitigation strategies specific to the soft-continuum robot body have also been incorporated into the design requirements. To ensure biocompatibility, the robot's body is fabricated using medical-grade silicone and a nitinol wire core, both of which meet biocompatibility standards such as ISO 10993-1 [8]. Medical-grade silicone is specifically formulated to be non-toxic, hypoallergenic, and chemically inert, making it suitable for prolonged contact with human tissue. It also exhibits key mechanical properties such as high flexibility, tear resistance, and thermal stability, which are essential for soft robotic applications [12]. The design also ensures that the nitinol wire remains fully encased within the silicone body, preventing it from protruding and causing tissue damage during operation. The material composition is carefully controlled to maintain flexibility without compromising the mechanical integrity required for successful navigation. Additionally, the 1:1.5 ratio limit on silicone to magnetic particles is maintained during fabrication to ensure that the material fully cures and achieves the desired mechanical properties.

For the final component, the robot navigation interface, the risk mitigation and compliance strategies are implemented with several targeted measures integrated for reliable performance within clinical settings. Firstly, real time software monitoring will continuously assess navigation commands, communication between the interface and the full system, and positional feedback to detect any latency that may compromise control. Many fail-safe mechanisms are implemented and can be activated in cases of data transmission failure and force the system to halt all operations. The interface incorporates intuitive, surgeon-friendly controls that are developed in accordance to ISO 62366-1 standards to reduce user error and cognitive load. The preclinical validation of the interface simulates varying surgical conditions such as emergency use or anatomical constraints to ensure responsiveness and accuracy. To maintain long-term reliability, any firmware updates

will only be conducted during scheduled maintenance periods in coordination with hospital IT system with override modes to prevent any disruptions during procedures.

These mitigation strategies are integral to the prototype's development and are embedded into the design to minimize hazards identified in the FTA. Further details on specific mitigation strategies and their associated verification steps are provided in the next section of this report.

3.2 Design Verification Plans

In the section below, each design output has been given a verification plan. Whether the plan pertains to a technical, non-technical, risk, or compliance strategy is specified for each output.

3.2.1 Verification of Prototype Design Outputs

1. High Level System Outputs

1.1. *Ergonomic Usability and Ease of Control:* Compliance to ISO 62366-1

Point of analysis: The user interface and operational response times are analyzed to ensure ease of use and effective risk mitigation in emergency situations.

Method of analysis: Conduct user testing with simulated surgical tasks, measuring response times and evaluating user comfort.

Verification plan 1: Operators (surgeons and surgical assistants) will perform simulated tasks using the soft-continuum robot and its actuation systems. Response times to activate safety mechanisms and complete tasks will be recorded.

Acceptable outcome: Users can operate the system smoothly with minimal physical strain or cognitive load. Immediate feedback during operation ensures task accuracy and safety mechanisms activate promptly when required.

1.2. *Electrical Safety and Thermal Limits:* Compliance to IEC 60601-1

Point of analysis: The coil-based magnetic actuation system and the gear-driven linear actuator are analyzed to ensure that maximum voltage and temperature limits are not exceeded, as part of risk mitigation and compliance requirements.

Method of analysis and Verification plan 2: Specific verification plans for temperature output and voltage output are detailed in subsections 3.1 and 3.3.

Acceptable outcome: Voltage remains $\leq 15V$ and coil temperatures $\leq 100^{\circ}C$, with safety mechanisms functioning properly under failure conditions.

1.3. *Biocompatibility of Materials:* Compliance to ISO 10993-1

Point of analysis: The biocompatibility of the robotic tip and nitinol wire materials is analyzed as a risk mitigation and compliance requirement for safe human tissue interaction.

Method of analysis and Verification plan 3: No in-house verification is required. The materials used—EcoFlex 00-30 silicone and medical-grade nitinol—are supported by manufacturer data and existing literature confirming biocompatibility under ISO 10993-1. Justifications and references for each material are provided in subsections 2.5 and 2.6.

Acceptable outcome: The materials are demonstrated, through existing certified data, to produce no cytotoxic or irritation responses, ensuring their suitability for clinical use in contact with nasal tissue.

2. Soft Continuum Robot Outputs

2.1.*Size of the robotic tip design output:* The diameter and length of the tip are 4 mm and 20 mm respectively.

Point of analysis: The dimensions of the robotic tip (length and diameter) are analyzed as a technical requirement.

Method of analysis: The size is measured using a digital caliper, a precise measurement tool widely used for determining linear dimensions [15].

Verification plan 4: The robotic tip dimensions are measured and recorded at multiple points along its body to ensure consistency in size. The diameter should be uniform at all cross-sections. A schematic of this test set-up can be seen in Figure 33.

Acceptable outcome: The caliper measurements confirm a consistent diameter of 4 mm \pm 0.1 mm and a length of 20 mm \pm 0.2 mm along the tip's body.

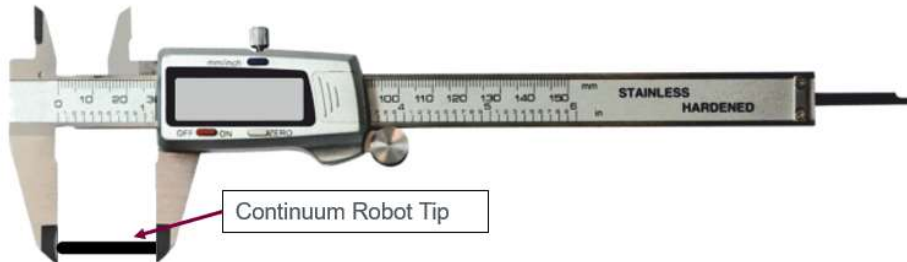


Figure 33. Schematic of the general set-up used for verification plan 4. A digital caliper will be utilized to gain accurate dimensional measurements. Above, the magnetized tip of the soft-continuum robot is measured to ensure consistency and adherence to design requirements.

2.2.*Size of the wire design output:* the gauge and length of the wire are 0.5mm and 245mm respectively. The length and gauge conform with design input 2.2.

Point of analysis: The diameter and length of the wire are analyzed as a technical requirement.

Method of analysis: The size is measured using a digital caliper, a precise measurement tool widely used for determining linear dimensions [15].

Verification plan 5: The wire gauge and length are measured at multiple points to ensure consistency and validate that they meet requirements. The test set up will be very similar to that seen in Figure 33, with a digital caliper used to gain dimensional measurements on the nitinol wire.

Acceptable outcome: The wire diameter should be $0.508\text{mm} \pm 0.01\text{ mm}$, and the length should be at least 15cm.

2.3.*Magnetization of robotic tip design output:* The tip is sufficiently magnetized to produce a magnetic field of strength averaging 32.3mT in magnitude at its north pole and 25.93mT at its south pole. This conforms with design input 2.3.

Point of analysis: The magnetic field strength of the robotic tip is analyzed as a technical requirement.

Method of analysis: The magnetic field strength produced by the tip was measured with a magneto-optical sensor, the CMOS-Magview. An image of this magnetic sensor and its output can be found in Figure 6.

Verification plan 6: The magnetic sensor is used to measure the tip's field strength at its tip and base (north and south poles) to confirm uniform magnetization.

Acceptable outcome: The magnetic sensor should record a consistent field strength of at least $10 \text{ mT} \pm 0.1 \text{ mT}$ at multiple locations along the tip. This ensures sufficient interaction with the magnetic actuation system.

2.4. *Magnetization of wire design output:* The wire is not magnetized. This conforms with design input 2.4.

Point of analysis: The magnetic properties of the wire are analyzed as a technical requirement.

Method of analysis: The magneto-optical sensor (CMOS-Magview) is used to verify that the wire exhibits no residual magnetization.

Verification plan 7: The wire is tested at multiple points along its length using the magnetic sensor to ensure that no magnetic field is detected. An equivalent test set up with a magnetic sensor can be found in Figure 6.

Acceptable outcome: The magnetic sensor should record a field strength of $0 \text{ mT} \pm 0.1 \text{ mT}$ along the entire wire. This ensures that the wire does not interfere with the tip's magnetic field or the coil-based actuation system.

2.5. *Materials of robotic tip design output:* the materials of the robotic tip are biocompatible and thus safe for use within a nasal cavity. This conforms with design input 2.5.

Point of analysis: The biocompatibility of the robotic tip materials is analyzed as a safety and compliance requirement.

Method of analysis: Literature review and reference to established studies in which the materials undergo cytotoxicity and irritation testing as outlined in ISO 10993-1 to confirm biocompatibility [6].

Verification plan: None.

Justification: Experimental verification of biocompatibility is considered out of scope for this project due to resource and time constraints. However, the materials selected are well-documented in literature as biocompatible in similar applications. The tip is fabricated using NdFeB powder embedded in EcoFlex 00-30, a silicone resin. When embedded within a biocompatible polymeric matrix, NdFeB powders have been shown to be biocompatible [16]. Additionally, EcoFlex 00-30, when properly mixed, cleaned, and fully cured, has been demonstrated to pass the ISO 10993-5 cytotoxicity biocompatibility test [16]. These references provide sufficient justification that the robotic tip, as fabricated, meets the intended biocompatibility requirements without the need for further in-house verification.

2.6. *Materials of wire design output:* the materials of the wire are biocompatible, and thus safe for use within a nasal cavity. This conforms with design input 2.6.

Point of analysis: The biocompatibility of the wire materials is analyzed as a safety and compliance requirement.

Method of analysis: Literature review and reference to ISO 10993-1 guidelines for evaluating medical-grade materials [17,10].

Verification plan: None

Justification: Experimental verification of biocompatibility is considered out of scope for this project. The nitinol wire used in the design is a commercially available medical-grade alloy that has been widely documented in the literature for use in implantable and surgical applications. It meets ISO 10993-1 requirements and has a long-standing record of clinical use in biocompatible devices [10]. Since the wire remains fully encased within the silicone body during operation, direct tissue contact is minimized. Therefore, the use of medical-grade nitinol is deemed suitable for this application without requiring additional in-house cytotoxicity or irritation testing.

2.7.*Mass design output:* the mass of the tip is 0.86g. This conforms with design input 2.7.

Point of analysis: The mass of the robotic tip is analyzed as a technical requirement.

Method of analysis: The tip mass is measured using a digital analytical balance with high sensitivity and precision.

Verification plan 8: The robotic tip is placed on the analytical scale, and its mass is recorded. Multiple measurements are taken to ensure consistency across all the fabricated tips. A schematic of this test set-up can be seen in Figure 34.



Figure 34. Schematic of the general set-up used for verification plan 8. A tared scale will be used to measure the mass of the magnetized tip.

Acceptable outcome: The tip mass should not exceed $1\text{g} \pm 0.05\text{g}$ to ensure compatibility with the magnetic field strength and actuation system.

2.8.*Flexibility design output:* The robot can bend to a 360° angle. This conforms with design input 2.8.

Point of analysis: The flexibility of the soft continuum robot is analyzed as a technical requirement.

Method of analysis: The robot's flexibility is tested by manually bending the soft body around a cylindrical mandrel (with a known radius that corresponds to 360° bending) while visually inspecting for signs of mechanical strain or failure. This method is a simpler alternative to methods involving specific structures and measurement algorithms to capture deformation state and sense bending [18].

Verification plan 9: The robot is manually wrapped around a cylindrical mandrel that matches the required bending radius. The test is repeated multiple times to ensure durability. Any signs of wire protrusion, tearing, or permanent deformation are documented. A schematic of this test set-up can be seen in Figure 35.

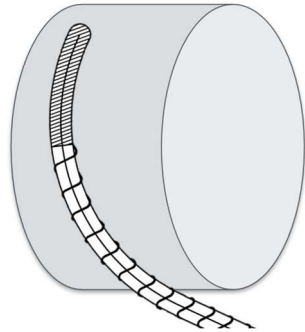


Figure 35. Schematic of the general set-up used for verification plan 9. The soft-continuum robot's flexibility and ability to bend in a 360° fashion can be demonstrated with a simplified version of bending analysis.

Acceptable outcome: The robot should wrap around the mandrel smoothly and return to its original shape after bending without visible damage or loss of functionality.

2.9.Robot Magnetic Deflection: The robot is responsive to the magnetic fields generated by the actuation system and has a deflection angle of 26°. This conforms with design input 2.9.

Point of analysis: The robot's magnetic responsiveness is analyzed as a technical and functional performance requirement to ensure proper actuation through external magnetic fields

Method of analysis: The robot is subjected to magnetic actuation using a 2-inch permanent magnet while the deflection angle is measured using a Mastercraft Digital Angle Finder Ruler.

Verification plan 10: The robot is fixed at its base and subjected to a magnetic field produced by a 2-inch permanent magnet. The resulting angular deflection of the robot tip is measured using the digital angle finder. Multiple trials are performed to confirm consistency and repeatability. An example of this test set-up can be seen in Figure 36.

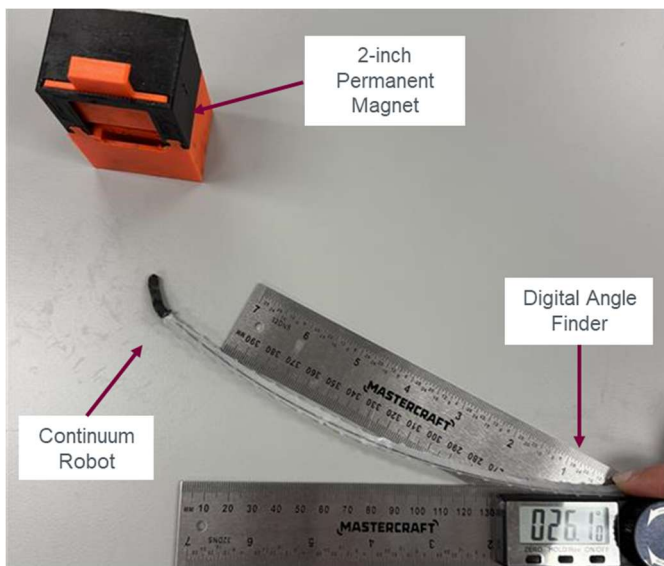


Figure 36. Schematic of the general set-up used for verification plan 10. The soft-continuum robot is acted upon by a permanent magnet and the angle of deflection is measured.

Acceptable outcome: The robot achieves a consistent deflection angle of $\geq 15^\circ$ in response to the actuation field without loss of structural integrity or responsiveness.

2.10. *Helical protrusion uniformity:* The body of the robot has uniform helical protrusions with a pitch of 10mm. This conforms with design input 2.10.

Point of analysis: Uniformity of the helical protrusions is analyzed as a technical requirement to ensure the mechanical performance of the soft continuum robot.

Method of analysis: The pitch of the helical protrusions is measured along the length of the robot using a digital caliper. Several points are sampled to check for consistency and uniform spacing.

Verification plan 11: A digital caliper is used to measure the distance between adjacent protrusions at multiple points along the robot's body. Deviations from the expected 10 mm pitch are recorded.

Acceptable outcome: The helical protrusions are uniform along the body with a measured pitch of $10 \text{ mm} \pm 0.1 \text{ mm}$ and show no defects or asymmetry that could hinder the continuum robot's movement through a passageway.

3. Magnetic Actuation System Outputs

3.1. *Temperature design output:* The temperature of the coils does not exceed 100°C . This conforms with design input 3.1.

Point of analysis: The temperature of the coil subsystem used for magnetic actuation control is analyzed.

Method of analysis: An Extech EX470A Multimeter and IR Thermometer are used to verify the temperature of the coils. This device can do both contact temperature measurements as well as non-contact temperature measurements using an IR laser pointer. Type K thermocouples are a reliable tool for measuring the surface temperature of a coil [19]. In this verification plan, to avoid the surface emissivity of a coil affecting the IR sensor, the contact temperature method, i.e. type K thermocouple method, is preferred.

Verification plan 12: The temperature of the coil should be taken at multiple time points as the system begins to heat up. The maximum time that any coil would be on is five seconds. Thus, once the coil is turned on, the temperature should be taken at zero seconds, 2 seconds, 5 seconds, and 30 seconds. This covers boundary cases of the coils being off, as well as run for too long, and covers the temperature during the expected run time. To take the temperature, the temperature probe is attached to the Extech EX470A Multimeter and can be directly placed onto the coil. This verification plan is a technical requirement as well as a risk mitigation strategy for the proof-of-concept. A schematic of this test set-up can be seen in Figure 37.

Acceptable outcome: Thermocouple reads 100°C or less at all time points analyzed. The coil should be at room temperature at the instant the coils are turned on (i.e. time = 0s).

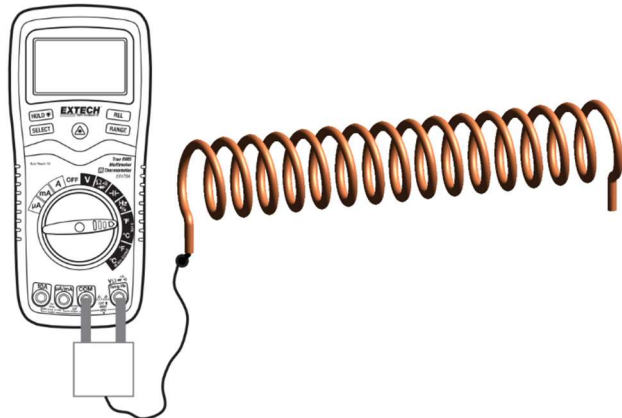


Figure 37. Schematic of the general set-up used for verification plan 12, using a photo taken from the manual of the Extech EX470A [20]. The Extech EX470A temperature probe is connected to the multimeter and in direct contact with the coil, allowing for a temperature measurement of the coil to be taken.

3.2.Magnetic field strength design output: The coils can produce a magnetic field strength of 5mT within 10cm from the edge of the coil, a field of 2mT within 20cm from the edge of the coil, and do not surpass a field strength of 100mT. This conforms with design input 3.2.

Point of analysis: The strength of the magnetic field produced by the coil subsystem is to be analyzed.

Method of analysis: An Infineon TLx493D Magnetic Sensor can be used to verify the strength of the magnetic field produced by the coils. Magnetic sensors are a common instrument used to directly measure the magnetic field strength [18]. Further, the simulation will be used to verify that the magnetic field produced by the coils is comparable to the theoretical calculations.

Verification plan 13: The simulation will calculate the magnetic field strength at various distances from the coils, corresponding to the experimental validation points: 0cm, 10cm, 20cm, and 40cm away from the edge of the coils. This covers boundary cases of the continuum robot being right beside or far away from the coils, as well as the expected use of approximately 10cm away. This ensures that there is enough force for the actuation of the robot while maintaining the design constraints.

Acceptable outcome A: The simulated magnetic field must not reach above 100mT at any distance from the edge of the coil. At 10cm from the coil edge, the simulation should show 5mT. At 20cm from the coil edge, the simulation should show 2mT. At 40cm from the coil edge, the simulation should show 0mT. The simulation visualization can be seen in Figure 38.

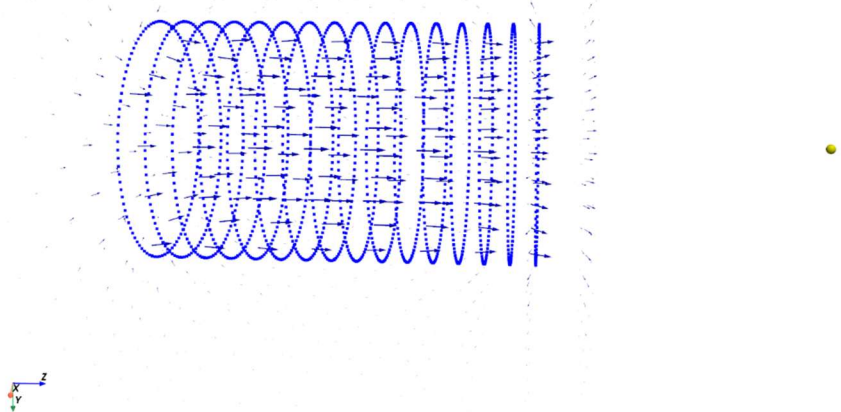


Figure 38.3D visualization of the coil's generated magnetic field using Python. The blue lines represent the electromagnetic coil with the magnetic sensor shown as a yellow sphere placed 16 cm away.

Verification plan 14: The strength of the magnetic field should be measured at multiple distances from the coil. The assumed average distance of the coil from the robot will be 10cm [3]. The assumed field strength required to actuate the continuum robot is 5mT. Therefore, the magnetic field strength should be tested at 0cm, 10cm, 20cm, and 40cm away from the edge of the coils. This covers boundary cases of the continuum robot being right beside or far away from the coils, as well as the expected use of approximately 10cm away. This verification plan is for a technical requirement as well as risk mitigation. A schematic of this test setup can be seen in Figure 39.

Acceptable outcome B: The magnetic sensor must not read above 100mT at any distance from the edge of the coil. At 10cm from the coil edge, the magnetic sensor reads 5mT. At 20cm from the coil edge, the magnetic sensor reads 2mT. At 40cm from the coil edge, the magnetic sensor reads 0mT.

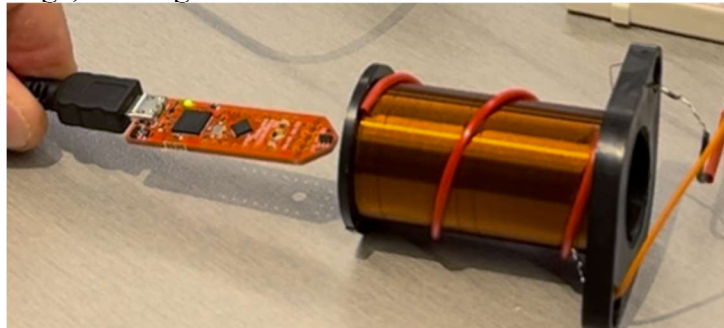


Figure 39. Photo of the general setup used for verification plan 13. The Infineon TLx493D-A1B6 3D Magnetic Sensor is placed near the coil, detecting the magnetic field being produced.

3.3. Voltage needs design output: The coils require no more than 60V to produce their magnetic field. This conforms with design input 3.3.

Point of analysis: The voltage requirements for the circuitry used to control the coil subsystem are to be analyzed.

Method of analysis: An Extech EX470A Multimeter can be used to verify that the voltage inputted into the coil system does not exceed our specified threshold. A multimeter is a very standard tool used to calculate voltage measurements [23].

Verification plan 15: As the coil system is not meant to produce varying magnetic fields, and is simply either a binary on or off, the system should always draw the same amount of voltage. Therefore, all that can be tested is the voltage required when the system is on and when it is off. To set this up, the black probe of the multimeter is connected to the circuit's ground and the red probe is connected to the positive terminal of the coil (i.e. where the voltage is applied to the coil). The multimeter can be read when the system is originally off, and then again once the system is on. This verification plan is for a technical requirement as well as risk mitigation. A schematic of this test set-up can be seen in Figure 40.

Acceptable outcome: The multimeter reads 0V when the system is off, and 60V or less when the system is on.

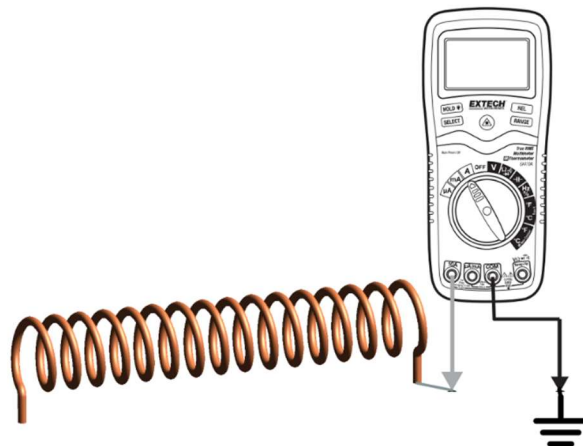


Figure 40. Schematic of the general set-up used for verification plan 15, using a photo taken from the manual of the Extech EX470A [23]. The Extech EX470A probes are connected to ground and the coil, allowing for a voltage measurement to be taken.

3.4. Directionality design output: The user can turn the coils on and off, effectively turning the produced magnetic field on and off. This conforms with design input 3.4.

Point of analysis: The coil subsystem used for magnetic actuation control is to be analyzed.

Method of analysis A: A Hantek 2D42 oscilloscope can be used to ensure that the circuitry to turn the coils on and off works as expected. Oscilloscopes can be used to verify electrical switching by recording the voltage within the system over time, allowing for the visualization of on/off transitions [24]. PWM control will be used to activate and deactivate the coils, which the oscilloscope will be able to measure.

Verification plan 16: The oscilloscope can be used to verify that the appropriate PWM is being sent into the motor driver. This verification plan is for a technical requirement as well as risk mitigation. A schematic of this test set-up can be seen in Figure 41.

Acceptable outcome A: The PWM waveform should be at 5V, with a 95% duty cycle (as this was the highest duty cycle the motor driver could recognize). This is to verify that the circuitry can communicate to the motor driver the specified coil strength, which is proportional to the duty cycle.

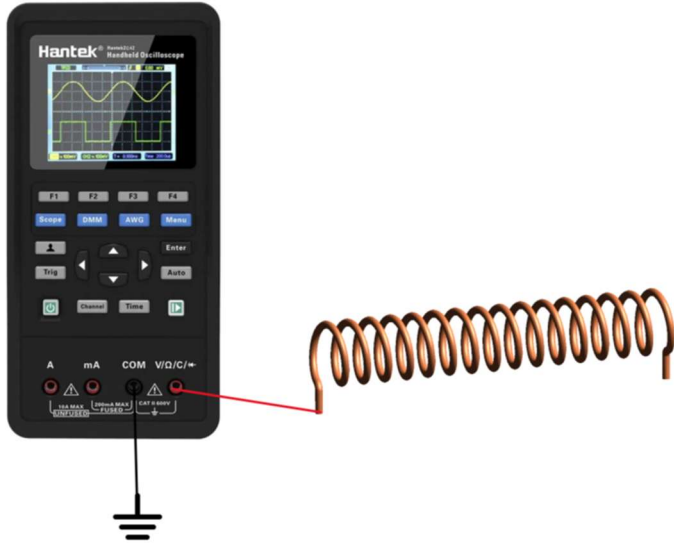


Figure 41. Schematic of the general set-up used for verification plan 16, using a photo taken from the manual of the Hantek website [26]. The Hantek 2D42 oscilloscope probes are connected to ground and the coil, allowing PWM measurements to be taken.

Verification plan 17: The oscilloscope will be used to measure the voltage going into the direction pin of the motor driver used to control a given coil. The oscilloscope will be able to read if the input voltage is high or low.

Acceptable outcome B: The oscilloscope will read a voltage of 5V when the direction is set to HIGH and a voltage of 0V when the direction is set to LOW. This is to verify that the circuitry can communicate to the motor driver the specified coil direction.

Verification plan 18: Once again, the input to the coil system does not vary and thus is a binary on or off. Therefore, the magnetic sensor can test the field produced by the coils in both its on and off state. The magnetic sensor will be placed inside the coil where the field is the strongest, and the field can be measured when the coils are off. Once the coils are switched on, the field can be measured again. Finally, the coils are switched off, and the field is measured again within one second of being turned off. This verification plan is for a technical requirement as well as risk mitigation. A schematic of this test set-up can be seen in Figure 39.

Acceptable outcome C: The magnetic sensor should read above 0mT when the coils are on, then 0mT within one second of the coils being turned off.

3.5. Indication design output: There is a visual indication showing when each coil is on or off. This conforms with design input 3.5.

Point of analysis: The subsystem of circuitry used to control the coils.

Method of analysis: The power supply units (PSUs) can be used to indicate when a coil is on or off, providing a clear visual signal for system status. When the value for current output is above 0A, the coils are on. When the value for current output is 0A, the coils are off.

Verification plan 19: Visual inspection can be used to verify when the coils are either on or off respectively. This verification plan is for a non-technical requirement as well as risk mitigation.

Acceptable outcome: The PSU shows a current of above 0A when the coil is turned on, and PSU shows a current of 0A when the coil is turned off.

4. Linear Actuation System Outputs

4.1. *Resolution design output:* the linear actuator has a resolution of 200 steps/revolution with 8 microsteps per step, totalling 1600 steps per revolution. This conforms with design input 4.1.

Point of analysis: The stepper motor's resolution is analyzed as a technical requirement.

Method of analysis: The resolution is verified by observing the distance traveled per step using a digital caliper and comparing the results to the theoretical step size. The step size is calculated using the helical pitch of the robot and stepper motor specifications. Step size calculations can be found in Appendix A: Design Output Calculations, subsection Calculation 2.

Verification plan 20: The stepper motor is programmed to move a full rotation of 1600 steps, and the distance traveled is measured. A schematic of this test set-up can be seen in Figure 42.



Figure 42. Schematic of the general set-up used for verification plan 19. The position of the soft continuum robot before and after each movement will be recorded. The displacement measured will allow for comparison with theoretical values.

Acceptable outcome: The measured displacement should match the theoretical displacement within $\pm 7\%$, ensuring consistent step resolution and accuracy. This error range is in line with the 7-8% discrepancy experienced by linear actuators found in literature [27].

4.2. *Load design output:* the linear actuator can handle a load of up to 150g. This conforms with design input 4.2.

Point of analysis: The friction forces when retracting the robot are increased due to higher surface area.

Method of analysis: The robot is extended and retracted while carrying a measured load.

Verification plan 21: The robot is to be retracted a set distance while pulling a measured load. The distance will be measured, and the average is taken to determine the impact of the load on its movement.

Acceptable outcome: A load of up to 150g should not impact the movement by more than 7%.

4.3. Directionality design output: the linear actuator can move the tip both in extension or retraction using the navigational interface. This conforms with design input 4.3. Point of analysis: The ability of the interface to control the linear actuator to achieve bidirectional control is analyzed as a technical requirement and risk mitigation measure.

Method of analysis: The motor is tested by alternating between extension or retraction using the navigational interface, and the final position is measured to ensure no cumulative error.

Verification plan 22: The robot is programmed to move forward for a set duration (e.g., 5 seconds) and then backward for the same duration. This is then repeated 10 times without pause. The initial and final positions are recorded using a digital ruler or caliper. Repeated trials (e.g., 10 cycles) are conducted to test for errors. Once again, a test set up similar to that seen in Figure 42 will be employed for this verification plan.

Acceptable outcome: The robot should return to its original position after extension or retraction motion, with an allowable deviation of 7%.

4.4. Size compatibility design output: the linear actuator can satisfy design input 4.1 with wire gauges between 1-4mm. This satisfies design input 4.4.

Point of analysis: Increasing size compatibility will prevent the need for change in the linear actuation throughout design changes in the continuum robot.

Method of analysis: The repeatability test is conducted at for various wire sizes.

Verification plan 23: Extend the wire for a set duration of time and measure the change in linear movement. Repeat the step multiple times, then average. After, change wire sizes and repeat the steps again.

Acceptable outcome: Wire sizes between 1-4mm are within 7% of movement deviation of each other.

5. Navigation Interface and Simulation Outputs

5.1. Simulated field strength output:

Point of analysis: The accuracy of the magnetic field output from the software must align with theoretical calculations and experimental sensor readings. This conforms with design input 3.2 and 5.1.

Method of analysis: The simulation applies the Bio-Savart law and finite-element analysis to model the magnetic field. The strength of the magnetic field produced by the simulated coils is to be analyzed against the experimental outputs using a magnetic sensor to ensure the software aligns with real-world data.

Verification plan 24: The magnetic field strength will be simulated at distances of 0cm, 5cm, 10cm, 15cm and 20cm from the coils with the same input parameters as the experimental setup, specifically positive current value. The results of the simulation will be compared against the sensor readings to assess the precision.

Acceptable outcome: The software correctly accumulated the individual coil fields with magnetic field results being within 25% of the expected results. The directionality of the combined magnetic fields should align with the theoretical expectations.

Verification plan 25: The magnetic field strength will be simulated at distances of 0cm, 5cm, 10cm, 15cm and 20cm from the coils with the same input parameters as the experimental setup, specifically negative current value. The results of the simulation will be compared against the sensor readings to assess the precision.

Acceptable outcome: The software correctly accumulated the individual coil fields with magnetic field results being within 25% of the expected results. The directionality of the combined magnetic fields should align with the theoretical expectations.

5.2. Magnetic field direction output:

Point of analysis: The interface's ability to correctly simulate the direction of the magnetic field vectors. This conforms with design input 3.2 and 5.2.

Method of analysis: The interface will compute magnetic field vector orientations at several points within the 3D visualization to verify the field is travelling in the expected direction. The results will be compared to the theoretical predictions based on the solenoid equation as well as the experimental results.

Verification plan 26: The interface will be testing coil configurations to ensure the interface can correctly model the positive field direction. The simulation output will be compared against analytical field diagrams to confirm the consistency.

Acceptable outcome: The simulated magnetic field vectors align with the theoretical expectations with correct directional patterns.

Verification plan 27: The interface will be testing coil configurations to ensure the interface can correctly model the negative field direction. The simulation output will be compared against analytical field diagrams to confirm the consistency.

Acceptable outcome: The simulated magnetic field vectors align with the theoretical expectations with correct directional patterns.

5.3. Magnetic field superposition output

Point of analysis: The interface's ability to correctly apply the superposition principle when computing the accumulated magnetic field generated from multiple coils. This conforms with design input 3.2 and 5.3.

Method of analysis: The experimental setup of the coils will be measured with the magnetic sensor at different points of the environment and will be compared to the simulation at the same points to verify the vector fields are accurately summed in the 3D space.

Verification plan 28: The interface will run cases with one active coil with positive current where the resultant field will be compared to the experimental setup and verify correct application of the superposition principle.

Verification plan 29: The interface will run cases with one active coil with negative current where the resultant field will be compared to the experimental setup and verify correct application of the superposition principle.

Verification plan 30: The interface will run cases with two active coils with positive current where the resultant field will be compared to the experimental setup and verify correct application of the superposition principle.

Verification plan 31: The interface will run cases with two active coils with positive and negative current where the resultant field will be compared to the experimental setup and verify correct application of the superposition principle.

Verification plan 32: The interface will run cases with three active coils with positive current where the resultant field will be compared to the experimental setup and verify correct application of the superposition principle.

Verification plan 33: The interface will run cases with three active coils with two positive currents and one negative current where the resultant field will be compared to the experimental setup and verify correct application of the superposition principle.

Acceptable outcome: The interface correctly accumulated the individual coil fields with magnetic field results being within 25% of the expected results. The directionality of the combined magnetic fields should align with the theoretical expectations.

5.4. Linear actuator output

Point of analysis: The interface's ability to correctly apply extension and retraction of the robot via linear actuation system. This conforms with design input 4.3 and 5.4.

Method of analysis: The experimental setup of the integrated system will be observed to verify the extension/retraction of the robot.

Verification plan 34: The interface will run cases with extension of the robot where the resultant linear movement observed will verify correct application of the linear actuator.

Verification plan 35: The interface will run cases with retraction of the robot where the resultant linear movement observed will verify correct application of the linear actuator.

Acceptable Outcome: The interface correctly executes the respective functions initiated by the interface and is observed in the physical setup.

5.5. Linear and magnetic actuation output

Point of analysis: The interface's ability to correctly apply extension and retraction of the robot via linear actuation system while also applying magnetic actuation on the robot using the magnetic actuation system. This conforms with design input 5.5.

Method of analysis: The experimental setup of the integrated system will be observed once initiated by the interface to verify the simultaneous extension/retraction and magnetic actuation of the robot.

Verification plan 36: The interface will run cases with extension of the robot with directional actuation where the resultant movement observed will verify correct application of both the magnetic and linear actuator.

Verification plan 37: The interface will run cases with retraction of the robot with directional actuation where the resultant movement observed will verify the deactivation of the magnetic actuation system while in retraction.

Acceptable Outcome: The interface correctly executes the respective functions initiated and is observed in the physical setup.

5.6. Safety mechanisms output

Point of analysis: The interface's ability to correctly apply safety mechanisms

implemented on the robot by halting either or both actuation systems. This conforms with design input 5.6.

Method of analysis: The experimental setup of the integrated system will be observed once initiated by the interface to verify the deactivation of the individual subsystems, resulting in no linear actuation and/or magnetic actuation.

Verification plan 38: The interface will run cases with magnetic actuation followed by initiation of “Complete Turn” where the resultant movement observed will verify correct deactivation of the magnetic actuation system.

Verification plan 39: The interface will run cases with extension of the robot with directional actuation followed by the initiation of “EMERGENCY STOP” where the resultant movement observed will verify correct deactivation of both the magnetic and linear actuation systems.

Acceptable Outcome: The interface correctly executes the respective functions initiated and is observed in the physical setup.

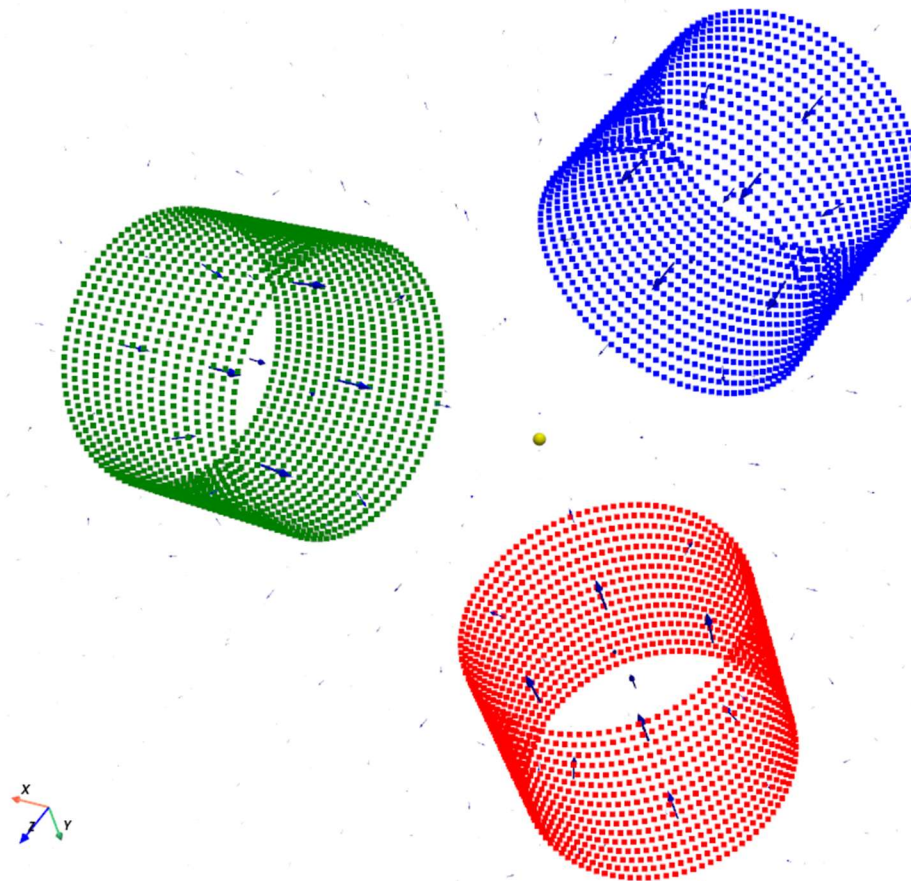


Figure 24. 3D visualization of three coils and the generated magnetic field using Python. The blue arrows represent the field direction vector with the magnetic sensor shown as a yellow sphere placed at the center.

Below is a table summarizing all the verification plans outlined in detail above.

Table 6. Summary of all verification plans and associated tests.

Plan Id	Design Output	Inputs	Expected Values	Actual Values	Pass /Fail
4	2.1	Robot tip dimensions	Diameter \leq 4 mm \pm 0.1 mm Length \leq 20 mm \pm 0.2 mm	Diameter = TBD Length = TBD	TBD
5	2.2	Nitinol wire dimensions	Gauge = 0.508 mm \pm 0.01 mm Length \geq 15 cm	Gauge = TBD Length = TBD	TBD
6	2.3	Robot tip magnetization	Magnetization \geq 10 mT \pm 0.1 mT	Magnetic Field = TBD	TBD
7	2.4	Nitinol wire magnetization	Residual magnetization = 0 mT \pm 0.1 mT	Magnetic Field = TBD	TBD
8	2.7	Robot tip	Mass \leq 1 g \pm 0.05 g	Mass = TBD	TBD
9	2.8	Robot bending test	Bending angle up to 360°, no visible damage or permanent deformation after bending	Bending angle = TBD	TBD
10	2.9	Robot deflection via magnetic field	Angle of deflection when attracted to 2inch permanent magnet \geq 15°	Angle of deflection = TBD	Pass
11	2.10	Robot body helical protrusion uniformity	Helical pitch = 10mm \pm 0.1mm	Helical pitch = TBD	TBD
12	3.1	Time1 = 0s Time2 = 2s Time3 = 5s Time4 = 30s	Temp1 = 22°C Temp2 < 100°C Temp3 < 100°C Temp4 < 100°C	Temp1 = TBD Temp2 = TBD Temp3 = TBD Temp4 = TBD	TBD
13	3.2	Distance1 = 0cm Distance2 = 10cm Distance3 = 20cm Distance4 = 40cm	10mT < Field1 < 100mT 5mT < Field2 < 100mT 2mT < Field3 < 100mT Field4 = 0mT	Field1 = TBD Field2 = TBD Field3 = TBD Field4 = TBD	TBD
14	3.2	Distance1 = 0cm Distance2 = 10cm Distance3 = 20cm Distance4 = 40cm	10mT < Field1 < 100mT 5mT < Field2 < 100mT 2mT < Field3 < 100mT Field4 = 0mT	Field1 = TBD Field2 = TBD Field3 = TBD Field4 = TBD	TBD
15	3.3	Coil1 = ON Coil2 = OFF	0V < Voltage1 < 60V Voltage2 = 0V	Voltage1 = TBD Voltage2 = TBD	TBD
16	3.4	DutyCycle1 = 95% DutyCycle2 = 0%	PWM1 = 5V PWM2 = 0V	PWM1 = TBD PWM2 = TBD	TBD
17	3.4	Direction1 = HIGH Direction2 = LOW	Voltage1 = 5V Voltage2 = 0V	Voltage1 = TBD Voltage2 = TBD	TBD
18	3.4	Coil1 = ON Coil2 = OFF	Field1 > 0mT Field2 = 0mT	Field1 = TBD Field2 = TBD	TBD

19	3.5	Coil1 = ON Coil2 = OFF	PSUcurrent1 > 0A PSUcurrent2 = 0A	PSUcurrent1 = TBD PSUcurrent2 = TBD	TBD
20	4.1	1600 microsteps	21.99mm ± 7% (1.5mm) of average movement	TBD	TBD
21	4.2	Loads of 5g, 10g, 20g, 50g, 100g, 150g, 200g, 300g	<7% (1.5mm) deviation of average movement under 150g of load compared to	TBD	TBD
22	4.3	10 rotations (1600 microsteps) of extension and retraction	<7% (1.5mm) deviation from initial position	TBD	TBD
23	4.4	0.5mm, 1mm, 2mm, 4mm wire gauge	1-4mm wire deviates <7% (1.5mm) from movement	TBD	TBD
24	5.1	Coil 1 Plane = Y Coil 1 Current: 15 A Coil 1 Radius: 0.05m Coil 1 Turns: 450 Coil 1 Length: 0.05m Distance1 = 0 m Distance2 = 0.05 m Distance3 = 0.10 m Distance4 = 0.15 m Distance5 = 0.20 m	Field1 > 80 mT Field2 > 30 mT Field3 > 5 mT Field4 > 2mT Field5 >1mT Coil 1 Colour = Green Coil 2 Colour = Grey Coil 3 Colour = Grey	Field1 = TBD Field2 = TBD Field3 = TBD Coil 1 Colour = TBD Coil 2 Colour = TBD Coil 3 Colour = TBD	TBD
25	5.1	Coil 1 Plane = Y Coil 1 Current: -15 A Coil 1 Radius: 0.05m Coil 1 Turns: 450 Coil 1 Length: 0.05m Distance1 = 0 m Distance2 = 0.05 m Distance3 = 0.10 m Distance4 = 0.15 m Distance5 = 0.20 m	Field1 > -80 mT Field2 > -30 mT Field3 > -5 mT Field4 > -2mT Field5 > -1mT Coil 1 Colour = Red Coil 2 Colour = Grey Coil 3 Colour = Grey	Field1 = TBD Field2 = TBD Field3 = TBD Coil 1 Colour = TBD Coil 2 Colour = TBD Coil 3 Colour = TBD	TBD
26	5.2			Field Direction = TBD	TBD

		<p>Coil 1 Plane = Y</p> <p>Coil 1 Current: 15 A</p> <p>Coil 1 Radius: 0.05m</p> <p>Coil 1 Turns: 450</p> <p>Coil 1 Length: 0.05m</p>	<p>Field Direction = Positive Y direction in interface</p> <p>Coil 1 Colour = Green</p> <p>Coil 2 Colour = Grey</p> <p>Coil 3 Colour = Grey</p>	<p>Coil 1 Colour = TBD</p> <p>Coil 2 Colour = TBD</p> <p>Coil 3 Colour = TBD</p>	
27	5.2	<p>Coil 1 Plane = Y</p> <p>Coil 1 Current: -15 A</p> <p>Coil 1 Radius: 0.05m</p> <p>Coil 1 Turns: 450</p> <p>Coil 1 Length: 0.05m</p>	<p>Field Direction = Negative Y direction in interface</p> <p>Coil 1 Colour = Red</p> <p>Coil 2 Colour = Grey</p> <p>Coil 3 Colour = Grey</p>	<p>Field Direction = TBD</p> <p>Coil 1 Colour = TBD</p> <p>Coil 2 Colour = TBD</p> <p>Coil 3 Colour = TBD</p>	TBD
28	5.3	<p>Coil 1 Plane = Y</p> <p>Coil 1 Current: 15 A</p> <p>Coil 1 Radius: 0.05m</p> <p>Coil 1 Turns: 450</p> <p>Coil 1 Length: 0.05m</p> <p>Distance = 0.10m</p>	<p>Field X = 0mT</p> <p>Field Y = 7.6 mT</p> <p>Field Z = 0mT</p> <p>Field Direction = Positive Y direction in interface</p> <p>Coil 1 Colour = Green</p> <p>Coil 2 Colour = Grey</p> <p>Coil 3 Colour = Grey</p> <p>Resultant field = 7.6 mT</p>	<p>Field X = TBD</p> <p>Field Y = TBD</p> <p>Field Z = TBD</p> <p>Field Direction = TBD</p> <p>Coil 1 Colour = TBD</p> <p>Coil 2 Colour = TBD</p> <p>Coil 3 Colour = TBD</p> <p>Resultant field = TBD</p>	TBD

29	5.3	<p>Coil 1 Plane = Y Coil 1 Current: -15 A Coil 1 Radius: 0.05m Coil 1 Turns: 450 Coil 1 Length: 0.05m Distance = 0.10m</p>	<p>Field X = 0mT Field Y = -7.6 mT Field Z = 0mT</p> <p>Field Direction = Negative Y direction in interface</p> <p>Coil 1 Colour = Red Coil 2 Colour = Grey Coil 3 Colour = Grey</p> <p>Resultant field = -7.6mT</p>	<p>Field X = TBD Field Y = TBD Field Z = TBD</p> <p>Field Direction = TBD</p> <p>Coil 1 Colour = TBD Coil 2 Colour = TBD Coil 3 Colour = TBD</p> <p>Resultant field = TBD</p>	TBD
30	5.3	<p>Coil 1 Plane = Y Coil 1 Current: 15 A Coil 1 Radius: 0.05m Coil 1 Turns: 450 Coil 1 Length: 0.05m Coil 2 Plane = Z Coil 2 Current: 15 A Coil 2 Radius: 0.05m Coil 2 Turns: 450 Coil 2 Length: 0.05m Distance = 0.10m</p>	<p>Field X = 0mT Field Y = 7.6 mT Field Z = 7.6 mT</p> <p>Field Direction = Positive YZ direction in interface</p> <p>Coil 1 Colour = Green Coil 2 Colour = Green Coil 3 Colour = Grey</p> <p>Resultant field = 10.75 mT</p>	<p>Field X = TBD Field Y = TBD Field Z = TBD</p> <p>Field Direction = TBD</p> <p>Coil 1 Colour = TBD Coil 2 Colour = TBD Coil 3 Colour = TBD</p> <p>Resultant field = TBD</p>	TBD
31	5.3	<p>Coil 1 Plane = Y Coil 1 Current: 15 A Coil 1 Radius: 0.05m Coil 1 Turns: 450 Coil 1 Length: 0.05m Coil 2 Plane = Z Coil 2 Current: -15 A Coil 2 Radius: 0.05m Coil 2 Turns: 450 Coil 2 Length: 0.05m Distance = 0.10m</p>	<p>Field X = 0mT Field Y = 7.6 mT Field Z = -7.6 mT</p> <p>Field Direction = Positive Y negative Z direction in interface</p> <p>Coil 1 Colour = Green Coil 2 Colour = Red Coil 3 Colour = Grey</p>	<p>Field X = TBD Field Y = TBD Field Z = TBD</p> <p>Field Direction = TBD</p> <p>Coil 1 Colour = TBD Coil 2 Colour = TBD</p>	TBD

			Resultant field = 10.75 mT	Coil 3 Colour = TBD Resultant field = TBD	
32	5.3	Coil 1 Plane = Y Coil 1 Current: 15 A Coil 1 Radius: 0.05m Coil 1 Turns: 450 Coil 1 Length: 0.05m Coil 2 Plane = Z Coil 2 Current: 15 A Coil 2 Radius: 0.05m Coil 2 Turns: 450 Coil 2 Length: 0.05m Coil 3 Plane = X Coil 3 Current: 15 A Coil 3 Radius: 0.05m Coil 3 Turns: 450 Coil 3 Length: 0.05m Distance = 0.10m	Field X = 7.6mT Field Y = 7.6 mT Field Z = 7.6 mT Field Direction = Positive XYZ direction in interface Coil 1 Colour = Green Coil 2 Colour = Green Coil 3 Colour = Green Resultant field = 13.16 mT	Field X = TBD Field Y = TBD Field Z = TBD Field Direction = TBD Coil 1 Colour = TBD Coil 2 Colour = TBD Coil 3 Colour = TBD Resultant field = TBD	
33	5.3	Coil 1 Plane = Y Coil 1 Current: 15 A Coil 1 Radius: 0.05m Coil 1 Turns: 450 Coil 1 Length: 0.05m Coil 2 Plane = Z Coil 2 Current: -15 A Coil 2 Radius: 0.05m Coil 2 Turns: 450 Coil 2 Length: 0.05m Coil 3 Plane = X Coil 3 Current: 15 A Coil 3 Radius: 0.05m Coil 3 Turns: 450 Coil 3 Length: 0.05m Distance = 0.10m	Field X = 7.6mT Field Y = 7.6 mT Field Z = -7.6 mT Field Direction = Positive XY and Negative Z direction in interface Coil 1 Colour = Green Coil 2 Colour = Red Coil 3 Colour = Green Resultant field = 13.16 mT	Field X = TBD Field Y = TBD Field Z = TBD Field Direction = TBD Coil 1 Colour = TBD Coil 2 Colour = TBD Coil 3 Colour = TBD Resultant field = TBD	
34	5.4	Linear Actuator: Extension	Linear Actuator: Extension	Linear Actuator: TBD	TBD
35	5.4	Linear Actuator: Retraction	Linear Actuator: Retraction	Linear Actuator: TBD	TBD
36	5.5				TBD

		<p>Coil 1 Plane = Y</p> <p>Coil 1 Current: 15 A</p> <p>Coil 1 Radius: 0.05m</p> <p>Coil 1 Turns: 450</p> <p>Coil 1 Length: 0.05m</p> <p>Distance = 0.05m</p> <p>Linear Actuator: Extension</p>	<p>Linear Actuator: Extension</p> <p>Coil 1 Colour = Green</p> <p>Coil 2 Colour = Grey</p> <p>Coil 3 Colour = Grey</p> <p>Field X = 0mT</p> <p>Field Y = 7.6 mT</p> <p>Field Z = 0mT</p>	<p>Linear Actuator: TBD</p> <p>Coil 1 Colour = TBD</p> <p>Coil 2 Colour = TBD</p> <p>Coil 3 Colour = TBD</p> <p>Field X = TBD</p> <p>Field Y = TBD</p> <p>Field Z = TBD</p>	
37	5.5	<p>Coil 1 Plane = Y</p> <p>Coil 1 Current: 15 A</p> <p>Coil 1 Radius: 0.05m</p> <p>Coil 1 Turns: 450</p> <p>Coil 1 Length: 0.05m</p> <p>Distance = 0.05m</p> <p>Linear Actuator: Retraction</p>	<p>Linear Actuator: Retraction</p> <p>Field X = 0mT</p> <p>Field Y = 0 mT</p> <p>Field Z = 0mT</p> <p>Coil 1 Colour = Grey</p> <p>Coil 2 Colour = Grey</p> <p>Coil 3 Colour = Grey</p>	<p>Linear Actuator: TBD</p> <p>Field X = TBD</p> <p>Field Y = TBD</p> <p>Field Z = TBD</p> <p>Coil 1 Colour = TBD</p> <p>Coil 2 Colour = TBD</p> <p>Coil 3 Colour = TBD</p>	TBD
38	5.6	<p>Coil 2 Plane = X</p> <p>Coil 2 Current: 15 A</p> <p>Coil 2 Radius: 0.05m</p> <p>Coil 2 Turns: 450</p> <p>Coil 2 Length: 0.05m</p> <p>Complete Turn: ON</p>	<p>Complete Turn: ON</p> <p>Field X = 0 mT</p> <p>Field Y = 0 mT</p> <p>Field Z = 0mT</p> <p>Coil 1 Colour = Grey</p>	<p>Complete Turn: TBD</p> <p>Field X = TBD</p> <p>Field Y = TBD</p> <p>Field Z = TBD</p>	TBD

			Coil 2 Colour = Grey Coil 3 Colour = Grey	Coil 1 Colour = TBD Coil 2 Colour = TBD Coil 3 Colour = TBD	
39	5.6	Coil 1 Plane = Y Coil 1 Current: 15 A Coil 1 Radius: 0.05m Coil 1 Turns: 450 Coil 1 Length: 0.05m Coil 2 Plane = X Coil 2 Current: 15 A Coil 2 Radius: 0.05m Coil 2 Turns: 450 Coil 2 Length: 0.05m Linear Actuator: Extension Emergency STOP: ON	Emergency STOP: ON Linear Actuator: Idle Field X = 0 mT Field Y = 0 mT Field Z = 0mT Coil 1 Colour = Grey Coil 2 Colour = Grey Coil 3 Colour = Grey	Emergency STOP: TBD Linear Actuator: TBD Field X = TBD Field Y = TBD Field Z = TBD Coil 1 Colour = TBD Coil 2 Colour = TBD Coil 3 Colour = TBD	TBD

Chapter 3 References

1. M. N. O. Sadiku, *Elements of electromagnetics*, 7th ed. New York: Oxford University Press, 2018.
2. David Jeffrey Griffiths and Cambridge University Press, *Introduction to Electrodynamics*, 4th ed. Cambridge I Pozostałe: Cambridge University Press, 2018.
5. Eland Cables, “AWG Chart and the metric system: Eland cables,” FAQ: AWG chart and the metric system | Eland Cables, <https://www.elandcables.com/the-cable-lab/faqs/faq-what-is-the-conversion-between-awg-and-the-metric-system> (accessed Feb. 1, 2025).
6. Electronics Area, “What is electrical resistivity? - electronics area,” Electronics Area - Electrical and Electronics Tutorials and Circuits, <https://electronicsarea.com/electrical-resistivity/> (accessed Feb. 2, 2025).
7. M. Ortner and L. G. Coliado Bandeira, “Magpylib: A free python package for Magnetic Field Computation,” *ScienceDirect*, <https://www.sciencedirect.com/science/article/pii/S2352711020300170> (accessed Feb. 6, 2025).
8. Y. A. Laksono, N. A. Pramono, and A. Sunaryono, “Using the Magpylib library to analyze the ferrofluids in magnetic field sourcing from cylinders,” *CoLab*, <https://colab.wis/10.1063%2F5.0121457> (accessed Feb. 6, 2025).
9. COMSOL Multiphysics Reference Manual, https://doc.comsol.com/5.5/doc/com.comsol.help.comsol/COMSOL_ReferenceManual.pdf (accessed Feb. 6, 2025).
10. ISO, "ISO 10993-1:2018 - Biological Evaluation of Medical Devices – Part 1: Evaluation and Testing Within a Risk Management Process," International Organization for Standardization, Geneva, Switzerland, 2018.
11. M. K. Koiri and A. K. Sharma, “Characterization and behavior study of nitinol shape memory alloy wire for effective and efficient use in soft robotics as an actuator,” *Indian Journal of Pure & Applied Physics*, pp. 216–222, Feb. 2021. doi:10.56042/ijpap.v59i3.67755.
12. J. Boisson, H. Strozyk, P. Diner, A. Picard, and N. Kadlub, “Feasibility of magnetic activation of a maxillofacial distraction osteogenesis, design of a new device,” *Journal of Cranio-Maxillofacial Surgery*, vol. 44, no. 6, pp. 684–688, Jun. 2016. doi:10.1016/j.jcms.2016.03.009.
13. F. Diemer and P. Calas, “Effect of pitch length on the behavior of Rotary Triple Helix Root Canal Instruments,” *Journal of Endodontics*, vol. 30, no. 10, pp. 716–718, Oct. 2004. doi:10.1097/01.don.0000125877.26495.69.
14. J [1] ISO, "ISO 14971:2019 - Medical Devices – Application of Risk Management to Medical Devices," *International Organization for Standardization*, Geneva, Switzerland, 2019.IEC, "IEC 60601-1-2:2014 - Medical Electrical Equipment – Part 1-2: General Requirements for Basic Safety and Essential Performance – Collateral Standard: Electromagnetic Compatibility," International Electrotechnical Commission, Geneva, Switzerland, 2014.
15. Consumer Product Testing Company, *Ecoflex 00-30 – In Vitro Toxicity Testing Report*, Test Report No. V23-0323.03, prepared for Smooth-On, Inc., Fairfield, NJ, USA, Feb. 23, 2023.

16. Consumer Product Testing Company, *Ecoflex 00-30 – In Vitro Toxicity Testing Report*, Test Report No. V23-0323.03, prepared for Smooth-On, Inc., Fairfield, NJ, USA, Feb. 23, 2023.
17. A. R. Pelton, D. Stöckel, and T. W. Duerig, “Medical Uses of Nitinol,” *Mater. Sci. Forum*, vol. 327–328, pp. 63–70, Jan. 2000, doi: 10.4028/www.scientific.net/MSF.327-328.63.
18. J. P. Fuehne, “Training with various tools to facilitate measurement instrument selection,” *NCSL International Workshop & Symposium Conference Proceedings 2020*, 2020. doi:10.51843/wsproceedings.2020.21
19. V.-A. Scarlatache *et al.*, “Analysis of coil characteristics using modern measurement techniques,” *2024 IEEE International Conference And Exposition On Electric And Power Engineering (EPEi)*, pp. 595–598, Oct. 2024. doi:10.1109/epei63510.2024.10758089.
20. M. B. Maia, J. De Brito, I. M. Martins, and J. D. Silvestre, “Toxicity of recycled concrete aggregates: Review on leaching tests,” *The Open Construction and Building Technology Journal*, vol. 12, no. 1, pp. 187–196, Jun. 2018. doi:10.2174/1874836801812010187.
21. K. Hanaoka, M. Shimizu, and T. Umedachi, “Development of 3D printed structure that visualizes bending and compression deformations for soft-bodied robots,” *2021 IEEE 4th International Conference on Soft Robotics (RoboSoft)*, pp. 155–162, Apr. 2021. doi:10.1109/robosoft51838.2021.9479224.
22. Y. Li, J. Li, and B. Samali, “On the magnetic field and temperature monitoring of a solenoid coil for a novel magnetorheological elastomer base isolator,” *Journal of Physics: Conference Series*, vol. 412, p. 012033, Feb. 2013. doi:10.1088/1742-6596/412/1/012033.
23. “Extech Instruments EX470A multimeter user Manual,” ManualsLib, <https://www.manualslib.com/manual/1514842/Extech-Instruments-Ex470a.html> (accessed Feb. 5, 2025).
24. D. Slomovitz, “Basic instruments: Multimeters,” *Modern Measurements*, pp. 149–173, Sep. 2015. doi:10.1002/9781119021315.ch5.
25. D. R. Larson, N. G. Paulter, and D. I. Bergman, “Pulse parameter dependence on transition occurrence instant and waveform epoch,” *IEEE Transactions on Instrumentation and Measurement*, vol. 54, no. 4, pp. 1520–1526, Aug. 2005. doi:10.1109/tim.2005.851076
26. “Hantek2000 Series,” Hantek2000 series - hantek electronic & your testing solution provider, <https://hantek.com/products/detail/13174> (accessed Feb. 5, 2025).
27. P. Cheng, J. Jia, Y. Ye, and C. Wu, “Modeling of a soft-rigid gripper actuated by a linear-extension soft pneumatic actuator,” *Sensors*, vol. 21, no. 2, p. 493, Jan. 2021. doi:10.3390/s21020493

Chapter 4

4.1 Implementation

4.1.1 Magnetized Continuum Robot

4.1.1.1 Iterative Process

The soft continuum robot underwent multiple design iterations to optimize flexibility, actuation response, and magnetization strength. Prototypes B, C, and D represent critical design alternatives evaluated prior to selecting the final iteration, Robot A. Each prototype was assessed based on its adherence to the soft-continuum robot design inputs outlined in Chapter 1, including dimensional constraints (≤ 5 mm diameter, ≤ 20 mm length), wire specifications (≤ 0.5 mm diameter, ≥ 10 cm length), minimum magnetization thresholds (≥ 20 mT), and structural performance indicators such as deflection angle, helical uniformity, and material biocompatibility.

Robot B: Magnetization Benchmark

For Robot B, magnetic (NdFeB) particles were mixed with the silicone resin at a 1:1.25 ratio of silicone to particles and then used to mould a magnetized tip. As follows in the primary fabrication process outlined in Chapter 3 section 3.1.2, this tip was then inserted into a secondary mould to form the robot body with helical protrusions. After fabrication, this robot had a 4 mm diameter silicone (EcoFlex 00-30) body with a 0.5 mm nitinol wire core. This iteration, seen in Figure 43, served as the first fully moulded prototype for testing complete form-factor, magnetic responsiveness, and field strength uniformity. This robot was also one of the first to have its tip magnetized by the impulse magnetizer which was much stronger than other methods of magnetization that were attempted previously.



Figure 43. Robot B, 4mm diameter and 0.5mm wire core, post-fabrication process detailed in section 3.1.2 of this report. The features of the magnetized tip and the body with helical protrusions are clearly visible. This iteration was essential in validating the fabrication process.

During magnetization verification using the CMOS-MagView, Robot B exhibited average field strengths of 31.73 mT at the north pole and 23.50 mT at the south pole. These values exceeded the 20 mT threshold outlined in design inputs, but were slightly lower than those achieved by the final prototype. This discrepancy was attributed in part to inconsistencies in the magnetic tip moulding process and variability in the silicone-to-particle mixing ratio. Robot B was functionally responsive to the magnetic actuation system and this success motivated further refinement of the tip fabrication, wire core choices, and magnetization processes. The field strength measurements will be discussed in detail in section 4.2.1 of the report and all data be found in the DHF.

Robot C: Flexibility-Driven Variant

Robot C retained the 4 mm diameter but had a thinner nitinol wire core at 0.2 mm in diameter to attempt to improve compliance and allow for greater curvature during actuation. This design choice was based on the need for stronger reactions to the magnetic actuation system in order to have smooth traversal through anatomically tortuous sinus pathways. However, under

actuation testing, the reduced core diameter led to structural instability. Specifically, Robot C exhibited buckling under axial loading during extension, resulting in failed mechanical transmission between the linear actuator and the robot tip.



Figure 44. Resulting from its thinner nitinol core of 0.2mm, Robot C was very soft and flexible, providing it with the ability to interact with the generated magnetic fields to a greater degree than robots with the thicker nitinol wire core. Despite the advantages of flexibility and dexterity, the thinner wire resulted in failed linear translation.

Magnetization testing revealed a further reduction in field strength, which can be attributed to the use of an earlier magnetization method prior to acquiring access to the impulse magnetizer. Despite its reduced magnetic field strength—23.5 mT (north) and 22.57 mT (south)—Robot C displayed the most pronounced angular deflection due to its minimal resistance to magnetic torque. However, without a means of reliable extension and retraction, the trade-off between flexibility and structural rigidity rendered it non-functional within the integrated system.

Robot D: Miniaturization Test Case

Robot D explored the feasibility of downscaling the soft continuum robot to a 2 mm outer diameter with a 0.2 mm nitinol core. While this dimension is more aligned with clinical demands for minimally invasive navigation, manufacturing limitations posed significant challenges. The smaller diameter inhibited the ability to produce well-defined robot bodies and could not support helical protrusions, which were a design requirement for rotational motion and friction mitigation during contact with surrounding tissue.



Figure 45. Robot D, 2mm diameter and 0.2mm wire core, the magnetized tip has a very small surface area for interaction and the body of the robot has many flaws due to the difficult demoulding process for such small robots. This iteration was essential in highlighting the limitations of the fabrication process.

Despite improved south pole field strength (27.33 mT), the tip lacked consistent north pole magnetization (24.37 mT), likely due to asymmetry in the embedded particle distribution and incomplete alignment during impulse magnetization. In addition, the shortened length of the body (9.7 mm) limited structural engagement with the actuation system, and increased fabrication defects were noted, as seen in Figure 45. Robot D highlighted the limitations of extreme miniaturization within the constraints of current fabrication methods, particularly in maintaining

surface fidelity and consistent magnetic loading. It was excluded from further development due to its insufficient structural and functional performance.

4.1.1.2 Final Prototype

Based on insights gained from previous iterations, Robot A was developed to meet all critical performance metrics defined in the soft-continuum robot design inputs. This iteration demonstrated the most effective balance of magnetization strength, mechanical compliance, and actuation compatibility.



Figure 46. Robot A, 4mm diameter and a 0.5mm nitinol wire core. The thicker 1.2mm actuator wire can also be seen at the tail end of the robot. This robot was developed using the insights gained by previous iterations and meets all design requirements outlined in section 1 of the report.

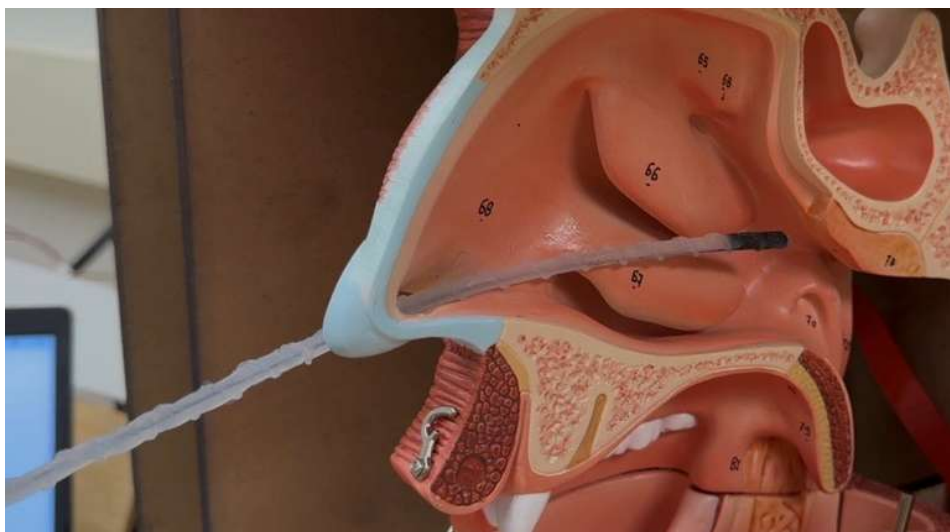


Figure 47. Robot A, the final iteration, passing through the nasal opening into the sinus area within a large-sized anatomical phantom model. The magnetized tip and helical protrusions are clearly visible on Robot A.

Robot A features a 4 mm diameter and 19.5 mm long body moulded from EcoFlex 00-30 silicone resin, selected for its mechanical softness and biocompatibility. A 0.5 mm nitinol wire

core helps to maintain rigidity during extension and retraction. This wire core leads to a 1.2mm actuation wire that is acted on by the linear actuation system. The tip was fabricated using a 1:1.5 silicone-to-NdFeB particle ratio, magnetized using an ACS impulse magnetizer to ensure longitudinal alignment and enhanced field strength. To ensure precise geometric dimensions and reproducibility, all moulds were fabricated using high-resolution CAD software and the dimensional accuracy of an Ultimaker 3D printer. The assembled robot was carefully demoulded to reduce the risk of air bubbles bursting and deformation. Visual inspection and digital caliper measurements confirmed adherence to the dimensional constraints.

Robot A was fully integrated with both the magnetic and linear actuation systems, serving as the primary robot for system-level verification. The nitinol wire core provided the necessary structural rigidity for linear extension and retraction, while the magnetized tip enabled real-time directional control through coil-based actuation. The helical protrusions were consistent and continuous, contributing to smooth movement in benchtop phantom pathway models as seen in Figure 47 and Figure 48.

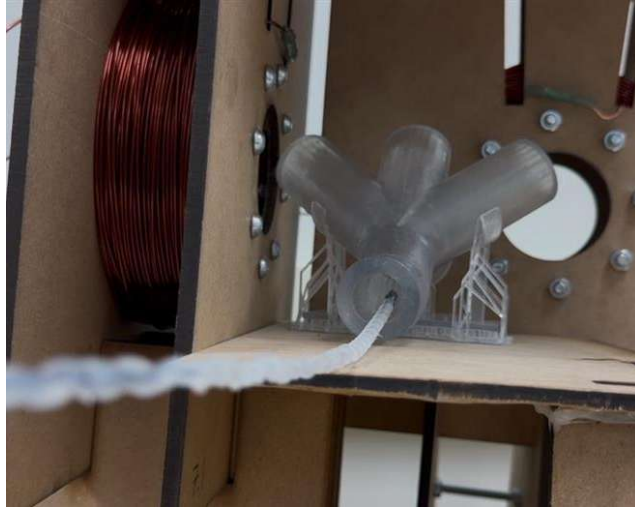


Figure 48. Robot A, the final iteration, traverses through a clear modeled phantom pathway.

This iteration marked the first instance of a robot meeting all critical design inputs simultaneously. As such, Robot A became the foundation for all final system testing, including deflection measurements, integration trials, and GUI-controlled navigation scenarios.

4.1.1.3 Final Prototype Validation

Robot A underwent a comprehensive validation process to ensure its mechanical, magnetic, and dimensional properties met the soft-continuum robot design requirements outlined in Chapter 1. Validation activities focused on verifying geometric tolerances, magnetization strength, mass limitations, mechanical responsiveness, and actuation compatibility. All experimental protocols and measurement procedures were documented and can be found in the project's Design History File (DHF).

The robot's final dimensions were confirmed using digital calipers, with the tip diameter measured at 3.9 mm and the total length at 19.5 mm, thereby satisfying the design constraints of ≤ 5 mm and ≤ 20 mm, respectively. The embedded nitinol wire was verified to be 0.5 mm in diameter and 245 mm in length, exceeding the minimum requirement of 10 cm for actuation integration. Mass verification was performed using a CGoldenwall high-precision lab scale, which recorded the robot tip weight as 0.86 g. This result is well within the design requirement of ≤ 1 g,

minimizing the risk of excessive force or strain during actuation and reducing inertial resistance during navigation.

The magnetic field strength of the robot tip was validated using a CMOS-MagView sensor, which provided optical and numerical feedback. The test setup for this validation process can be seen in Figure 6. The north pole field strength averaged 32.3 mT, while the south pole averaged 25.93 mT—both exceeding the 20 mT minimum defined in the design inputs. The field direction was confirmed to be longitudinal, aligned with the axis of the nitinol wire, thereby enabling precise directional control when actuated by external electromagnetic coils.

Flexibility and structural integrity were validated through benchtop insertion trials using a sinusoidal phantom model. Robot A achieved deflection angles exceeding 15°, meeting the requirement for directional maneuverability in complex anatomical pathways. The embedded nitinol wire resisted buckling under retraction, and the robot was capable of smooth, repeatable extension and retraction motions when driven by the linear actuator system. This was observed in both free movement and within semi-constrained tube structures mimicking nasal cavity conditions. The uniform helical protrusions played a critical role in reducing friction and enhancing rotational behavior. Visual inspection confirmed consistency in helix geometry along the robot body. No significant deformation or shearing was observed over repeated cycles of actuation.

The materials selected for Robot A, including EcoFlex 00-30 and medical-grade nitinol, align with ISO 10993-1 guidelines for biocompatibility. The NdFeB particles were fully embedded within the silicone matrix, avoiding direct exposure to tissue. Although formal cytotoxicity testing was beyond the project's scope, future validation efforts will include ISO-certified testing to confirm compliance with medical-grade standards.

With all performance metrics confirmed through testing, Robot A was deemed the final validated iteration for system-level integration.

4.1.2 Magnetic Actuation System

4.1.2.1 Iterative Process

Throughout the design process, multiple iterations were developed and validated to optimize the magnetic actuation system's performance, safety, and controllability. While minor adjustments were made continuously, two significant design iterations, each with distinct hardware and control logic changes, were validated then subsequently rigorously tested before converging on the final prototype. Below, the subcomponents and validation methods for each iteration are documented.

Magnetic Actuation System Iteration #1

This initial iteration consisted of the use of a handmade coil, as seen in Figure 49, connected directly to a power supply unit (PSU), as seen in Figure 50. The coil was controlled with no active circuitry; it was powered and turned off by directly switching the PSU on and off. While this iteration did not involve any circuitry, it was still important since it was the first handmade coil that was created, and as such, it still required meaningful validation before progressing. Up until this point, only store-bought coils had been used and these coils required significantly less power to generate a field.

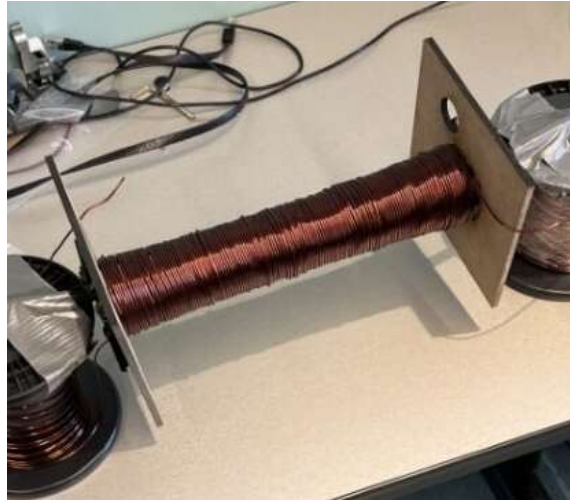


Figure 49. Hand-Wound Coil (Iteration #1) – A custom built, hand-wound solenoid coil with a radius of 2.5 cm, length of 25 cm, and 145 turns of AWG 14 enameled copper wire.



Figure 50. The power supply unit features reverse polarity protection, a built-in breaker switch and is rated for up to 60V and 30A.

Magnetic Actuation System Iteration #1 Validation

The validation process first confirmed the PSU's ability to reliably deliver controlled current to the coil system. Incremental testing at 5A, 10A, 15A, 20A, 25A, and 30A demonstrated stable voltage regulation (12-35V DC range) with corresponding power dissipation of 60-1050W, as confirmed by the PSU's integrated multimeter (pictured in Figure 3). This established the power system's capability to maintain the required operational envelope for magnetic field generation.

With power delivery validated, subsequent validation testing focused on the fundamental question of the coil's field generation capability. Measurements using a TLV493D-A1B6 magnetic sensor confirmed the hand-wound coil produced a maximum field strength of 45.2 mT, correlating well with MagPy simulations and MATLAB calculations documented in the design history file. This successful validation of basic electromagnetic functionality addressed the primary

stakeholder concern regarding the custom coil's ability to generate clinically relevant fields, while revealing opportunities for improvement in control dynamics and safety for subsequent iterations.

Magnetic Actuation System Iteration #1 Takeaways

The validation successfully confirmed that the electromagnetic performance was viable but revealed critical clinical needs that were not addressed in this iteration. The direct PSU control method proved fundamentally unsuitable for surgical applications due to two key limitations: the complete lack of a dynamic control interface requiring manual current adjustment and the inability to coordinate multiple coils simultaneously.

Magnetic Actuation System Iteration #2

These operational shortcomings identified in Iteration #1 necessitated significant architectural changes for Iteration #2, which would introduce microcontroller-based control through an ESP32 to enable real-time multi-coil coordination while preserving the ability to generate a strong magnetic field. The transition to digital control represented an essential evolution from proof-of-concept validation to clinically operable system design. A new coil was wound with a larger radius and shorter length (see Figure 51), to verify its ability to generate a field. And the ESP32 was wired to a simple MOSFET switch circuit (Figure 52), such that a high GPIO output (3.3V signal) will allow the power source, which in this iteration is a 9V battery, to supply the coil with current, turning the coil on. A low GPIO output (0V signal) will turn the coil off.

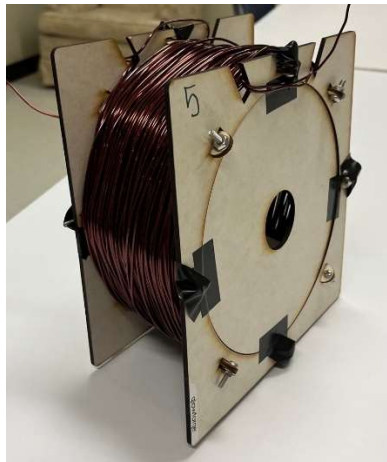


Figure 51. Hand-Wound Coil (Iteration #2) – A custom built, hand-wound solenoid coil with a radius of 10 cm, length of 10 cm, and 87 turns of AWG 14 enameled copper wire.

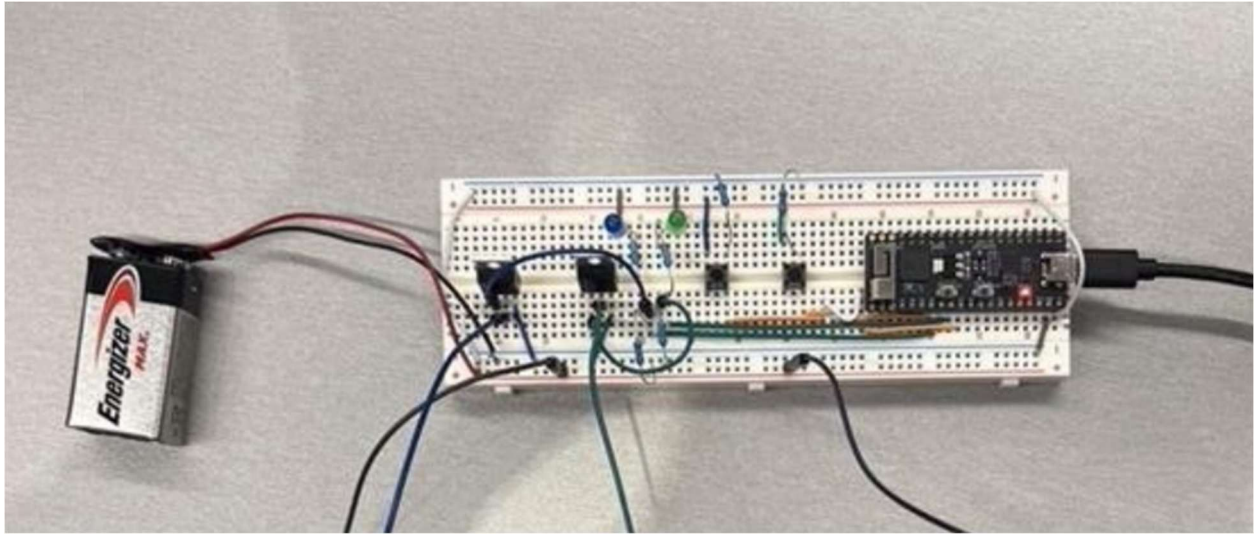


Figure 52. An ESP32 on a breadboard with 2 MOSFET switch circuits; when the left button is pressed, the GPIO output will provide a PWM (Pulse Width Modulation) signal to the left MOSFET, which will connect the 9V power source to the coil, providing it with current. The same happens with the right button and right MOSFET. The MOSFET is rated up to 9V to protect the 9V battery from interacting with the ESP.

Magnetic Actuation System Iteration #2 Validation

The validation process for Iteration #2 focused on demonstrating digital control capabilities while maintaining field generation. The implementation used an ESP32 microcontroller with dual MOSFET switch circuits to enable independent coil activation through simple digital high/low signals (3.3V/0V). Testing confirmed successful digital control with immediate coil activation upon GPIO state changes, validating the basic control architecture. This testing also validated that the new coil parameters can still successfully generate a field.

Magnetic Actuation System Iteration #2 Takeaways

While the digital control set up successfully demonstrated basic functionality, the lack of proper isolation between the ESP32 and power systems risked microcontroller damage during operation with a larger power source. Most critically, the double-coil configuration could not provide the necessary 3D field vectoring required for surgical navigation. These findings directly informed the final iteration's specifications, mandating industrial motor drivers for safe high-voltage operation, a return to 30V power, and expansion to a triaxial coil configuration with proper protection circuitry.

4.1.2.2 Final Prototype

The final prototype of the magnetic actuation system comprises three coils (Figure 53), each driven by motor driver boards (Figure 54), which are independently powered by 30V/20A from a DC power supply (Figure 50). An ESP32 microcontroller generates pulse width modulated (PWM) signals to regulate the current going into the coil as well as general high/low digital signals to control the direction. These signals are input into dedicated motor driver control pins, ensuring isolation between low-voltage logic of the microcontroller and high-power current going into the coils. The ESP32 can only generate an output PWM and direction signal of 3.3V, but the motor

driver requires an input of 5V; therefore, this prototype iteration also has an amplification circuit to amplify the signal going into the motor drivers (Figure 55) [2]. An overview of each subcomponent for the magnetic actuation system can be seen below, with its specific validation methods documented.

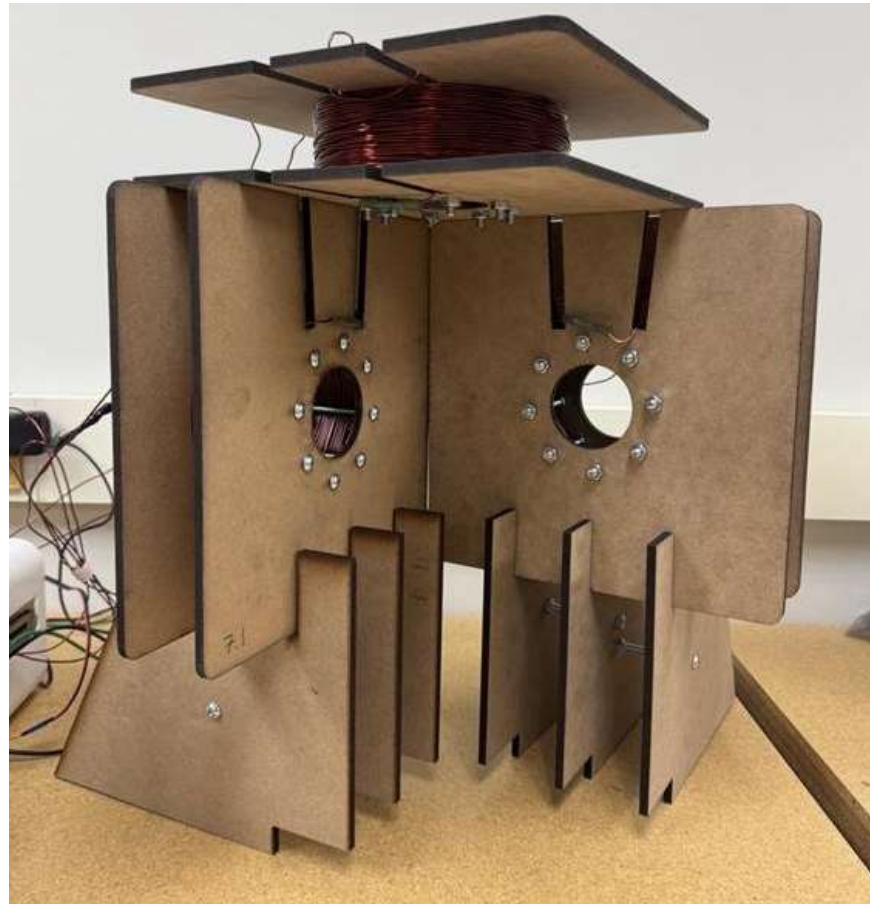


Figure 53. Three custom built, hand-wound solenoid coils configured to be along the X, Y and Z planes, each with the same 5 cm radius, 5 cm length, and 450 turns using 14 AWG enameled copper wire. The coils generate a maximum field strength of 120mT at the center when powered by 30V/20A.

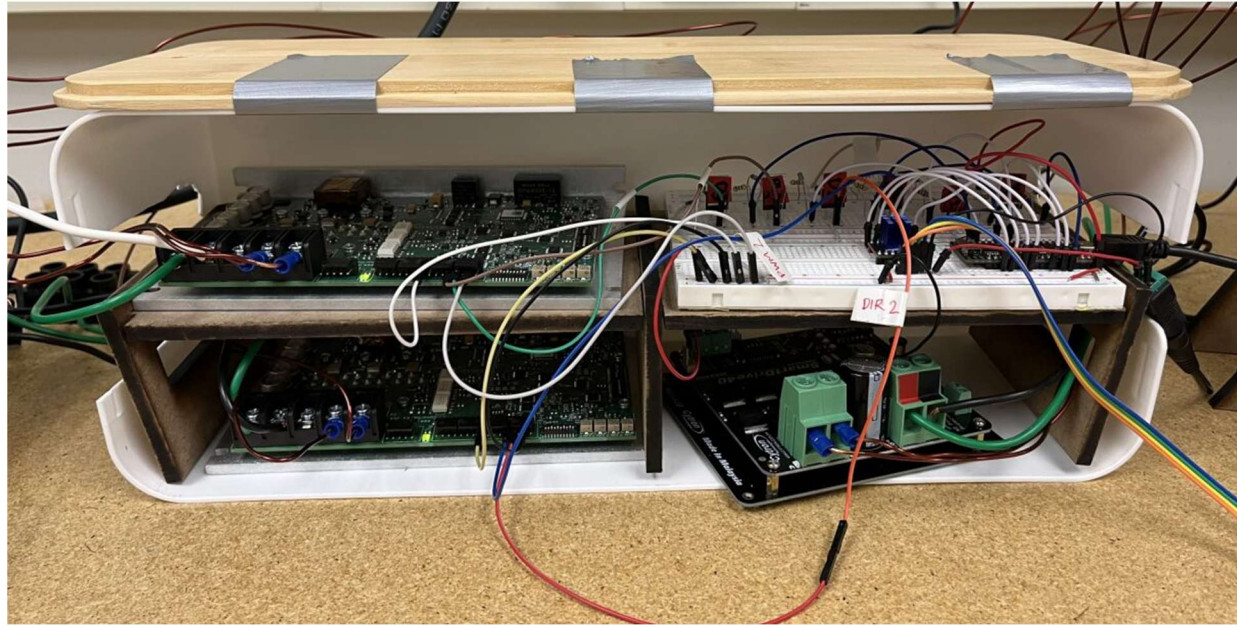


Figure 54. Final design motor driver boards (x3) inside a box to conceal the wiring. The boards stored in the top left and bottom left are both AMC AB50A200I Motor Drivers. The bottom right stores a Cytron MDS40B Motor Driver, and the top right stores the ESP32 board with the amplification circuit.

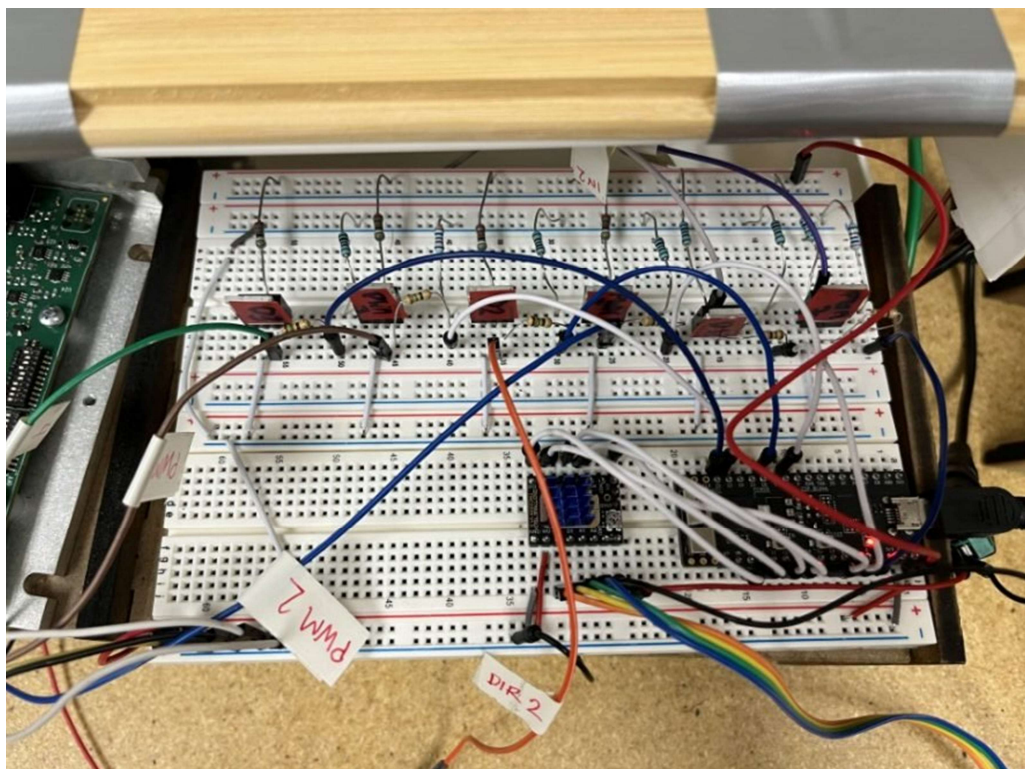


Figure 55. A photo of the custom-designed level-shifting circuit converting the ESP32's 3.3V PWM/direction signals to 5V logic required by motor drivers. The breadboard on top contains the MOSFET amplification circuit, and the breadboard below contains the ESP32, and the motor driver connected to the linear actuator. Note that the linear actuation system is unrelated to the magnetic actuation system and will be elaborated in subsequent sections.

4.1.2.3 Coils

The final coil design implemented, seen in Figure 53, consists of three identically fabricated coils. These three coils were made with a sturdy 6mm MDF board that is held together with screws. They have a 5 cm radius, are 5 cm in length, and have 450 turns using 14 AWG enameled copper wire. A stand was made to hold the coils such that they can consistently be placed in the X, Y, and Z axes. When the setup needs to be moved, the base ensures the reproducibility of the setup, guaranteeing that the coils can be placed the same way with respect to one another, allowing the field interactions between the coils to remain reproducible.

4.1.2.4 Motor Drivers

The coils are connected to individual motor driver boards. The boards connect the power supply to the coils and have input pins to control the coil strength and direction. Two different motor drivers were used in this final prototype: two AMC AB50A200I boards and one Cytron MDS40B board. These two boards function identically for the scope of this project, as they both take an input 5V PWM signal to drive the field of the coil and a 5V/0V DC signal to control the directionality of the coil. They are also both rated for over 30V/20amps, allowing them to function identically in this project,. The motivation for having two different kinds of motor drivers came down to budget and resources available to the group. The HeART Lab provided access to the three boards used in this final design, allowing the groups budget to be spent on other aspects of the project.

The two input pins of note are PWM and direction (referred to as DIR). The PWM (connected to pin 5 on the AMC AB50A200I and pin 1 on the Cytron MDS40B) determines the magnitude of the voltage applied to the coil. The duty cycle of the PWM signal (ranging from 0% to 100%) directly controls the intensity of the magnetic field generated by the coil. Thus, increasing the duty cycle increases the strength of the field generated by the coils. The DIR pin (corresponding to pin 4 on the AB50A200I board and pin 2 on the Cytron MDS40B) sets the polarity of the current flowing through the coil, thereby reversing the direction of the generated magnetic field. These two pins, controlled together, allow for fine-tuned bidirectional magnetic field control using simple digital signals.

The use of separate drivers for each coil axis (X, Y, and Z) ensures that the fields can be independently controlled in real time, allowing for complex vector field generation. Moreover, the motor drivers are fully isolated from the control logic, meaning that the high voltage and current used to energize the coils (maximized up to 30V and 20) is safely separated from the low-voltage logic signals provided by the microcontroller. This isolation protects the sensitive ESP32 microcontroller from potential back electromagnetic field or other high-power anomalies.

Each coil axis is associated with a dedicated pair of output signals from the ESP32: one for modulating the strength of the field (PWM) and another for determining its polarity (DIR), therefore, six independent signals were needed to control the three coils. However, since the ESP32 outputs digital signals at a logic level of 3.3V, a level mismatch arises, since the motor driver boards (AMC AB50A200I and Cytron MDS40B) require 5V logic for proper signal recognition,.

To resolve this, a custom level-shifting and amplification circuit was developed using N-channel MOSFETs. This circuit is shown in Figure 55. The design uses the MOSFETs as open-drain switches that translate the 3.3V signal from the ESP32 up to a clean 5V output, sourced from an external regulated 5V rail shared by the motor drivers. Each signal (PWM and DIR) passes through its respective MOSFET-based shifter, ensuring reliable edge detection and voltage compatibility with the motor driver inputs.

The MOSFET amplification circuit was implemented on a small breadboard stacked above the ESP32 module for compact prototyping. Care was taken to use fast-switching logic-level MOSFETs to maintain signal integrity at the PWM frequencies used (typically 10–20 kHz). Pull-up resistors on the drain side ensured that when the MOSFET is off (input from ESP32 is low), the output line is pulled high to 5V, and when the MOSFET is on (input high enough to saturate the gate), the line is pulled low producing a proper digital signal swing between 0V and 5V.

4.1.2.5 Final Prototype Validation

The final prototype was validated through a series of structured, functional tests targeting the primary performance criteria established by earlier iterations: safe high-power operation, independent real-time control of all three coils, and reliable digital signal transmission from the ESP32 microcontroller.

First, the magnetic coils were individually tested under full load using 30V power supplies and industrial-grade motor drivers (two AMC AB50A200I and one Cytron MDS40B). Each coil demonstrated stable operation under continuous current up to 15A without triggering fault conditions, validating the thermal and electrical robustness of both the coils and driver systems. Field strength measurements, again using the TLV493D-A1B6 sensor, confirmed reproducible and directional field generation across all three axes, satisfying the core requirement for 3D vector field synthesis.

Next, the focus was on validating the control subsystem. PWM signals generated by the ESP32 were monitored using an oscilloscope, confirming proper duty-cycle modulation and direction toggling in response to software commands (Figure 56). The custom-designed MOSFET-based amplification circuit successfully level-shifted these 3.3V outputs to clean 5V signals (



Figure 57), fully compatible with the motor driver input requirements. Signal integrity was preserved at 10 kHz (the frequency compatible with both motor driver boards), with no observed signal degradation or erratic behavior.

Together, the system validated full independent actuation of each coil in real time, with reliable response to ESP32-generated control signals and isolation from the high-power domain. This successful validation confirms that the final prototype meets all critical user needs: reproducible 3D magnetic actuation, digital controllability, independent coil controllability, and electrical isolation of high-voltage and low-voltage applications for system protection.

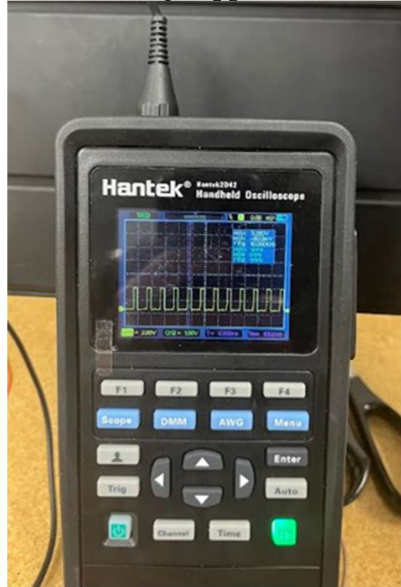


Figure 56. A PWM wave measured on a Hantek oscilloscope probed from the ESP32 output pin, before the amplification circuit. The oscilloscope is showing a PWM wave going from 0V to 3.3V with a Duty cycle at around 5%.



Figure 57. A separate PWM wave measured on a Hantek oscilloscope, this time probed from after the amplification circuit. The oscilloscope is showing a PWM wave going from 0V to 4.72V, with a Duty cycle at around 95%. This showcases that the amplification circuit can get a 3.3V signal into a 5V signal.

4.1.2.6 Magnetic Actuation System Risk Management

The magnetic actuation system is comprised of various high-current components which require thorough risk mitigation. Specific details pertaining to the risk management strategies can be found in the risk portion of section 4.2.2.3.

4.1.3 Linear Actuation System

4.1.3.1 Iterative Process

The final design of the linear actuation system works in tandem with the magnetized soft continuum robot in achieving precise directional linear control. The design process focused on improving the system's accuracy, smoothness, and robot size compatibility.

Linear Actuation System Iteration #1

The first iteration was a proof-of-concept prototype to determine the validity of the linear actuator. The first iteration was designed based on a 3D printer's extruder mechanism, which feeds the robot's actuation wire through two gears, controlled by a stepper motor. The L298 motor driver was used to drive the stepper motor.

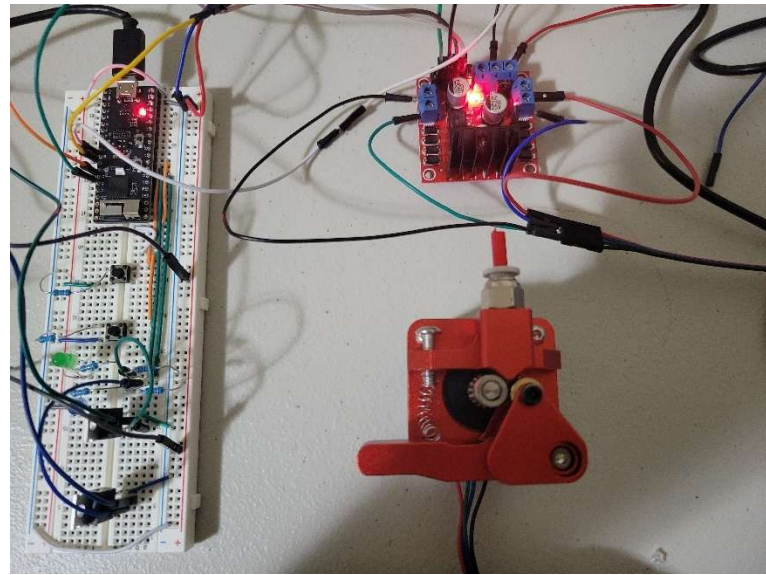


Figure 58. First iteration of the linear actuator and L298 motor driver.

This iteration revealed new design requirements and inputs needed for the linear actuator. First, The L298 driver is lacking in its current control and microstepping capabilities, which resulted in mechanical vibration and noise. The mechanical vibration transferred onto the robot, affecting its accuracy and smoothness. The actuator lacked size compatibility, as it was designed to work with 2.75mm wires. Although it would be able to extend or retract thinner sizes, the accuracy would be limited, due to excessive slipping.

Linear Actuation System Iteration #2

The second iteration aimed to improve the linear actuator's smoothness and accuracy by implementing a new motor driver and designing a new system.



Figure 59. Second iteration of the linear actuator. Parts were printed from grey resin and red PLA.

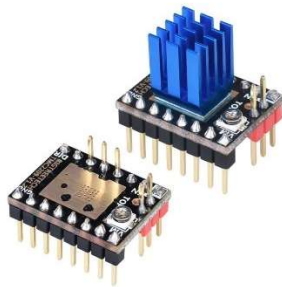


Figure 60. New TMC 2209 motor driver.

The L298 motor driver was replaced with a TMC2209 motor driver, which introduced several key improvements to address the limitations identified in the previous design. Mainly, the TMC2209 allowed microstepping up to 256 steps per full step, in which 16 microsteps per steps was used in the actual circuit. This significantly enhanced the smoothness and accuracy of the actuation. It also included more advanced current control, which resulted in silent stepping, eliminating the noise of the L298 driver, as well as the mechanical vibrations. It also improved power efficiency, reducing the power needed from 12V to 9V, which helps the magnetic actuation system which, during this stage of the design process, was looking to require as much voltage as possible. Additionally, the new driver included built-in diagnostic and protection features, such as overtemperature and short-circuit detection, enhance system robustness and safety. Overall, this new driver was a significant upgrade to the system.

However, the same could not be said about the new design. During the modelling process using Autodesk Inventor Professional 2025, the design was focused on improving robot size compatibility and improving grip on the actuating wire, for improved actuation force. However, limitations were seen in the quality of the 3D printed parts. Excluding the stepper motor, the design consisted of 14 individual parts, with each rotating gear shaft having 3-4 parts each. Due to the inconsistencies of the 3D printer, the tolerances of the parts went upwards of 2mm. This meant that although the bottom part of the shaft was tightened and secured, the spinners that would actuate the robot wire would not be able to grip the wire with any substantial force to proper actuation. Therefore, although the TMC 2209 improved the functionalities of the stepper motor itself, its improvements could not be utilized properly with the 3D design.

4.1.3.2 Final Prototype

The final iteration took the best parts from the previous two iterations, while learning from its limitations. The TMC 2209 driver was kept, and the gear system from the first iteration was also used. The design also included a stepper mount and base, which offered better stability during linear actuation. The spring was also replaced by a screw, which allowed control over the tension of the gears, which would allow for a higher size compatibility. The moving parts were also reduced, with each part attached securely to either the stepper motor or the base, with no more than 2 parts per attachment that required tolerances. This resulted in a much more secure system, allowing a firm grip on the wire.

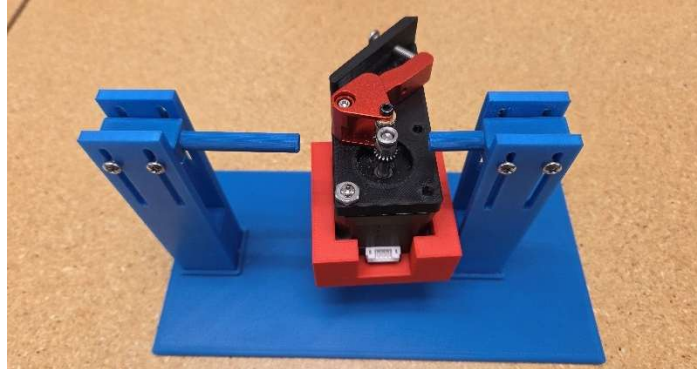


Figure 61. Side view of the final prototype

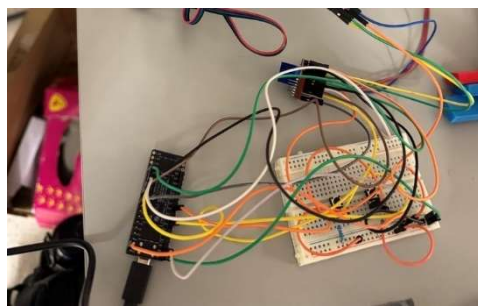


Figure 62. The circuit of the TMC 2209 motor driver connected to an ESP32 microcontroller. The final integration combined the TMC2209 into the circuit of the magnetic actuation system.

TMC 2209 Motor Driver

In the system, the TMC2209 stepper motor driver is connected to a microcontroller using a combination of digital I/O and UART communication pins. The main pins for controlling the stepper include: EN_PIN (enable), which is Boolean that states if the driver is allowed to send steps to the motor; DIR_PIN (direction), which is a Boolean that sets the direction of motor rotation; and STEP_PIN, which receives pulses from the motor to increment motor position. The enable pin allows for quick and permanent shut down of the driver, preventing stepper movement. Bidirectional UART communication is established using software-serial pins SW_TX (transmission) and SW_RX (receiver), which allows access to the driver's internal configuration registers. The RX and TX pins internalize the micro stepping current control to within the TMC 2209 itself, instead of needing manual instruction from the microcontroller, which results in a more efficient ESP32 code, enabling a precise and smoother system.

4.1.3.3 Testing Methods

A series of tests were conducted to determine the linear actuator's accuracy under various conditions. The testing of the reliability of the ESP32 was mentioned in section 4.1.2.2, under the final prototype of the magnetic actuation system. First, the motor was instructed to spin one full rotation, to determine the linear motion of one full rotation. As shown in Figure 19, a wire was placed onto the ruler, with an initial position at 10mm. The gear then rotated one full rotation, and the final position was measured. The answer was then compared to the theoretical calculated value.

The diameter of the gears was measured to be 7mm using a digital caliper. Therefore, the theoretical linear motion per rotation rounds up to 22mm (21.99mm), since the accuracy of measurement for these tests will be in millimeter range.

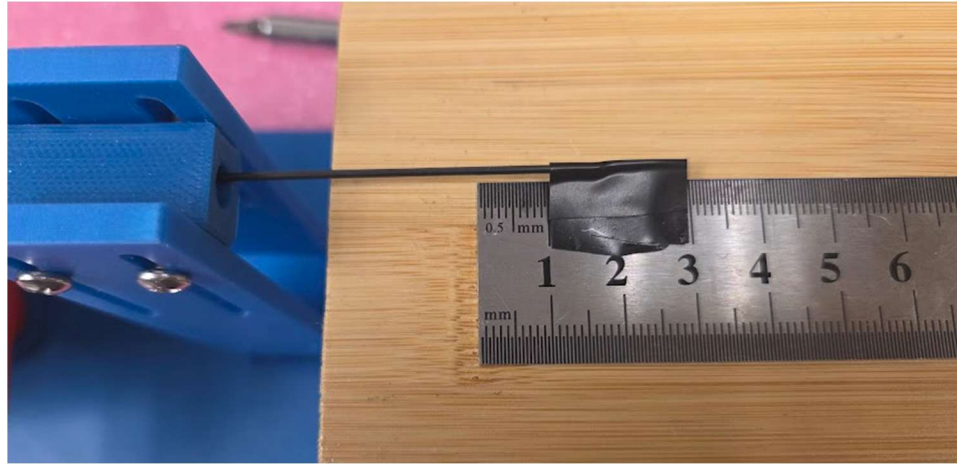


Figure 63. A tape was attached to a wire and placed at the 10mm mark of a ruler. The stepper motor is then instructed to rotate 360°, and the difference in initial and final position is measured.

The results of this test showed a linear motion of 22mm, which verifies the accuracy of the actuation. Repeatability, load and size compatibility testing and results will be shown in section 4.2.3.1 and 4.2.3.2.

4.1.4 Robot Navigation Interface and Simulations

Prior to hardware implementation, a Python-based simulation framework was developed to model the magnetic field distribution of the coils that were designed. These simulations allowed for visualization and quantification of the resultant magnetic field distribution at varying distances, configurations and orientations to understand the magnetic field superposition effects in the 3D visualization, especially within the libraries. The insights from this computation model helped develop hardware specifications and layout of the coil system in the final robot navigation interface. The implementation of this can be found in Appendix B: Software Implementation, subsection Code 3.

The graphical user interface (GUI) for robot navigation is developed to provide real-time, intuitive control of the integrated system, including the soft-continuum robot, magnetic actuation and linear actuation systems. The interface utilizes a 3D anatomical skull for spatial reference and visual feedback for ease of use.

The interface will be used for serial communication with the ESP32 microcontroller which in turn can control both of the magnetic actuation and linear actuation systems. The GUI will incorporate interactive elements in a 3D visualization using the PyVista library in Python which can send commands to the ESP32 microcontroller using Arduino software. There are various checkbox buttons available as well as small yellow interactive spheres on cyan arrows for intuitive control of the magnetized tip. Overall, this can drive the logic behind the various drivers to execute extension and retraction, variable magnetized tip orientations in the X, Y, and Z planes, or various fail-safe mechanisms. Furthermore, there are magnetic actuation and linear actuation status

updates in real-time for easy reference for the user. A full outline of the interface can be seen in Figure 64, which illustrates the surgical visualization, system layout, and user interaction mapping. As well, the Python framework and Arduino logic can be found in Appendix B: Software Implementation, subsection Code 4 and Code 5.

There are mitigation strategies embedded in this design, such as system-wide shutoff to avoid unintended activation, restriction of magnetic actuation during retraction, and use of color-coded visual feedback to reduce cognitive error. The interface assumes operator familiarity with basic joystick-style inputs as well as stable USB serial communication.

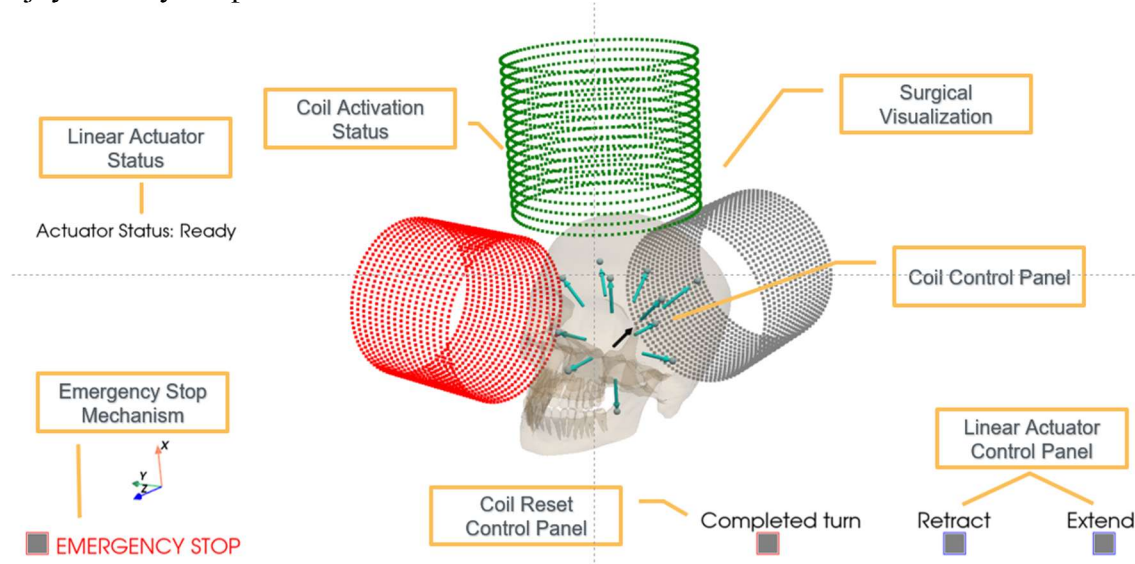


Figure 64. 3D visualization of robot navigation interface presenting control panels for the magnetic actuation system and linear actuation system as well as fail-safe mechanisms.

4.1.4.1 Framework

The navigation interface is architecturally designed for real-time control over the two actuation domains: magnetic actuation for directional control of the magnetized robot tip along with the linear displacement via the linear actuator. The software supports direction control of the magnetized robot tip, extension or retraction of the soft continuum robot, as well as multiple fail-safe mechanisms for clinical and hardware safety considerations. There are buttons across the interface which enable various actions, the coils are represented by the coil-like shapes within the surgical visualization, and the black arrow at the center of the visualization represents the robot tip. This visual metaphor is intended to simplify user interaction and support mitigation of human errors. However, the framework lacks positional feedback with the magnetized tip in the surgical environment which may limit the system's performance in complex anatomical environments. Figure X presents the workflow between the robot navigation interface and the physical hardware components with the subsequent steps outlined.

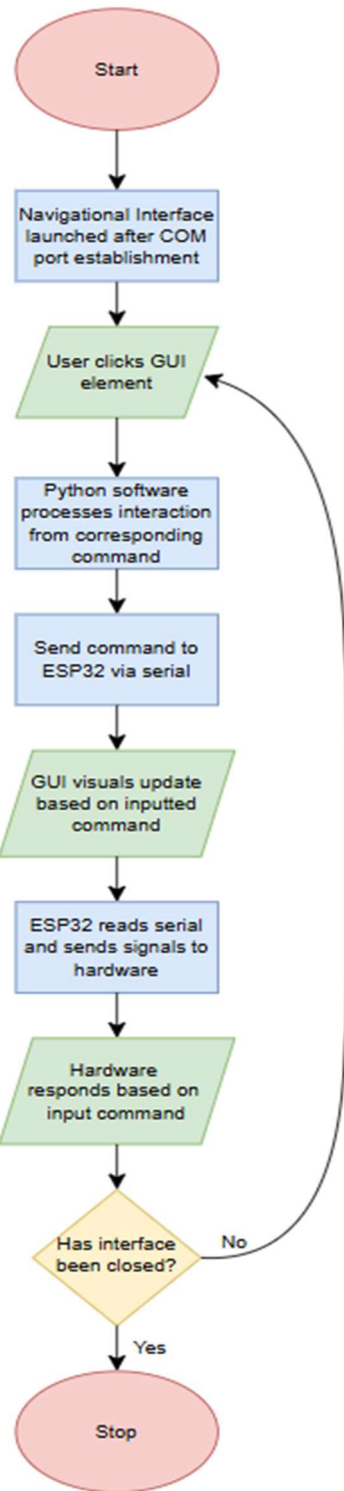


Figure 65. Workflow between the robot navigation interface and the physical hardware with subsequent components outlined.

4.1.4.2 Software Architecture Magnetic Actuation System

Magnetic actuation of the system is achieved by sending direction-specific commands from the GUI to the ESP32 microcontroller via Arduino logic. These commands correspond to predefined combinations of coil activation. The GUI utilizes PyVista to visually render each coil in 3D, with dynamic colour adjustments to symbolize whether the coil is executing an attraction force (green), a repulsion force (red), or is in idle mode (grey). For instance, if the interactive arrow results in the magnetized tip facing the positive X axis, by clicking on the interactive yellow sphere on the associated cyan arrow, this will turn the X-axis coil on to green with its current vector pointing to the center. This coil activation causes the magnetized tip to point in the X positive axis direction. With real-time updates of the magnetized tip to follow the same direction of the interacted arrows, users are able to interpret the resulting magnetic field direction without needing to individually control each coil with directionality in mind, thereby offering a more intuitive approach. This simplification of user input supports intentional, error-minimized movements. Within the software, each magnetized tip direction maps to an encoded message sent via serial communication to control the MOSFET logic that regulates the current that travels through each coil. This control assumes the robot tip moves predictably in response to the directional commands, without accounting for differences caused by anatomical environment variance.

Linear Actuation System

The GUI integrates a linear actuator control module that toggles the stepper motor which causes extension or retraction of the soft continuum robot. Using checkbox widgets labeled “Extend” or “Retract”, the software sends encoded messages to the ESP32 which drives the stepper motor controller. When clicked once, the stepper motor will continually execute the corresponding function until the checkbox is clicked again to turn it off. As these actions are being executed, the status of the stepper motor is presented on the linear actuator status panel on the left side of the interface. The status initially states “Ready” for when the interface is first brought up to let the user know that the linear actuator is ready to be used. If it is in extension or retraction, the status reads “Extending” or “Retracting”. When the linear actuator is not in use, the status reads “Idle” to notify the user it is halted. This ensures there is reduced uncertainty during usage and a clear confirmation of system behaviour. One limitation of the interface is the lack of positional feedback or mechanical boundaries to confirm the physical extension limits of the magnetized tip in the anatomical environment.

Fail-Safe Mechanisms

Multiple fail-safe mechanisms are implemented as safety precautions to prioritize patient safety. Upon opening the interface, there is a shut-off signal sent to the full system which prompts the ESP32 microcontroller to turn off all the coil and motor outputs. Visually, the black arrow at the center is reset to mimic the current direction of the robot tip in real life, the linear actuator status states “Ready” for usage and all the coils are set to grey to depict inactivation.

Another mechanism is the “EMERGENCY STOP” mechanism, which disables the magnetic and linear actuation systems. This is built in such that if there are unexpected movements or an issue arises, the system can halt all operations. Visually, this displays a message in red stating “EMERGENCY STOPPED!” on the top left side of the interface with user interaction temporarily locked for about 5 seconds. During this time, the coils turn grey to represent coil inactivation.

An additional fail-safe mechanism occurs when the robot is in retraction. With the understanding that magnetic actuation, the retraction mechanism automatically disabled all coils to be turned off and changes the colour to be grey to avoid any unnecessary motions. By preventing simultaneous magnetic actuation, this mitigates risk of unintended compounded actuation. Furthermore, the actuator status text provides live feedback which enhances clarity and user

confidence during usage. These aforementioned mechanisms are designed to prevent potential hazards from unintentional or improper operations. However, they rely on consistent serial communication with the ESP32. A disruption can pose potential risk from delayed command execution. The system assumes the operator will verify hardware connectivity and calibration prior to use.

4.1.4.3 Hardware Integration

The software interfaces with the physical system using a USB serial connection to an ESP32 microcontroller. The system assumes uninterrupted power and communication stability during usage. As the interface is launched, it auto-detects the appropriate COM port that is connected to the ESP32 microcontroller. Without this established connection, the interface does not interact with the microcontroller.

Once the connection is established, user interaction with the interface prompts the Python software to transmit an associated command string to the Arduino logic that is programmed on the ESP32. For instance, if the robot is set to extend, when clicked on the interface, the python software sends a command over to the Arduino software which is converted into the associated digital signal to the stepper motor driver to execute that action, along with real-time visual updates. The same applies for all of the various interactions that can occur on the interface including the magnetic actuation system. This coupling of the user interface with the firmware ensures there is accurate synchronization between the user input, visual feedback, and system response.

4.1.4.4 Building, Testing, Verifying

The robot navigation interface was designed to integrate both the magnetic and linear actuation system to achieve precise and controlled movement. This section focuses on the creation, validation, and fine-tuning of the subsystems. The following discusses the procedures taken to build, test, and verify the navigation capabilities of the full system.

Building Navigation Interface

The development of the navigation interface was executed through an iterative process which began with a simplified 2D model to progressively build the system's control logic and integration strategies. The evolution of the interface can be seen in Figure 66. The early iterations were intentionally constrained to a 2D plane to facilitate a clearer understanding of the fundamental dynamics between the electromagnetic field vectors and the robot's directional behavior as seen in Figure X. This allowed for direct testing between the electromagnetic field responses using various coil activation configurations which provides the foundation for verifying magnetic field generation, directional consistency and control resolution before applying into a full 3D domain.

Crucially, these early interface versions were not only applied for visual and functional prototyping, but also to develop and debug the Arduino control logic. The phase enabled the identification and mapping of all necessary considerations to achieve real-time control in aspects such as GPIO pin configuration and state management. The iterative testing allowed the team to validate concerns such as digital control timing and system response latency. As well it evolved the fundamental aspects of the interface to include anatomical reference, safety mechanisms, status indicators for more of an intuitive layout for the user which can be seen in Figure 64.

With the foundational logic and structural mapping established from previous iterations, the interface had evolved into a 3D spatial model which reflects the layout of the physical coils in the experimental setup. The transition from 2D to 3D required implementation of three-axis superposition to visually update the resultant magnetic fields in real time to match the robot's

orientation to field directionality. Furthermore, the interface was redesigned to incorporate more interactive features to enhance usability and safety. These updates include real-time coital status indicators (i.e. green coil to represent its exertion of an attraction force, red for repulsion force, and grey for inactivation), button-triggered state activation, and dynamic feedback in the actuation of both systems. Together, the upgrades applied to the final interface iteration transformed the system from a basic control utility into a robust, intuitive interface that enables precise magnetic navigation with clear visual and operational cues for the user.

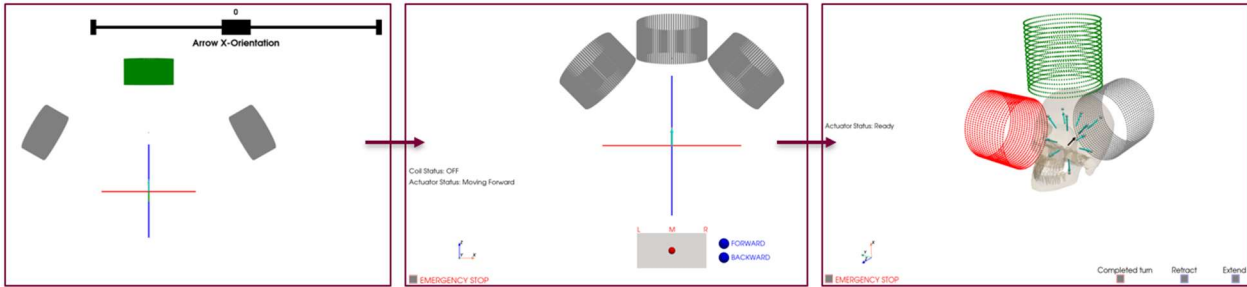


Figure 66. Left image shows preliminary build of interface showcasing basic functionality of the magnetic actuation system in 2D space. Middle image presents the enhancement of the interface from the previous iteration with integration of linear actuation system in 2D space. Right image presents the final iteration of the interface presenting the magnetic actuation system, linear actuation system, and the safety mechanisms implemented in 3D space.

Testing Procedure

The subsystems were independently and jointly tested to validate motion precision and system reliability. The initial testing of the navigation interface was performed using software-based validation with serial print statements. This was done to track the output of user interaction and induced control actions. The preliminary stage enabled verification of basic Arduino logic, monitor signal states, and identify potential areas of logic conflicts or timing issues in a controlled environment. As the control framework had evolved, the system migrated to a physical breadboard circuit with LEDs as a visual indicator of magnetic and linear actuation as seen in Figure 67. This allowed for confirmation that the microcontroller outputs are correctly triggering the desired circuit behavior to validate the implementation of button debouncing, state toggling, and independent subsystem control logic.

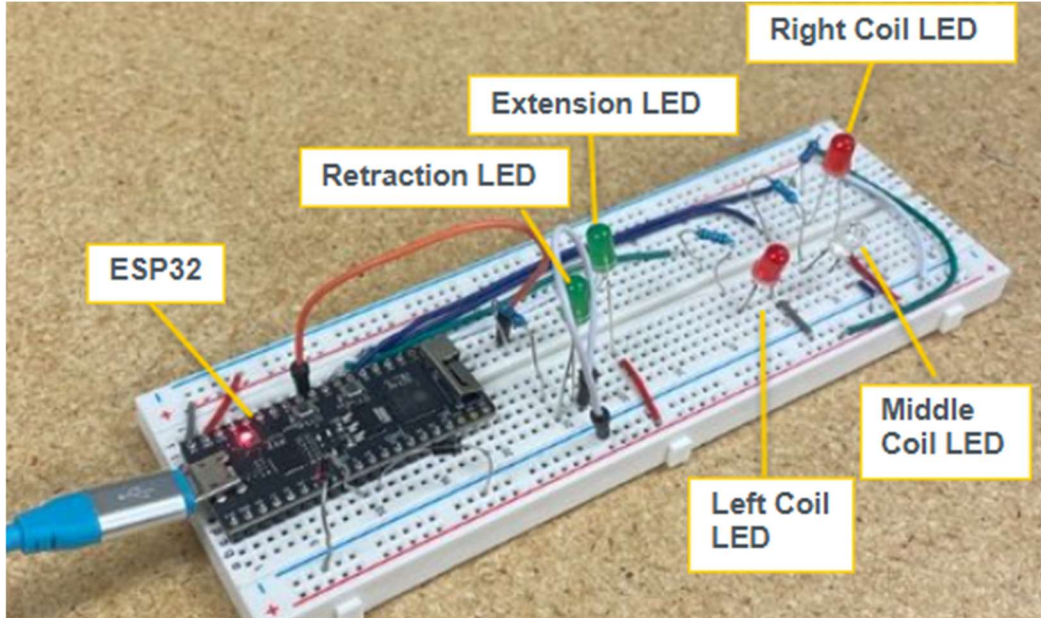


Figure 67. Breadboard circuit applied in early testing phase to observe the Arduino logic housed by the ESP32 microcontroller that was initiated by the interface with visual indicators of the magnetic and linear actuation systems usage.

As the full interface and its integration with the other subsystems, the testing progressed to using the interface with the physical setup. The objective of this phase is to assess the system's performance in real-world settings where the interface governs the activation of the magnetic and linear actuation systems. This phase focuses on the interactions observed between the electromagnetic fields and linear actuation to ensure the control logic in Arduino is effectively translated from software to the physical setup. The initial testing that occurred was applying electromagnetic field forces on the robot in the proposed surgical environment space without a phantom to observe sole interactions between the coils and robot seen in Figure 68. As well, the magnetic field strengths were measured using the TLVD493 -A106 magnetic sensor and compared against the theoretical and simulated values as mentioned previously. These results can be observed in the following chapter section. The observations confirm the functionality of the integrated system and validated the physical field outputs are within the anticipated ranges for reliability. Through this phase, the robot navigation interface was refined for accuracy, responsiveness, and coherence across the hardware and software implementations.

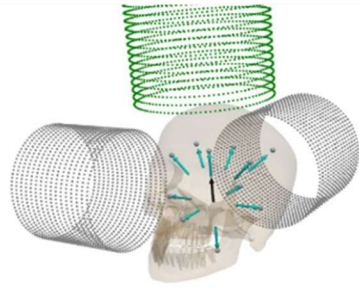


Figure 68. Left image presents the robot behaviour to the activation of the X plane coil causing an attraction force of the robot to the coil. Right image presents the interface interaction that caused the X plane coil activation (in green), resulting in the robot position seen on the left.

Verification of Navigation Interface

Integrated testing was performed using the interface to promote magnetic and linear actuation to observe real-time navigation within a phantom sinus model. The purpose of this phase was to assess how accurately and intuitively the interface could direct the robot's movement in a simulated surgical environment, specifically within the anatomical constraints of the sinus. Through observation, it was seen that the interface could control the electromagnetic coils and linear actuator in real time.

The robot responds precisely to the magnetic and linear actuation systems initiated by the interface as can be seen in Figure 69. The magnetized tip of the robot responds accurately to the coil activation sequences with observable and consistent deflections with both magnitude and direction. These movements aligned with the expected behavior which was predicted by the superposition principle of magnetic field vectors applied in the interface.

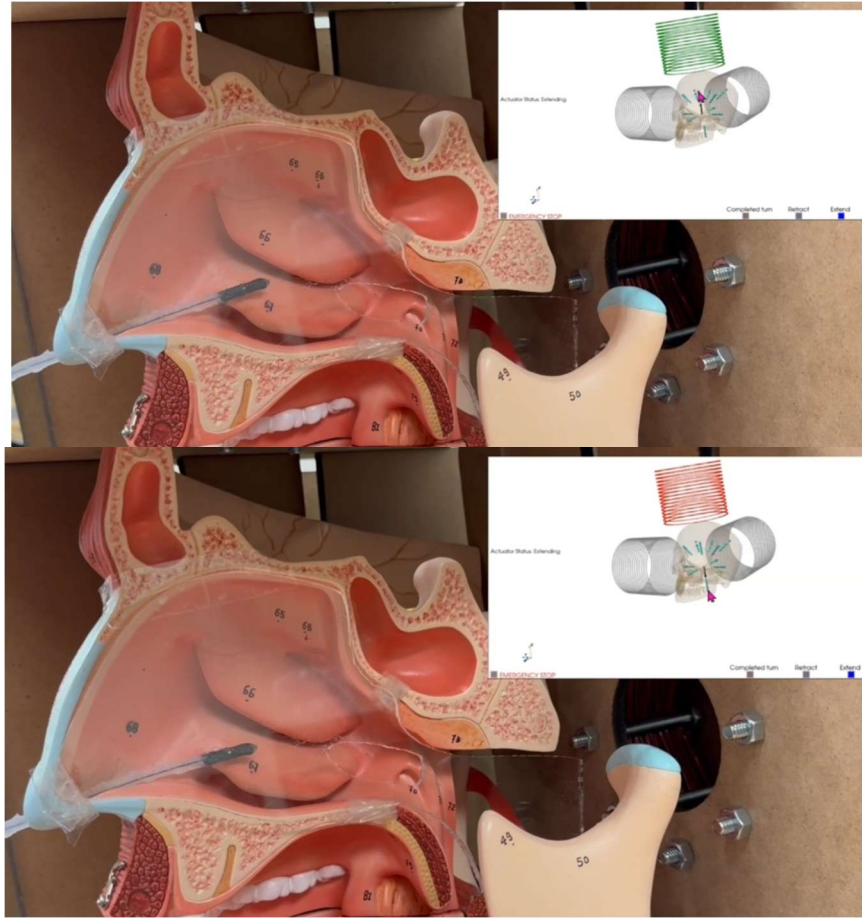


Figure 69. Top image shows the integrated system at use inside phantom model with upwards orientation via attraction force from the magnetic actuation system on the robot using the interface. Bottom image shows the integrated system at use inside phantom model with downwards orientation via repulsion force from the magnetic actuation system on the robot using the interface.

The precise alignment between the interface commands and robot responses applied by Arduino logic indicated that the system could perform reliably under integrated load conditions. Repeated trials were performed which demonstrated reproducibility in robot behavior across different movement sequences. To verify the generated magnetic field, the TLVD493-A106 magnetic sensor was used to measure the magnetic field at various points. These measurements confirm alignment with prior simulations that were conducted with the set coil parameters supporting the accuracy between both the computational model and physical implementation.

The integrated testing phase demonstrated the system's functionality as well as provided critical feedback for tuning interface parameters such as response latency, visual feedback, and control sensitivity, which enhance the surgical precision requirements and intuitiveness. Overall, the successful performance of the integrated system confirmed the viability of the proposed control mechanism for safe and responsive navigation within the surgical environment.

4.2 Results and Discussions

4.2.1 Soft Continuum Robot

4.2.1.1 Verification Results

The verification of the soft continuum robot iterations focused on confirming compliance with the dimensional, mechanical, and magnetic design inputs outlined in Chapter 1. For more detailed methods and visuals, refer to Chapter 3 and the accompanying DHF file [Robot Design Verification Plan and Data](#). The verification results in this report cover the testing of Robots A through D mentioned in section 4.1.1.1.

- Plan ID 4. A digital caliper is used to measure diameter and length of the robot tip. This verifies that the robot tip satisfies the geometric requirements of $4 \text{ mm} \pm 0.1 \text{ mm}$ and a length of $20 \text{ mm} \pm 0.2 \text{ mm}$. This test confirms dimensional consistency and ensures the robot fits within the anatomical constraints of the nasal cavity.



Figure 70. Experimental set up for Plan 4. Digital caliper can be seen with robots A to D.

- Plan ID 5. The nitinol wire core is measured for both diameter and length using a digital caliper. This plan verifies that the wire meets the specified gauge of $0.508 \text{ mm} \pm 0.01 \text{ mm}$ and a minimum length of 15 cm. Measurements are taken along the wire at several locations to confirm consistency and dimensional integrity.
- Plan ID 6. The magnetic field strength of the robot tip is measured using a CMOS-MagView magneto-optical sensor. This test evaluates whether the magnetized tip meets the minimum requirement of $10 \text{ mT} \pm 0.1 \text{ mT}$ at both the north and south poles. Measurements are taken at the tip and base of the robot to assess uniformity and polarity. Consistent field strength confirms the robot's ability to interact effectively with the external magnetic actuation system. Figure 6. Results from the CMOS-Magview, measuring the magnetic field strength of the robotic tip, producing an optical and graphical representation of the field generated at its north pole. The image on the top left shows the CMOS-Magview in use, the magnetized tip of the robot is placed such that the strength of the north pole can be read by the Magview sensor. The images on the top right and bottom are produced by the Magview system, the red indicates the north pole magnetic field, and the blue indicates the south pole magnetic field. Multiple measurements were taken for the north and south poles of the robot tip and the average of all the

measurements was considered in the outputs. An example of the test set up and results can be found in Figure 6 and in the DHF.



Figure 71. Test setup for Plan 6 with the CMOS-Magview sensor.

- Plan ID 7. The nitinol wire is tested for magnetization using the same magneto-optical sensor. Measurements are recorded along the length of the wire to ensure the field strength does not exceed $0 \text{ mT} \pm 0.1 \text{ mT}$. This test confirms that the wire remains non-magnetic, as required to prevent interference with the magnetic field used to actuate the tip. Ensuring the wire is magnetically inert helps maintain precise directional control.
- Plan ID 8. The mass of the robot tip is measured using a digital analytical balance. The acceptable range for the tip mass is $\leq 1 \text{ g} \pm 0.05 \text{ g}$. A tip mass within this threshold ensures the robot does not exceed the force capabilities of the magnetic and linear actuation systems and reduces the risk of excessive inertial loading on delicate sinus tissues.
- Plan ID 9. The robot's flexibility is evaluated by manually wrapping it around a cylindrical mandrel with a radius corresponding to 360° bending. This test assesses whether the robot can achieve full curvature without visible deformation, tearing, or permanent structural damage. The robot is expected to return to its original shape after multiple bending cycles. This confirms that the soft body design can navigate through complex sinus anatomy while maintaining mechanical resilience.
- Plan ID 10. The robot's magnetic deflection angle is assessed using a 2-inch permanent magnet. With the end of the tail fixed in place, the robot is exposed to the magnetic field, and the angular deflection of the tip is measured using a digital angle finder. The robot is expected to achieve a minimum deflection of 15° without loss of form or responsiveness. This test ensures sufficient interaction with magnetic fields for directional steering during procedures.
- Plan ID 11. The helical protrusions along the robot body are evaluated for uniformity. A digital caliper is used to measure the pitch between adjacent protrusions at several points along the length of the robot. The acceptable range for pitch is $10 \text{ mm} \pm 0.1 \text{ mm}$. Consistency in protrusion spacing supports smoother movement

through anatomical pathways and minimizes the risk of friction-induced resistance or motion instability.

The verification plans outlined in this section are applied across multiple design iterations of the soft continuum robot—specifically Robots B, C, D, and the final validated prototype, Robot A. Each robot undergoes systematic testing aligned with the verification framework described above and in Chapter 3, with results analyzed against the dimensional, mechanical, and magnetic requirements defined in Chapter 1. These tests are used not only to evaluate performance compliance, but also to guide iterative improvements throughout the development process.

Robot B

Table 7. Verification results for Robot B

Plan Id	Design Output	Inputs	Expected Values	Actual Values	Pass /Fail
4	2.1	Robot tip dimensions	Diameter \leq 4 mm \pm 0.1 mm Length \leq 20 mm \pm 0.2 mm	Diameter = 3.8mm Length = 20mm	Pass
5	2.2	Nitinol wire dimensions	Gauge = 0.508 mm \pm 0.01 mm Length \geq 15 cm	Gauge = 0.5mm Length = 242mm	Pass
6	2.3	Robot tip magnetization	Magnetization \geq 10 mT \pm 0.1 mT	Magnetic Field = 31.73mT north pole, 23.5mT south pole	Pass
7	2.4	Nitinol wire magnetization	Residual magnetization = 0 mT \pm 0.1 mT	Magnetic Field = 0.07mT (negligible)	Pass
8	2.7	Robot tip	Mass \leq 1 g \pm 0.05 g	Mass = 0.84g	Pass
9	2.8	Robot bending test	Bending angle up to 360°, no visible damage or permanent deformation after bending	Bending angle of 360° achieved	Pass
10	2.9	Robot deflection via magnetic field	Angle of deflection when attracted to 2inch permanent magnet \geq 15°	Angle of deflection = 25.4°	Pass
11	2.10	Robot body helical protrusion uniformity	Helical pitch = 10mm \pm 0.1mm	Helical pitch = 10.0mm	Pass

The verification results for Robot B demonstrate full compliance with all defined design inputs, including tip dimensions, wire specifications, magnetization strength, and structural flexibility. This iteration served as the first fully molded prototype to validate the core fabrication workflow and confirm that a magnetized tip could be successfully actuated. While Robot B exhibited strong performance, it lacked the consistency and system integration refinements achieved in the final iteration, Robot A.

Robot C

Table 8. Verification results for Robot C

Plan Id	Design Output	Inputs	Expected Values	Actual Values	Pass /Fail
4	2.1	Robot tip dimensions	Diameter $\leq 4 \text{ mm} \pm 0.1 \text{ mm}$ Length $\leq 20 \text{ mm} \pm 0.2 \text{ mm}$	Diameter = 3.8mm Length = 21.2mm	Fail
5	2.2	Nitinol wire dimensions	Gauge = 0.508 mm $\pm 0.01 \text{ mm}$ Length $\geq 15 \text{ cm}$	Gauge = 0.2mm Length = 235mm	Fail
6	2.3	Robot tip magnetization	Magnetization $\geq 10 \text{ mT} \pm 0.1 \text{ mT}$	Magnetic Field = 23.5mT north pole, 22.57mT south pole	Pass
7	2.4	Nitinol wire magnetization	Residual magnetization = 0 mT $\pm 0.1 \text{ mT}$	Magnetic Field = 0.07mT (negligible)	Pass
8	2.7	Robot tip	Mass $\leq 1 \text{ g} \pm 0.05 \text{ g}$	Mass = 0.88g	Pass
9	2.8	Robot bending test	Bending angle up to 360°, no visible damage or permanent deformation after bending	Bending angle of 360° achieved	Pass
10	2.9	Robot deflection via magnetic field	Angle of deflection when attracted to 2inch permanent magnet $\geq 15^\circ$	Angle of deflection = 89.1°	Pass
11	2.10	Robot body helical protrusion uniformity	Helical pitch = 10mm $\pm 0.1\text{mm}$	Helical pitch = 10.0mm	Pass

The verification results for Robot C indicate that the robot passed nearly all performance criteria, including magnetic responsiveness and exceptional flexibility. The use of a thinner 0.2 mm nitinol wire significantly increased the robot's deflection angle, highlighting the benefits of reduced core stiffness. However, the robot failed the length constraint and exhibited structural instability under linear actuation, ultimately making it unsuitable for integration into the final system.

Robot D

Table 9. Verification results for Robot D

Plan Id	Design Output	Inputs	Expected Values	Actual Values	Pass /Fail
4	2.1	Robot tip dimensions	Diameter $\leq 4 \text{ mm} \pm 0.1 \text{ mm}$ Length $\leq 20 \text{ mm} \pm 0.2 \text{ mm}$	Diameter = 2.2mm Length = 9.7mm	Pass
5	2.2	Nitinol wire dimensions	Gauge = 0.508 mm $\pm 0.01 \text{ mm}$ Length $\geq 15 \text{ cm}$	Gauge = 0.2mm Length = 175mm	Fail

6	2.3	Robot tip magnetization	Magnetization $\geq 10 \text{ mT} \pm 0.1 \text{ mT}$	Magnetic Field = 24.37mT north pole, 27.33mT south pole	Pass
7	2.4	Nitinol wire magnetization	Residual magnetization = $0 \text{ mT} \pm 0.1 \text{ mT}$	Magnetic Field = 0.07mT (negligible)	Pass
8	2.7	Robot tip	Mass $\leq 1 \text{ g} \pm 0.05 \text{ g}$	Mass = 0.46g	Pass
9	2.8	Robot bending test	Bending angle up to 360°, no visible damage or permanent deformation after bending	Bending angle of 360° achieved	Pass
10	2.9	Robot deflection via magnetic field	Angle of deflection when attracted to 2inch permanent magnet $\geq 15^\circ$	Angle of deflection = 103.9°	Pass
11	2.10	Robot body helical protrusion uniformity	Helical pitch = $10\text{mm} \pm 0.1\text{mm}$	No helical protrusions	Fail

Robot D passes many of the verification criteria and demonstrates the highest deflection angle of all prototypes, a result of its minimized diameter and reduced core stiffness. However, it fails to support the fabrication of helical protrusions, which are essential for rotational control and friction reduction, and cannot be actuated by the linear actuation system. These manufacturing limitations and the lack of key features ultimately render Robot D unsuitable for final system integration despite its promising responsiveness.

Robot A

Table 10. Verification results for Robot A, the final iteration.

Plan Id	Design Output	Inputs	Expected Values	Actual Values	Pass /Fail
4	2.1	Robot tip dimensions	Diameter $\leq 4 \text{ mm} \pm 0.1 \text{ mm}$ Length $\leq 20 \text{ mm} \pm 0.2 \text{ mm}$	Diameter = 3.9mm Length = 19.9mm	Pass
5	2.2	Nitinol wire dimensions	Gauge = $0.508 \text{ mm} \pm 0.01 \text{ mm}$ Length $\geq 15 \text{ cm}$	Gauge = 0.5mm Length = 245mm	Pass
6	2.3	Robot tip magnetization	Magnetization $\geq 10 \text{ mT} \pm 0.1 \text{ mT}$	Magnetic Field = 32.3mT north pole, 25.93mT south pole	Pass
7	2.4	Nitinol wire magnetization	Residual magnetization = $0 \text{ mT} \pm 0.1 \text{ mT}$	Magnetic Field = 0.07mT (negligible)	Pass
8	2.7	Robot tip	Mass $\leq 1 \text{ g} \pm 0.05 \text{ g}$	Mass = 0.86g	Pass
9	2.8	Robot bending test	Bending angle up to 360°, no visible damage or	Bending angle of 360° achieved	Pass

			permanent deformation after bending		
10	2.9	Robot deflection via magnetic field	Angle of deflection when attracted to 2inch permanent magnet $\geq 15^\circ$	Angle of deflection = 26.1°	Pass
11	2.10	Robot body helical protrusion uniformity	Helical pitch = $10\text{mm} \pm 0.1\text{mm}$	Helical pitch = 10.0mm	Pass

These results show that the final prototype, Robot A, meets all defined design inputs and passes every verification test outlined in the design plan. This confirms that Robot A satisfies the required dimensional tolerances, magnetic performance thresholds, mechanical flexibility, and structural consistency necessary for safe and effective integration into the overall system. The consistent compliance across all parameters supports its selection as the final validated iteration for integration testing and development.

Robots B, C, and D serve as critical design alternatives that explore trade-offs in wire diameter, overall size, and tip fabrication strategies. Their performance under verification testing highlights key limitations, such as geometric fabrication constraints during miniaturization (Robot D). By contrast, Robot A meets all verification criteria, demonstrating robust magnetic responsiveness, structural flexibility, and integration compatibility. This structured testing progression enables a data-driven selection of the final design and provides a clear record of the design refinement process.

4.2.1.2 Modelling and Analysis Results

Although formal simulations were not performed for the soft continuum robot subsystem, the design is strongly grounded in theoretical principles of soft robotics, magnetostatics, and flexible structural mechanics. The modeling process is inherently experimental, with empirical data used to validate performance trends and guide design decisions through iterative prototyping.

The robot operates based on magnetic actuation, where a magnetic torque τ is induced at the tip by an externally applied field B , interacting with the tip's magnetic moment m . The resulting torque is described by the standard vector cross-product:

$$\tau = m \times B \quad (28)$$

This relationship implies that the magnitude of torque—and hence the deflection of the robot—is maximized when the field is perpendicular to the magnetic dipole and both m and B are large. In this context, maximizing m involved optimizing both the concentration of NdFeB particles embedded in the silicone tip and the efficacy of the magnetization process. This was achieved using an impulse magnetizer, which ensured strong and uniform field alignment within the cured magnetic composite.

To validate this design logic, the magnetic field strength at the robot tip was measured across multiple prototypes. As illustrated in the Deflection Angle vs Magnetization plot (Figure X), the correlation between field strength and angular deflection is not strictly linear. While Robot A exhibits the highest north pole field strength, it does not produce the largest deflection. Instead, Robot C, which has a lower magnetic field strength, achieves the greatest deflection angle. This finding highlights the importance of mechanical flexibility in enabling effective actuation.

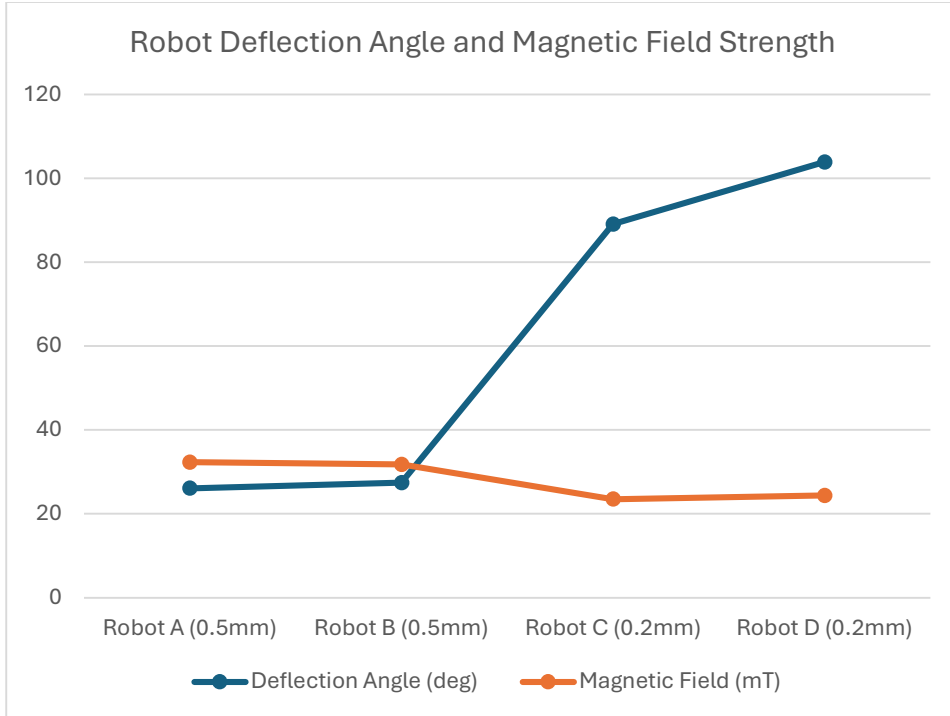


Figure 72. Comparing the results from verification plans 6 and 10, demonstrating the relationship between robot nitinol wire core diameter, deflection angle, and magnetic field strength.

The increased deflection observed in Robot C is directly attributed to its thinner nitinol wire core (0.2 mm). There is a clear inverse relationship: as the wire diameter decreases, the deflection angle increases substantially. This supports the expectation from classical bending theory that reduced cross-sectional stiffness allows for greater curvature under the same applied torque. However, these benefits come with trade-offs. Robot C, while highly compliant, was found to buckle immediately under linear translation loading, rendering it incompatible with the actuator system. This limitation illustrates a core principle in soft robot design: gains in flexibility must be balanced against losses in structural stability.

Robot D further demonstrates the implications of miniaturization. At 2 mm in diameter, it approaches the clinical gold standard for minimally invasive probes. However, this scale introduces significant challenges in fabrication precision. The robot's body could not support the formation of uniform helical protrusions—key features that reduce friction and assist with axial motion. Despite Robot D exhibiting the highest deflection angle in raw testing, its lack of structural fidelity and integration compatibility made it an impractical candidate for continued development. This observation aligns with known limitations in soft robotics manufacturing, where reduced feature size often comes at the cost of design accuracy, material uniformity, and handling reliability.

The final iteration, Robot A, achieves an optimal balance of geometric compliance, magnetic responsiveness, and actuation compatibility. It passes all design verification criteria without exhibiting structural failure. The trends observed in the verification data support the theoretical predictions underlying the design and establish a foundation for future analytical work.

4.2.1.3 Technical, Non-Technical, Risk, and Compliance Strategies

Technical Strategies

A number of technical and non-technical strategies are integrated into the design of the soft continuum robot to ensure its safe function, regulatory alignment, and suitability for clinical use. At the technical level, material selection plays a critical role in mitigating biological and mechanical risks. The robot body is fabricated using EcoFlex 00-30 silicone, which offers the required flexibility for soft tissue navigation while being broadly recognized in literature and industry as biocompatible. The internal core is composed of 0.5 mm nitinol wire, selected for its superelastic properties that allow both high flexibility and consistent shape memory, essential for repetitive linear actuation cycles. The tip, which contains the magnetized portion of the robot, is molded separately using a mixture of NdFeB particles embedded in silicone at a carefully controlled ratio to preserve both magnetic responsiveness and mechanical softness. This two-stage fabrication process ensures the embedded magnetic material is not exposed to surrounding tissue, a key design principle for reducing cytotoxicity risks associated with uncoated neodymium particles, as identified in prior studies.

To avoid interference from unintended magnetic fields, only the tip is magnetized, and magneto-optical sensor measurements (Plan ID 7) confirm that the wire core remains magnetically inert throughout the robot's length. This design choice minimizes the risk of uncontrolled actuation and ensures precise steering via external magnetic fields. The overall robot dimensions were verified through Plan ID 4 and Plan ID 5, which confirmed that the final prototype, Robot A, met the defined thresholds for diameter and length. Additionally, the inclusion of uniform helical protrusions, confirmed through Plan ID 11, provides a passive mechanism to address friction and traction concerns, promoting rotational motion and reducing shear force buildup at the robot-tissue interface.

Non-Technical Strategies

From a non-technical perspective, risk management extends beyond design to operational procedures and intended clinical workflows. The robot is designed to be single use with the addition of a sterile sheath or protective barrier to isolate the actuation system components from the surgical field, supporting compliance with infection control guidelines. This is discussed in more detail in section 2.3 of this report. User training is another central aspect of non-technical risk mitigation. Operators will be trained to understand the robot's flexibility, safe deflection limits, and emergency retraction methods. This training will include both theoretical instruction and hands-on simulation using phantom models. Detailed documentation will accompany the robot, including procedural guides, visual inspection checklists, and a maintenance schedule for reusable configurations.

Risk Strategies

Risk strategies focus on both mechanical and procedural safeguards to prevent device failure or injury during clinical use. An extensive breakdown of risk management and regulatory compliance can also be found in section 2.3 of this report. The robot's mechanical performance is verified through Plan ID 9 and Plan ID 10, which demonstrated that Robot A could undergo full 360° bending and sustain magnetic deflection angles of around 26°, with no structural degradation observed across repeated cycles. In addition to inherent design resilience, the system features a redundancy mechanism: if magnetic actuation is disrupted, the robot can be fully retracted using the mechanical linear actuator, ensuring recovery without dependence on external fields.

Compliance Strategies

Compliance with applicable regulatory standards is a key consideration for future clinical translation. The soft continuum robot is designed in accordance with ISO 10993-1, which establishes biological evaluation standards for medical devices in contact with tissue. All materials used are either known to be biocompatible or encapsulated to prevent exposure. In addition, ISO 14971 provides the overarching risk management framework applied throughout the project. All potential hazards—including mechanical failure, tissue abrasion, magnetic interference, and sterilization lapses—are identified and mitigated through the strategies described in section 2.3 of the report. Risks are evaluated based on both severity and probability, and control measures are applied to ensure residual risks are reduced to acceptable levels. ISO 62366-1, which governs usability and human factors engineering, informs the robot's planned integration with user interfaces and future navigation systems. Lastly, as the robot is intended to enter the human body, its design adheres to the principles outlined in IEC 60601-2-18 for endoscopic systems, particularly concerning thermal exposure, optical isolation, and device geometry.

4.2.1.4 Assumptions, Limitations, and Constraints

Assumptions

Several assumptions are made throughout the development and testing of the soft continuum robot, which are necessary to interpret results and establish baseline expectations for system behavior. It is assumed that the magnetic field strength generated by the electromagnetic coil system is stable and sufficient to actuate the robot tip consistently throughout operation. It is also assumed that magnetic fields diminish with distance in a predictable and symmetric gradient, allowing directional control to be repeatable and precise. This assumption is based on simulation outputs and prior studies on coil-generated field dynamics as outlined in previous sections of the report. Furthermore, ambient electromagnetic interference in the testing environment is assumed to be negligible, as no shielding or compensation mechanisms were implemented in the benchtop setup. In terms of biological considerations, it is assumed that the selected materials maintain their biocompatibility under the proposed conditions, and that their mechanical properties do not degrade.

Limitations

The project also faces several limitations, particularly with respect to prototyping capacity and test resources. One significant limitation is the challenge of fabricating reliable miniaturized prototypes. Attempts to produce a 2 mm diameter robot (Robot D) resulted in structural inconsistencies and an inability to form uniform helical features. This highlights a fundamental limitation of the current mould-based fabrication technique, which is not optimized for sub-3 mm geometries. Additionally, the robot was not tested under prolonged cyclic loading or long-term fatigue conditions. As such, the durability of the nitinol wire and the magnetic field retention of the embedded tip under extended use remain unverified. Another limitation is that rotational actuation is not yet implemented. While the robot features helical geometry that supports rotational traction, it cannot currently be spun along its axis, limiting its maneuverability in particularly complex anatomical regions. Moreover, magnetization testing was constrained to benchtop magnetic field strengths; access to more powerful clinical-grade field generators would be necessary to fully evaluate the robot's actuation potential.

Constraints

Externally imposed constraints also shape the robot's final design. All materials in contact with the patient must be biocompatible and non-toxic, which restricts the use of certain

adhesives, coatings, and structural reinforcements that may have improved fabrication fidelity. The robot must also remain lightweight to ensure compliance with both actuation requirements and patient safety thresholds. In terms of workspace geometry, the robot must conform to the limited spatial environment of both phantom test rigs and human nasal anatomy, which restricts its maximum extension and the required curvature radius for flexible navigation. Additionally, fabrication repeatability remains constrained by the resolution of available 3D-printed molds and the manual variability introduced during silicone pouring and curing. These constraints must be addressed in future work to transition the design from a successful prototype to a clinically viable medical device.

4.2.2 Magnetic Actuation System

4.2.2.1 Verification Results

The three significant versions of the magnetic actuation system, including the two significant iterations (outlined in section 4.1.2.1 of this chapter), as well as the final design (outlined in section 4.1.2.2 of this chapter), are verified. Each verification plan is laid out in more detail in section 3.2 in Chapter 3. A brief overview of the verification plans can be seen below:

- Plan ID 12. Take the temperature of the coil using an Extech EX470A Multimeter and IR Thermometer, when it is first turned on (time = 0s), and again at time = 2s, time = 5s, and time = 30s (which is a boundary case as the coils are not expected to be used for this length of time). In all test cases, 15A of current is applied. This is to verify that the temperature of the coils never exceeds 100°C during the expected operation time.
- Plan ID 13. Simulate the magnetic field strength produced by the coil using the MagPy simulations at the edge of the coil (distance = 0cm), and again at distance = 10cm, distance = 20cm, and distance = 40cm. The workspace is defined at 10cm from the coils' edge. In all test cases, 15A of current is applied. This is to verify that the chosen coil specifications will theoretically produce a field of at least 5mT within the working bounds of the system, up to 2mT from 20cm away, and near 0mT from 40cm away.
- Plan ID 14. Measure the magnetic field strength produced by the coil using an Infineon TLV493D-A1B6 Magnetic Sensor at the edge of the coil (distance = 0cm), and again at distance = 10cm, distance = 20cm, and distance = 40cm. The workspace is defined at 10cm from the coils' edge. In all test cases, 15A of current is applied. This is to verify that the coils will experimentally produce a field of at least 5mT within the working bounds of the system, up to 2mT from 20cm away, and near 0mT from 40cm away. Photos of the experimental setup (for all three coils tests) can be seen below in Figure 73. The resulting graphs showing the measured magnetic field can be seen in Figure 74. Figure 74. A screenshot of the resulting magnetic field measurements acquired using the TLV493D-A1B6 Magnetic Sensor. In these verification test cases, the X-axis (red) represented the field of interest.

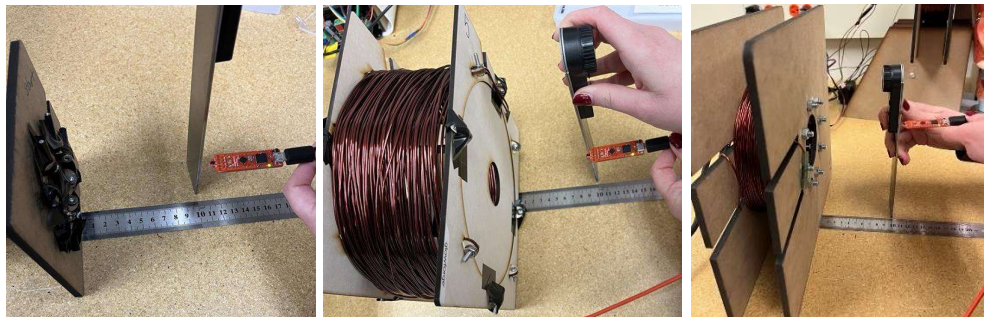


Figure 73. Experimental set-up for 13. From left to right, the images show TLV493D-A1B6 Magnetic Sensor being used to measure a field at 10cm of the coil edges of iterations 1 and 2, then the final prototype.

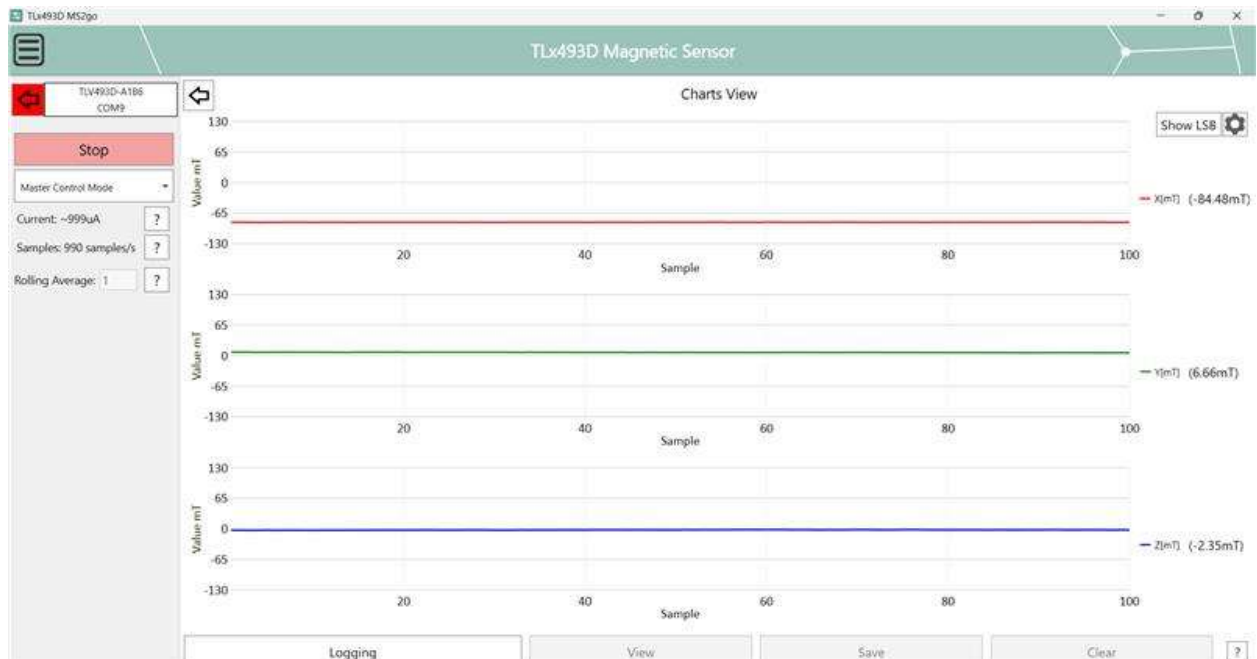


Figure 74. A screenshot of the resulting magnetic field measurements acquired using the TLV493D-A1B6 Magnetic Sensor. In these verification test cases, the X-axis (red) represented the field of interest.

- Plan ID 15. Measure the voltage being drawn from the power supply while a coil is off and again when it is on. In all test cases, 15A of current are applied. This is to verify that the coils draw a safe amount of voltage (less than 60V). A photo of a voltage being displayed on the PSU can be seen in Figure 75.
- Plan ID 16. Measure the signal going into the PWM motor driver using a Hantek 2D42 oscilloscope. The PWM waveform should be at 5V, with a 95% duty cycle (as this was the highest duty cycle the motor driver could recognize). This is to verify that the circuitry can communicate to the motor driver the specified coil strength, which is proportional to the duty cycle. Sample outputs showing the duty cycle set to 95% and 0% can be seen below in Figure 75.



Figure 75. Experimental setup for 15. Sample Hantek 1 2D42 oscilloscope outputs showing the PWM duty cycle set to 95% (left) and 0% (right). These photos were taken when testing the final prototype.

- Plan ID 17. Measure the voltage going into the direction pin of the motor driver using a Hantek 2D42 oscilloscope, both when the direction is set to be high and low. This is to verify that the circuitry can communicate to the motor driver the specified coil direction. Sample outputs showing the direction pin set to high and low can be seen below in Figure 76.



Figure 76. Experimental set up for 16. Sample Hantek 2D42 oscilloscope outputs showing the direction pin voltage set to high (left) and low (right). These photos were taken when testing the final prototype.

- Plan ID 18. Measure the magnetic field strength produced by the coil using an Infineon TLV493D-A1B6 Magnetic Sensor when it is on and then again one second after it shuts off. This field will be measured inside the coil, where it is strongest. This is to verify that the magnetic field is effectively able to be turned on and off. A similar set-up to that seen in Figure 73 was used, but instead of measuring the field 10cm from the edge, the magnetic sensor was placed inside the coil openings.
- Plan ID 19. Measure the magnetic field strength produced by the coil using an Infineon TLV493D-A1B6 Magnetic Sensor when the current is set to positive and then

negative. This field will be measured inside the coil, where it is strongest. This is to verify that the magnetic field direction is effectively able to be switch.

Magnetic Actuation System Iteration 1 Verification

Table 11. Verification results for magnetic actuation system iteration 1.

Plan ID	Design Output	Inputs	Expected Values	Actual Values	Pass /Fail
12	3.1	Time1 = 0s Time2 = 2s Time3 = 5s Time4 = 30s	Temp1 = 22°C Temp2 < 100°C Temp3 < 100°C Temp4 < 100°C	Temp1 = 22.1°C Temp2 = 22.7°C Temp3 = 25.6°C Temp4 = 43.2°C	Pass
13	3.2	Distance1 = 0cm Distance2 = 10cm Distance3 = 20cm Distance4 = 40cm	10mT < Field1 < 100mT 5mT < Field2 < 100mT 2mT < Field3 < 100mT Field4 = 0mT	Field1 = 84.8mT Field2 = 7.6mT Field3 = 1.2mT Field4 = 0mT	Pass
14	3.2	Distance1 = 0cm Distance2 = 10cm Distance3 = 20cm Distance4 = 40cm	10mT < Field1 < 100mT 5mT < Field2 < 100mT 2mT < Field3 < 100mT Field4 = 0mT	Field1 = 3.23mT Field2 = 0.29mT Field3 = 0mT Field4 = 0mT	Fail
15	3.3	CoilStatus1 = ON CoilStatus2 = OFF	0V < Voltage1 < 60V Voltage2 = 0V	Voltage1 = 30V Voltage2 = 0V	Pass
16	3.4	N/A: not using PWM in this iteration			Fail
17	3.4	N/A: not controlling direction with motor driver in this iteration			Fail
18	3.4	CoilStatus1 = ON CoilStatus2 = OFF	Field1 > 0mT Field2 = 0mT	Field1 = 11mT Field2 = 0mT	Pass
19	3.5	CoilStatus1 = ON CoilStatus2 = OFF	PSUcurrent1 > 0A PSUcurrent2 = 0A	PSUcurrent1 = 15A PSUcurrent2 = 0A	Pass

These results show that iteration 1 did not pass verification plans 14, 16, and 17. Failing plan 14 shows that the coil design is not strong enough to produce the required magnetic field of 5mT within 10cm from the edge of the coil and 2mT within 20cm from the edge of the coil. Not being able to complete plans 16 and 17 shows that the circuit design to control the coils is insufficient, as the coils are not controlled by a PWM signal at all, and there is no control of the magnetic field direction.

Magnetic Actuation System Iteration 2 Verification

Table 12. Verification results for magnetic actuation system iteration 2.

Plan ID	Design Output	Inputs	Expected Values	Actual Values	Pass /Fail
12	3.1	Time1 = 0s Time2 = 2s Time3 = 5s Time4 = 30s	Temp1 = 22°C Temp2 < 100°C Temp3 < 100°C Temp4 < 100°C	Temp1 = 22.0°C Temp2 = 22.9°C Temp3 = 26.2°C Temp4 = 47.5°C	Pass

13	3.2	Distance1 = 0cm Distance2 = 10cm Distance3 = 20cm Distance4 = 40cm	10mT < Field1 < 100mT 5mT < Field2 < 100mT 2mT < Field3 < 100mT Field4 = 0mT	Field1 = 84.8mT Field2 = 7.6mT Field3 = 1.2mT Field4 = 0mT	Pass
14	3.2	Distance1 = 0cm Distance2 = 10cm Distance3 = 20cm Distance4 = 40cm	10mT < Field1 < 100mT 5mT < Field2 < 100mT 2mT < Field3 < 100mT Field4 = 0mT	Field1 = 7mT Field2 = 1.4mT Field3 = 0.4mT Field4 = 0mT	Fail
15	3.3	CoilStatus1 = ON CoilStatus2 = OFF	0V < Voltage1 < 60V Voltage2 = 0V	Voltage1 = 30V Voltage2 = 0V	Pass
16	3.4	N/A: not using PWM in this iteration			
17	3.4	N/A: not controlling direction with motor driver in this iteration			
18	3.4	CoilStatus1 = ON CoilStatus2 = OFF	Field1 > 0mT Field2 = 0mT	Field1 = 8.9mT Field2 = 0mT	Pass
19	3.5	N/A: not using a PSU in this iteration			

These results show that iteration 2 did not pass verification plans 14, 16, 17, or 19. Failing plans 14 shows that the coil design is not strong enough to produce the required magnetic field of 5mT within 10cm from the edge of the coil, and 2mT within 20cm from the edge of the coil. Note that this iteration did achieve stronger fields than the previous iteration, showing that the design was improving. Not being able to complete plans 16 and 17 shows that the circuit designed to control the coils is insufficient, as the coils are not controlled by a PWM signal at all, and there is no control of the magnetic field direction. Not being able to complete 19 shows that a power supply needed to be implemented back into the design. This can be accomplished in methods other than through a PSU, so not being able to complete the plan does not necessarily mean the design could not meet design output 3.5.

Magnetic Actuation System Final Design Verification

Table 13. Verification results for the final design of the magnetic actuation system.

Plan Id	Design Output	Inputs	Expected Values	Actual Values	Pass /Fail
12	3.1	Time1 = 0s Time2 = 2s Time3 = 5s Time4 = 30s	Temp1 = 22°C Temp2 < 100°C Temp3 < 100°C Temp4 < 100°C	Temp1 = 22.2°C Temp2 = 23.0°C Temp3 = 27.0°C Temp4 = 51.7°C	Pass
13	3.2	Distance1 = 0cm Distance2 = 10cm Distance3 = 20cm Distance4 = 40cm	10mT < Field1 < 100mT 5mT < Field2 < 100mT 2mT < Field3 < 100mT Field4 = 0mT	Field1 = 84.8mT Field2 = 7.6mT Field3 = 1.2mT Field4 = 0mT	Pass
14	3.2	Distance1 = 0cm Distance2 = 10cm Distance3 = 20cm Distance4 = 40cm	10mT < Field1 < 100mT 5mT < Field2 < 100mT 2mT < Field3 < 100mT Field4 = 0mT	Field1 = 48mT Field2 = 6.5mT Field3 = 2mT Field4 = 0mT	Pass
15	3.3	CoilStatus1 = ON CoilStatus2 = OFF	0V < Voltage1 < 60V Voltage2 = 0V	Voltage1 = 30V Voltage2 = 0V	Pass

16	3.4	DutyCycle1 = 95% DutyCycle2 = 0%	PWM1 = 5V PWM2 = 0V	PWM1 = 4.72V ≈ 5V PWM2 = 160mV ≈ 0V	Pass
17	3.4	Direction1 = HIGH Direction2 = LOW	Voltage1 = 5V Voltage2 = 0V	Voltage1 = 4.72V ≈ 5V Voltage2 = 160mV ≈ 0V	Pass
18	3.4	CoilStatus1 = ON CoilStatus2 = OFF	Field1 > 0mT Field2 = 0mT	Field1 = 66mT Field2 = 0mT	Pass
19	3.5	CoilStatus1 = ON CoilStatus2 = OFF	PSUcurrent1 > 0A PSUcurrent2 = 0A	PSUcurrent1 = 15A PSUcurrent2 = 0A	Pass

These results show that the final design of the magnetic actuation system passed all its verification tests. Thus, the team can be confident that the coils and their associated circuitry will meet all the design outputs defined for the scope of this project.

4.2.2.2 Modelling and Analysis Results

Since the goal was to produce a magnetic field of 5mT at 10 cm and 2mT at 20 cm from the coil's edge, one of the first steps in the coil design process was to optimize its specifications to meet this field pattern. The plot seen in Figure 77 shows testing that was done to find the minimum current required to meet the magnetic field requirements. It was found that the ideal magnetic field specifications could be met when 15A was applied to the coils.

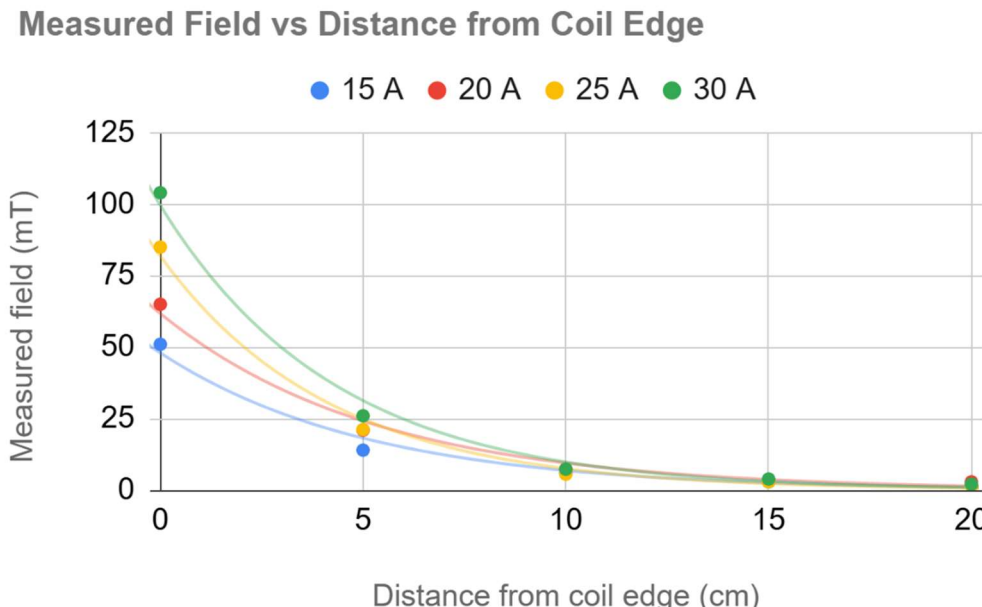


Figure 77. Plot of measured magnetic field vs. distance from the edge of the coil, for one of the final coils when various currents are applied to the coil.

Once a final coil design was decided, three coils of identical specifications had to be built. To ensure consistency, it was important to compare and analyze the performance of the three coils. Thus, the magnetic field was measured at various distances from the edge of the coil while 15A was applied across the coil. A plot showing the measured magnetic field with varying distance for

all three final coils can be seen in Figure 78. The plot shows agreement in measured values between all three coils, verifying that they should all produce the same strength magnetic fields.

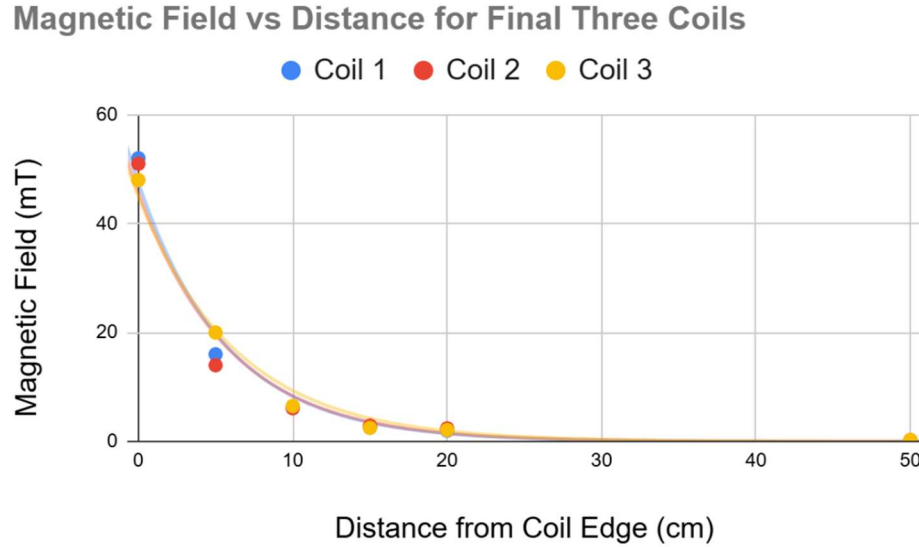


Figure 78. Plot of the measured magnetic field vs distance from the edge of the coil, for all three coils used in the final prototype. 15A were applied to all three coils. The plot shows agreement between the magnetic fields produced by all three coils.

Verification for the field generated by three coils at once in the X, Y, and Z planes can be seen in the Navigation Interface section; that section integrates the whole set up together, and tests and shows the verification of the three coils interacting together.

4.2.2.3 Technical, Non-Technical, Risk, and Compliance Strategies

Technical Strategies

Technical strategies encompass the engineering solutions integrated into the design to enhance its functionality, safety, and performance. One such strategy pertains to thermal management. The coils are only activated in short, intermittent bursts as needed to reduce heat buildup. The coils do not need to be on for more than seconds at a time, keeping it well under the upper limit of the appropriate thermal verification results. Furthermore, the power supply system is limited to output a maximum of 60V and 20A. By limiting the current output to 20A rather than the 30A the PSU is rated for, the heat produced by the coils is reduced.

Current isolation strategies are also in place. The high-voltage motor driver circuitry is kept completely isolated from the low-voltage microcontroller logic via MOSFET logic. Similarly, all electrical components related to the high-voltage circuitry are rated to be able to withstand higher current and high voltage loads (60V for the MOSFETs and over 120V for the motor driver boards),. To further protect surrounding electronics from the high-voltage design components, power bars and PSUs with built-in breakers are used to protect the system from sudden faults.

Non-Technical Strategies

Non-technical strategies include operational procedures, training, and planning approaches that support safe and effective use. The magnetic actuation system has many features in place to ensure intuitive and safe operation; examples include real-time power displays from the PSU,

clearly labeling all equipment, and ensuring there is no exposed wiring anywhere. However, it is expected that only trained personnel will operate the system to ensure safety and minimize risk.

Operators will undergo dedicated training to understand critical safety concepts such as coil heating limits, magnetic field exposure thresholds, and emergency response protocols. This training will include both theoretical instruction and hands-on simulation with the system. Comprehensive documentation will be provided, including detailed operational manuals, startup/shutdown procedures, troubleshooting guides, and emergency handling checklists.

Regular maintenance and inspection schedules are also part of the risk management strategy. These include checks on wiring integrity, PSU output stability, coil insulation, and general mechanical wear. Any abnormalities would trigger mandatory diagnostics before system reactivation.

Additionally, to mitigate interference risks—especially in clinical or lab settings—clearly defined magnetic field boundaries will be established. Physical floor markers and posted safety signage will indicate active field zones, akin to safety measures in MRI environments. These precautions will ensure that nearby electronic equipment and unshielded ferromagnetic objects remain outside the influence of the magnetic field.

Risk Strategies

Risk strategies aim to reduce the likelihood and impact of hazards during operation. Firstly, heat shrink tubing is used around connected copper wires within the coils. This, along with clean cable routes, prevents wire exposure and thus minimizes the risk of electric shock and short circuits. Next, the GUI has an emergency stop button built-in to allow for quick system shutdown if any problems were to arise. Further, the user could easily press the power buttons to turn off the PSUs to quickly shut down the system as well. Additionally, the non-technical strategy of a marked magnetic field zone will be strictly enforced. This includes guidelines to keep any magnetic-sensitive devices, including pacemakers and credit cards, out of the designated zone.

Compliance Strategies

Compliance strategies ensure the system aligns with regulatory and safety standards. The most relevant electrical safety standard for this project is IEC 60601-1. This standard covers the general requirements for basic safety and essential performance of medical electrical equipment. It covers electrical, mechanical, and thermal safety requirements, emphasizing risk management, usability, and protection for both the patient and the operator. This standard applies to any device that uses electrical power in a medical environment. There are some specific sections of interest for this project. Section IEC 60601-1-2 covers the requirements and tests for electromagnetic disturbances. Here, the focus is on ensuring the device does not emit harmful electromagnetic interference (EMI), as well as ensuring the device is resistant to external EMI. Section IEC 60601-2-18 covers the requirements for the basic safety of endoscopic equipment. This section specifies safety requirements for endoscopic systems going inside the human body, including thermal safety, optical radiation limits, and material selection. Section IEC 60601-2-46 covers the requirements for electrical equipment used at operating tables. This section focuses on the mechanical strength, stability, and electrical safety of electrical devices used in or around operating tables. It includes requirements for mobility, locking mechanisms, and protection from tipping.

4.2.2.4 Assumptions, Limitations, and Constraints

Assumptions

For the final design, it is assumed that the power supplied to the coils by the PSUs is stable, providing consistent voltage and current levels throughout operation. This ensures predictable coil behavior and reliable system performance. It is also assumed that magnetic fields generated by the coils diminish consistently with distance, following a predictable gradient without significant localized anomalies or distortions. Furthermore, ambient electromagnetic interference from surrounding equipment is assumed to be negligible.

Limitations

Limitations are regarded as internal factors that hinder the team's ability to fully meet objectives. The biggest limitation of this project is that the team only has access to standard benchtop power supplies, rather than medical-grade power generators. In a hospital setting, a 1.5T MRI will require around 480V and 320A. The PSUs used in this project are rated to only 60V and 30A. This limits the maximum achievable field strength produced by the magnetic actuation system. Furthermore, the achievable magnetic field strength is inherently limited by the physical properties of the coils, particularly the number of wire turns. While increasing the number of turns can enhance field intensity, it also leads to greater resistive heating. As such, the maximum allowable number of turns is directly limited by the system's thermal capacity. To prevent overheating, a balance must be maintained, placing an upper bound on the field strength that can be safely generated. Additionally, the resolution and accuracy of the magnetic field measurement is limited by the precision of the TLV493D-A1B6 magnetic sensor.

Constraints

Constraints are regarded as external factors that restrict the project. A large constraint to this project is that all circuit components connected to the coils must be rated for high-current operation to ensure safety, prevent overheating, and maintain reliable performance under sustained loads. This constrains the options for potential motor driver circuits and connecting wires. Another important consideration is that the physical dimensions of the magnetic actuation set-up are constrained by the available workspace within the OR. There must be open space for the surgeon to have easy access to the sinus cells as well as room for the anesthesiologist to access the patient. Further, the coils are constrained to not exceed 100°C during operation to ensure safe use and prevent damage to adjacent components. Additionally, the magnetic field generated by the coils is constrained to not extend past 50cm of the workspace. This ensures that the system will not interfere with other electronics within the OR.

4.2.3 Linear Actuation System

4.2.3.1 Verification Results

For more details behind each testing method, refer to chapter 3. As a brief overview, the plans center around testing the linear actuator's repeatability, accuracy under load and size compatibility. For results of each test, refer to the [linear actuator testing results document](#). Note that for normal tests, the 1.2mm wire was used, which was the actuation wire size of the final magnetized continuum robot design.

Plan ID 20. Repeatability test: The wire was extended one full gear rotation, and the change in position was measured. The process was repeated 20 times.

Plan ID 21. Accuracy under load: A plate was attached to the wire, and the wire was retracted 1 full rotation. Weight is then incrementally added until the accuracy falls under 90%

of the original position (<19mm of movement instead of 21mm). Each load is tested 5 times, then averaged.



Figure 79 (Left) and Figure 80 (Right). The initial and final positions of the wire under a load.

Plan ID 22. Forward and reverse accuracy: The stepper will spin one full rotation in extension, then retract by one full rotation, ten times each. The final position will then be measured to see the deviation in position after continuous extension and retraction motion.

Plan ID 23. Wire size compatibility: The repeatability test was repeated for wires of size 0.5mm, 1.2mm, and 4mm.



Figure 81 (Left) and Figure 82 (Right). Initial and final positions of the wire after ten oscillating extension and retraction motion.

Although there were multiple iterations of the linear actuator, the first iteration could no longer be tested due to failure of the driver, and the second iteration could not actuate the wire properly to yield any results. However, since the third iteration passed all verification tests, further development stopped to pivot focus on integration.

As shown in the table below, all the test plans passed. This demonstrates the consistency of the linear actuator for use current and future iterations of the system.

Table 9. Verification test results for the linear actuator

Plan Id	Design Output	Inputs	Expected Values	Actual Values	Pass/Fail
20	4.1	1600 microsteps	21.99mm \pm 7% (1.5mm) of average movement	21.7mm \pm 0.75mm	Pass
21	4.2	Loads of 5g, 10g, 20g, 50g, 100g, 150g, 200g, 300g	<7% (1.5mm) deviation of average movement under 150g of load compared to	21.3mm average under 100g	Pass
22	4.3	10 rotations (1600 microsteps) of extension and retraction	<7% (1.5mm) deviation from initial position	0.65mm median	Pass
23	4.4	0.5mm, 1.2mm, 2mm, 4mm wire gauge	1-4mm wire deviates <7% (1.5mm) from movement	1-4mm within 7% of value	Pass

4.2.3.2 Modelling and Analysis Results

The results of the repeatability test can be seen in below in Figure 83. The test is done with 20 datapoints.

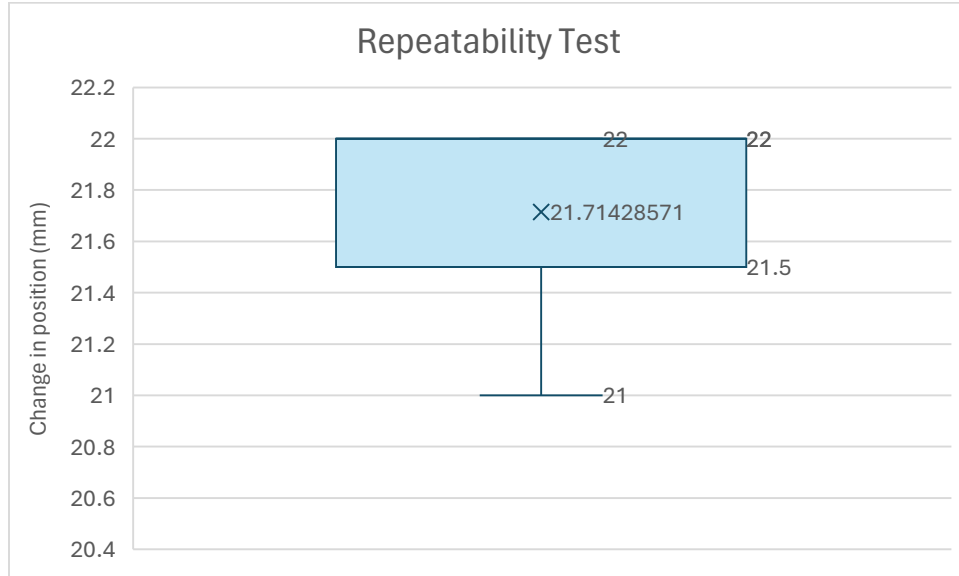


Figure 83. The repeatability test results of Plan ID 20.

The results show a median of 21.71mm, with an IQR of 21.5 mm to 22mm, with the minimum value of 20mm. This shows a maximum deviation of 1mm, indicating a repeatability of $\pm 1\text{mm}$.

Next, the results of load test can be seen in Figure 84 below. The test was done with just the plate, then 10g, 20g, 50g, 100g, 150g, 200g and 300g of load.

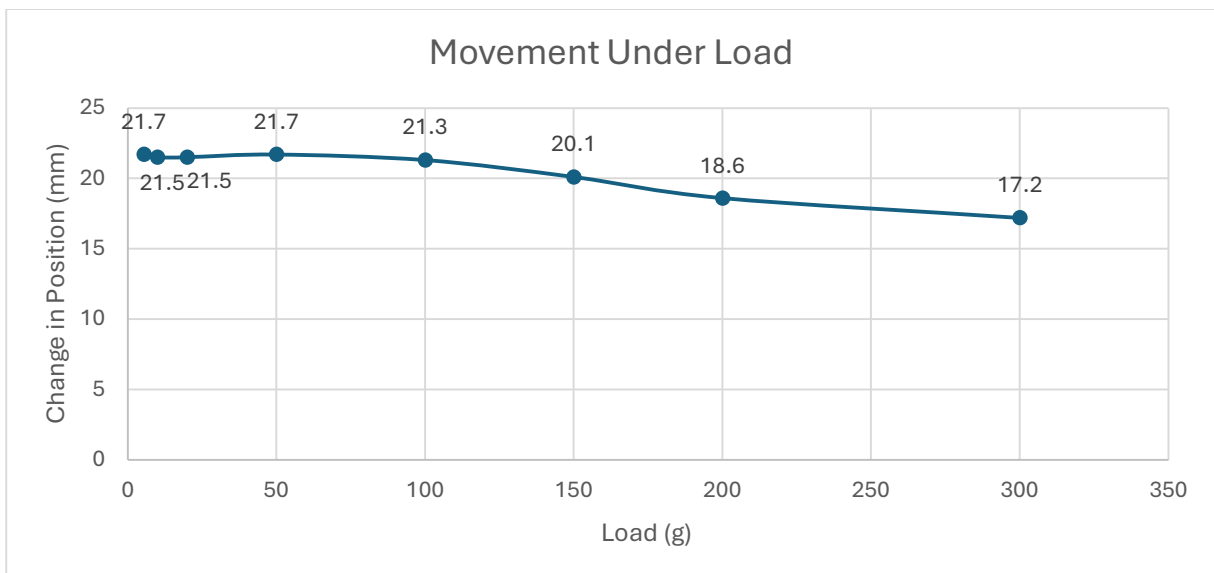


Figure 84. Accuracy under load test results of Plan ID 21

The results show that within 100g of weight, the accuracy falls within the specifications determined by the repeatability test. However, there is a decline in accuracy in the loads of 150g and beyond.

The result of the oscillation test is shown in Figure 85 below. The test was repeated ten times, each oscillating forward and reverse ten times.

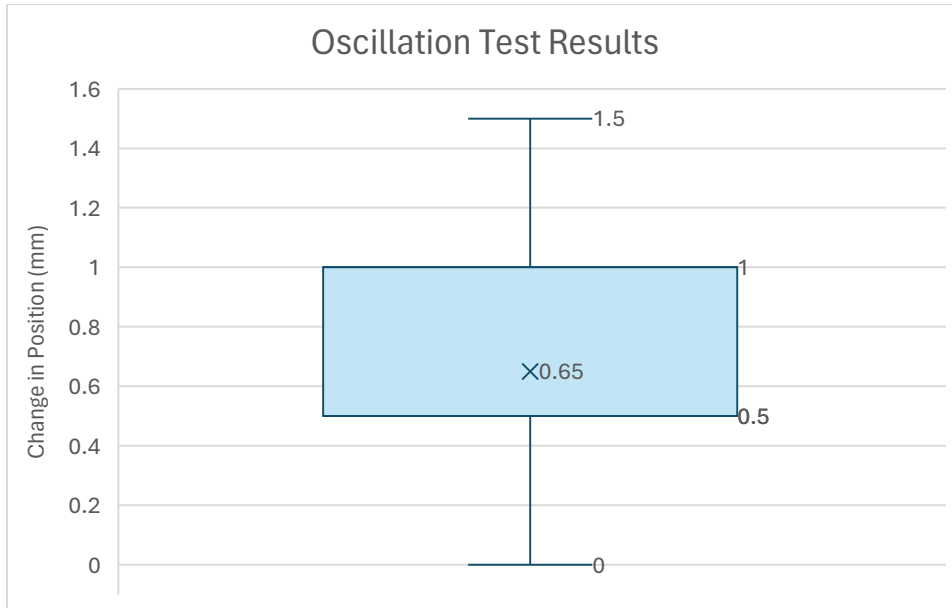


Figure 85. Results of oscillation test of Plan ID 22.

The maximum position change is 1.5mm, with a median of 0.65mm shows consistency in the extension and retraction motions.

Lastly, the results of the wire compatibility tests are displayed in Figure 86 below. The repeatability tests were repeated, and the results averaged.

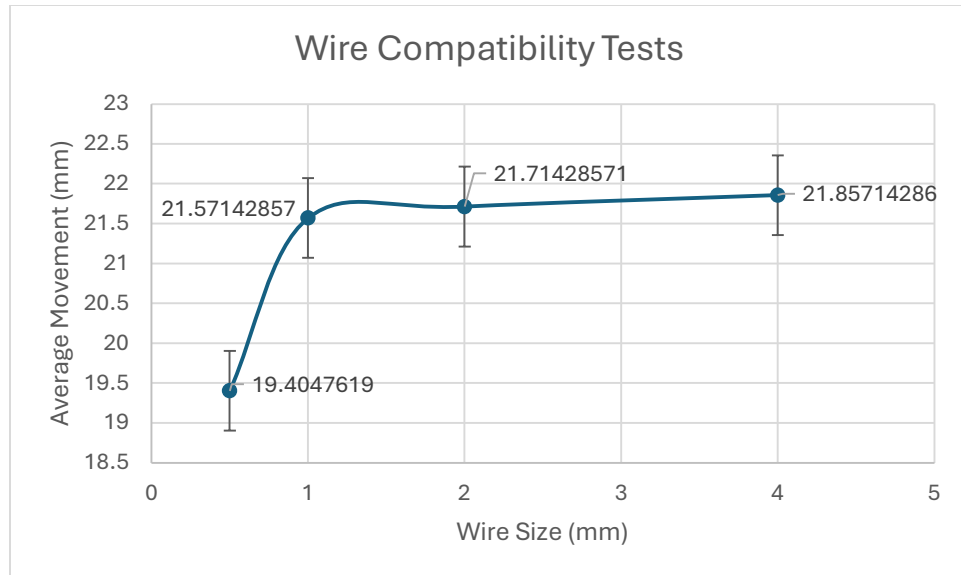


Figure 86. The results of the wire compatibility tests of Plan ID 23.

There is a significant drop in movement in the 0.5mm wire. The space between the gears is 1mm in diameter, which means that any wire less than 1mm in diameter will only be pushed by one gear, and not both, relying only on the friction instead of the “pinching” rotational motion to extend or retract the wire. This leaves the wire prone to slipping, which is indicated by the drop in movement. Therefore, through these results, the wire compatibility of the linear actuator is between 1mm to 4mm in diameter. The actuator may be compatible with larger diameters; however, it is unnecessary since the objective is to miniaturize the robot to be smaller than the current size of 4mm.

4.2.3.3 Technical, Non-Technical, Risk and Compliance Strategies

Technical Strategies

Similar to the magnetic actuation system, the TMC2209 motor driver isolates the current of the stepper’s power supply from the microcontroller signal. Additionally, the driver’s ability for UART control allows monitoring of the stepper motor during actuation [13]. The driver can detect mechanical stalls and shut off upon detection. Additionally, monitoring allows the driver closed loop control of stepper micro stepping, allowing for smooth actuation without mechanical noise or vibrations compared to other motor drivers.

Non-Technical Strategies

Many further non-technical strategies are implemented in the robot navigation interface, refer to section 4.2.4.3 for further explanation. Detailed instructions on sterilization should be considered in the future, however the current design allows for easy assembly and disassembly for sterilization purposes.

Risk Strategies

Many strategies chosen are related to technical strategies. The lack of mechanical vibrations prevent harm to the patient’s tissue as the robot traverses its pathway. Stall detection is also implemented to prevent excessive force if a robot’s component gets stuck, and the low actuation speed allows for more precise control compared to faster movement.

Compliance Strategies

Similar to the magnetic actuation system, IEC 60601-1 is also a key standard in this application. As mentioned in the magnetic actuation system, 60601-1 sets the general requirements for basic safety and essential performance of medical electrical equipment. This means electrical safety of motor drivers and circuitry, mechanical integrity under loading and thermal management.

Due to high electromagnetic fields generated by the magnetic actuation system, the actuator must be resistant to EMF interference, which were tested during verification and integration testing. Additionally, load testing was also performed during verification and complies with general expected loads during integration testing.

4.2.3.4 Assumptions, Limitations and Constraints

Assumptions

There are many assumptions made regarding the functionalities of the electronic components in the circuit. Namely, the calculations assume constant step accuracy and a stable power supply for motor torque and load handling. Also, the speed is assuming constant step signals from the microcontroller without significant variance in pulse intervals. It is also assumed that there is a unidirectional force on the actuating wire through the stepper gear.

Limitations

The main limitation of the linear actuator's design is the materials and machining tolerances. Sterilization testing could not be accomplished due to lack of biomaterial manufacturing resources, and 3D printed PLA gears required tolerances that are incompatible when working the millimeter scale. Additionally, the magnetic actuator's requirements of higher voltage limit the voltage supplied to the stepper motor, limiting its torque and loading capabilities.

Constraints

The biggest constraint in this project is size and power consumption. The size of the continuum robot must be compatible with the linear actuator, and the power consumption of the motor must not interfere with the power consumption of the magnetic actuation system. The size of the actuator is also a constraint, since it should not interfere with the surgery during the procedure. Lastly, sterilization constrains the design possibilities and materials, requiring a system that can be disassembled for sterilization.

4.2.4 Robot Navigation Interface and Simulations

The robot navigation interface was evaluated through targeted verification tests that were aligned with specified design inputs and associated risk mitigation strategies. The tests focus on assessing interface functionality, responsiveness, and system safety. The results indicate that the interface enables reliable activation in real-time through intuitive user interaction with the navigation system. Recursive simulations using the MagPy library in Python were performed in the development phase of the interface to model and visualize resultant magnetic field vector from various coil configurations. The interface successfully meets safety, usability, and precision requirements which have been validated through functional demonstrations and test point measurements. Remaining challenges, such as improved current modulation and enhanced intuitiveness with MRI scans can be future areas of refinement. This section presents a detailed discussion of the interface performance and implications for surgical applications.

4.2.4.1 Verification Results

A brief overview of the verification plans can be seen below:

- Plan ID 24. Measure the magnetic field from the MagPy simulation framework for one coil with positive current direction using the built-in library sensor as well as mathematical implementation at varying distances (distance = 0m, 0.05m, 0.10m, 0.15m, 0.20m). This is to verify the simulation results with the expected theoretical mathematical results.
- Plan ID 25. Measure the magnetic field from the MagPy simulation framework for one coil with negative current direction using the built-in library sensor as well as mathematical implementation at varying distances (distance = 0m, 0.05m, 0.10m, 0.15m, 0.20m). This is to verify the simulation results with the expected theoretical mathematical results.
- Plan ID 26. Observe the positive magnetic field direction produced by the coil using the interface. This is to verify that the coils field directionality executed from the interface aligns with the experimental results of the physical setup.
- Plan ID 27. Observe the negative magnetic field direction produced by the coil using the interface. This is to verify that the coils field directionality executed from the interface aligns with the experimental results of the physical setup.
- Plan ID 28. Observe the superposition principle of the generated magnetic field produced in the positive direction by one coil using the interface. This is to verify the magnetic field superposition on the interface results align with the experimental results of the physical setup.
- Plan ID 29. Observe the superposition principle of the generated magnetic field produced in the negative direction by one coil using the interface. This is to verify the magnetic field superposition on the interface results align with the experimental results of the physical setup.
- Plan ID 30. Observe the superposition principle of the generated magnetic field produced direction by two coils, both using positive current direction in the interface. This is to verify the magnetic field superposition on the interface results align with the experimental results of the physical setup.
- Plan ID 31. Observe the superposition principle of the generated magnetic field produced direction by two coils, one using positive current direction and the other using negative current direction in the interface. This is to verify the magnetic field superposition on the interface results align with the experimental results of the physical setup.
- Plan ID 32. Observe the superposition principle of the generated magnetic field produced direction by three coils, all using positive current direction in the interface. This is to verify the magnetic field superposition on the interface results align with the experimental results of the physical setup.
- Plan ID 33. Observe the superposition principle of the generated magnetic field produced direction by three coils, two using positive current direction and the other using negative current direction in the interface. This is to verify the magnetic field superposition on the interface results align with the experimental results of the physical setup.

- Plan ID 34. Observe the linear extension produced by the linear actuation system using the interface. This is to verify the linear actuation executed by the interface can present the extension of the robot in the physical setup.
- Plan ID 35. Observe the linear retraction produced by the linear actuation system using the interface. This is to verify the linear actuation executed by the interface can present the retraction of the robot in the physical setup.
- Plan ID 36. Observe the linear extension produced by the linear actuation system using the interface while the magnetic actuation of the robot is also enabled. This is to verify the linear and magnetic actuation executed by the interface can be presented in robot in the physical setup for real-time control.
- Plan ID 37. Observe the linear retraction produced by the linear actuation system using the interface while the magnetic actuation of the robot is also enabled. This is to verify the linear and magnetic actuation executed by the interface causes deactivation of the magnetic actuation system while the robot is retracting in the physical setup for real-time control.
- Plan ID 38. Observe the Complete Turn mechanism executed by the interface while the magnetic actuation of the robot is also enabled. This is to verify the deactivation of the magnetic actuation system after linear and magnetic actuation executed by the interface can be presented in the physical setup for real-time control.
- Plan ID 39. Observe the Emergency STOP mechanism executed by the interface while the magnetic actuation of the robot is also enabled. This is to verify the deactivation of the magnetic and linear actuation system after linear and magnetic actuation executed by the interface can be presented in the physical setup for real-time control.

Plan Id	Design Output	Inputs	Expected Values	Actual Values	Pass/Fail
24	5.1	Coil 1 Plane = Y Coil 1 Current: 15 A Coil 1 Radius: 0.05m Coil 1 Turns: 450 Coil 1 Length: 0.05m Distance1 = 0 m Distance2 = 0.05 m Distance3 = 0.10 m Distance4 = 0.15 m Distance5 = 0.20 m	Field1 > 80 mT Field2 > 30 mT Field3 > 5 mT Field4 > 2mT Field5 >1mT Coil 1 Colour = Green Coil 2 Colour = Grey Coil 3 Colour = Grey	Field1 = 84.8mT Field2 = 29.9mT Field3 = 7.6mT Field4 = 2.7mT Field5 = 1.2mT Coil 1 Colour = Green Coil 2 Colour = Grey Coil 3 Colour = Grey	Pass
25	5.1	Coil 1 Plane = Y Coil 1 Current: -15 A Coil 1 Radius: 0.05m Coil 1 Turns: 450 Coil 1 Length: 0.05m Distance1 = 0 m Distance2 = 0.05 m	Field1 > -80 mT Field2 > -30 mT Field3 > -5 mT Field4 > -2mT Field5 > -1mT Coil 1 Colour = Red	Field1 = -84.8mT Field2 = -29.9mT Field3 = -7.6mT Field4 = -2.7mT Field5 = -1.2mT	Pass

		Distance3 = 0.10 m Distance4 = 0.15 m Distance5 = 0.20 m	Coil 2 Colour = Grey Coil 3 Colour = Grey	Coil 1 Colour = Red Coil 2 Colour = Grey Coil 3 Colour = Grey	
26	5.2	Coil 1 Plane = Y Coil 1 Current: 15 A Coil 1 Radius: 0.05m Coil 1 Turns: 450 Coil 1 Length: 0.05m	Field Direction = Positive Y direction in interface Coil 1 Colour = Green Coil 2 Colour = Grey Coil 3 Colour = Grey	Field Direction = Positive Y direction in interface Coil 1 Colour = Green Coil 2 Colour = Grey Coil 3 Colour = Grey	Pass
27	5.2	Coil 1 Plane = Y Coil 1 Current: -15 A Coil 1 Radius: 0.05m Coil 1 Turns: 450 Coil 1 Length: 0.05m	Field Direction = Negative Y direction in interface Coil 1 Colour = Red Coil 2 Colour = Grey Coil 3 Colour = Grey	Field Direction = Negative Y direction in interface Coil 1 Colour = Red Coil 2 Colour = Grey Coil 3 Colour = Grey	Pass
28	5.3	Coil 1 Plane = Y Coil 1 Current: 15 A Coil 1 Radius: 0.05m Coil 1 Turns: 450 Coil 1 Length: 0.05m Distance = 0.10m	Field X = 0mT Field Y = 7.6 mT Field Z = 0mT Field Direction = Positive Y direction in interface Coil 1 Colour = Green Coil 2 Colour = Grey Coil 3 Colour = Grey Resultant field = 7.6 mT	Field X = 0 mT Field Y = 5.3 mT Field Z = 0 mT Field Direction = Positive Y direction in interface Coil 1 Colour = Green Coil 2 Colour = Grey	Pass

				Coil 3 Colour = Grey Resultant field = 5.3mT	
29	5.3	Coil 1 Plane = Y Coil 1 Current: -15 A Coil 1 Radius: 0.05m Coil 1 Turns: 450 Coil 1 Length: 0.05m Distance = 0.10m	Field X = 0mT Field Y = -7.6 mT Field Z = 0mT Field Direction = Negative Y direction in interface Coil 1 Colour = Red Coil 2 Colour = Grey Coil 3 Colour = Grey Resultant field = -7.6mT	Field X = 0mT Field Y = -5.28 mT Field Z = 0mT Field Direction = Negative Y direction in interface Coil 1 Colour = Red Coil 2 Colour = Grey Coil 3 Colour = Grey Resultant field = -5.28mT	Pass
30	5.3	Coil 1 Plane = Y Coil 1 Current: 15 A Coil 1 Radius: 0.05m Coil 1 Turns: 450 Coil 1 Length: 0.05m Coil 2 Plane = Z Coil 2 Current: 15 A Coil 2 Radius: 0.05m Coil 2 Turns: 450 Coil 2 Length: 0.05m Distance = 0.10m	Field X = 0mT Field Y = 7.6 mT Field Z = 7.6 mT Field Direction = Positive YZ direction in interface Coil 1 Colour = Green Coil 2 Colour = Green Coil 3 Colour = Grey Resultant field = 10.75 mT	Field X = 0 mT Field Y = 5.27 mT Field Z = 5.29 mT Field Direction = Positive YZ direction in interface Coil 1 Colour = Green Coil 2 Colour = Green Coil 3 Colour = Grey Resultant field = 7.47 mT	Pass

31	5.3	<p>Coil 1 Plane = Y Coil 1 Current: 15 A Coil 1 Radius: 0.05m Coil 1 Turns: 450 Coil 1 Length: 0.05m Coil 2 Plane = Z Coil 2 Current: -15 A Coil 2 Radius: 0.05m Coil 2 Turns: 450 Coil 2 Length: 0.05m Distance = 0.10m</p>	<p>Field X = 0mT Field Y = 7.6 mT Field Z = -7.6 mT</p> <p>Field Direction = Positive Y negative Z direction in interface</p> <p>Coil 1 Colour = Green Coil 2 Colour = Red Coil 3 Colour = Grey</p> <p>Resultant field = 10.75 mT</p>	<p>Field X = 0mT Field Y = 5.29 mT Field Z = -5.28 mT</p> <p>Field Direction = Positive Y negative Z direction in interface</p> <p>Coil 1 Colour = Green Coil 2 Colour = Red Coil 3 Colour = Grey</p> <p>Resultant field = 7.47 mT</p>	Pass
32	5.3	<p>Coil 1 Plane = Y Coil 1 Current: 15 A Coil 1 Radius: 0.05m Coil 1 Turns: 450 Coil 1 Length: 0.05m Coil 2 Plane = Z Coil 2 Current: 15 A Coil 2 Radius: 0.05m Coil 2 Turns: 450 Coil 2 Length: 0.05m Coil 3 Plane = X Coil 3 Current: 15 A Coil 3 Radius: 0.05m Coil 3 Turns: 450 Coil 3 Length: 0.05m Distance = 0.10m</p>	<p>Field X = 7.6mT Field Y = 7.6 mT Field Z = 7.6 mT</p> <p>Field Direction = Positive XYZ direction in interface</p> <p>Coil 1 Colour = Green Coil 2 Colour = Green Coil 3 Colour = Green</p> <p>Resultant field = 13.16 mT</p>	<p>Field X = 5.29mT Field Y = 5.19mT Field Z = 5.59mT</p> <p>Field Direction = Positive XYZ direction in interface</p> <p>Coil 1 Colour = Green Coil 2 Colour = Green Coil 3 Colour = Green</p> <p>Resultant field = 9.28mT</p>	Pass
33	5.3	<p>Coil 1 Plane = Y Coil 1 Current: 15 A Coil 1 Radius: 0.05m Coil 1 Turns: 450 Coil 1 Length: 0.05m Coil 2 Plane = Z</p>	<p>Field X = 7.6mT Field Y = 7.6 mT Field Z = -7.6 mT</p>	<p>Field X = 5.0mT Field Y = 6.6mT Field Z = -6.6mT</p> <p>Field Direction = Positive XY and</p>	Pass

		<p>Coil 2 Current: -15 A Coil 2 Radius: 0.05m Coil 2 Turns: 450 Coil 2 Length: 0.05m Coil 3 Plane = X Coil 3 Current: 15 A Coil 3 Radius: 0.05m Coil 3 Turns: 450 Coil 3 Length: 0.05m Distance = 0.10m</p>	<p>Field Direction = Positive XY and Negative Z direction in interface Coil 1 Colour = Green Coil 2 Colour = Red Coil 3 Colour = Green Resultant field = 13.16 mT</p>	<p>Negative Z direction in interface Coil 1 Colour = Green Coil 2 Colour = Red Coil 3 Colour = Green Resultant field = 10.59mT</p>	
34	5.4	Linear Actuator: Extension	Linear Actuator: Extension	Linear Actuator: Extension	Pass
35	5.4	Linear Actuator: Retraction	Linear Actuator: Retraction	Linear Actuator: Retraction	Pass
36	5.5	<p>Coil 1 Plane = Y Coil 1 Current: 15 A Coil 1 Radius: 0.05m Coil 1 Turns: 450 Coil 1 Length: 0.05m Distance = 0.05m</p> <p>Linear Actuator: Extension</p>	<p>Linear Actuator: Extension Coil 1 Colour = Green Coil 2 Colour = Grey Coil 3 Colour = Grey Field X = 0mT Field Y = 7.6 mT Field Z = 0mT</p>	<p>Linear Actuator: Extension Coil 1 Colour = Green Coil 2 Colour = Grey Coil 3 Colour = Grey Field X = 0mT Field Y = 5.19 mT Field Z = 0mT</p>	Pass
37	5.5	<p>Coil 1 Plane = Y Coil 1 Current: 15 A Coil 1 Radius: 0.05m Coil 1 Turns: 450 Coil 1 Length: 0.05m Distance = 0.05m</p> <p>Linear Actuator: Retraction</p>	<p>Linear Actuator: Retraction Field X = 0mT Field Y = 0 mT Field Z = 0mT Coil 1 Colour = Grey Coil 2 Colour = Grey Coil 3 Colour = Grey</p>	<p>Linear Actuator: Retraction Field X = 0mT Field Y = 0 mT Field Z = 0mT Coil 1 Colour = Grey Coil 2 Colour = Grey Coil 3 Colour = Grey</p>	Pass

				Coil 3 Colour = Grey	
38	5.6	<p>Coil 2 Plane = X Coil 2 Current: 15 A Coil 2 Radius: 0.05m Coil 2 Turns: 450 Coil 2 Length: 0.05m</p> <p>Complete Turn: ON</p>	<p>Complete Turn: ON Field X = 0 mT Field Y = 0 mT Field Z = 0mT</p> <p>Coil 1 Colour = Grey Coil 2 Colour = Grey Coil 3 Colour = Grey</p>	<p>Complete Turn: ON Field X = 0mT Field Y = 0 mT Field Z = 0mT</p> <p>Coil 1 Colour = Grey Coil 2 Colour = Grey Coil 3 Colour = Grey</p>	Pass
39	5.6	<p>Coil 1 Plane = Y Coil 1 Current: 15 A Coil 1 Radius: 0.05m Coil 1 Turns: 450 Coil 1 Length: 0.05m Coil 2 Plane = X Coil 2 Current: 15 A Coil 2 Radius: 0.05m Coil 2 Turns: 450 Coil 2 Length: 0.05m</p> <p>Linear Actuator: Extension Emergency STOP: ON</p>	<p>Emergency STOP: ON Linear Actuator: Idle Field X = 0 mT Field Y = 0 mT Field Z = 0mT</p> <p>Coil 1 Colour = Grey Coil 2 Colour = Grey Coil 3 Colour = Grey</p>	<p>Emergency STOP: ON Linear Actuator: Idle Field X = 0mT Field Y = 0 mT Field Z = 0mT</p> <p>Coil 1 Colour = Grey Coil 2 Colour = Grey Coil 3 Colour = Grey</p>	Pass

4.2.4.2 Modelling and Analysis Results

To validate the feasibility and accuracy of the integrated system, multiple simulations and experimental testing occurred with variations of current and distances between coil edge and magnetic sensor under controlled conditions. The following graphs present the relationship between the simulated and experimental results.

Magnetic Field vs. Distance

The initial phase of testing involved MagPy-based simulations of the magnetic field strength emitted from the edge of a single coil over increasing axial distances. At a constant current of 15A, the simulation results demonstrate an exponential decay with the magnitude of the magnetic field seen in Figure 87. It is observed that the initial field at 0cm was approximately 85mT and it rapidly decreased to less than 5 mT at 20 cm away from the coil edge. This behaviour aligns with the solenoid field equations stated below:

$$B_{solenoid} = \frac{\mu_0 \cdot I_{solenoid} \cdot N_{turns}}{l_{solenoid}} \quad (24)$$

Once measurements are taken outside of the solenoid, especially along the central axis, the field diminishes quickly due to spatial dispersion of magnetic flux. The same behaviour as above can be seen in Figure 88. By applying the same current in the negative direction, this confirmed the reversibility of the magnetic field seen be the decayed trend in the negative direction. This symmetric relationship confirms These findings present the directional field control can be theoretically achieved through current inversion. The simulated support the design aspects of directional magnetic control by validating the predictable field decay, demonstrating reversible magnetic actuation, and informing optical coil placements.

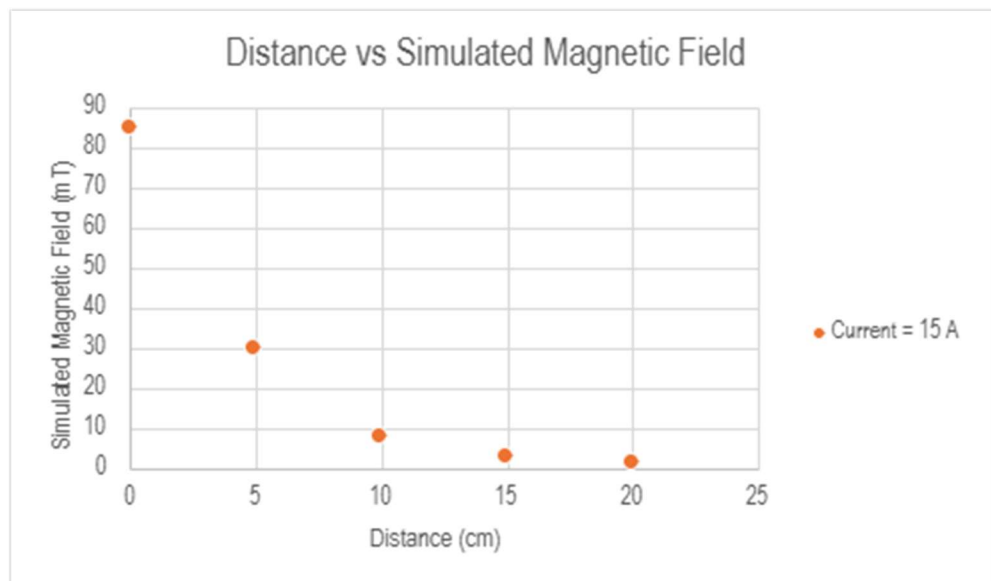


Figure 87. Simulated results of magnetic field generated over varying distances with a constant current of 15A applied.

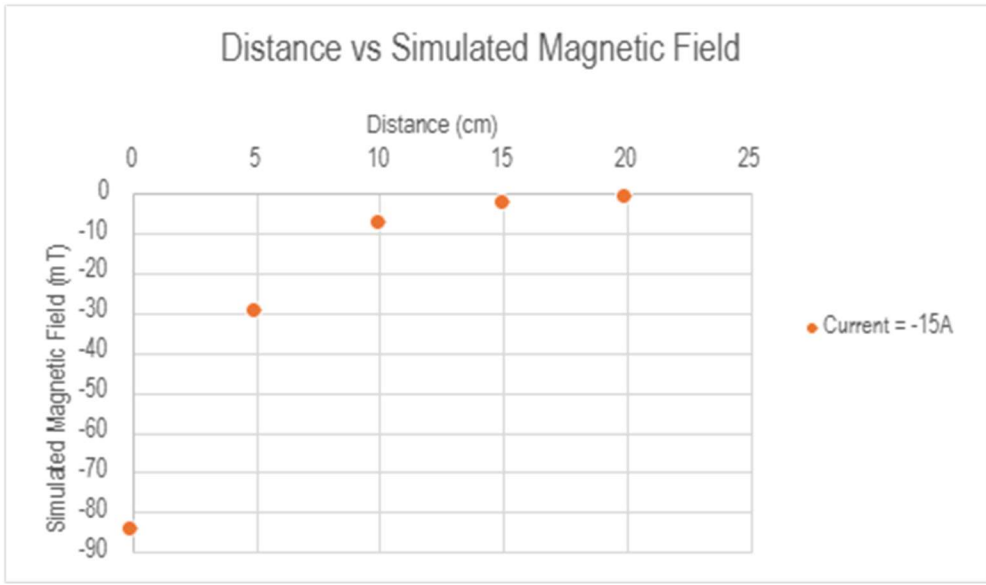


Figure 88. Simulated results of magnetic field generated over varying distances with a constant current of -15A applied.

Magnetic Field vs. Current and Directionality

To further validate the behaviour of the magnetic actuation system under varying current magnitudes and direction, the simulated and experimental results were conducted over a range of positive and negative current values. The results below present the relationship between current and magnetic field strength for both polarities.

As seen in Figure 89, the current was increased from 15A to 30A. The results of the graph show the strong linear correlation between increasing current and magnetic field strength in both of the simulated and experimental results by about 10mT. The discrepancy can be attributed to minor losses from the physical setup such as resistance from contacting wires or coil winding inconsistencies that are not present in the simulations. Despite the difference the experimental field strength follows the same trend confirming the theoretical relationship that the magnetic field is proportional to the current, which aligns with the equation given above.

As well with Figure 90, the testing uses the same current magnitudes as above but in the negative direction. As stated, the simulation and experimental results present the same linear trend. The polarity of the magnetic field is reversed as expected, confirming the system's ability to dynamically change the field direction for more positionings of magnetized robot tip. The confirms the design requirement to produce magnetic fields in opposite directions for multi-directional robot motion.

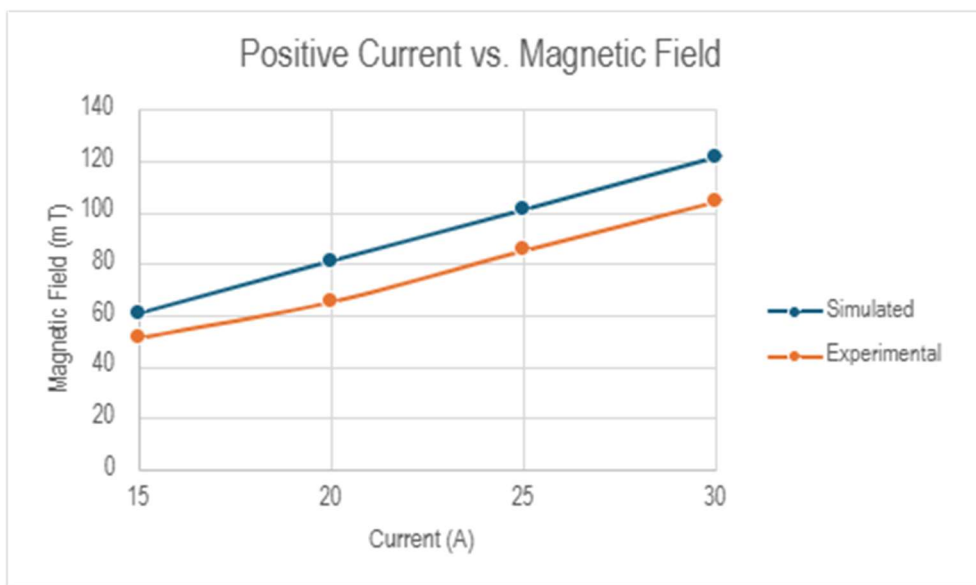


Figure 89 Simulated and experimental magnetic field strength from positive current variations

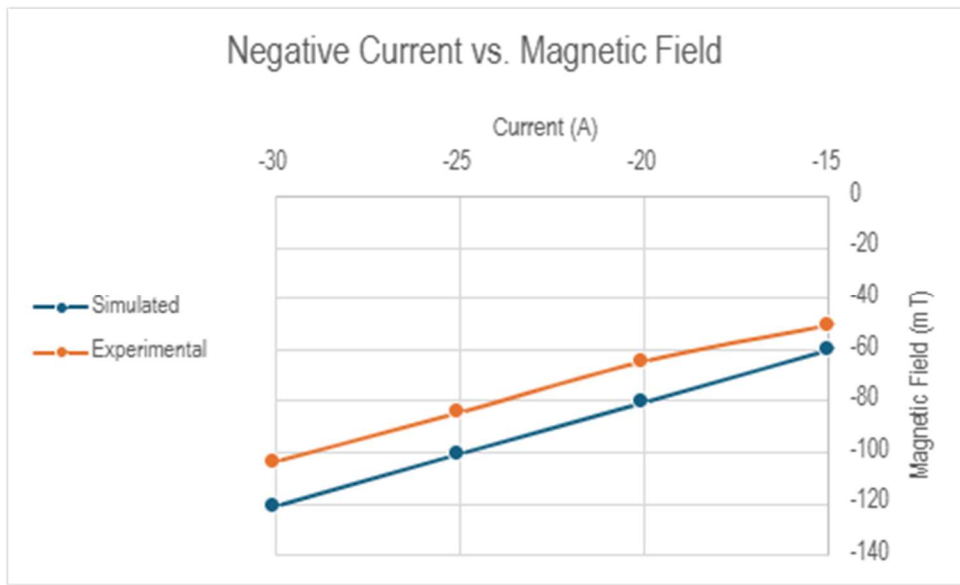


Figure 90 Simulated and experimental magnetic field strength from negative current variations

Magnetic Field Superposition Analysis

To validate the theoretical principle of magnetic field superpositioning, further simulations and experimental tests were conducted using one, two, and three coils, using the equation below:

$$B_{total} = \sum_{i=1}^n B_i \quad (18)$$

The coils were all equidistantly placed like the physical setup, 10cm away from a central measurement point. Each test was repeated for both positive and negative currents of 15A or -

15A. To achieve the resultant magnetic field generated at a central point, the following equation was applied.

$$|B_{total}| = \sqrt{B_x^2 + B_y^2 + B_z^2} \quad (27)$$

The results from the positive and negative current testing demonstrate a clear additive relationship between the number of coils and the magnetic field magnitude as seen in Figure 91 and Figure 92. As expected by the principle, the combined field strength increases with each additional coils outputting the same field. The simulated and experimental data are relatively close, but the differences can be due to resistance at contact points or thermal loss. The consistency between the simulated and experimental results confirms the reliability of the field model which is crucial for the control scheme of the robot as it requires the combination of various field configurations to achieve multi-positioning of the robot tip. These tests confirm the bidirectional nature of the magnetic actuation system and support the integration of the robot navigation interface with the integrated system.

**Validation of Magnetic Field Superposition Equidistant (10cm)
from Coils with Positive Current**

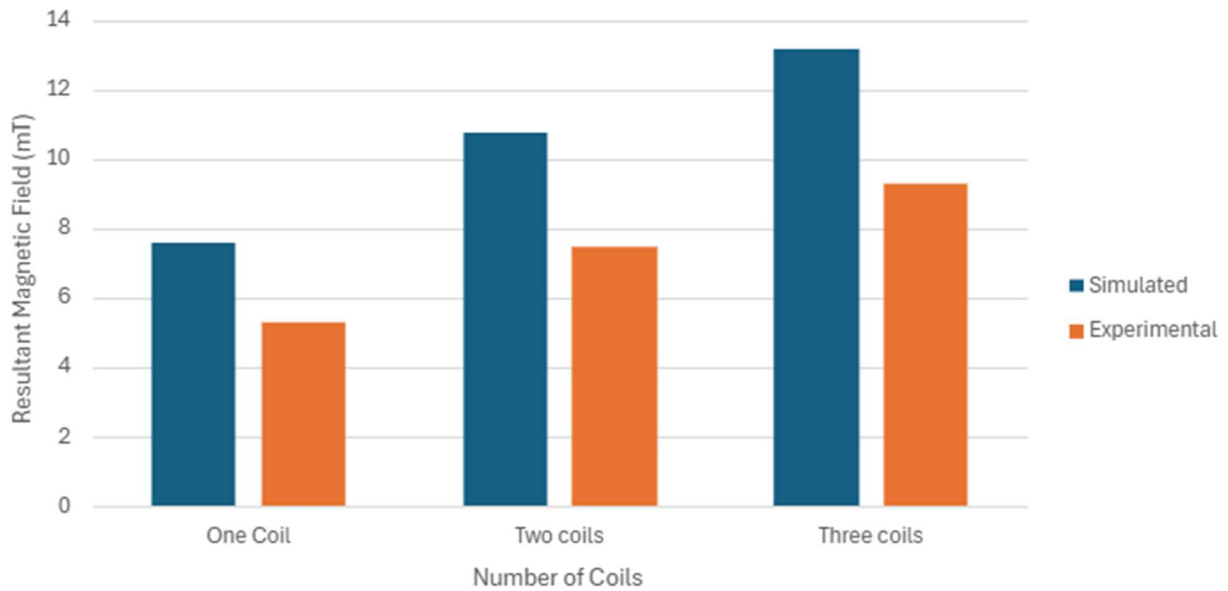


Figure 91 Magnetic field superposition principle with positive current input of 15A

Validation of Magnetic Field Superposition Equidistant (10cm) from Coils with Negative Current

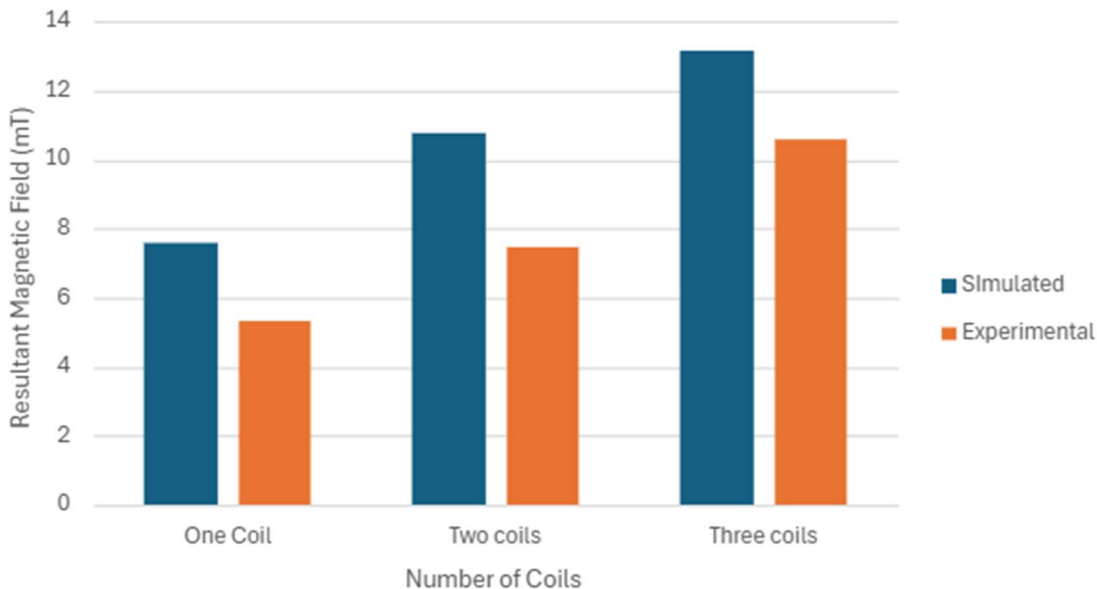


Figure 92 Magnetic field superposition principle with negative current input of -15A

Integrated System and Safety Mechanisms

To validate the functionality and reliability of the integrated system, a series of experimental trials were conducted in alignment to the verification plans. The trials were designed to assess the independent control of the magnetic and linear actuation system, as well as their synchronized behaviour and response to safety protocols.

Linear and Magnetic Actuation Coordination

The testing of these systems confirmed the system's ability to independently and simultaneously operate the magnetic and linear actuation systems. Multiple trials of extension and retraction were initiated from the interface and the corresponding physical response was matched with consistent repeatability. Each configuration successfully achieved the expected output confirming the communication between the interface, microcontroller logic, and mechanical subsystems.

Fail-Safe Mechanism Evaluation

Critical safety features such as Complete Turn and Emergency Stop were tested vigorously. The mechanisms were designed to instantly deactivate the magnetic actuation system and/or the linear actuation system in the event of unexpected behaviour. The Complete Turn mechanism was able to successfully shift to the active coils in all configurations regardless of the

number of coils activated. As well, the Emergency Stop mechanism was able to halt both systems which was confirmed with the interface feedback as well as the observed system behaviour.

In conclusion, each test that was executed from the verification plan had passed, demonstrating the full validation of the integrated system in compliance with safety requirements

4.2.4.3 Technical, Non-Technical, Risk, and Compliance Strategies

Technical Strategies

The robot navigation interface is developed over a robust software hardware integration framework. The commands issued by interactions on the Python based visualization are sent to an ESP32 microcontroller that actuates the magnetic and linear actuation systems. This architecture allows for reliable real time control of the robot's movement by translating user inputs into electrical signals that drive the electromagnetic coils and stepper motor. The precision and stability of the full system is enhanced by the embedded logic, including debouncing routines and toggling mechanisms. The system's efficacy is further validated through numerous simulations as well as measurements of the integrated system using tools like oscilloscopes and multimeters to confirm accurate signal transmission and actuation across all components. As well, the interface has colour-based feedback mechanisms that reflect the status of the coils to provide visual cues to the user. This closed loop feedback between the interface and hardware ensures that the surgical tool can be utilized with high fidelity during the experimental and simulated process.

The integration of real time feedback mechanisms, such as haptic feedback, is important to enhance the precision and safety of robotic surgical systems. Studies have shown that haptic feedback can significantly improve surgical performance through tactile information which can be essential for delicate procedures. A study from 2022 regarding the use of real time feedback on surgical performance demonstrated that real time sensory feedback, specifically in the form of haptic cues, significantly reduced error rates and improved task efficiency during soft tissue dissection using a robotic system [13]. The study found that novice users were able to make notable improvements with confidence given the provided continuous feedback. This showcases the importance of integrating such feedback mechanisms within the interface, specifically for procedures involving delicate anatomical navigation. Although physical haptics are not yet implemented into the current robot navigation system, the visual feedback offered by the software visualization aligns with the underlying principles of real time feedback to overall enhance user awareness and precision. By incorporating and expanding real time feedback into future iterations of the design, this enhances the surgical user experience based on the best practices in robotic system design.

Furthermore, the application of advanced microcontrollers like the ESP32 in robotic systems has been explored in various studies. The microcontroller's capabilities in handling complex tasks and integration with IoT applications allows it to be a suitable choice for such applications. As a result the interface can achieve higher efficiency and responsiveness with the integrated system which is critical for surgical applications.

Non-Technical Strategies

The design of the interface prioritizes user-centric principles to ensure that clinicians can operate the system intuitively and safely without extensive technical training. This approach is based on the IEC 62366-1:2015, which is an international standard that emphasizes the application of usability to medical devices focusing on effectiveness and user safety [8]. The interface utilizes intuitive controls and visual indicators to address ergonomic challenges faced by surgeons by reducing cognitive load and enhancing ease of use. This philosophy is supported by studies that highlight the importance of user centred design in surgical robots. An example is Senhance, which incorporates ergonomic features such as open cockpit design to allow surgeons to operate from a comfortable seated position which can result in improved procedural outcomes and reduced physical strain on surgeons during long procedure [16].

The iterative development process of the interface involved usability testing and feedback from stakeholders. This ensures that the interface can meet the practical needs of clinicians to enhance both functionality and user satisfaction. This user focussed development was important in creating the interface to ensure it was both effective and aligns with clinical workflows. As well, the integration haptic feedback mechanisms into the interface design have shown enhanced performance which improves the precision in the delicate procedures. By incorporating feedback systems as such, it aligns with the best practices in surgical robots which aim to enhance user experience and procedural safety. By adherent to established standards and incorporating feedback from stakeholders, the design ensures that the system is not only technically robust but meets the ergonomic and practical needs of its users, thereby contributing to safer and effective procedures.

Risk Strategies

The interface incorporates comprehensive risk mitigation strategies for safe deployment of surgical robotic systems which have been guided by the ISO 14971:2019 for risk management in medical devices [7]. The integration fail-safe mechanisms such as the Emergency Stop and Complete Turn functions enable immediate deactivation of the magnetic and linear actuation systems in response to unexpected behavior. These functions mitigate risks related to uncontrolled motions which in surgical environments can lead to tissue trauma or procedural failure. Research supports the role of such immediate shutdown systems in robotic platforms. Specifically, robotic-assisted percutaneous coronary intervention (RA-PCI) systems have presented high clinical success rates with minimal adverse events, which show the importance of integrated safety features, especially during navigation in anatomical regions for robotic surgical applications [17].

Ergonomics in system design further strengthen the risk strategy by directly addressing user error, which is a major source of device-related harm in clinical settings. Pressure surgical environments, the predictability and clarity of the user interface is necessary to reduce cognitive load and avoiding unintended actions. According to ISO 62366-1:2015, medical device developers must incorporate usability considerations to minimize risks associated with usage to ensure that user interaction errors do not translate into patient harm [8]. This is important in minimally invasive robotic surgery where surgeons rely on system responsiveness and intuitive controls to perform the complex manipulations. In alignment with this standard, the navigation interface utilizes multiple safeguards focused on the user. Visual feedback is encoded through the system with colour-coded visualizations to indicate real time status of electromagnetic coils, where green is for an attraction exerted by the coil, red for repulsion force and grey for inactivation of the coil. These visual cues are continuously updated in tandem with the microcontroller logic such that users can make immediate and confident decisions about their robot's state. This design choice was informed by findings in surgical robotic literature, where real time visual feedback has shown to significantly improve situational awareness and reduce response time in critical moments.

In adherence to IEC 60601-1-6, which highlights the integration of usability features into safety performance requirements of medical equipment, there were multiple considerations made [9]. For instance, button placements on the interface, actuation latency, and feedback latency between the user interface inputs and mechanical outputs have been refined to ensure that users can timely receive confirmation of their inputs without ambiguity. As well, activating a coil results in visual updates within milliseconds, which minimizes uncertainty and overall avoids unsafe overlap of magnetic fields during navigation. Beyond the visual design, ergonomic considerations were included in the interface layout. Buttons for linear and magnetic actuation are spatially grouped and labeled according to their function and orientation to reduce the cognitive load required for executing different commands. These design strategies are based on the principles of cognitive ergonomics where Alignment between interface behavior and user expectations is key.

Therefore, the focus on human factors with the interface not only fulfills regulatory standards but also acts as preventative safety mechanisms for the user. By minimizing uncertainty, streamlining control interactions, and embedding multimodal feedback loops, the interface can reduce the likelihood of hazardous scenarios resulting from cognitive overload, misinterpretation, or control delay.

Compliance Strategies

As stated above, the interface design is in line with international standards to ensure safety, usability, and compliance with medical device development. Guided by the ISO 62366-1:2015, analyzing and developing the usability of medical devices is related to safety [8]. By adhering to the standard, developers can assess and mitigate risks associated with correct usage and errors to enhance the overall safety of the system. As well integration of ISO 14971 in the design process ensures that all potential risks are systematically addressed through the interface [7]. As mentioned above, the user centred design principles incorporated minimize the chance of usage errors. This includes intuitive controls, clear labeling, and real time feedback mechanisms to enhance user interaction. These design considerations are important to prevent errors that could arise from complex or non intuitive interfaces.

By integrating these standards and design principles the interface complies with regulatory requirements and provides a safer and effective user experience. The approach to compliance and usability is essential to the development of the interface to ensure safety and user friendliness.

4.2.4.4 Assumptions, Limitations, and Constraints

Assumptions

The development and implementation of the robot navigation interface were executed under several key assumptions which account for both system development and clinical use. One assumption was that the robot would operate along a pre-defined surgical. This would be developed in advance to the surgery from patient imaging or surgical planning, to ultimately avoid relying on dynamic real-time pathfinding. This would significantly reduce the computation burden of the system and cognitive load of the operator and instead, allow enhanced focus on the actuation accuracy and responsiveness opposed to the complex navigational actuation. Furthermore, it is assumed that the system operator, primarily surgeons or trained clinicians, would have prior training and familiarity of the interface in terms of layout and basic control logic to therefore, minimize the learning curve that may come with the integrated system at first. This assumption had further informed design decisions of incorporating labeled toggle buttons for magnetic and

linear actuation, status indicators, and real-time visual updates for ease of usage. Lastly, the system was developed under the assumption of reliable operation conditions, meaning that the system is expected to function without interferences from cases such as sudden power loss or hardware connectivity issues.

Limitations

Although the system fulfills the core design objectives, there are several limitations that affected the scope and generalizability of the robot navigation interface. A notable limitation is that the interface has not been tested in a clinical or operating room environment, where several factors such as surgical lighting, proximity to other equipment, and time-sensitive user demands can impact system performance. As a result, the findings drawn from this testing phase are restricted to controlled lab conditions and may not accurately represent the interface's performance in clinical settings. Another limitation is that usability testing of the interface was limited to a small sample of internal testers that are on the team. While the feedback from the team was valuable for refining button logic and feedback timing, it does not represent the concerns of the intended users with the clinical background, experience level, or ergonomic expectations. This restricts the ability to generalize usability results or make definitive claims about the system's ease of use.

Constraints

The development process was based on several hardware and environmental constraints that shaped the final design. The computational limitations of both the ESP32 microcontroller along with the development computer limited the complexity of real-time updates. When running multiple libraries simultaneously, such as MagPy and PyVista for magnetic field visualization along with user interface and control logic scripts, the system experienced a reduced frame rate update and delayed signal responsiveness. The performance issues hindered the ability to support continuous real-time feedback of the interface. As a result, advanced features such as sensor-feedback integration or smooth user interaction animations were excluded to preserve functionality. The constraints emphasize the need for high-performance hardware for the interface to be well-applicable for real-time clinical applications.

4.3 Future Work

While the final iteration of the magnetically actuated soft continuum robot for ENT surgery met the functional requirements for the scope of this project, several enhancements are necessary to transition the system from a capstone project to a clinically viable device:

4.3.1 Soft Continuum Robot

4.3.1.1 Miniaturization to <4 mm Diameter:

While the current 4 mm robot diameter aligns with standard nasal endoscopes and is clinically acceptable for navigating the paranasal sinuses, literature suggests that smaller-diameter instruments may offer meaningful advantages. A comparative study by Neel et al. found that 3 mm endoscopes enabled better maneuverability and access than 4 mm scopes, especially in anatomically narrow regions such as the middle meatus and frontal recess. Reducing the robot diameter to less than 4 mm would allow for improved access in these challenging anatomical locations, enhance patient safety, and reduce mucosal trauma during navigation.

Achieving this will require two parallel improvements: (1) enhancing the magnetic field strength of the robot tip by increasing NdFeB particle density or adopting alternative magnetically responsive materials (e.g., Fe₃O₄ nanoparticle composites), and (2) improving magnetic field generation with higher-efficiency coils or upgraded power supplies. Manufacturing approaches must also be refined, as previous attempts at 2 mm diameter prototypes (e.g., Robot D) suffered from inconsistent molding and the inability to form helical protrusions at that scale.

4.3.1.2 Fatigue, Durability, and Long-Term Performance Testing:

The current prototype was verified under short-duration testing conditions. For translation to clinical use, the robot must undergo fatigue testing to evaluate degradation of nitinol wire performance, potential delamination or tearing of the silicone body, and stability of the embedded magnetic field under repeated actuation. This aligns with standards for surgical tool reliability and is critical for determining long-term viability under cyclic loads .

4.3.1.3 Functional Enhancements for Surgical Use:

A key area of expansion involves integrating functional tools directly into the robot body. This would evolve the soft continuum robot from a navigational probe into a multifunctional surgical device. Possible embedded modules include: high-resolution microcameras for real-time visual feedback during endoscopic procedures, miniaturized biopsy forceps or graspers for tissue sampling, localized drug delivery ports (e.g., steroid injection for inflammation control), or laser ablation tips for minimally invasive removal of tissue or polyps. These additions mirror modular catheter systems used in interventional cardiology and robotic ENT tools currently under review in endoscopic robotics literature , . Embedding such tools will require further miniaturization and control integration, creating opportunities for multidisciplinary collaboration with biomedical imaging, signal processing, and surgical robotics teams.

4.3.1.4 Surgical Navigation Integration

To increase clinical relevance in ENT surgeries specifically, the soft continuum robot should be integrated into navigation platforms such as the Medtronic StealthStation S8, allowing real-time localization of the robot within CT-based anatomical models. This would enable the robot to replace rigid probes typically used in navigation-guided ENT surgeries and allow for dynamic, magnetic navigation within tracked environments. As well, these are platforms already being used in ENT surgeries and would be familiar to healthcare professionals.

4.3.2 Magnetic Actuation System

4.3.2.1 Stronger Power Supply

As discussed in the limitations portion in section 4.2.2.4, one of the biggest limitations is that the team only has access to standard benchtop power supplies, rather than medical-grade power generators. Future work could include sourcing stronger power supplies, capable of supplying more current to the coils, effectively increasing the achievable magnetic field. In a hospital setting, a 1.5T MRI will use approximately 480V and 320A . Acquiring a power generator capable of supplying 320A is not realistic as an upcoming next step of the project. However, acquiring a power generator capable of supplying around 100A is realistic. A power supply of that strength retails for around \$1,300 , which was out of scope for a capstone budget, however for a project receiving external funding, this is a more reasonable cost.

4.3.2.2 Cooling System

As discussed in the constraints portion in section 4.2.2.4, a major point of consideration for this project is ensuring the coils do not surpass 100°C during operation. Currently, this is done by ensuring the coils are only activated for short bursts of approximately two to five seconds. In future iterations, a proper cooling system can be integrated so that the system can be activated for longer periods of time. For an MRI system, the cooling is typically done using liquid helium. Unfortunately, liquid helium is very costly as it is a limited resource . Other cheaper options including cooling with water, liquid nitrogen, and even air can be considered . Future work can include starting with an air-cooling system as this will be simplest to implement on a low budget.

4.3.2.3 Improved Housing

Future work can include improving the housing for the coils to conceal them from the patient. In an MRI machine, the coils are completely hidden from the patient, which helps with patient comfort overall. This project will implement something similar; a clean and simple housing that covers the coils to improve the patient's experience.

4.3.3 Linear Actuation System

4.3.3.1 Rotational Movement

A major next step would be proper rotational movement in tandem with linear movement, to match the helical design of the robot itself. During testing, it was found that rotational movement decreases frictional forces and facilitates turning when navigating through winding and narrower pathways.

4.3.3.2 Faster and Custom Velocity Control

Increase stepper motor's maximum speed to allow for faster and variable speeds while still maintaining a high level of precision, and maintaining torque and load capacities. Future work could speed up the surgical process, while maintaining or improving the precision of the linear actuator. For easier pathways, allowing the surgeon to speed up the movement, as well as slow down the robot during more precise segments will increase the usability of the system.

4.3.3.3 Sterilization

Design the entire device to be autoclavable or isolate the robot from the rest of the device with a sterile barrier. This step is necessary to abide by the standards and guidelines that were mentioned throughout this report.

4.3.4 Robot Navigation Interface and Simulations

4.3.4.1 Integration of Real-Time Positional Feedback Mechanisms

A major enhancement for the navigation interface is the application of real time positional feedback to inform the user of the robot's spatial state during operation. Currently, the interface operates under open loop assumptions. This means the user inputs are sent to the robot without confirmation of the resultant robot tip orientation. It introduces ambiguity as navigating the robot through confined anatomical spaces like the sinus, where vision is limited, can be difficult. Future iterations of the project should integrate sensor-based feedback by embedding magnetic sensors within the robot tip. The sensor data can be presented on the interface and used to generate dynamic 3D positional visualizations to improve surgical precision. As well, filters could be added to the sensor feedback to reduce noise and ensure reliability. This closed loop system would enhance the interface from a reactive control tool to a feedback-based system, aligning with current innovations in surgical robots to improve clinical safety and confidence.

4.3.4.2 Magnetic Field Modulation and Visualization

The current interface uses binary states to actuate the electromagnetic coils meaning there is limited control over the magnetic field generated. This restricts maneuverability and precision specifically in spaces with high curvature. To enhance the systems capability, the future work should implement field modulation through current variation for real time control with magnetic actuation. This modification would allow for incremental directional changes opposed to discrete states. This would reduce any unintentional overshoot with the robot motion. As well, with further back-end magnetic field calculations, the interface could display real time 3D magnetic field visualization. This allows users to understand the expected field superposition effects and help optimize their actuation sequences.

4.3.4.3 Interface Redesign for Surgical Ergonomics

Although the current interface is functionally robust, it can be further optimized by restructuring the control logic in visual feedback to align with surgical ergonomics. In high stress clinical settings, it is important to prioritize ease of interaction with the interface. For future iterations implementing a gesture based input system along with screen prompts and live status indicators could improve current ENT surgical operations. The interface could adapt based on the type of actuation (magnetic or linear) Which would reduce visual clutter and streamline decision making during usage. As well, the use of heat maps or previously visited regions could support spatial pathway planning. To further understand the usability of the interface the design should be tested with practicing surgeons to evaluate intuitiveness, failure recovery, and workload impact.

4.4 Reflections and Recommendations

4.4.1 Successes, Failures, and Setbacks

Overall, this capstone project was a success, meeting major milestones and most design requirements and goals set out during the project's initial conception. Before discussing each component, an initial reflection on the entire project is important to encompass the more general issues. The total number of deliverables, as well as the requirements for each deliverable was a big challenge throughout the course. Our group's struggle in understanding the topic and goal of each report was a core and recurring issue throughout the stages of this project, and most setbacks will be centered around this issue.

The initial project proposal demonstrated each member's willingness to contribute to the project. This can be shown through Chapter 1's Gantt chart, where deadlines were met at every step. However, the team failed to look ahead to chapter 2 during the project proposal, which led to delays. Specifically, the design inputs, user needs and preliminary risk assessment were made with the idea that it can be modified and changed throughout the course of the project, as opposed to attempting to match future projects and design requirements to the best of our ability. Therefore, although the early process for design configuration matched closely with Chapter 2's Gantt chart's timelines, the project was delayed midway, since the team had to redefine the design inputs, user needs and redo the risk analysis due to the drastic change in the conceptual design between Chapter 1 and Chapter 2. This could have been prevented had we taken the time to better understand the goal and purpose of the project proposal in Chapter 1. For example, in the Chapter 1 report, multiple possible continuum robot designs were discussed and mentioned. However, a final design concept was never chosen, so the design inputs attempted to cover inputs for all the designs, instead of specifically to one. This continued to be a problem in Chapter 2 design configurations, despite the team having decided on a final design concept. The team attempted to match the design outputs of the specific design to the inputs meant for a broader scope. This led to compounding issues for the rest of the project.

The setbacks were seen as unforeseen delays, and the team increased the working times to meet the deadlines of the proof-of-concept. Although the Chapter 2 Gantt chart still showed a delay that lasted until the end of the fall term, this was due to a different reason. The original plan for the proof-of-concept was to show low-fidelity prototypes of each individual component (actuator, coils and robot). However, since each component was completed early, there was time to integrate the components together for the fall demonstration. Additionally, the team took the time to understand each requirement for the proof-of-concept, and the setbacks of Chapter 1 were slowly getting addressed, heading closer to the deadline for Chapter 2. This resulted in a fully integrated proof-of-concept, which clearly demonstrated the final vision of the project. This can be seen in the logged internal meetings on the final Gantt chart. The team met up the most throughout late October to mid-November, discussing design updates, decisions, and requirements.

Transitioning to Chapter 3, the final design concept was finalized, and efforts were focused on building and prototyping. However, a lack of meetings and general complacency led to a major delay in the testing and validation phase. Verification and testing methods should have been considered when writing Chapter 2 outputs. This relates back to the theme of understanding the purpose of the reports. Therefore, despite the success of Chapter 2 deliverables, it had not prepared the team to properly consider the testing and validation of Chapter 3. Many testing methods were not properly considered when stating output in Chapter 2. This resulted in a one-week delay

between the projected deadline and actual submission, highlighted in Chapter 3 and 4's Gantt chart.

With the final prototype, the team organized and planned every deadline and deliverable, learning from the setbacks throughout the course of the project. Personal commitments such as midterms and assignments were taken into consideration, and every deliverable and deadline were planned out and assigned to each person well in advance. Each deadline was also organized and listed to include more details in a separate file titled “capstone calendar”, found in our DHF. The schedules had been planned out, and communication was thoroughly maintained and updated throughout the final stretch of the project. Although the deliverables were still delayed, the pre-assigned deadlines had accounted for delays and setbacks, and all testing and prototyping were completed for submission.

Overall, there were major setbacks throughout the course of the project. However, the team’s willingness to learn from each setback and adaptability ensured proper completion and success in delivering a working prototype which met the stakeholder’s design requirements.

4.4.2 Advice to the Future Cohort

Mackenzie: Having a team calendar with individual deadlines set throughout the semester was helpful in keeping the project moving forward, especially during the ‘middle months’.

Jack: You have less time than you anticipate, so just start prototyping and building from the very start. It’ll make Semester two less busy!

Jiaqi: Build your first prototype as soon as possible. You’ll learn a lot more about oversights and design requirements.

Sharon: Keep everyone, including yourself, consistently updated on progress—clear, regular communication keeps the whole team on the same page, avoids confusion, and improves overall efficiency.

Raidah: Start early, test often, and document everything with pictures and excel sheets. Communicate clearly with your team, ask for help, and enjoy the experience!

Chapter 4 References

- [1] ISO, "ISO 10993-1:2018 - Biological Evaluation of Medical Devices – Part 1: Evaluation and Testing Within a Risk Management Process," International Organization for Standardization, Geneva, Switzerland, 2018.
- [2] Advanced Motor Controls, "Advanced Motor Controls AB50A200I Datasheet," 02 02 2022. [Online]. Available: <https://www.a-m-c.com/product/ab50a200i/>. [Accessed 15 02 2025].
- [3] Cytron Technologies, "Cytron Marketplace," 2004. [Online]. Available: https://www.cytron.io/p-40amp-10v-45v-smartdrive-dc-motor-driver?srsltid=AfmBOop0VEwLkpEuSMz0Cbbmn25_WpWChOqPOE_wVB25VuGA12jtRJg_. [Accessed 02 04 2025].
- [4] A. D. Marchese, R. K. Katzchmann and D. Rus, "A Recipe for Soft Fluidic Elastomer Robots," *Soft Robotics*, vol. 2, no. 1, 2015.
- [5] X. Gong and A. Pelton, "Finite Element Analysis on Nitinol Medical Applications," *Engineering, Medicine, Materials Science*, pp. 439-440, 2002.
- [6] V. Iacovacci, G. Lucarini, C. Innocenti, N. Comisso, P. Dario, L. Ricotti and A. Menciassi, "Polydimethylsiloxane films doped with NdFeB powder: magnetic characterization and potential applications in biomedical engineering and microrobotics," *Biomedical Microdevices*, vol. 17, 2015.
- [7] ISO, "ISO 14971:2019 - Medical Devices – Application of Risk Management to Medical Devices," International Organization for Standardization, Geneva, Switzerland, 2019.
- [8] ISO, "ISO 62366-1:2015 - Medical Devices – Part 1: Application of Usability Engineering to Medical Devices," International Organization for Standardization, Geneva, Switzerland, 2015.
- [9] IEC, "IEC 60601-1-2:2014 - Medical Electrical Equipment – Part 1-2: General Requirements for Basic Safety and Essential Performance – Collateral Standard: Electromagnetic Compatibility," International Electrotechnical Commission, Geneva, Switzerland, 2014.
- [10] Mouser Electronics, "RFP30N06LE MOSFET," 01 2004. [Online]. Available: <https://www.mouser.ca/datasheet/2/308/rfp30n06le-1195941.pdf>. [Accessed 17 11 2024].
- [11] International Electrotechnical Commission (IEC), International Electrotechnical Commission (IEC), 3.2 Ammendment, IEC 60601-1 ed., Geneva: International Electrotechnical Commission (IEC), 2020.
- [12] C. F. M. A. E. D. a. J. S. J. Cardoso das Neves Neto, "Investigation of Harmonic Resonance from Reactive Compensation in Hospital Electrical Installations with Magnetic Resonance Imaging (MRI)," in *International Conference on Harmonics & Quality of Power (ICHQP)*, Naples, Italy, 2022.
- [13] Trinamic Motion Control GmbH, "TMC2209 Stepper Motor Driver Datasheet, Rev. 1.09," Trinamic Motion Control GmbH, January 2021. [Online]. Available:

https://www.trinamic.com/fileadmin/assets/Products/ICs_Documents/TMC2209_data_sheet.pdf. [Accessed 4 April 2025].

- [14] J. A. Laca, R. Kocielnik, J. H. Nguyen and J. You, "Using Real-time Feedback To Improve Surgical Performance on a Robotic Tissue Dissection Task," *ResearchGate*, p. 21, 2022.
- [15] M. Espinoa-Gavira, A. Aguera-Perez and J. Palomares-Salas, "Characterization and Performance Evaluation of ESP32 for Real-time Synchronized Sensor Networks," *Procedia Computer Science*, vol. 237, pp. 261-268, 2024.
- [16] M.-A. Salvador, M.-M. Arturo and P.-E. Fernando, "Effects of Real Time Feedback on Novice's Laparoscopic Learning Curve," *Journal of Surgical Education*, vol. 81, no. 8, pp. 1133-1153, 2024.
- [17] P. Picozzi, U. Nocco, C. Labate and I. Gambini, "Advances in Robotic Surgery: A Review of New Surgical Platforms," *Electronics*, 2024.
- [18] 2. - . R.-A. P. C. Intervention, "Robotic-assisted percutaneous coronary intervention," *Handbook of Robotic and Image-Guided Surgery*, pp. 341-362, 2020.
- [19] C. E. Reiley, T. Akinbiyi and D. Burschka, "Effects of visual force feedback on robot-assisted surgical task performance," *The Journal of Thoracic and Cardiovascular Surgery*, vol. 135, no. 1, pp. 196-202, 2008.
- [20] G. S. Neel, R. L. Kau, S. F. Bansberg and D. Lal, "Comparison of 3mm versus 4mm rigid endoscope in diagnostic nasal endoscopy," *World Journal of Otorhinolaryngology - Head and Neck Surgery*, vol. 3, no. 1, pp. 32-36, 2017.
- [21] P. Allia, "Fe₃O₄ nanoparticles and nanocomposites with potential application in biomedicine and in communication technologies: Nanoparticle aggregation, interaction, and effective magnetic anisotropy," *Journal of Applied Physics*, vol. 116, no. 11, 2014.
- [22] ISO, "ISO 10993-1:2018 - Biological Evaluation of Medical Devices – Part 1: Evaluation and Testing Within a Risk Management Process," International Organization for Standardization, Geneva, Switzerland, 2018.
- [23] Z. Yang, "Magnetically Actuated Continuum Medical Robots: A Review," *Advanced Intelligent Systems*, vol. 5, no. 6, 2023.
- [24] S. Bergeles and G. Z. Yang, "From passive tool holders to microsurgeons: safer, smaller, smarter surgical robots," *IEEE Transactions on Biomedical Engineering*, vol. 61, no. 5, p. 1565–1576, 2014.
- [25] "ATO 120A 30V 3600W Variable DC Power Supply," 2025. [Online]. Available: https://www.ato.com/120a-30v-variable-dc-power-supply?affiliate=shopping&gad_source=1&gbraid=0AAAAAoOej0Z3vuiNVYd24QkWWj4X9bN3v&gclid=CjwKCAjwktO_BhBrEiwAV70jXqF8ZlVcT7NI4dZuooOgaXhFzfcPj7dI2cw6eGHFwFdKKe9SDCTzsRoCXpkQAvD_BwE. [Accessed 08 04 2025].
- [26] G. L. Y. D. Z. L. M. L. Changhao Luo, "Design and optimization of liquid helium-free cooling systems for magnetic resonance imaging device using multi-physical modeling," *Case Studies in Thermal Engineering*, vol. 66, p. 15, February 2025.

- [27] T. M. T. J. O. Faith Natukunda, "Approaches in cooling of resistive coil-based low-field Magnetic Resonance Imaging (MRI) systems for application in low resource settings," *BMC Biomedical Engineering*, vol. 3, 12 02 2021.

Chapter 5

Summary

To summarize, this project set out to address issues with ENT surgeries, as they often face significant challenges due to the intricate and tight sinus pathways being navigated. Conventional surgical instruments frequently require invasive procedures, such as bone removal, leading to prolonged recovery time, higher risks, and increased costs. To address these limitations, this project proposes a magnetically actuated soft-continuum robot designed to enhance dexterity in navigating complex, confined anatomical spaces while remaining less invasive than current tools. The design integrates four key subsystems: a soft-continuum robot with a magnetized tip, a linear actuator, a directional magnetic actuation system, and a navigational interface. The magnetic actuation system uses three electromagnetic coils to generate desired magnetic fields, for real-time orientation adjustments. The linear actuator uses a stepper motor to extend and retract the robot. The continuum robot's soft silicone body surrounds a nitinol wire core to adapt to narrow pathways. Its magnetized tip, embedded with Neodymium iron boron (NdFeB) particles, interacts with the magnetic fields to achieve precise directional control. By integrating the hardware with real-time software controls, the system is operated through a custom-built navigation interface that coordinates the linear and magnetic actuation systems within a graphical interface. The proposed system is designed to seamlessly integrate into existing surgical workflows, offering enhanced control, reduced operative times, and improved patient outcomes. Beyond clinical advantages, the broader economic and societal benefits are significant and include increased healthcare efficiency, sustainable resource use, and improved personalized, patient-centered surgical methodologies. This solution has the potential to revolutionize ENT surgery, setting new standards for patient care.

Implementation, Analysis and Results

The implementation of this project resulted in a fully functional magnetic actuation system, integrated with a custom-designed soft continuum robot and a real-time robot navigation interface. The actuation platform consists of independently controlled coils capable of generating dynamic magnetic fields within a working volume of $10\text{cm} \times 10\text{cm} \times 10\text{cm}$. These coils produced fields over 5mT, sufficient to influence a magnetized robotic tip. The robot itself features a scalable, biocompatible, and reproducible design with a helical body structure to minimize the risk of tissue damage. Its tip was magnetized to exhibit a 30mT north pole and a 20mT south pole, enabling responsive and controllable interaction with external magnetic fields. The linear actuator can extend and retract at a speed of 7.7mm/s. All of these components are seamlessly integrated with the GUI. During analysis, the magnetic field generation was verified using field mapping and simulation data, confirming the directional capability of the system. Experimental results verified that all design outputs were within the required specifications, and the GUI effectively orchestrated coil activations and direction control in real. These results confirmed the system's responsiveness, directionality, and field strength, demonstrating successful navigation via coordinated field interactions. The full integration of magnetic actuation, robot mechanics, and GUI control established a robust proof of concept. This showcases the feasibility of this approach. The results confirm the system as a reliable and complete proof of concept for magnetically actuated robotic navigation.

Proposed Future Work

Future work on this project could focus on several key areas for enhancement. First, increasing the magnetic field strength by upgrading the power supply is crucial. Currently, the system operates with a 30V power supply, but in medical applications, medical-grade power generators capable of providing up to 300V could be employed. This power increase would boost the magnetic field intensity, expanding the robot's effective movement area and improving the precision of directional control, essential for more intricate tasks. Further miniaturization of the robot is another potential improvement. A smaller robot could reduce invasiveness, making it more suitable for medical procedures where space and precision are critical. Although miniaturized components are costly and beyond the scope of this project, the successful prototype paves the way for such advancements. Adding a payload to the robot would also enhance its functionality. Possible additions include a camera, laser, or forceps, allowing for more diverse medical applications. Testing with more complex and intricate pathways would refine the robot's movement precision, and continuous updates to the GUI would ensure it adapts to the evolving design. These advancements could significantly enhance the robot's capabilities, making it more versatile for medical use. Overall, the project shows promising potential, warranting further development and investment in miniaturized technologies and power systems for practical applications.

Appendix A: Design Output Calculations

Calculation 1: Coil Temperature

The calculation for temperature change in the coil is related to the power dissipated. A sample calculation is provided given a solenoid coil radius of 0.05m ($r_{solenoid}$), 450 turns (N), and 15A (I) being applied for 5 seconds (t). The first step is to calculate the length of wire required (l_{wire}):

$$l_{wire} = 2\pi * r_{solenoid} * N = 2\pi * 0.05m * 450$$
$$l_{wire} = 141.37m$$

Next the resistance of the wire (R_{wire}) can be calculated. This requires two different constants; the cross-sectional area of the wire (A_{wire}), which is $2.08 * 10^{-6} m^2$ for a 14-gauge wire, and the resistivity constant (ρ), which is $1.68 * 10^{-8} \Omega m$ for copper.

$$R_{wire} = \frac{l_{wire} * \rho}{A_{wire}} = \frac{141.37m * 1.68 * 10^{-8} \Omega m}{2.08 * 10^{-6} m^2}$$
$$R_{wire} = 1.14 \Omega$$

Now, the power in the wire (P) can be calculated:

$$P = I * R_{wire}^2 = 15A * 1.14 \Omega^2$$
$$P = 256.92 W$$

Using the power, the generated heat (H) can be calculated:

$$H = P * t = 256.92 W * 5 s$$
$$H = 1284.58 J$$

Next the mass of the wire (m_{wire}) can be calculated. This requires the unit weight in meters of the wire, which is stated to be 54 m/kg on the datasheet.

$$m_{wire} = \frac{1}{54} * l_{wire} = \frac{1}{54 m/kg} * 141.37m$$
$$m_{wire} = 2.62 kg$$

Finally, the change in temperature (ΔT) can be calculated. This requires the specific heat capacity of copper (c) which is defined as $385 \frac{J}{kg * ^\circ C}$.

$$\Delta T = \frac{H}{m_{wire} * c} = \frac{1284.58 J}{2.62 kg * 385 \frac{J}{kg * ^\circ C}}$$
$$\Delta T = 1.27^\circ C$$

Therefore, using an ambient temperature assumed to be $22^\circ C$, the temperature of the coil when powered is:

$$T_{coil} = T_{ambient} + \Delta T = 22 + 1.27^\circ C$$
$$T_{coil} = 23.27^\circ C$$

Calculation 2: Linear Actuation Resolution and Velocity

Given:

Gear outer diameter: 7 mm

Step interval: 1.78 ms per step

The following calculations can be completed:

Steps per revolution: 1600

$$\text{Step frequency} = \frac{1}{0.00178} = 560 \text{ steps/second}$$

Gear radius: 3.5mm

Rotations per second:

$$\frac{\text{frequency}}{\text{steps per revolution}} = \frac{560}{1600} = 0.35 \text{ rev/s}$$

Angular velocity:

$$\omega = 2\pi \cdot RPS = 2\pi \cdot 0.833 = 2.2 \text{ rad/s}$$

Velocity of wire:

$$v_{\text{wire}} = \omega \cdot r = 2.2 \text{ rad/s} \cdot 3.5 \text{ mm} = 7.7 \text{ mm/s}$$

Note: speed can be doubled or halved by halving or doubling the step interval to match future design requirements

Appendix B: Software

Code 1: Coil Control

```
//Initializing pins
const int buttonOnePin = 27;
const int buttonTwoPin = 26;
const int buttonThreePin = 25;
const int LedOnePin = 32; // blue: 100 ohms
const int LedTwoPin = 33; // green: 220 ohms
const int LedThreePin = 34; // green: 220 ohms
const int coilOnePin = 9; // 'blue' coil
const int coilTwoPin = 10; // 'green' coil
const int coilThreePin = 11; // 'green' coil

int coilOneState = 0;
int coilTwoState = 0;
int coilThreeState = 0;
byte coilOneLastState = LOW;
byte coilTwoLastState = LOW;
byte coilThreeLastState = LOW;
byte LedOneState = LOW;
byte LedTwoState = LOW;
byte LedThreeState = LOW;

unsigned long lastDebounceTime1 = 0;
unsigned long lastDebounceTime2 = 0;
unsigned long lastDebounceTime3 = 0;
unsigned long debounceDelay = 50; // 50ms debounce

void setup() {
    //Serial.begin(115200);
    pinMode(buttonOnePin, INPUT);
    pinMode(buttonTwoPin, INPUT);
    pinMode(buttonThreePin, INPUT);
    pinMode(LedOnePin, OUTPUT);
    pinMode(LedTwoPin, OUTPUT);
    pinMode(LedThreePin, OUTPUT);
    pinMode(coilOnePin, OUTPUT);
    pinMode(coilTwoPin, OUTPUT);
    pinMode(coilThreePin, OUTPUT);
}

void loop() {
    int currentState1 = digitalRead(buttonOnePin);
    int currentState2 = digitalRead(buttonTwoPin);
    int currentState3 = digitalRead(buttonThreePin);

    // Debounce Button 1
    if (currentState1 != coilOneLastState) { // State change detected
        lastDebounceTime1 = millis(); // Reset debounce timer
    }
    if ((millis() - lastDebounceTime1) > debounceDelay) { // Debounce check
```

```

        if (currentState1 != coilOneState) { // Confirm stable state
            coilOneState = currentState1;
            if (coilOneState == HIGH) { // Button 1 pressed
                LedOneState = (LedOneState == HIGH) ? LOW : HIGH; // Toggle LED 1
                digitalWrite(LedOnePin, LedOneState);
                digitalWrite(coilOnePin, LedOneState);
            }
        }
    }
    coilOneLastState = currentState1; // Update last state

    // Debounce Button 2
    if (currentState2 != coilTwoLastState) { // State change detected
        lastDebounceTime2 = millis(); // Reset debounce timer
    }
    if ((millis() - lastDebounceTime2) > debounceDelay) { // Debounce check
        if (currentState2 != coilTwoState) { // Confirm stable state
            coilTwoState = currentState2;
            if (coilTwoState == HIGH) { // Button 2 pressed
                LedTwoState = (LedTwoState == HIGH) ? LOW : HIGH; // Toggle LED 2
                digitalWrite(LedTwoPin, LedTwoState);
                digitalWrite(coilTwoPin, LedOneState);
            }
        }
    }
    coilTwoLastState = currentState2; // Update last state
}

```

Code 2: Linear Actuation Control

```

#include <Bluepad32.h>

// Bluetooth controller variables
ControllerPtr myControllers[BP32_MAX_GAMEPADS];

// Motor control pins for stepper motor
#define IN1 9
#define IN2 10
#define IN3 18
#define IN4 23

// LED pins
const int LedOnePin = 32;
const int LedTwoPin = 33;

// Variables for motor stepping, idk I got this from gpt
int stepSequence[4][4] = {
    {1, 0, 1, 0},
    {1, 0, 0, 1},
    {0, 1, 0, 1},
    {0, 1, 1, 0}
};
int currentStep = 0;
unsigned long lastStepTime = 0; //Tracks the last step time

```

```

unsigned long stepInterval = 6; //Time between steps in milliseconds
int motorDirection = 0; //Motor direction: 1 (forward), -1 (backward), 0 (stopped)

const int joystickThreshold = 300; //Threshold for joystick Y-axis activation, set high

// Callback for controller connection
void onConnectedController(ControllerPtr ctl) {
    for (int i = 0; i < BP32_MAX_GAMEPADS; i++) {
        if (myControllers[i] == nullptr) {
            myControllers[i] = ctl;
            Serial.printf("Controller connected: index=%d\n", i);
            return;
        }
    }
    Serial.println("No empty slot for new controller!");
}

// Callback for controller disconnection
void onDisconnectedController(ControllerPtr ctl) {
    for (int i = 0; i < BP32_MAX_GAMEPADS; i++) {
        if (myControllers[i] == ctl) {
            myControllers[i] = nullptr;
            Serial.printf("Controller disconnected: index=%d\n", i);
            return;
        }
    }
    Serial.println("Controller not found!");
}

// Process gamepad inputs
void processControllers() {
    for (auto myController : myControllers) {
        if (myController && myController->isConnected() && myController->hasData())
    {
        if (myController->b()) { //Button B pressed (technically A)
            motorDirection = 1; //moves the gears backward
        } else if (myController->x()) { //Button X pressed (technically Y on
switch controller)
            motorDirection = -1; //move gears forward
        } else {
            motorDirection = 0; //Stop the motor
        }
        //Left joystick Y-axis controls the higher or lower coil
        int joystickY = myController->axisY(); //Left joystick Y-axis
        if (joystickY > joystickThreshold) { //Joystick pushed up, threshold is
300
            digitalWrite(LedOnePin, HIGH); //Activate LED1 and coil
            digitalWrite(LedTwoPin, LOW); //Deactivate LED2 and coil
        } else if (joystickY < -joystickThreshold) { // Joystick pushed down
            digitalWrite(LedOnePin, LOW); //Deactivate LED1 and coil
            digitalWrite(LedTwoPin, HIGH); //Activate LED2 and coil
        } else { //Joystick centered
            digitalWrite(LedOnePin, LOW); //Deactivate both coils if joystick
neutral
            digitalWrite(LedTwoPin, LOW);
        }
    }
}

```

```

        }
    }
}

// Stepper motor function
void stepMotor(int direction) {
    if (direction == 1) {
        currentStep = (currentStep + 1) % 4;
    } else if (direction == -1) {
        currentStep = (currentStep + 3) % 4;
    }
    digitalWrite(IN1, stepSequence[currentStep][0]);
    digitalWrite(IN2, stepSequence[currentStep][1]);
    digitalWrite(IN3, stepSequence[currentStep][2]);
    digitalWrite(IN4, stepSequence[currentStep][3]);
}

// stops the stepper motor, sets them to low
void stopMotor() {
    digitalWrite(IN1, LOW);
    digitalWrite(IN2, LOW);
    digitalWrite(IN3, LOW);
    digitalWrite(IN4, LOW);
}

void setup() {
    //Initialize motor pins, 9, 10, 18, 23
    pinMode(IN1, OUTPUT);
    pinMode(IN2, OUTPUT);
    pinMode(IN3, OUTPUT);
    pinMode(IN4, OUTPUT);

    //Initialize LED pins, for the coils
    pinMode(LedOnePin, OUTPUT);
    pinMode(LedTwoPin, OUTPUT);

    //Setup Bluetooth, idk how this works
    Serial.begin(115200);
    BP32.setup(&onConnectedController, &onDisconnectedController);
    BP32.forgetBluetoothKeys();
    Serial.println("Setup complete. Waiting for controllers...");
}

void loop() {
    //this checks the controller's state, if there's buttons being pressed
    if (BP32.update()) {
        processControllers();
    }
    if (motorDirection != 0) {
        unsigned long currentTime = millis();
        if (currentTime - lastStepTime >= stepInterval) { //calculates when the motor
step should happen
            lastStepTime = currentTime;
            stepMotor(motorDirection);
        }
    }
    else {
        stopMotor();
    }
}

```

```

    }
    delay(1);
}

```

Code 3: Python Simulation

```

import numpy as np
import magpylib as magpy
import pyvista as pv
import os

os.system('cls')

# Define parameters for the solenoid
solenoid_current = 15.3 # Current in amperes
solenoid_radius = 0.1 # Radius in meters
solenoid_length = 0.1 # Length of the solenoid in meters
solenoid_turns = 145 # Number of turns
mu_0 = 4 * np.pi * 1e-7 # Permeability of free space (T·m/A)

# Create the solenoid using Magpylib
solenoid = magpy.Collection()

# Solenoid: continuous cylindrical coil along the z-axis
for z in np.linspace(-solenoid_length / 2, solenoid_length / 2, solenoid_turns):
    winding = magpy.current.Circle(
        current=solenoid_current,
        diameter=2 * solenoid_radius,
        position=(0, 0, z),
    )
    solenoid.add(winding)

# Define sensor positions (on-axis and off-axis)
sensing_positions = [
    (0, 0, 0), # Center of solenoid
    (0, 0, solenoid_length / 2), # Edge of solenoid
    (0, 0, solenoid_length / 2 + 0.20), # 20 cm away from edge
    (0.02, 0, solenoid_length / 2 + 0.10), # Off-axis, outside solenoid
]

# Function to compute on-axis magnetic field
def solenoid_field_on_axis(z, N, I, L, R):
    n = N / L # Turns per unit length

    # If sensor position is within coil
    if abs(z) < L / 4:
        return (mu_0 * n * I)

```

```

# If sensor position is outside of coil / at edge
else:
    # Approximate field at end using modified formula for edge
    term1 = (L / 2) / np.sqrt((L / 2) ** 2 + R ** 2)
    term2 = (L / 2) / np.sqrt((L / 2) ** 2 + R ** 2)
    return (mu_0 * I * N / (2 * L)) * (term1 + term2)

# Function to compute off-axis field using Biot-Savart Law
# Position = x,y,z point
def biot_savart_field(position, N, I, L, R):
    # Gets X,Y,Z from position
    x, y, z = position
    # Setting vector to 0
    B_total = np.array([0.0, 0.0, 0.0])

    # Iterate over each loop of wire (N turns along z-axis) along coil length
    for z_turn in np.linspace(-L / 2, L / 2, N):
        # Iterate over small current elements per loop
        loop_points = 100
        for theta in np.linspace(0, 2 * np.pi, loop_points): # 100 points per loop
            # Position of current element on circular turn
            x_turn = R * np.cos(theta)
            y_turn = R * np.sin(theta)

            # Differential length element
            dl = np.array([-np.sin(theta), np.cos(theta), 0]) * (2 * np.pi * R / loop_points)
            # Vector from current element
            r_vec = np.array([x - x_turn, y - y_turn, z - z_turn])
            # Magnitude of r_vec (distance between element and observation point)
            r_mag = np.linalg.norm(r_vec)

            # Edge case to avoid observation point collides with current element
            if r_mag == 0:
                continue

            # Compute differential magnetic field with Bio-Savart Law
            dB = mu_0 * I * np.cross(dl, r_vec) / (4 * np.pi * r_mag**3)
            # Sum all field contributions
            B_total += dB

        # Returns magnetic field vector in T
        return B_total

# Compute and print field at sensor positions
for position in sensing_positions:
    z_pos = position[2]

```

```

# On-axis: Use solenoid formula
if position[0] == 0:
    B_theoretical = np.array([0, 0, solenoid_field_on_axis(z_pos, solenoid_turns,
solenoid_current, solenoid_length, solenoid_radius)])
# Off-axis: Use Bio-savert Integration
else:
    B_theoretical = biot_savart_field(position, solenoid_turns, solenoid_current,
solenoid_length, solenoid_radius)

# Compute Magpylib field
B_magpylib = solenoid.getB(position)

# Print results
print(f"\nMagnetic Field at position {position}:")
print(f"Theoretical Calculation: B_x: {B_theoretical[0]:.5f} T, B_y: {B_theoretical[1]:.5f} T, B_z: {B_theoretical[2]:.5f} T")
print(f"Magpylib Sensor: B_x: {B_magpylib[0]:.5f} T, B_y: {B_magpylib[1]:.5f} T, B_z: {B_magpylib[2]:.5f} T")

# Visualization of the solenoid
pl = pv.Plotter()

# Create PyVista representation of solenoid
solenoid_points = []
theta = np.linspace(0, 2 * np.pi, 100)
x = solenoid_radius * np.cos(theta)
y = solenoid_radius * np.sin(theta)

for z in np.linspace(-solenoid_length / 2, solenoid_length / 2, solenoid_turns):
    solenoid_points.append(np.column_stack((x, y, np.full_like(theta, z)))))

solenoid_lines = pv.PolyData(np.vstack(solenoid_points))
pl.add_mesh(solenoid_lines, color="blue", line_width=3, label="Solenoid")

# Add spheres at sensor positions
sensor_colors = ['yellow', 'green', 'red', 'cyan']
for idx, position in enumerate(sensing_positions):
    sensor_sphere = pv.Sphere(radius=0.002, center=position)
    pl.add_mesh(sensor_sphere, color=sensor_colors[idx], specular=0.5, name=f"Sensor {idx+1}")

# Add magnetic field vectors
grid_points = np.array(np.meshgrid(np.linspace(-0.1, 0.1, 10),
np.linspace(-0.1, 0.1, 10),
np.linspace(-0.1, 0.1, 10))).T.reshape(-1, 3)

```

```

B_field = np.array([biot_savart_field(pos, solenoid_turns, solenoid_current, solenoid_length,
solenoid_radius) for pos in grid_points]) * 1000

grid = pv.PolyData(grid_points)
grid["B_magnitude"] = np.linalg.norm(B_field, axis=1)
grid["B_vectors"] = B_field

glyphs = grid.glyph(
    orient="B_vectors",
    scale=True,
    factor=0.001,
)
pl.add_mesh(
    glyphs,
    color="blue",
    show_scalar_bar=True,
    label="Magnetic Field Vectors",
)

# Add axes and set camera
pl.add_axes()
pl.camera.position = (0.2, 0.2, 0.2)

# Show the 3D scene
pl.show()

```

Code 4: Python Interface

```

import numpy as np
import magpylib as magpy
import pyvista as pv
from scipy.spatial.transform import Rotation as R
import os
import time
from functools import partial
import serial # Import serial for ESP32 communication
import serial.tools.list_ports

os.system("cls")

#####
##### Setup
skull = pv.read("C:/Users/raida/OneDrive/Documents/Year 5/IBEHS Cpstone/Magnetization
Resources/Skull/skull/leFabShop/to-make-or-not-to-make/Scull_geant_fix02.stl")

```

```

logo = pv.read("C:/Users/raida/OneDrive/Documents/Year 5/IBEHS Cpstone/Magnetization
Resources/EXT_RTR/Heart.png")

arrow_label_global = ["X pos", "X neg", "Y pos", "Y neg", "Z pos", "Z neg", "XY pos", "XY
neg", "XZ neg", "XYZ Z neg", "XYZ YZ neg"]
global tip_actor

##### Setup Serial Communication
BAUD_RATE = 115200
ports = serial.tools.list_ports.comports()
serial_port = "COM3"
found = False
for p in ports:
    #print(p.manufacturer)
    if p.manufacturer == "Silicon Laboratories" or p.manufacturer == "Silicon Labs":
        serial_port = p.device
        found = True
        print("Detected ESP32 in", serial_port)
if found == False:
    print("COM ESP port not found")

# Open Serial connection
try:
    esp32 = serial.Serial(serial_port, BAUD_RATE, timeout=1)
    time.sleep(2)
    print(f'Connected to ESP32 on {serial_port}')

except serial.SerialException:
    print("Failed to connect to ESP32. Check the port and try again.")
    esp32 = None
    exit

##### Send commands to ESP32
def esp_command(message):
    if esp32:
        try:
            esp32.write(message.encode())
            print(f'Command sent: {message}')
        except serial.SerialException:
            print("Serial write failed. Check ESP32 connection.")

##### Stepper status update
def update stepper_status(message):
    """Updates the stepper status text """
    status_text = f'Actuator Status: {message}'

```

```

# Remove the old label if it exists
if "stepper_text" in pl.actors:
    pl.remove_actor("stepper_text")

# Add updated text
pl.add_text(
    status_text,
    position=(10,560),
    font_size=12,
    color="black",
    name="stepper_text"
)

#####
# Update arrow positioning
def update_arrow (direction):
    global tip_actor

    # Remove old arrow
    if "tip" in pl.actors:
        pl.remove_actor("tip")

    # Create new arrow in the desired direction
    new_tip = pv.Arrow(start=(0,0,0), direction=direction, scale=0.02)
    tip_actor = pl.add_mesh(new_tip, color="black", name="tip")

#####
# Solenoid visualization
def create_solenoid(plane, solenoid_current, solenoid_radius=0.1, solenoid_length=0.1,
solenoid_turns=145, rotation_angle=0):
    # Create coil 1
    offset = 1 # Offset of 30cm for each coil to be away from center

    if plane == "z":
        coil1 = magpy.Collection() # Create a collection to hold multiple loops
        for z in np.linspace(-solenoid_length / 2, solenoid_length / 2, solenoid_turns): # Position
loops along the z-axis
            winding = magpy.current.Circle( # Define a single circular loop
                current=solenoid_current, # Current in the loop (in amperes)
                diameter=2 * solenoid_radius, # Diameter of the loop (in meters)
                position=(0, 0, z+offset), # Position of the loop in 3D space
            )
            coil1.add(winding) # Add the loop to the collection

        # Create PyVista representation of the coil(1) for visualization
        coil_points_Z = [] # List to hold the points of all loops
        for z in np.linspace(-0.16, -0.08, 16): # Loop positions along the z-axis
            theta = np.linspace(0, 2 * np.pi, 100) # Define angles for the circular loop

```

```

x = 0.05 * np.cos(theta) # x-coordinates of the loop
y = 0.05 * np.sin(theta) # y-coordinates of the loop
z_points = np.full_like(theta, z) # z-coordinates for the loop
coil_points_Z.append(np.column_stack((x, y, z_points))) # Combine points into 3D
coordinates
return coil_points_Z

# Create Coil 2
elif plane == "y":
    coil2 = magpy.Collection()
    for y in np.linspace(-solenoid_length / 2, solenoid_length / 2, solenoid_turns): # Position
loops along the z-axis
        winding = magpy.current.Circle( # Define a single circular loop
            current=solenoid_current, # Current in the loop (in amperes)
            diameter=2 * solenoid_radius, # Diameter of the loop (in meters)
            position=(0, y+offset, 0), # Position of the loop in 3D space
        )
        coil2.add(winding) # Add the loop to the collection

# Create PyVista representation of the coil(2) for visualization
coil_points_Y = [] # List to hold the points of all loops
for y in np.linspace(0.16, 0.08, 16): # Loop positions along the z-axis
    theta = np.linspace(0, 2 * np.pi, 100) # Define angles for the circular loop
    x = 0.05 * np.cos(theta) # x-coordinates of the loop
    z = 0.05 * np.sin(theta) # y-coordinates of the loop
    y_points = np.full_like(theta, y) # z-coordinates for the loop
    coil_points_Y.append(np.column_stack((x, y_points, z))) # Combine points into 3D
coordinates
return coil_points_Y

elif plane == "x":
    coil3 = magpy.Collection()
    for x in np.linspace(-solenoid_length / 2, solenoid_length / 2, solenoid_turns): # Position
loops along the z-axis
        winding = magpy.current.Circle( # Define a single circular loop
            current=solenoid_current, # Current in the loop (in amperes)
            diameter=2 * solenoid_radius, # Diameter of the loop (in meters)
            position=(x+offset, 0, 0), # Position of the loop in 3D space
        )
        coil3.add(winding) # Add the loop to the collection

# Create PyVista representation of the coil(3) for visualization
coil_points_X = [] # List to hold the points of all loops
for x in np.linspace(0.16, 0.08, 16): # Loop positions along the z-axis
    theta = np.linspace(0, 2 * np.pi, 100) # Define angles for the circular loop
    x_points = np.full_like(theta, x) # z-coordinates for the loop

```

```

y = 0.05 * np.cos(theta) # x-coordinates of the loop
z = 0.05 * np.sin(theta) # y-coordinates of the loop
coil_points_X.append(np.column_stack((x_points, y, z))) # Combine points into 3D
coordinates
return coil_points_X

#####
# Coil simulator
def simulate_coil(solenoid_current=15):
    """Runs the solenoid simulation and visualization."""
    # Coil Parameters
    solenoid_radius = 0.1
    solenoid_length = 0.1
    solenoid_turns = 145
    solenoid_current = 20

    solenoid_x = create_solenoid("x",solenoid_current, solenoid_radius, solenoid_length,
solenoid_turns)
    solenoid_y = create_solenoid("y", solenoid_current, solenoid_radius, solenoid_length,
solenoid_turns)
    solenoid_z = create_solenoid("z",solenoid_current, solenoid_radius, solenoid_length,
solenoid_turns)

    # Create a 3D grid of points for magnetic field visualization
    x = np.linspace(-0.2, 0.2, 10) # Grid along the x-axis
    y = np.linspace(-0.2, 0.2, 10) # Grid along the y-axis
    z = np.linspace(-0.2, 0.2, 10) # Grid along the z-axis
    grid_points = np.array(np.meshgrid(x, y, z)).T.reshape(-1, 3) # Combine into a 3D grid

    coil_linesX = pv.PolyData(np.vstack(solenoid_x)) # Create a PolyData object for the coil
    coil_linesY = pv.PolyData(np.vstack(solenoid_y)) # Create a PolyData object for the coil
    coil_linesZ = pv.PolyData(np.vstack(solenoid_z))

    # Add the grey coil mesh to the scene
    # pl.add_mesh(coil_linesX, color="blue", line_width=3, label="Coil 1")
    # pl.add_mesh(coil_linesY, color="red", line_width=3, label="Coil 2")
    # pl.add_mesh(coil_linesZ, color="green", line_width=3, label="Coil 3")
    pl.add_mesh(coil_linesX, color="grey", line_width=3, label="Coil X")
    pl.add_mesh(coil_linesY, color="grey", line_width=3, label="Coil Y")
    pl.add_mesh(coil_linesZ, color="grey", line_width=3, label="Coil Z")

    # Heart Lab logo not working - TODO
    # pl.add_logo_widget(logo, (1,1), (1,1), 1)

#####
# Skull Visualization
# Adding skull model
skull_copy = skull.copy()

```

```

# Scale down STL
skull_copy.points *= 0.00072
# Rotate skull Z-axis to X-axis
r = R.from_euler('y', 90, degrees=True)
# Rotate -90° around Y
skull_copy.points = r.apply(skull_copy.points)
# Centering skull to coils
skull_copy.points[:, 0] -= 0.035
pl.add_mesh(skull_copy, color="tan", opacity=0.15)

#####
Robot tip
# Create an tip at the center pointing in the Z-direction
tip_start = (0, 0, 0)
tip_direction = (0, 0, -1) # Initial direction
tip_scale = 0.02 # Scale for visibility
tip = pv.Arrow(start=tip_start, direction=tip_direction, scale=tip_scale)
tip_actor = pl.add_mesh(tip, color="black", name="tip")

#####
3D Joystick arrows / coil activation
def coil_activation(_, arrow_label):
    # green is going into to coil (attract towards coil) - DIR PIN
    # red is going out from coil (repel away from coil) - DIR PIN
    if arrow_label == arrow_label_global[0]:
        print(f"Activating coils for {arrow_label}")
        pl.add_mesh(coil_linesX, color="green", line_width=3, label="Coil X")
        pl.add_mesh(coil_linesY, color="grey", line_width=3, label="Coil Y")
        pl.add_mesh(coil_linesZ, color="grey", line_width=3, label="Coil Z")
        update_arrow([1,0,0])
        esp_command(f'{arrow_label}\n')

    if arrow_label == arrow_label_global[1]:
        print(f"Activating coils for {arrow_label}")
        pl.add_mesh(coil_linesX, color="red", line_width=3, label="Coil X")
        pl.add_mesh(coil_linesY, color="grey", line_width=3, label="Coil Y")
        pl.add_mesh(coil_linesZ, color="grey", line_width=3, label="Coil Z")
        update_arrow([-1,0,0])
        esp_command(f'{arrow_label}\n')

    if arrow_label == arrow_label_global[2]:
        print(f"Activating coils for {arrow_label}")
        pl.add_mesh(coil_linesX, color="grey", line_width=3, label="Coil X")
        pl.add_mesh(coil_linesY, color="green", line_width=3, label="Coil Y")
        pl.add_mesh(coil_linesZ, color="grey", line_width=3, label="Coil Z")
        update_arrow([0,1,0])
        esp_command(f'{arrow_label}\n')

```

```

if arrow_label == arrow_label_global[3]:
    print(f"Activating coils for {arrow_label}")
    pl.add_mesh(coil_linesX, color="grey", line_width=3, label="Coil X")
    pl.add_mesh(coil_linesY, color="red", line_width=3, label="Coil Y")
    pl.add_mesh(coil_linesZ, color="grey", line_width=3, label="Coil Z")
    update_arrow([0,-1,0])
    esp_command(f'{arrow_label}\n')

if arrow_label == arrow_label_global[4]:
    print(f"Activating coils for {arrow_label}")
    pl.add_mesh(coil_linesX, color="grey", line_width=3, label="Coil X")
    pl.add_mesh(coil_linesY, color="grey", line_width=3, label="Coil Y")
    pl.add_mesh(coil_linesZ, color="red", line_width=3, label="Coil Z")
    update_arrow([0,0,1])
    esp_command(f'{arrow_label}\n')

if arrow_label == arrow_label_global[5]:
    print(f"Activating coils for {arrow_label}")
    pl.add_mesh(coil_linesX, color="grey", line_width=3, label="Coil X")
    pl.add_mesh(coil_linesY, color="grey", line_width=3, label="Coil Y")
    pl.add_mesh(coil_linesZ, color="green", line_width=3, label="Coil Z")
    update_arrow([0,0,-1])
    esp_command(f'{arrow_label}\n')

if arrow_label == arrow_label_global[6]:
    print(f"Activating coils for {arrow_label}")
    pl.add_mesh(coil_linesX, color="green", line_width=3, label="Coil X")
    pl.add_mesh(coil_linesY, color="green", line_width=3, label="Coil Y")
    pl.add_mesh(coil_linesZ, color="grey", line_width=3, label="Coil Z")
    update_arrow([1,1,0])
    esp_command(f'{arrow_label}\n')

if arrow_label == arrow_label_global[7]:
    print(f"Activating coils for {arrow_label}")
    pl.add_mesh(coil_linesX, color="green", line_width=3, label="Coil X")
    pl.add_mesh(coil_linesY, color="red", line_width=3, label="Coil Y")
    pl.add_mesh(coil_linesZ, color="grey", line_width=3, label="Coil Z")
    update_arrow([1,-1,0])
    esp_command(f'{arrow_label}\n')

if arrow_label == arrow_label_global[8]:
    print(f"Activating coils for {arrow_label}")
    pl.add_mesh(coil_linesX, color="green", line_width=3, label="Coil X")
    pl.add_mesh(coil_linesY, color="grey", line_width=3, label="Coil Y")
    pl.add_mesh(coil_linesZ, color="green", line_width=3, label="Coil Z")
    update_arrow([1,0,-1])
    esp_command(f'{arrow_label}\n')

```

```

esp_command(f'{arrow_label}\n')

if arrow_label == arrow_label_global[9]:
    print(f'Activating coils for {arrow_label}')
    pl.add_mesh(coil_linesX, color="green", line_width=3, label="Coil X")
    pl.add_mesh(coil_linesY, color="green", line_width=3, label="Coil Y")
    pl.add_mesh(coil_linesZ, color="green", line_width=3, label="Coil Z")
    update_arrow([1,1,-1])
    esp_command(f'{arrow_label}\n')

if arrow_label == arrow_label_global[10]:
    print(f'Activating coils for {arrow_label}')
    pl.add_mesh(coil_linesX, color="green", line_width=3, label="Coil X")
    pl.add_mesh(coil_linesY, color="red", line_width=3, label="Coil Y")
    pl.add_mesh(coil_linesZ, color="green", line_width=3, label="Coil Z")
    update_arrow([1,-1,-1])
    esp_command(f'{arrow_label}\n')

# Coil X
joystick_size = 0.02
X_pos = pv.Arrow(start=(0.02,0,0), direction=(1,0,0), scale=joystick_size)
X_pos_actor = pl.add_mesh(X_pos, color="cyan", name=arrow_label_global[0])
coil_activation_callback = partial(coil_activation, arrow_label=arrow_label_global[0])
pl.add_sphere_widget(callback=coil_activation_callback, center=(0.02 + joystick_size, 0, 0), radius=0.002, test_callback=False)

X_neg = pv.Arrow(start=(-0.02,0,0), direction=(-1,0,0), scale=joystick_size)
X_neg_actor = pl.add_mesh(X_neg, color="cyan", name=arrow_label_global[1])
coil_activation_callback = partial(coil_activation, arrow_label=arrow_label_global[1])
pl.add_sphere_widget(callback=coil_activation_callback, center=(-0.02 - joystick_size, 0, 0), radius=0.002, test_callback=False)

# Coil Y
Y_pos = pv.Arrow(start=(0,0.02,0), direction=(0,1,0), scale=joystick_size)
Y_pos_actor = pl.add_mesh(Y_pos, color="cyan", name=arrow_label_global[2])
coil_activation_callback = partial(coil_activation, arrow_label=arrow_label_global[2])
pl.add_sphere_widget(callback=coil_activation_callback, center=(0, 0.02 + joystick_size, 0), radius=0.002, test_callback=False)

Y_neg = pv.Arrow(start=(0,-0.02,0), direction=(0,-1,0), scale=joystick_size)
Y_neg_actor = pl.add_mesh(Y_neg, color="cyan", name=arrow_label_global[3])
coil_activation_callback = partial(coil_activation, arrow_label=arrow_label_global[3])
pl.add_sphere_widget(callback=coil_activation_callback, center=(0, -0.02 - joystick_size, 0), radius=0.002, test_callback=False)

# Coil Z

```

```

Z_pos = pv.Arrow(start=(0,0,0.02), direction=(0,0,1), scale=joystick_size)
Z_pos_actor = pl.add_mesh(Z_pos, color="cyan", name=arrow_label_global[4])
coil_activation_callback = partial(coil_activation, arrow_label=arrow_label_global[4])
pl.add_sphere_widget(callback=coil_activation_callback, center=(0,0,0.02 + joystick_size),
radius=0.002, test_callback=False)

Z_neg = pv.Arrow(start=(0,0,-0.02), direction=(0,0,-1), scale=joystick_size)
Z_pos_actor = pl.add_mesh(Z_neg, color="cyan", name=arrow_label_global[5])
coil_activation_callback = partial(coil_activation, arrow_label=arrow_label_global[5])
pl.add_sphere_widget(callback=coil_activation_callback, center=(0,0,-0.02 - joystick_size),
radius=0.002, test_callback=False)

# Extra Arrows
XY_pos = pv.Arrow(start=(0.02,0.02,0), direction=(1,1,0), scale=joystick_size)
XY_pos_actor = pl.add_mesh(XY_pos, color="cyan", name=arrow_label_global[6])
coil_activation_callback = partial(coil_activation, arrow_label=arrow_label_global[6])
pl.add_sphere_widget(callback=coil_activation_callback, center=(0.03414, 0.03414, 0),
radius=0.002, test_callback=False)

XY_neg = pv.Arrow(start=(0.02,-0.02,0), direction=(1,-1,0), scale=joystick_size)
XY_neg_actor = pl.add_mesh(XY_neg, color="cyan", name=arrow_label_global[7])
coil_activation_callback = partial(coil_activation, arrow_label=arrow_label_global[7])
pl.add_sphere_widget(callback=coil_activation_callback, center=(0.03414, -0.03414, 0),
radius=0.002, test_callback=False)

##### CHANGE CENTERS FOR FOLLOWING CODE - TODO

#XZ_pos = pv.Arrow(start=(0.02,0,0.02), direction=(1,0,1), scale=joystick_size)
#XZ_pos_actor = pl.add_mesh(XZ_pos, color="cyan", name="XZ pos")
XZ_neg = pv.Arrow(start=(0.02, 0, -0.02), direction=(1,0,-1), scale=joystick_size)
XZ_neg_actor = pl.add_mesh(XZ_neg, color="cyan", name=arrow_label_global[8])
coil_activation_callback = partial(coil_activation, arrow_label=arrow_label_global[8])
pl.add_sphere_widget(callback=coil_activation_callback, center=(0.0341, 0, -0.0341),
radius=0.002, test_callback=False)

# XYZ_Xneg = pv.Arrow(start=(-0.02,0.02,0.02), direction=(-1,1,1), scale=joystick_size)
# XYZ_Xneg_actor = pl.add_mesh(XYZ_Xneg, color="cyan", name="XYZ X neg")
# XYZ_Yneg = pv.Arrow(start=(0.02,-0.02,0.02), direction=(1,-1,1), scale=joystick_size)
# XYZ_Yneg_actor = pl.add_mesh(XYZ_Yneg, color="cyan", name="XYZ Y neg")
# Need to fix - TODO
XYZ_Zneg = pv.Arrow(start=(0.02,0.02,-0.02), direction=(1,1,-1), scale=joystick_size)
XYZ_Zneg_actor = pl.add_mesh(XYZ_Zneg, color="cyan", name=arrow_label_global[9])
coil_activation_callback = partial(coil_activation, arrow_label=arrow_label_global[9])
pl.add_sphere_widget(callback=coil_activation_callback, center=(0.0341, 0.0341, -0.0341),
radius=0.002, test_callback=False)

```

```

# XYZ_XYneg = pv.Arrow(start=(-0.02,-0.02,0.02), direction=(-1,-1,1),
scale=joystick_size)
# XYZ_XYneg_actor = pl.add_mesh(XYZ_XYneg, color="cyan", name="XYZ XY neg")
# Need to fix - TODO
XYZ_YZneg = pv.Arrow(start=(0.02,-0.02,-0.02), direction=(1,-1,-1), scale=joystick_size)
XYZ_YZneg_actor = pl.add_mesh(XYZ_YZneg, color="cyan",
name=arrow_label_global[10])
coil_activation_callback = partial(coil_activation, arrow_label=arrow_label_global[10])
pl.add_sphere_widget(callback=coil_activation_callback, center=(0.0341, -0.0341, -
0.0341), radius=0.002, test_callback=False)

# XYZ_XZneg = pv.Arrow(start=(-0.02,0.02,-0.02), direction=(-1,1,-1),
scale=joystick_size)
# XYZ_XZneg_actor = pl.add_mesh(XYZ_XZneg, color="cyan", name="XYZ XZ neg")

#####
##### Extend / Retract Functionality
def extend(state):
    if state:
        update_stepper_status("Extending")
        esp_command("EXT\n")
    else:
        update_stepper_status("Idle")
        esp_command("OFF\n")

def retract(state):
    if state:
        pl.add_mesh(coil_linesX, color="grey", line_width=3, label="Coil X")
        pl.add_mesh(coil_linesY, color="grey", line_width=3, label="Coil Y")
        pl.add_mesh(coil_linesZ, color="grey", line_width=3, label="Coil Z")
        update_stepper_status("Retracting")
        esp_command("RTR\n")
    else:
        update_stepper_status("Idle")
        esp_command("OFF\n")

def turn_Complete(state):
    if state:
        pl.add_mesh(coil_linesX, color="grey", line_width=3, label="Coil X")
        pl.add_mesh(coil_linesY, color="grey", line_width=3, label="Coil Y")
        pl.add_mesh(coil_linesZ, color="grey", line_width=3, label="Coil Z")
        esp_command("Coil OFF\n")

# Extend / Retract Buttons
pl.add_checkbox_button_widget(extend, value = False, position=(1600, 10), size=30,
border_size=2, color_on="blue")
pl.add_text("Extend", position=(1565, 40), font_size=14, color="black")

```

```

pl.add_checkbox_button_widget(retract, value = False, position=(1400, 10), size=30,
border_size=2, color_on="blue")
pl.add_text("Retract", position=(1365, 40), font_size=14, color="black")

pl.add_checkbox_button_widget(turn_Complete, value = False, position=(1150, 10),
size=30, border_size=2, color_on="green")
pl.add_text("Completed turn", position=(1075, 40), font_size=14, color="black")

#####
Emergency Stop Mechanism
def stop_callback(state):
    if state: # If button is clicked (ON)
        print("EMERGENCY STOP ACTIVATED! Turning off all coils.")
        esp_command("SHUT OFF\n")
        pl.add_mesh(coil_linesX, color="grey", line_width=3, label="Coil X")
        pl.add_mesh(coil_linesY, color="grey", line_width=3, label="Coil Y")
        pl.add_mesh(coil_linesZ, color="grey", line_width=3, label="Coil Z")
        update_arrow([0, 0, -1])
        msg = pl.add_text("EMERGENCY STOPPED!", position="upper_left", font_size=20,
color="red")
        update stepper status("OFF")
        pl.render()
        time.sleep(5)
        pl.remove_actor(msg) # Remove the text
        pl.render()

button_position = (10, 10)
pl.add_checkbox_button_widget(stop_callback, value = False, position=button_position,
size=30, border_size=2, color_on="red")
pl.add_text("EMERGENCY STOP", position=(button_position[0] + 40, button_position[1]
- 5), font_size=14, color="red")

#####
Camera settings

# Add axes and set the camera position
pl.add_axes() # Add axes to the scene
pl.camera_position =
[(0, 0, 1),
(0, 0, 0),
(1, 0, 0),
]

# Show the 3D scene
pl.show()

```

```

if __name__ == "__main__":
    # Create a PyVista plotting scene
    pl = pv.Plotter()
    #Shut off coils- check to see if it works
    #pl.add_close_callback(on_close)
    update_stepper_status("Ready")
    simulate_coil()

```

Code 5: Arduino Integration

```

#include <TMCStepper.h>

////////////////// Coil control pins for coils

// PWM Pins
const int coilPinOne = 4;
const int coilPinTwo = 10;
const int coilPinThree = 22;

// Direction Pins
const int directionPinOne = 2;
const int directionPinTwo = 18;
const int directionPinThree = 21;

// PWM Channels
const int pwmChannelOne = 0;
const int pwmChannelTwo = 1;
const int pwmChannelThree = 2;

// PWM Settings
const int pwmFrequency = 10000; // 10kHz - 30kHz
const int pwmResolution = 5; // 0-255

////////////////// Motor control pins for stepper motor

#define EN_PIN      13 // Enable pin (LOW = enabled, HIGH = disabled)
#define DIR_PIN     25 // Direction pin left and right
#define STEP_PIN    26 // Step pin, spins motor when high stops when low
#define SW_TX       33 // ESP32 UART TX to TMC2209 RX
#define SW_RX       27 // ESP32 UART RX to TMC2209 TX
#define DRIVER_ADDRESS 0b00 // Default driver address
#define R_SENSE      0.11f // Set according to your TMC2209 module

HardwareSerial mySerial(1);
TMC2209Stepper driver(&mySerial, R_SENSE, DRIVER_ADDRESS);

```

```
unsigned long lastStepTime = 0; // Track time for step pulses
const int stepDelay = 500; // Adjust timing for speed
bool motorSpin = false;

void setup() {
    Serial.begin(115200);

    //Coil setup
    // Setup PWM channels
    ledcSetup(pwmChannelOne, pwmFrequency, pwmResolution);
    ledcSetup(pwmChannelTwo, pwmFrequency, pwmResolution);
    ledcSetup(pwmChannelThree, pwmFrequency, pwmResolution);

    // Attach PWM channels to pins
    //7.1
    ledcAttachPin(coilPinOne, pwmChannelOne);
    //7.2
    ledcAttachPin(coilPinTwo, pwmChannelTwo);
    //7.3
    ledcAttachPin(coilPinThree, pwmChannelThree);

    // Set direction pins as output
    pinMode(directionPinOne, OUTPUT);
    pinMode(directionPinTwo, OUTPUT);
    pinMode(directionPinThree, OUTPUT);

    // Stepper setup
    mySerial.begin(115200, SERIAL_8N1, SW_RX, SW_TX);
    pinMode(EN_PIN, OUTPUT);
    pinMode(STEP_PIN, OUTPUT);
    pinMode(DIR_PIN, OUTPUT);
    digitalWrite(EN_PIN, LOW);
    digitalWrite(DIR_PIN, HIGH);
    driver.begin();
    driver.toff(5);
    driver.rms_current(600);
    driver.microsteps(16);
    driver.en_spreadCycle(false);
    driver.pwm_autoscale(true);

    Serial.println("Setup Done");
}

void loop() {
```

```

// Generate step pulses at regular intervals
if (motorSpin) {

    Serial.print("Moving motor");
    digitalWrite(STEP_PIN, HIGH);
    delayMicroseconds(500);
    digitalWrite(STEP_PIN, LOW);
    delayMicroseconds(500);
}

else {
    digitalWrite(STEP_PIN, LOW);
    delayMicroseconds(500);
}

if (Serial.available()) {
    String command = Serial.readStringUntil('\n');
    command.trim();

    Serial.print("Received Command: ");
    Serial.println(command);

    // Coil control
    if (command == "X pos"){
        //away from bert coil 3
        digitalWrite(directionPinThree, LOW); // AWAY FROM BERT
        ledcWrite(pwmChannelThree, 5); // Coil ON
    }
    else if (command == "X neg"){
        //towards bert coil 3
        digitalWrite(directionPinThree, HIGH); // TOWARDS BERT
        ledcWrite(pwmChannelThree, 5); // Coil ON
    }
    else if (command == "Y pos"){
        //away from bert coil 1
        digitalWrite(directionPinOne, LOW); // AWAY FROM BERT
        ledcWrite(pwmChannelOne, 5); // Coil ON
    }
    else if (command == "Y neg"){
        //towards bert coil 1 **add hole in acrylic?
        digitalWrite(directionPinOne, HIGH); // TOWARDS BERT
        ledcWrite(pwmChannelOne, 5); // Coil ON
    }
    else if (command == "Z pos"){
        // towards bert coil 2
        digitalWrite(directionPinTwo, HIGH); // TOWARDS BERT
    }
}

```

```
ledcWrite(pwmChannelTwo, 5); // Coil ON
}
else if (command == "Z neg"){
    //away from bert coil 2
    digitalWrite(directionPinTwo, LOW); // AWAY FROM BERT
    ledcWrite(pwmChannelTwo, 5); // Coil ON
}
else if (command == "XY pos"){
    //away from bert coil 3
    digitalWrite(directionPinThree, LOW); // AWAY FROM BERT
    digitalWrite(directionPinOne, LOW); // AWAY FROM BERT
    ledcWrite(pwmChannelThree, 5); // Coil ON
    ledcWrite(pwmChannelOne, 5); // Coil ON
}
else if (command == "XY neg"){
    digitalWrite(directionPinThree, LOW); // AWAY FROM BERT
    digitalWrite(directionPinOne, HIGH); // TOWARDS BERT
    ledcWrite(pwmChannelThree, 5); // Coil ON
    ledcWrite(pwmChannelOne, 5); // Coil ON
}
else if (command == "XZ neg"){
    digitalWrite(directionPinThree, LOW); // AWAY FROM BERT
    digitalWrite(directionPinTwo, LOW); // AWAY FROM BERT
    ledcWrite(pwmChannelThree, 5); // Coil ON
    ledcWrite(pwmChannelTwo, 5); // Coil ON
}
else if (command == "XYZ Z neg"){
    digitalWrite(directionPinThree, LOW); // AWAY FROM BERT
    digitalWrite(directionPinOne, LOW); // TOWARDS BERT
    digitalWrite(directionPinTwo, LOW); // AWAY FROM BERT
    ledcWrite(pwmChannelThree, 5); // Coil ON
    ledcWrite(pwmChannelOne, 5); // Coil ON
    ledcWrite(pwmChannelTwo, 5); // Coil ON
}
else if (command == "XYZ YZ neg"){
    digitalWrite(directionPinThree, LOW); // AWAY FROM BERT
    digitalWrite(directionPinOne, HIGH); // TOWARDS BERT
    digitalWrite(directionPinTwo, LOW); // AWAY FROM BERT
    ledcWrite(pwmChannelThree, 5); // Coil ON
    ledcWrite(pwmChannelOne, 5); // Coil ON
    ledcWrite(pwmChannelTwo, 5); // Coil ON
}
else if (command == "Coil OFF"){
    ledcWrite(pwmChannelThree, 100); // Coil OFF
    ledcWrite(pwmChannelOne, 100); // Coil OFF
    ledcWrite(pwmChannelTwo, 100); // Coil OFF
```

```
}

// Linear Actuator Control
if (command == "EXT"){
    motorSpin = true;
    digitalWrite(DIR_PIN, LOW);
}
else if (command == "RTR"){
    //turn coils off
    ledcWrite(pwmChannelThree, 100); // Coil OFF
    ledcWrite(pwmChannelOne, 100); // Coil OFF
    ledcWrite(pwmChannelTwo, 100); // Coil OFF
    motorSpin = true;
    digitalWrite(DIR_PIN, HIGH);
}
else if (command == "OFF"){
    motorSpin = false;
}

// Emergency OFF
if (command == "SHUT OFF"){
    //Coil and actuator is stopped
    ledcWrite(pwmChannelThree, 100); // Coil OFF
    ledcWrite(pwmChannelOne, 100); // Coil OFF
    ledcWrite(pwmChannelTwo, 100); // Coil OFF
    digitalWrite(directionPinThree, HIGH); // AWAY FROM BERT
    digitalWrite(directionPinOne, HIGH); // TOWARDS BERT
    digitalWrite(directionPinTwo, HIGH);
    motorSpin = false;
}

Serial.print("A");

}
```

Appendix C: Hazards and Risk Analysis

Table C.1 — Examples of hazards

Energy hazards	Biological and chemical hazards	Performance-related hazards
Acoustic energy	Biological agents	Data
— infrasound	Bacteria	— access
— sound pressure	Fungi	— availability
— ultrasonic	Parasites	— confidentiality
Electric energy	Prions	— transfer
Electric fields	Toxins	— integrity
Leakage current	Viruses	Delivery
— earth leakage		— quantity
— enclosure leakage	Chemical agents	— rate
Magnetic fields	Carcinogenic, mutagenic, reproductive	Diagnostic information
Static discharge	Caustic, corrosive	— examination result
Voltage	— acidic	— image artefacts
Mechanical energy	— alkaline	— image orientation
Kinetic energy	— oxidants	— image resolution
— falling objects	Flammable, combustible, explosive	— patient identity / information
— high pressure fluid injection	Fumes, vapors	Functionality
— moving parts	Osmotic	— alarm
— vibrating parts	Particles (including micro- and nanoparticles)	— critical performance
Potential (stored) energy	Pyrogenic	— measurement
— bending	Solvents	
— compression	Toxic	
— cutting, shearing	— asbestos	
— gravitational pull	— heavy metals	
— suspended mass	— inorganic toxicants	
— tension	— organic toxicants	
— torsion	— silica	
Radiation energy	Immunological agents	
Ionizing radiation	Allergenic	
— accelerated particles (alpha particles, electrons, protons, neutrons)	— antiseptic substances	
— gamma	— latex	
— x-ray	Immunosuppressive	
Non-ionizing radiation	Irritants	
— infrared	— cleaning residues	
— laser	Sensitizing	
— microwave		
— ultraviolet		
Thermal energy		
Cryogenic effects		
Hyperthermic effects		

Figure 93. Table C.1 – Examples of hazards from ISO 14971:2019.